A Study of Aerodynamics in Kevlar-Wall Test Sections

Kenneth A. Brown

Thesis submitted to the faculty of the Virginia Polytechnic Institute and State University
in partial fulfillment of the requirements for the degree of

Master of Science
In
Mechanical Engineering

William J. Devenport
Aurelien Borgoltz
Wing F. Ng

April 30, 2014
Blacksburg, VA

Keywords: aerodynamics, wind tunnel, anechoic, Kevlar-wall, hard-wall, lift interference, blockage, porosity, panel method

A Study of Aerodynamics in Kevlar-Wall Test Sections

Kenneth A. Brown

Abstract

This study is undertaken to characterize the aerodynamic behavior of Kevlar-wall test sections and specifically those containing two-dimensional, lifting models. The performance of the Kevlar-wall test section can be evaluated against the standard of the hard-wall test section, which in the case of the Stability Wind Tunnel (SWT) at Virginia Tech can be alternately installed or replaced by the Kevlar-wall test section. As a first step towards the evaluation of the Kevlar-wall test section aerodynamics, a validation of the hard-wall test section at the SWT is performed, in part by comparing data from NACA 0012 airfoil sections tested at the SWT with those tested at several other reliable facilities. The hard-wall test section showing good merit, back-to-back tests with three different airfoils are carried out in the SWT's hard-wall and Kevlar-wall test sections. Kevlar-wall data is corrected for wall interference with a panel method simulation that simulates the unique boundary conditions of Kevlar-wall test sections including the Kevlar porosity, wall deflection, and presence of the anechoic chambers on either side of the walls. Novel measurements of the boundary conditions are made during the Kevlar-wall tests to validate the panel method simulation. Finally, sensitivity studies on the input parameters of the panel method simulation are conducted. The work included in this study encompasses a wide range of issues related to Kevlar-wall as well as hard-wall tunnels and brings to light many details of the performance of such test sections.

Acknowledgements

I am very grateful to my adviser, Dr. Devenport, for preparing and educating me so thoroughly to this point. He always has an eye out for my long-term interests as well as the short-term goals and has given good advice both professionally and personally. Dr. Borgoltz has also contributed significant time to teaching me about wind tunnel testing for which I am very grateful. I would like to thank Dr. Ng, also, for serving on my committee and giving me key contacts in the industry. I am also grateful to Dr. William Mason for sharing his knowledge on panel methods with me.

The tests performed for this study would not have been made without the worthwhile work of Bill Otejens and Mike Morton. Liselle Joseph gave much needed help multiple times when we were running out of time in the wind tunnel. Also, thank you to Nanya Intaratep for her help with trip fabrication and other testing issues. The Aerospace and Ocean Engineering Shop has been integral to my work in the last 2 years, and I want to say thank you to James Lambert, Scott Patrick, Andy Tawney, Cameron Hollandsworth, and Matt Mills.

The Lab 7 research group members have become good friends including Nathan Alexander, Manuj Awasthi, Liselle Joseph, Tim Meyers, Ian Clark, David Wisda, and Nathaniel Ross, as well as Dan Cadel.

I also appreciate my roommates of the last 4 years, including Lucas Shoults, Scott Hopkins, Mark Bychowski, Eli White, and Patrick Trail – who once gave me the advice, "Don't give up man; I know you're winded, but there's a light at the end of the tunnel."

Table of Contents

List of Tables

List of Figures

CHAPTER 1. Introduction

Since 2006, the Virginia Tech SWT has pioneered a new type of test section for aeroacoustic and aerodynamic testing. Applications for the Kevlar-wall anechoic test section, as it is called, are the collection of noise data from wind turbine blades, research of surface roughness effects on pressure fluctuations in the boundary layer, and study of rotors embedded in a boundary layer, for example. The Kevlar-wall test section has the advantage in all these cases of providing detailed acoustic measurements without the need for an open-jet test section.

The Kevlar-wall test section is novel in that the flow is contained within tensioned side walls made of Kevlar fabric. It was first developed at the Virginia Tech SWT and later adopted at the Japan Aerospace Exploration's (JAXA) 2m-by-2m Low Speed Wind Tunnel (Remillieux *et al.* 2008, Ito *et al.* 2010). In less than a decade, the Kevlar-wall wind tunnel has matured to use in full-scale testing through improvements to both the aeroacoustic and aerodynamic measurement capabilities as reviewed in (Devenport *et al.* 2010b, Devenport *et al.* 2013).

The advantages of such a Kevlar-wall test section from an aeroacoustic standpoint are fairly apparent. The test section acts acoustically as if an open-jet test section yet does not produce the large shear layers characteristic of such test sections, thus reducing parasitic noise and permitting closer microphone mounting. The advantages from an aerodynamic standpoint, compared to an open-jet section, are a dramatic reduction in lift interference for a much closer simulation of free-flight. On the other hand, compared to a hard-wall test section, the Kevlar-wall test sections exhibits a reduction in wall interference effects, at least for low to moderate loading conditions. This reduction is due to the boundary conditions of the porous, flexible Kevlar-walls which tend to place the test section's aerodynamic performance between that of a hard-wall and an open-jet test section.

This study examines wall interference corrections for Kevlar-wall test sections to build upon knowledge of the fundamental behavior of such test sections and refine interference prediction methods already in place. For comparison purposes and to put the Kevlar-wall corrections in context, the wall interference and aerodynamic performance of hard-wall test sections will be described in full. The work focuses on the wall interference experienced by two-dimensional airfoil models, though the application of many of the methods discussed here are applicable to other types of models, as well.

CHAPTER 2. Literature Review

When considering aerodynamic corrections in wind tunnels, there are three freestream conditions experienced by a model that are affected by the presence of the wind tunnel walls which are the dynamic pressure, angle of attack, and Mach number (Ulbrich 2009). Corrections to account for changes in these values with wind tunnel walls are typically first-order; they correct the freestream, or far-field, value but neglect changes in distribution of these values across the model. Mach number is typically of lessor importance for low-speed testing such as performed at the SWT, so corrections for dynamic pressure and angle of attack will be the focus of this study.

Corrections to dynamic pressure are usually termed blockage corrections. Blockage occurs when mass flow must accelerate or decelerate to maintain continuity while passing through a test section. For the case of closed, or hard-wall, test sections, blockage leads to an increase in dynamic pressure as the flow must accelerate past a model blocking its path. For the case of open-jet test sections, blockage effects generally lead to a decrease in the dynamic pressure as the flow expands and thus decelerates beyond the dimensions of the nozzle outlet. Blockage corrections can be divided into two categories. First, solid blockage accounts for the change in dynamic pressure of the flow in the region around the model due to the change in test section area caused by the presence of the model. Second, wake blockage occurs by the same principal as solid blockage except that the model's wake, a viscous region of low momentum flow separate from the freestream flow, is the structure creating the change in test section area.

Corrections to angle of attack are usually termed lift interference corrections. Lift interference, by definition, is any effect that alters the circulation around the model (Ewald 1998), so these effects usually can be accounted for by a correction to the angle of attack. Specifically, the streamline curvature around a model due to the presence of the wind tunnel walls is altered from the free-flight case. Streamline curvature produces an increase in angle of attack, lift, and quarter-chord pitching moment for hard-wall test sections and a decrease in these for open-jet test sections. Furthermore, in the case of semi-span wings, the presence of the wind tunnel test section affects the downwash normal to the freestream direction. For the hard-wall test section, a wing will have a smaller downwash and larger upwash relative to the same angle of attack in free-flight. This can be accounted for by calculating an effective angle of attack, slightly larger than the measured geometric angle of attack, which is equivalent to the free-flight angle of attack. The measured lift and drag must then be transformed to align with the effective angle of attack. The same process occurs for open-jet test sections, but the downwash and upwash changes are in the reverse directions.

This chapter presents a review of past work in wall interference corrections. The first three sections focus on well-established methods used amongst the wind tunnel community: classical corrections, panel method corrections, and measured variable corrections. The final section reviews the fundamentals and progress of methods made in the Kevlar-wall wind tunnel community. Included throughout these will be discussion on the details of the blockage and lift interference corrections and their application to wind tunnel testing.

2.1. Classical Corrections

Classical corrections are defined by four characteristics: the use potential flow theory, inclusion of wall effects as perturbations to the flow, assumption that model geometries small relative to the wind tunnel size and have straight, downstream trailing wakes, and assumption of wind tunnel walls that are straight, infinite, and require either constant pressure or zero normal velocity (Ewald 1998). An analysis known as the *method of images* adheres to these characteristics

and represents the model as a set of singularities that produce a flow field similar to that of the actual model. The singularities typically employed are doublets to model solid blockage, sources to model wake blockage, and vortices to model circulation. In addition to the singularity placed at the model location, appropriate placement of singularities outside the test section is then sought to exactly cancel the normal velocity produced by the internal singularity at the test section walls. This placement takes the form of images, alternatively positively and negatively signed, located in the model's streamwise location but spaced apart in the normal direction by the test section height and extending to infinity. When the velocity induced by these images is summed over a sufficiently large number of images, the streamlines at the location of the wind tunnel walls become straight, and they thus simulate the actual wind tunnel wall if the boundary layer thickness is neglected. The result is that the singularities outside the test section describe the incremental interference for a given component of velocity due to the presence of the walls which allows for correction of the measured angle of attack and aerodynamic coefficient data.

2.1.1. Blockage Corrections

In contrast to free-flight where the flow is free to expand or contract in the direction normal to the freestream, mass flow through a test section must be conserved, so changes in flow area lead to changes in flow velocity. Both solid blockage and wake blockage are accounted for by a correction factor, ε, given by

$$\varepsilon = \frac{\Delta V}{V_u} \qquad \text{Equation 2.1}$$

where ΔV is the incremental velocity in the streamwise direction and V_u is the uncorrected freestream velocity. The factor ε is used to correct the dynamic pressure, q, by

$$q = q_u(1 + 2\varepsilon + \varepsilon^2) \qquad \text{Equation 2.2}$$

where the subscript u indicates the uncorrected value. The higher order ε term is negligible since ε is a small number. The corrected dynamic pressure is ultimately used to adjust lift, moment, and drag coefficients which are normalized on dynamic pressure.

2.1.1.1. Solid Blockage

For two-dimensional flows over airfoils, Allen and Vincenti (1944) recommend the following solid blockage correction

$$\varepsilon_{sb} = \frac{1}{[1 - M^2]^{3/2}} \Lambda\sigma \qquad \text{Equation 2.3}$$

$$\Lambda = \frac{16}{\pi} \int_0^l \frac{y}{c} \left\{ \left[1 - P\left(\frac{x}{c}\right) \right] \left(1 + \frac{dy}{dx} \right) \right\}^{0.5} d\left(\frac{x}{c}\right) \qquad \text{Equation 2.4}$$

$$\sigma = \left(\frac{\pi^2}{48}\right)\left(\frac{c}{h}\right)^2 \qquad \text{Equation 2.5}$$

where M is the uncorrected Mach number, x and y are the abscissa and ordinate of the base profile of the airfoil, P is the measured pressure distribution at the given chordwise location, c is the airfoil chord, and h is the test section dimension in the thickness-wise direction. The derivation of this correction, described in part below, is given in full detail by Lock (1929) and Glauert (1933). This correction is based upon a relation between the airfoil's thickness and chord and an equivalent upstream-pointing doublet of strength $\frac{\pi}{2}\Lambda t^2 U_\infty$ which produces a potential flow-field equivalent to

that of a cylinder $t\sqrt{\Lambda}$ in diameter. Using an infinite series of images of the doublet above and below the test section, the increment to the freestream velocity in the streamwise direction is calculated ignoring higher order terms of $\frac{t}{h}$ and $\frac{c}{h}$. In order to find the value of Λ, the experimentally measured pressure distribution around the airfoil is used to calculate the velocity along the airfoil surface by Bernoulli's equation which is then integrated and used to give the effective doublet strength. An additional refinement to this correction is to adjust the value of h to account for boundary layer growth.

2.1.1.2. Wake Blockage

Similarly to solid blockage, wake blockage induces a change in the streamwise velocity felt at the model location due to the blockage of the wake behind the model. The wake has less dynamic pressure than the surrounding freestream fluid due to the viscous effects experienced by the flow which result in transfer of dynamic pressure to thermal energy (Allen and Vincenti 1944). Although the dynamic pressure, and thus the velocity, in the wake are reduced, the total mass flow through the test section must be maintained to satisfy mass continuity, so the inviscid flow outside the wake must accelerate to account for the loss of velocity in the wake.

To calculate the blockage effect of a wake in two-dimensions, a source whose strength is determined by the measured drag coefficient is placed at the airfoil location along with an infinite series of source images on either side of the test section. The flow created by this series of sources does not violate the boundary condition of the closed wind tunnel walls, but does induce both a velocity acting against the freestream velocity in the upstream and a velocity acting with the freestream in the downstream. An incremental addition to the freestream is then required to maintain the upstream freestream velocity at its measured value which is given by

$$\varepsilon_{wb} = \frac{1 + 0.4M^2}{1 - M^2}\tau C_d \qquad \text{Equation 2.6}$$

$$\tau = \frac{c/h}{4} \qquad \text{Equation 2.7}$$

where C_d is the uncorrected drag coefficient (Allen and Vincenti 1944).

2.1.2. Streamline Curvature

In two-dimensional flow such as the flow over a full span model in a wind tunnel, the lift interference correction is due to streamline curvature. The presence of the wind tunnel walls alters the path of the streamlines as compared to their free-flight behavior; the streamlines become more curved as a result of the walls. The effect for a hard-wall test section amounts to an additional upwash in the upstream of the airfoil that would not exist in free-flight.

Allen and Vincenti (1944) again use a method of images analysis to correct for the streamline curvature. The lift of the airfoil is represented by a vortex sheet spread over the chordline. The sum of images of the vortex sheet moving progressively away from the test section produce a zero transverse velocity at the tunnel boundaries. Along the singularity location on the chordline, the result is that the streamwise component of velocity due to the vortex sheet images cancels while the velocity normal to the chord due to the images adds one to another. This additive velocity is the walls' interference on the flow. The analysis assumes that the model is small relative to the test section, the model is negligibly thin, and angles of attack are small, however, experience has shown the method to valid for airfoils of finite thickness and angles of attack up to flow separation. It is interesting to note that there is a streamwise component of induced velocity, also, as one moves away from the singularity location. This component is only significant for large models and is usually neglected.

The upwash induced by the walls can be accounted for with a correction to the angle of attack, lift, and pitching moment as

$$\Delta\alpha_{sc} = \frac{1}{\sqrt{1-M^2}}\frac{57.3\sigma}{2\pi}(C_l + 4C_{m,\frac{1}{4}c}) \quad \text{Equation 2.8}$$

$$\Delta C_{l,sc} = \frac{1}{1-M^2}\sigma C_l \quad \text{Equation 2.9}$$

$$\Delta C_{m,\frac{1}{4}c,sc} = -\frac{1}{1-M^2}\frac{\sigma}{4}\,C_l \quad \text{Equation 2.10}$$

where C_l is the uncorrected lift coefficient and $C_{m,\frac{1}{4}c}$ is the uncorrected coefficient of moment about quarter-chord.

This preceding correction is accurate to the second order of $\left(\frac{c}{h}\right)$ meaning that only the first and second order terms of chord over tunnel height have been retained and the others assumed negligible. Ewald (1998) warns that such a second order analysis is valid only for models with $\left(\frac{c}{h}\right) < 0.4$ for the incompressible case and with $\left(\frac{c}{\beta h}\right) < 0.4$ for the compressible case. For cases outside these envelopes, they recommends the corrections to the fourth order of $\left(\frac{c}{h}\right)$

$$\Delta\alpha_{sc} = \frac{\pi c^2}{96\beta h^2}(C_l + 4C_{m_{0.25c}}) - \frac{7\pi^3 c^4 C_l}{30720\beta^3 H^4} \quad \text{Equation 2.11}$$

$$\Delta C_{l,sc} = C_l\left\{-\frac{\pi^2}{48}\left(\frac{c}{\beta h}\right)^2 + \frac{7\pi^4}{3072}\left(\frac{c}{\beta H}\right)^4\right\} \quad \text{Equation 2.12}$$

$$\Delta C_{m,\frac{1}{4}c,sc} = C_l\left\{\frac{\pi^2}{192}\left(\frac{c}{\beta h}\right)^2 - \frac{7\pi^4}{15360}\left(\frac{c}{\beta H}\right)^4\right\} \quad \text{Equation 2.13}$$

2.1.3. Drag

Pressure gradients at the model location in a wind tunnel develop due to boundary layer growth on the wind tunnels walls along the length of the tunnel and the presence of the wake behind a model, both of which cause a decrease in total flow area and thus higher velocities and lower pressures downstream than upstream. In the presence of a pressure gradient in a wind tunnel, an additional correction required for the drag data is for horizontal buoyancy. There are two factors that contribute to horizontal buoyancy, both of which stem from the pressure gradient present in wind tunnels of constant cross-section (Glauert 1933). The first contribution to horizontal buoyancy comes directly from the streamwise pressure gradient, $\frac{\mathrm{dp}}{\mathrm{dx}}$, which when multiplied by the volume of the model yields a drag force on the model that would not exist in free-flight. The second contribution is a result of the squeezing of streamlines as the wall boundary layer grows which acts to accelerate the flow. The model and a virtual mass around the model can be thought of as accelerating relative to the flow, and this causes an additional drag force on the model. For an open test section, on the other hand, this effect produces a thrust force instead as the flow expands and decelerates. The total buoyancy drag force, $\mathrm{D_B}$, including both contributions is

$$D_B = \frac{6h^2}{\pi}\Lambda\sigma\frac{dp}{dx} \quad \text{Equation 2.14}$$

where h is the height of the test section, Λ and σ are as defined in the blockage section ,and $\frac{\mathrm{dp}}{\mathrm{dx}}$ is the streamwise pressure gradient (Allen and Vincenti 1944). A method of images calculation yields the pressure gradient due to the presence of the wake as

$$\frac{dp}{dx} = -\left\{\frac{1+0.4M^2}{[1-M^2]^{\frac{3}{2}}}\right\}\frac{\pi C_d q c}{6h^2} \qquad \text{Equation 2.15}$$

where q is the uncorrected dynamic pressure. Combining Equations 2.14 and 2.15, the drag due to the pressure gradient caused by the wake is

$$C_{dc,b} = C_d\left\{\frac{1+0.4M^2}{[1-M^2]^{\frac{3}{2}}}\right\}\Lambda\sigma \qquad \text{Equation 2.16}$$

where the subscript c refers to the corrected quantity and the subscript b indicates it is the buoyancy correction to drag only. This correction to drag is added to the corrections for solid and wake blockage as in Equations 2.3 and 2.6, respectively. Barlow *et al.* (1999) state that the buoyancy effect caused by the growing boundary layer on the wind tunnel walls is usually insignificant for wings, only becoming significant for longer models such as full airplane or torpedo models.

2.1.4. Combined Corrections

The blockage and streamline curvature corrections of the previous sections can be combined with the aid of Equation 2.2 to produce several useful formulas to compute all the aerodynamic corrections of a hard-wall test section.

$$\Delta\alpha_{sc} = \frac{1}{\sqrt{1-M^2}}\frac{57.3\sigma}{2\pi}(C_l + 4C_{m,\frac{1}{4}c}) \qquad \text{Equation 2.8}$$

$$C_{lc} = C_l\left[1 - \frac{1}{1-M^2}\sigma - \frac{2-M^2}{[1-M^2]^{\frac{3}{2}}}\Lambda\sigma - \frac{2M^2(1+0.4M^2)}{1-M^2}\tau C_d\right] \qquad \text{Equation 2.17}$$

$$C_{mc,\frac{1}{4}c} = C_{m,\frac{1}{4}c}\left[1 - \frac{2-M^2}{[1-M^2]^{\frac{3}{2}}}\Lambda\sigma - \frac{2M^2(1+0.4M^2)}{1-M^2}\tau C_d\right] - C_l\frac{1}{1-M^2}\frac{\sigma}{4} \qquad \text{Equation 2.18}$$

$$C_{dc} = C_d\left[1 - \frac{2-M^2}{[1-M^2]^{\frac{3}{2}}}\Lambda\sigma - \frac{2M^2(1+0.4M^2)}{1-M^2}\tau C_d\right] \qquad \text{Equation 2.19}$$

The buoyancy drag correction is not included in Equaiton 2.19 above because drag data taken with a wake rake such as at the SWT, do not detect the presence of any streamwise pressure gradient and therefore do not measure buoyancy drag. As noted above, for small models such as airfoils this is not believed to introduce significant error to the drag measurement.

In the preceding method of images analyses, the wall interference effect on either the dynamic pressure or angle of attack is evaluated either at the model center, the center of loading, quarter-chord, or an average over the model.

2.2. Panel Method Corrections

Another approach to corrections are through panel methods which fall under the category of conventional corrections as specified by Ewald (1998) as they are less restrictive than classical corrections, the only assumption remaining from the classical assumptions being that wall effects can be treated as perturbations to the flow. Panel methods may be used for corrections either standalone or in combination with static wall pressure measurements. First, several examples of standalone approaches will be examined followed by the static wall pressure approaches in the following section. All the examples presented are three-dimensional panel method codes unless otherwise noted.

Ulbrich and George (2000) describe the panel method code ANTARES used at the NASA Ames 11 ft. Transonic Wind Tunnel. The model is represented with both a point doublet to simulate blockage and a line doublet to simulate lift interference. The walls are represented by a paneling of linearly varying source panels. As with all panel methods, the coefficient matrix describing the effect of each panel's source strength on the velocity components at the center, or control point, of every other panel is calculated from potential flow theory. The resultant matrix is found by summing the freestream velocity and a term that specifies the porosity of each panel. Inverting the coefficient matrix using a double-precision solver and multiplying it by the resultant matrix yields the strengths of all the panels. The wall panels are then considered independently with their contribution to the streamwise and transverse velocity around the model being equal to the blockage and lift interference of the walls. The paper includes a procedure to use the Prandtl-Glauert transformation to handle compressible flow, as well as incompressible.

Of interest to the present paper is the paneling technique of the rectangular wind tunnel walls which included 7200 panels in total: 60 panels in the streamwise direction and 120 panels in the circumferential direction around the cross-section of the test section for 30 panels per wall. Cosine spacing was used in streamwise direction with a total test section length of 8 tunnel widths. For verification of the closed wall panel code, the panel method solution was compared to the exact method of images solution. For the perforated wall condition, two different classical solutions were used for comparison.

Joppa (1973) used a vortex-filament panel method to produce corrections to wind tunnel data of high lift wings in closed test sections. The lift produced by the wing is represented by a vortex at the quarter-chord location, and the walls by a set of vortex panels, a vortex lattice. Joppa's work is innovative in that it uses an iterative procedure to calculate the wake trajectory behind the airfoil rather than assume a linear deflection or no deflection at all. The primary goal of Joppa's paper is to show that the difference in trajectory of the wake from free-flight to tunnel conditions which equates to less deflection in the tunnel will impact the pitching moment significantly. It is noted that the streamwise wall interference caused by the difference in wake trajectory between the freestream and tunnel conditions is just 3% even at extreme wake deflections, so transverse interference, or angle of attack correction, is all that is considered. Unlike the method of Ulbrich and George (2000) which considers the wall's contribution to velocity at the model, the angle of attack correction of Joppa is found by directly differencing the flow solution around the model in the wind tunnel and that outside the wind tunnel. Corrections to drag coefficient and pitching moment coefficient are compared with and without the deflected wake with only the latter being considerably affected by the wake treatment.

Joppa states that the vorticity shed at the wingtips rolls up into a cylindrical shape just downstream of the wing. It is shown for a simple case that the wake's vortex sheet can be represented by two vortex filaments extending downstream from quarter- and three-quarter span with only 2.5% difference from the full vortex sheet representation. The trajectory of these two vortex filament lines are found by sweeping and iterating. First, a downstream sweep is performed calculating the angle of each new vortex segment from the contribution of the upstream segments

and bound vortex. This procedure is repeated for several iterations until convergence occurs. Practically, a double-pass iteration is performed: first an iteration allowing deflection only in the downwash direction, then an iteration allowing deflection only in the spanwise direction. This maintains stability and allows convergence in 3 or 4 double iterations.

This same iteration procedure is used for both the case with tunnel walls and in the freestream. Once the flow solution for both of these is calculated, the correction angle of attack is given by

$$\Delta\alpha = \tan^{-1}\left(\frac{V_y}{V_x}\right)_T - \tan^{-1}\left(\frac{V_y}{V_x}\right)_{FS} \qquad \text{Equation 2.20}$$

where V_x and V_y are the horizontal and vertical velocity components, respectively, at some sample point on or about the model. This change in angle of attack is related to the traditional boundary correction factor, δ, by

$$\delta = \left(\frac{CU_\infty}{2\Gamma b}\right)\left[\tan^{-1}\left(\frac{V_y}{V_x}\right)_T - \tan^{-1}\left(\frac{V_y}{V_x}\right)_{FS}\right] \qquad \text{Equation 2.21}$$

where C is the cross-sectional area of the tunnel, Γ is the circulation produced by the model, and b is the span length of the model.

It is also useful to observe the wall modeling used by Joppa which is in contrast to the arrangement of Ulbrich and George (2000). For a square tunnel, 16 panels per wall were found sufficient for convergence in a study that examined cases with 12, 16, and 20 panels per wall. For a model with vortex span to tunnel height ratio of 0.4, convergence was found with 3-4 tunnel diameters paneled length in the streamwise direction. These differences from Ulbrich may be due to the difference in wall panel type from linearly varying source panels in Ulbrich to a vortex filament lattice in Joppa. In Joppa's code, the streamwise filaments of the most downstream row of vortex panels are extended far downstream of the model so as to accurately model vorticity of the trailing vortices while the control point are kept in their same locations.

Another panel method is given by Smyth (1984) with results about the wake deflection. Smith states in agreement with Joppa's results that the wake will have only a large effect on the pitching moment correction, and moreover the effect decreases with increasing aspect ratio of the model. Two wake models were used to achieve two different levels of accuracy. The lower accuracy method uses an undeflected wake trailing straight back from the model trailing edge and parallel with the walls for the wind tunnel panel method. For the freestream panel method, it uses a half-deflected wake that trails at an angle halfway between the undeflected case and the angle formed by the chordline of the model. For the more sophisticated modeling, the author uses an iterative wake solution similar to that of Joppa. Smith also comments that the singularities used in a single domain panel method are either vortices or doublets. For a dual domain method where there exterior and interior flow fields are separated by paneling at the entrance and exit of the test section, doublets and sources are typically used.

A two-dimensional approach, the panel method of Bowcutt (1985) shows a slightly different approach. Less attention is given to the wake as in Joppa and Smith, however, Bowcutt models several other viscous phenomenon with great detail. An airfoil model is paneled with constant strength source panels on the outer airfoil profile to create solid blockage and constant strength vortex panels on the camber line to create lift. Four different viscous flow phenomena are accounted in Bowcutt's code including boundary layer growth on the wind tunnel walls, the separation bubble, if applicable, behind a stalled wing, the free-shear layer, if applicable, between the freestream and separation bubble, and the viscous wake in the downstream. These phenomena lead to corrections for horizontal buoyancy, solid blockage, wake blockage, and streamline curvature. Bowcutt's approach to the corrections parameters follows the same method as Joppa in that it takes the difference in tunnel and free-flight solutions and applies that same difference to the

measured wind tunnel data. Rather than angle of attack, however, Bowcutt differences the coefficients of lift, moment, and drag from the two solutions. The author notes that methods such as these that compare the wind tunnel and free-flight solutions leverage the fact that the same errors present in the wind tunnel solution due to the invicid modeling should also be present in the free-fight solution and should roughly cancel.

Mokhtar and Britcher (2004) use an approach that is especially interesting because the boundary shape changes in an iterative fashion. Their panel method uses a horseshoe vortex to create lift on a simulated airfoil. The study was done for open-jet test sections and included a two-step iteration procedure to arrive at the final boundary conditions. First, the wind tunnel walls are formed from solid, straight panels which impose non-penetration through the walls. Second, the slopes of the wall panels are adjusted according to the velocity distribution and the flow solution resolved using a constant pressure boundary condition. The second step involves iterations and was facilitated with the one-step method, leading to convergence usually within 4 iterations. To verify the accuracy of the blockage of the panel method simulation, the author used the three-dimensional method of images solution from Krynytzky (1998) and compared the velocity increment with that produced by a three-dimensional doublet inserted into the panel method simulation.

In all the preceding panel method examples, a set of inviscid singularities is used to represent the wind tunnel flow, the accuracy of which may understandably be called into question. Of course, the internal singularities used to represent the airfoil in the test section are not an exact replication of the actual flow field in the wind tunnel. However, wind tunnel corrections are far-field effects (Joppa 1973, Bowcutt 1985), and these effects on singularities are the same as those on the actual model. The far-field effects of the tunnel walls are generally small in and of themselves, so small errors in interference solution will have an even smaller effect on the corrected global quantities (Bowcutt 1985). Thus, errors in the interference modeling and solution can be considered to have a second-order effect on the final corrected quantities. Similarly, Iyer and Everhart (2001) state that the exact placement of singularities is not important due to the far-field nature of wind tunnel corrections.

Panel methods model the flow solution in a wind tunnel more accurately than method of images analyses in almost every case, and they are also adaptable for slotted- and porous-walled wind tunnels where the wall boundary streamlines are no longer straight although the methods for such are not fully proven (Barlow *et al.* 1999). Panel method corrections can be applied in the case of a slotted-wall tunnel with vortex lattice paneling by using lattices for the solid sections and source panels for the slots (*ibid.)*. Lee (1981) also agrees that for the paneling of slotted-walled sections, both sources and doublets are used. Mokry (1985) indicates that in slotted-walled corrections, it is important to match as best as possible the mass and momentum flow across the slots. Porous, or perforated wall, tunnels have different corrections because viscous effects play an important role in the flow through the walls.

While such research may not be a high priority for most wind tunnels, the usefulness of the panel method in modeling porous Kevlar makes it a useful tool for Kevlar-wall test section corrections. As such, panel methods are chosen as the correction method of choice by the author.

2.3. Measured Variable Corrections

The last category of correction methods are measured variable methods which are inherently not *a priori*. They are useful when linear theory used by the classical corrections is not valid (Ashill *et al.* 1998). Measured variable methods consist of the one-variable method, also

known by the wall pressure signature or "Hackett-Wilsden" method and the two-variable method, also known as the "Ashill-Keating" method.

2.3.1. One-variable method

The one-variable method uses steamwise rows of static wall pressure taps to infer the solid and wake blockage. This method was developed at NASA Langley by J.E. Hackett in the 1970's and later modified by Ulbrich in 1998 (Iyer and Everhart 2001). The one-variable method also makes use of panel methods but in a different way. First, the pressure on the wind tunnel walls is measured without the model in the test section, and then subsequently for every test condition with the model in the test section. The presence of the airfoil is represented as before with a set of singularities, in the case of Mokry (1985) with a discrete distribution of horseshoe vortices to represent lift, with distributed sources to represent wake blockage, and with distributed doublets to represent solid blockage. From the measured wall pressure data with the model is subtracted the pressure induced by the model singularities and the measured wall pressure data without the model, thus yielding the component of wall interference acting on the lift and blockage, respectively. Placing a source or sink at each wall pressure port, a least-squares regression provides a best fit of the source and sink strengths that matches the wall interference signature. From these singularity strengths, the wall interference at any point in the test section can be calculated in a panel method solution. The number of measurement points required for an accurate correction is surprisingly low, with only around 10 points total required for a test section with model chord to test section width equal to 0.2 (Ashill *et al.* 1998).

The known boundary conditions at the wind tunnel walls allow for the solution of the Dirchlet boundary condition problem as given below. The disturbance velocity of the flow in the test section is represented by ϕ which satisfies the governing potential equation. The scalar ϕ is composed of contributions from ϕ_F, the disturbance velocity caused by a model in the freestream, and ϕ_W, the disturbance velocity induced by the test section walls. Using the measured wall pressures and the freestream disturbance, the x-direction velocity, u, (the "one-variable") induced by the tunnel walls at the walls themselves is

$$\frac{u}{U_\infty} = -\frac{1}{2}C_p - \frac{1}{U_\infty}\frac{\partial \phi_F}{\partial X} \qquad \text{Equation 2.22}$$

where C_p is the measured wall pressure coefficient at the given location in the test section and $\frac{\partial \phi_F}{\partial X}$ is the derivative of freestream disturbance potential with respect to the streamwise direction. The freestream disturbance potential is calculated using measured coefficients of lift and drag and the model volume where the circulation, Γ, source strength, σ, and volume, V, used to specify the potential, respectively, of the freestream model's lift, wake blockage, and solid blockage are

$$\Gamma = \sum_m \Gamma_m = \tfrac{1}{2}AC_L \qquad \sigma = \sum_m \sigma_m = \tfrac{1}{2}AC_D \qquad \mathrm{V} = \sum_m \mathrm{V}_m \qquad \text{Equation 2.23}$$

where A is the reference area, C_L is the measured coefficient of lift, and C_D is the measured coefficient of drag. Inserting these values of circulation, source strength, and volume into the discrete distribution of horseshoe vortices, the distribution of sources, and distribution of doublets, provides the necessary equations to form an influence matrix given geometry of the test section. Specifying the u velocities at each panel on the wall as well as the entrance and exit plane velocities, the theoretical Dirchlet problem given by the governing potential equation using u and Equation 2.22 can be numerically solved for the u velocities anywhere in the test section with a panel method solver. The blockage is given by this u velocity evaluated at the model center or an average around the model. Furthermore, using the irrotationallity of potential flow, the v velocities everywhere in

the test section can be found by an integration process, the lift interference being given by the v velocity evaluated at the same location as the u velocity.

Mokry (1985) gives the setup and results for a three-dimensional half-model, doublet panel method used for measured variable interference corrections in ventilated test sections. Four streamwise rails of static pressure taps above and below an airplane model provide the basis for quadratic or cubic spanwise interpolations that yield the required boundary conditions in the test section.

Ulbrich and Steinle (1995) use a slightly extended version of the pressure signature method. The procedure uses the measured pressures to set the influence coefficients in a three-dimensional panel method solution. The matching condition between the panel method and measured wall pressures is the velocity at the walls which is computed from measured static pressures with the energy equation. Once the panel method solution is found, the freestream panel method solution is subtracted from that with the wind tunnel walls. On a practical note, the experimental validation used 198 wall static pressure measurements spaced along six rows in the NASA Ames 12 ft. wind tunnel. The authors recommend a minimum of 50 wall pressure measurements. It is noted that by running a calibration run with no model present and subtracting this solution from all test runs, the effects of boundary layer growth on the wind tunnel walls, change in test section dimensions in the streamwise direction, and wall orifice errors are removed from the final data.

Moses (1983) employs a closed wall, three-dimensional panel method correction approach that also uses measured wall static pressures to calculate interference corrections. The test section is represented by 140 rectangular panels with the constant strength doublet panels on either end of the test section extending far upstream and downstream, respectively. The panels are extended in either direction to prevent toroidal flow around the test section in the case of the upstream panels and to provide tunnel panels to interact with the wake panels in the case of the downstream panels. The author takes the approach of holding the measured pressure distribution on the airfoil constant as the effect of the walls are iteratively removed from the panel method calculation. This is done with an inner and outer flow solution which are synced with each other using a cylindrical surface that acts as an interface. The outer solver calculates the perturbation velocity along the interface starting from measured wall static pressures and passes this velocity to the inner solver. The inner solver then calculates the perturbation pressure on the interface due to such a change in perturbation velocity and returns the result to the outer solver. This iteration continues as the non-penetration boundary condition of the tunnel walls iteratively is removed. The result is that the angle of attack, twist, camber, and other geometric values are varied along the span to keep the pressure distribution the same throughout the change in boundary condition.

2.3.2. Two-variable method

The two-variable method (Ashill *et al.* 1998) is founded in the use of perturbation potential theory where the perturbation potential of the walls can be found by taking the difference of the wind tunnel perturbation potential and the free-flight perturbation potential. A Green's function, $G = \frac{1}{r}$, is used to analyze this difference, and the result is that two-variables need to be measured at the wind tunnel boundary such as streamwise velocity and transverse velocity. The streamwise velocity can be determined as with one-variable method from static wall pressures. For hard-wall tunnels, the transverse velocity is everywhere zero. For porous-walled tunnels it is more difficult to determine the transverse velocity. A major advantage of the two-variable method is that no mathematical model of the model is necessary. Ashill notes that while one-variable methods are suited best for attached flows because the model can be represented relatively easily by a set or singularities, for high-lift situations or for models with detached and complex flow, the two-variable method offers the better solution. A trade-off between the methods is in the number of pressure measurements required, with the two-variable method requiring significantly more

boundary pressure measurements and a means to determine the transverse velocity in porous- or slotted-walled tunnels. The two-variable method also can handle walls of arbitrary shape such as is the case with the focus of this paper on Kevlar-wall test sections.

2.4. Hybrid Test Sections and Corrections

Hybrid test sections are here given as those that are neither fully open nor fully closed. A review of the types of hybrid test sections and their use is presented to give background to the developments of the hybrid Kevlar-wall test section as they share some commonalities.

2.4.1. Minimum-Correction Test Sections

Several types of hybrid test sections for low-speed wind tunnel testing are in existence that attempt to reduce wall interference corrections by replicating the free-flight conditions experienced a model in the model's far-field which is at the tunnel walls. These are adaptive wall, ventilated, and active wall test sections.

Adaptive wall test sections attempt to replicate the shape of the streamlines that would be present in free-flight in the far-field of a given model. The shape is iteratively adjusted until the static pressure distribution along the walls matches as close as possible that computed by potential flow theory for the model in free-flight (Barlow *et al.* 1999).

Ventilated test sections such as those with slotted or porous walls are often used in transonic testing with the slots used to dissipate shocks at high Mach numbers, and they have also been used in some low-speed testing cases (*ibid.*). When these tunnels are used for subsonic testing, the correction methods must be altered because the wall boundary streamlines are no longer straight. For a panel method correction scheme, Barlow *et al*. state that vortex lattice paneling for a slotted-wall tunnel should have vortex lattices for the solid sections and source panels for the slots. The corrections for porous, or perforated wall, tunnels must include the viscous effects of the flow through the walls. The main barrier in this work is determining the flow at the wall from the suction-side.

The active wall tunnel as demonstrated by Bernstein and Joppa (1976) uses suction and blowing in an attempt to match the free-flight flow at the two control surfaces of the wind tunnel floor and ceiling. The conditions to be matched are the mass and momentum flow normal to the control surface. As it is not practical to have a continuously variable distribution of suction or blowing along the streamwise direction, a series of 12 plenums each above and below the tunnel floor and ceiling provide the suction or blowing over a full-span model. The use of discrete plenums leads to choice of matching either the integrated mass flow or integrated momentum flow over the corresponding free-flight control surface but not both. Matching mass flow leads to overcorrecting the lift data to be below the free-flight lift value. The reverse is true for matching momentum flow. The experimental study was performed at Reynolds number equal to 0.4 million and with wall open-area ratios of 5 and 31%, the higher porosity producing lift results closer to the correct value. The authors note there is still uncertainty as to whether the injection of flow into the test section is consistent with the potential flow representation of the model.

2.4.2. Kevlar-Wall Test Sections

While the Kevlar-wall test section was not designed to reduce aerodynamic corrections, per say, as most of the minimum-correction test sections were, the test section offers some of the aerodynamic benefits of these test sections. The previous work in the field of Kevlar-wall corrections will be reviewed first for two-dimensional lifting configurations and then for three-dimensional lifting configurations.

The layout of a generic Kevlar-wall test section is shown in Figure 2.1. The Kevlar-wall configuration consists of a test section flanked by two anechoic chambers. The most unique features of the test section are the large rectangular openings in the side walls which extend in the streamwise direction and cover the full height of the test section to serve as acoustic windows. These openings are covered with tensioned sheets of plain woven Kevlar 120 cloth which act to contain the freestream flow, thus shielding acoustic instrumentation inside the anechoic chambers from the flow. The ceiling and floor surfaces are rigid panels also covered with Kevlar that cover acoustically treated sections above and below the test section, respectively, except in the regions of the model mounting.

2.4.2.1. Two-Dimensional Flow

Kevlar-wall aerodynamics have been a subject of research at Virginia Tech's SWT ever since this configuration was first developed (Smith *et al.* 2005, Remillieux *et al.* 2008, Devenport *et al.* 2010b, Devenport *et al.* 2013). Pressure data measured from airfoils were originally corrected with a modified and extended version of the traditional hard-wall corrections as documented in Devenport *et al.* (2010b) and (2013) and given here

$$\frac{u'_{pw}}{U_\infty} = \Omega \frac{u'_{sw}}{U_\infty} \qquad \text{Equation 2.24}$$

$$|\Delta\alpha| \sim |C_l \frac{c}{h}| \qquad \text{Equation 2.25}$$

where the subscript *pw* indicates porous, or Kevlar-wall values, the subscript *sw* indicates solid, or hard-walled, values, Ω is a dimensionless value between 0 and 1, c is the chord of the airfoil, and h is the height of the test section. Equation 2.24 represents the blockage correction where Ω acts to scale the blockage effects of hard walls to a smaller value for use with flexible, porous walls which was first derived from the work in Ewald (1998). In Devenport *et al.* (2010b), an empirically determined scaling constant of 0.42 was used. For the lift interference correction, Devenport *et al.* (2010b) derive Equation 2.25 which accounts for the porosity effect of the Kevlar on the angle of attack which scales with the lift, and so circulation, felt at the Kevlar wall. Equation 2.25 is used in conjunction with the streamline curvature correction of Equation 2.8.

Investigation towards a more fundamental consideration of the complicated flow physics in Kevlar-wall test sections culminated with the development, by Devenport *et al.* (2013), of corrections based entirely on first principles and the independently measured or known physical characteristics of the system. The method accounts for the transpiration of air through the Kevlar-walls, the deflection of those walls under aerodynamic load, and the leakage of air between chambers. These characteristics are incorporated into a two-dimensional panel method model of the flow over the airfoil between the test section walls, which is then used to infer the influence of the walls upon the model flow, and thus the equivalent free flight conditions. The model involves no adjustable constants. Devenport *et al.* (2013) show a close match between aerodynamic characteristics measured in the Kevlar-wall test section and a matched hard-wall test section when corrections are applied.

The method described by Devenport *et al.* (2013) is a linear vortex/source panel method that places a paneled model of a test airfoil between two rows of panels representing the test section walls, including the flexible, porous areas associated with the Kevlar acoustic windows. The paneling of the test section walls includes power-law spacing in the streamwise direction to provide higher density paneling near the model location. The airfoil is typically modelled using 200 variable-length panels. The Kutta condition is enforced by the placement of two vortex panels on the finite-thickness trailing edge. One panel bridges the trailing edge from the pressure-side to the chordline and the other from the chordline to the suction-side. The strengths of these panels are determined by requiring that the flow pass smoothly over the trailing edge; in other words, that

there is zero vorticity at the corners of the trailing edge. A source panel parallel to these vortex panels and spanning the full trailing edge thickness is used to represent the wake.

The panel method code is unique from other wind tunnel panel methods because of its treatment of the boundary conditions at the port and starboard walls with both the deflection and pressure generated by aerodynamic load varying across the Kevlar portions of the walls. To model these effects the panel method uses two nested iterative loops. The inner loop solves the two-dimensional inviscid flow problem to find the pressure distribution along the airfoil and walls for a given initial deflection of the walls and by characterizing the transverse velocity through the Kevlar through an experimentally determined relationship

$$v_{normal} = k_c \Delta p^{0.5} \left(\frac{\Delta p}{\Delta p + k_p} \right)^{0.073} \qquad \text{Equation 2.26}$$

where Δp is the pressure difference across the Kevlar wall and k_c and k_p are constants obtained from independent tests of the Kevlar cloth (Devenport *et al.* 2013). The inner loop iteratively adjusts the pressure inside the test section and chambers until the mass balance entering and leaving each chamber is satisfied. The pressures, p, between chambers are related by Bernoulli's equation

$$p_{suction} = p_{pressure} - \frac{\rho}{2} sgn(\dot{m}_p) \left(\frac{\dot{m}_p}{A_{leak}} \right)^2 \qquad \text{Equation 2.27}$$

where ρ is the air density, $\dot{m}_p$, is the mass exchange from the pressure to suction chambers, and A_{leak} is the effective free-flow leakage area between chambers. The A_{leak} describes the area of an opening from a given anechoic chamber that for the same pressure difference would pass a mass flow equal to the summed mass flow seeping through the distributed leakage areas throughout the chamber.

The outer loop adjusts the wall deflections so that the tension in each wall produces static equilibrium with the pressure load acting on it through a finite difference solution of the simplified thin membrane equation

$$\frac{\partial^2 w}{\partial x^2} + \frac{\partial^2 w}{\partial y^2} = \frac{\Delta p}{T} \qquad \text{Equation 2.28}$$

where T is the Kevlar tension per unit lateral length, Δp is again the pressure difference across the Kevlar, and w is the out-of-plane deflection (Timoshenko 1940). Here, an isotropic tension has been assumed and the shear term neglected. By taking the second derivatives of deflection and inputting the tension of the wall, the pressure difference across the wall is determined. Convergence of the whole nested loop calculation takes a few seconds on a laptop computer.

With a flow solution in-hand, interference corrections can be obtained multiple ways. A free-flight solution is calculated for the same airfoil, and the pressure distributions over the airfoils in the wind tunnel and free flight maybe compared. In this case the wind tunnel solution is corrected for blockage and lift interference, as in Allen and Vincenti (1944), except that the blockage and lift interference parameters are fed into an optimization problem between the wind tunnel and free flight pressure distributions. The pressure distributions over the airfoil from the tunnel solution and free-flight solution are optimized by adjusting the free-flight angle of attack and the wind tunnel blockage factor, producing a porosity-adjusted angle of attack, α_e, and a blockage scaling variable, Ω. Both α_e and Ω are then input to Equations 2.8, 2.17, 2.18, and 2.19 to calculate the corrected angle of attack, lift, moment, and drag coefficients, respectively. Therefore, the hard-wall correction of Allen and Vincenti is adapted for use in test sections with wall porosity and deflection which is justified since the changes in angle of attack and blockage induced by the Kevlar walls are predominantly far-field effects that can still be modelled by classical wind tunnel analyses.

The α_e in the preceding paragraph is an intermediate angle of attack which gives the far-field angle of attack, corrected for the presence of the Kevlar porosity and deflection, but not corrected for streamline curvature. This is the angle of attack at which the model would be positioned in an equally dimensioned hard-wall test section to replicate as close as possible the flow experienced in the Kevlar-wall test section. The relationship between α_c, α_e, the streamline correction, $\Delta\alpha_{sc}$, and the porosity influence on far-field angle of attack, $\Delta\alpha_{porosity}$, is

$$\alpha_c = \alpha_e + \Delta\alpha_{sc} = \alpha_g + \Delta\alpha_{porosity} + \Delta\alpha_{sc}. \qquad \text{Equation 2.29}$$

An alternate way to infer the interference corrections is through a purely far-field approach which relies on the principle that the wall interference can be captured by the effect of the walls on the flow velocity and its derivatives at the airfoil location. In this approach, as followed by many of the studies reviewed in Section 2.2, the model is represented simply by a set of singularities: a doublet, vortex, and source. This simplifies and quickens the panel method solution without noticeable loss of accuracy since the walls are in the aerodynamic far-field of the model. Unpublished work has been done to this extent at Virginia Tech but is not treated in this study.

It is noted that as the panel method code described in this section uses a two-dimensional inviscid flow solver, it is appropriate as long as the boundary layer on the airfoil remains small and therefore attached. For this reason, the panel method code is not strictly valid after an airfoil has stalled.

TABLE 2.1. Inputs to the panel method simulation.

Input Parameter	**Value**
Kevlar Tension, $\boldsymbol{T}$	1500 N/m
Kevlar Modulus, $\boldsymbol{E}$	2643841 Pa
Kevlar Strain Multiplier, $\boldsymbol{a_\varepsilon}$	2.7283
Inflow Multiplier, $\boldsymbol{a_f}$	2
Effective Leakage Area, $\boldsymbol{A_{leak}}$	0.15 m^2
$\boldsymbol{C_p}$ Convergence Tolerance, $\boldsymbol{C_{p,tol}}$	1e-4
Tension Convergence Tolerance, $\boldsymbol{T_{tol}}$	1e-5

There are 7 inputs to the panel method as shown in Table 2.1. Kevlar tension, T, is the uniform, initial unloaded tension assumed for both Kevlar walls which is typically set as the stated value in the SWT per Devenport *et al.* (2010b). Kevlar modulus, E, is the effective modulus of elasticity of the woven Kevlar fibers calculated from the modulus of Kevlar 49 fibers (DuPont Technical Guide to Kevlar) and the cross-sectional density of those fibers in plain woven 120 weave. Kevlar strain multiplier, a_ε, is used to simulate the increase in pore size of Kevlar with stretching by augmenting the porosity coefficient, k_c, of Equation 2.26 as

$$dk_c = \frac{\overline{\varepsilon}_{port} + \overline{\varepsilon}_{starboard}}{2\sqrt{\rho}} a_\varepsilon \qquad \text{Equation 2.30}$$

where $\overline{\varepsilon}$ is the average strain over the specified wall and ρ is the air density. This relationship is theoretically derived from the narrowing of the Kevlar fibers during straining due to the Poisson effect. The inflow multiplier, a_f, scales the velocity of the flow re-entering the test section from the anechoic chambers to model the blockage created in the actual tunnel by flow re-entering the test section with zero streamwise momentum. Effective leakage area, A_{leak}, is the means to lump the distributed leakage areas throughout the chamber into a single effective free-flow area as given in Equation 2.27, and the convergence values for C_p and tension, $C_{p,tol}$ and T_{tol}, respectively, set the tolerance required to break the iteration loops in the panel method. Their values have been determined by studying the convergence of the panel method solution during the iteration loops and are conservatively small to assure convergence in both iteration loops is reached if at all possible.

2.4.2.2. Three-Dimensional Flow

Somewhat less attention has been paid to three-dimensional configurations. Work by Ito *et al.* (2010) found that the corrected hard-wall drag and uncorrected Kevlar-wall drag were nearly identical, suggesting that the Kevlar-wall flow was already nearly identical to that of free-flight. However, the uncorrected Kevlar-wall lift proved too high, so they proposed, based on empirical observations, that the lift coefficient, C_L, be corrected simply by the difference in $C_p$between the two chambers, i.e.

$$\Delta C_L = C_{p,starboard} - C_{p,port} \qquad \text{Equation 2.31}$$

where a capital *L* is used to denote the lift coefficient in the three-dimensional case. This equation is physically intuitive since both the difference in chamber C_p's and the correction magnitude of Kevlar-wall data both appear to scale with C_L. No rigorous derivation was presented, but nonetheless the correction gives an approximate correction. The method was found to correctly predict lift corrections for the high-lift model studied by Ito *et al*. Ito *et al.* specified no correction method for the pitching moment.

Most recently, a study by the author adapted the panel method approach of Section 2.4.2.1 to the three-dimensional case and applied the result to data from the Japan Aerospace Exploration Agency's (JAXA) 2m-by-2m Low Speed Wind Tunnel (Brown *et al.* 2014). The performance of the Kevlar-wall test section at JAXA was surprisingly close to that of the hard-wall test section there even before correction. The Kevlar-wall test section featured a substantial reduction in lift interference from the hard-wall case.

2.4.3. Kevlar-Wall Interference Mechanisms

Corrections due to Kevlar-walls are attributed to two factors: porosity and flexibility. As outlined in Devenport *et al.* (2013), there are three main mechanisms by which the porosity and deflection of the Kevlar-wall tunnels produce behavior different from the wall interference observed in hard-wall test sections. On top of the effects produced by streamline curvature and standard solid and wake blockage, there are the three contributions from porosity and deflection as given below.

First, compared to hard-wall wall interference, the angle of attack and thus the lift interference are reduced due to wall porosity in Kevlar-wall tunnels. The porosity of the Kevlar, combined with a pressure difference between the tunnel and chamber sides imposed by the model causes normal velocity into and out of the test section on suction and pressure walls, respectively, which reduces the far-field effective angle of attack experienced by the airfoil which is accounted for by the $\Delta\alpha_{porosity}$ term in Equation 2.29.

Second, the pressure difference across the Kevlar imposed by the model creates deflection into and out of the test section for the suction and pressure-side walls, respectively. The resulting flow around the curved walls experiences a smaller effective test section and thus increased blockage as the streamlines trailing straight downstream and indicate the effective test section height are moved inboard from both walls.

Thirdly, in the case of a model at low lift, the blockage of the model cause flow in the upstream to be diverted out of the test section. Since mass must be conserved in the chambers and the chamber sealing is relatively tight compared to the mass of air coming through the Kevlar windows, the flow re-enters the test section around the airfoil where static pressure is lower. This re-entering flow creates blockage similar in many respects to wake blockage behind an airfoil. In summary, Kevlar-wall tunnels cause a decrease in lift interference correction and have two competing effects on the blockage, one increasing and one decreasing it.

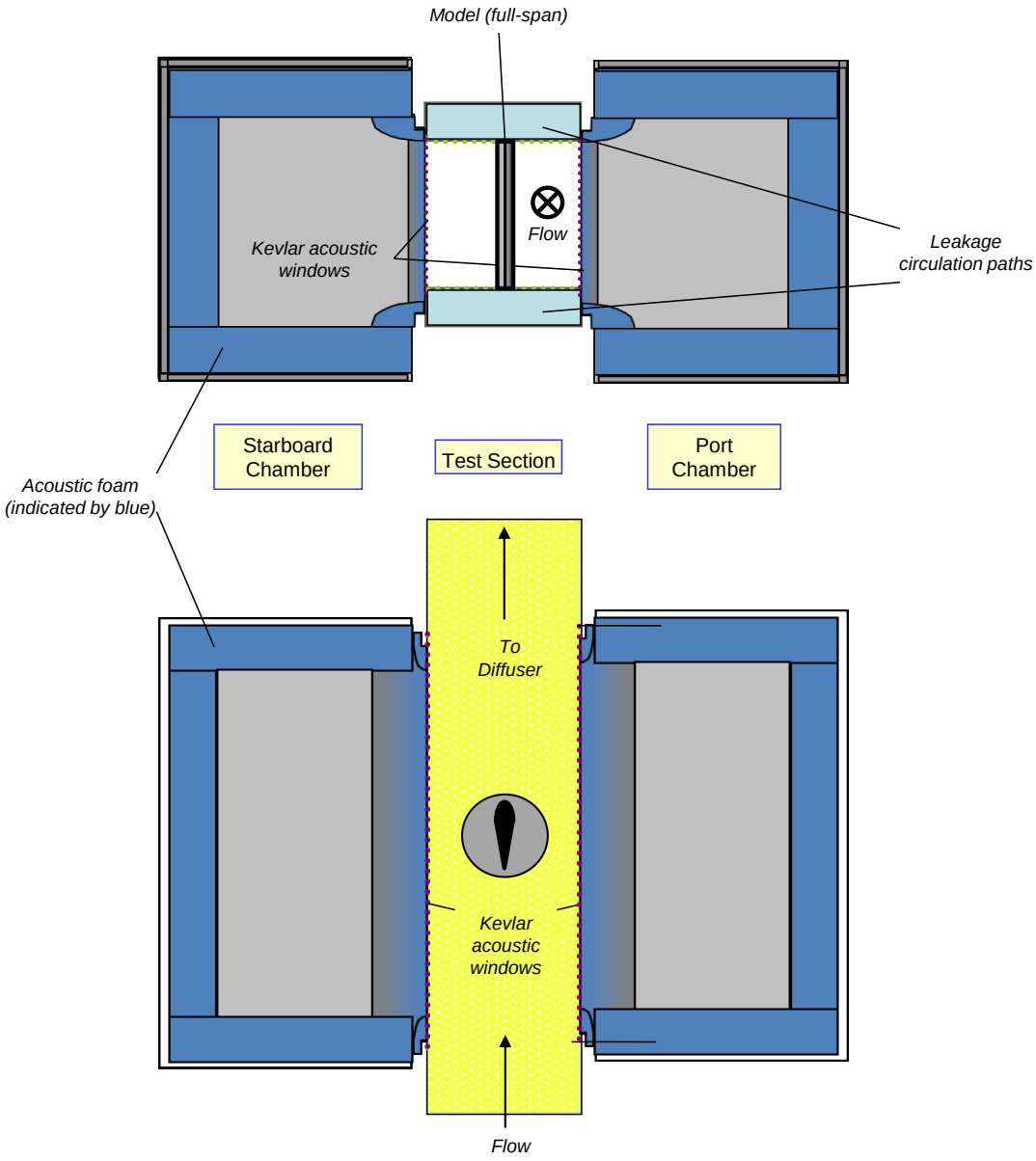

FIGURE 2.1. Schematic drawings of a generic Kevlar-walled test section showing (a) the cross-sectional view and (b) the plan-form view. (Illustration credit: Dr. William J. Devenport.)

CHAPTER 3. Experimental Goals

The fundamental assumption of wind tunnel testing is that there exists an equivalent free-flight flow with which the aerodynamic quantities measured under strictly controlled and defined conditions can be associated (Newman and Everhart 1998). Wall interference corrections aim to correlate the measured quantities to their free-flight values. The goal of this work is to demonstrate that wind tunnel flow over lifting bodies in two-dimensional test sections with Kevlar walls and anechoic chambers can be corrected with a known degree of certainty to the equivalent free-flight condition. As free-flight data are difficult to measure, the path to achieve this goal will be indirectly routed through the use of the hard-wall test section, whose corrections are well-documented and understood by the wind tunnel community.

The objectives of this study are to:

1. Solidify knowledge of boundary conditions in the Kevlar-wall test section
2. Validate the performance of the Kevlar-wall test section at the SWT
3. Identify and improve areas of inconsistency between panel method modeling of the Kevlar-wall test section and its actual characteristics.

The foundational approach to meeting these goals is to perform duplicate tests of identical airfoils in the hard-wall and Kevlar-wall test sections. Preceding the examination of the Kevlar-wall results, the performance of the hard-wall test section at the SWT will be validated against credible wind tunnel data from other facilities. Lift, drag, and moment data from the hard-wall test section will be used for this validation and also for comparison with the Kevlar-wall test section as in (2), which will additionally include pressure comparisons between test sections. Towards (1), there will be direct measurement of key boundary conditions in the Kevlar-wall test section, including independent tests of the Kevlar pressure-velocity relationship and anechoic chamber leakage areas. Additionally, wall deflections, wall pressures, and chamber pressures will be recorded during airfoil tests to help increase the fidelity of the panel method simulation used for corrections in the Kevlar-wall test section as in (3). Through the boundary measurements above, the effectiveness of novel measurement techniques in Kevlar-wall test sections will also be demonstrated.

CHAPTER 4. Facility, Instrumentation, and Measurement Techniques

4.1. Stability Wind Tunnel

The Stability Wind Tunnel (SWT) was fabricated originally at the NACA Langley Research Center in the 1930's before being relocated to Virginia Tech in the late 1950's. The subsonic tunnel's test section and sealed control room sit inside Randolph Hall on the Virginia Tech campus, and the rest of its closed-circuit exposed to the environment as shown in Figure 4.1a.

The schematic of the single-return circuit can be seen in Figure 4.1b. The drive and fan send the wind tunnel flow first into an air exchange tower where air from the atmosphere is mixed with tunnel air to stabilize the tunnel flow temperature. From the tower, the air turns two corners with the aid of guide vanes and passes into the 5.5m-by-5.5m square settling chamber which is coated on all 4 walls with 50mm thick urethane foam liner do dampen fan and motor noise. The flow next passes through 7 turbulence-reducing screens with open area ratio of 60% before accelerating through the 9:1 contraction. The removable test section has a constant 1.85m-by-1.85m (~6 ft.-by-6 ft.) cross section and is 7.3m (24 ft.) long. Vortex generators at the rear of the test section add vorticity to the flow to promote mixing and prevent boundary layer separation as it enters the 3-degree slanted diffuser which is lined with 50mm thick melamine foam to again reduce noise contamination of the test section from the fan and motor. Finally, the flow turns 180 degrees again and returns to the fan. Pressure equalization of the tunnel flow with the control room pressure occurs at the rear of the test section where slots for a rake traverse are located. A pressure equalization opening in the downstream exists but was covered for the present testing.

The tunnel is powered by a 0.45-MW, variable speed, DC drive turning a 4.3m diameter, 8-bladed fan. The fan produces flow velocities in the test section up to 80 m/s with no blockage for a maximum chord Reynolds per meter up to 5 million. Turbulence intensities levels are as low as 0.016% and no more than 0.031%, the higher levels occurring at higher freestream velocities as shown in Table 4.1.

TABLE 4.1. Freestream turbulence levels.

Freestream Velocity	**RMS Streamwise Fluctuations**
U_∞ *(m/s)*	u'/U_∞
12	0.016%
21	0.021%
30	0.024%
48	0.029%
57	0.031%

The SWT features two interchangeable test sections, the hard-wall and Kevlar-wall test sections which are each installed and removed by overhead lifts. When installed, a test section rests on support elements so that its leading and trailing edges adjoin with the contraction and diffuser, respectively. Strips of aluminum and sometimes expanding foam filler cover the several centimeters clearance openings at the leading and trailing edges.

4.2. Hard-Wall Test Section

The hard-wall test section can be seen from its upstream end with a vertically-mounted airfoil in Figure 4.2a. The floor and ceiling are aluminum plates, 0.61 m (2 ft.) on a side with 12 streamwise rows and 3 width-wise rows. The plates are fixed to the tunnel at each corner with bolts countersunk into the aluminum to yield a smooth flow surface. At the joints where plates meet each other, foil tape is used if necessary to smooth any steps in the flow surface which may be on the order of 1-2 mm. Where the floor and ceiling plates meet the walls, there can be a partially sealed streamwise gap up to 2 cm until the vertical walls are reached.

The port and starboard wall flow surfaces are formed from 12.7 mm thick Lexan panels and their supporting steel frame. Each panel runs 0.76 m streamwise and 1.70 m spanwise, nearly the full span height of the tunnel. Each panel is bolted to the steel frame along all 4 edges and if necessary any steps in the flow surface at the meeting of the panels and frame are smoothed with foil tape.

The dimensions of the test section vary little from the nominal dimensions. The width at the floor is between 1.850 m-1.856 m (72.8 in.-73.1 in.) measured from the fore to aft of the test section. Using a Pro 360 digital protractor with a ±0.2° maximum error, the angularity of each of the 4 walls was found to be everywhere within 0.8 degrees of the nominal value and everywhere within 0.4 degrees of the nominal at the model location.

A common testing configuration at the SWT is two-dimensional flow over airfoil sections. Full-span models with tubular quarter-chord spars on either end are rotated through angles of attack by a bearing and turntable system. The bearing and its mounting plate are located below the test model, providing support for the airfoil and allowing rotation about the airfoil quarter-chord axis. The spar of the airfoil, typically 8.9 cm (3.5 in.) outer diameter, slides into a collar mounted to the bearing. The turntable is located above the test section and again has a collar to receive the airfoil spar as seen in the cross-section *A-A* of Figure 4.2b. The spar is fixed to a collar with pins so that the turntable governs the rotation of the airfoil. The turntable is a Kinematics model ZE14C slew drive powered by a BK Precision 9123A variable DC power supply and capable of applying torques up to 1000N-m. The turntable moves in increments of 0.01 degrees, but the angle of attack is measured by a Renishaw LM10 linear magnetic encoder which reads rotation of the turntable with a resolution of 0.003 degrees. Disk elements attached to the collar of either the turntable or bearing rotate with the airfoil while the surrounding plates remain stationary. The axis of rotation is midway between the test section walls and 3.56m from the leading edge of the test section.

4.3. Kevlar-Wall Anechoic Test Section

The Kevlar-wall test section, shown from the upstream view in Figure 4.3a, uses the same turntable system for airfoils and has the identical 1.85 m-by-1.85 m cross section and 7.3 m length as the hard-wall test section, however, the port and starboard walls are made from tensioned Kevlar fabric and the ceiling and floor surfaces from perforated plates that are also covered with Kevlar fabric.

The Kevlar windows are the test section's most unique feature, extending 4.2 m of the 7.3 m test section length and spanning from the floor to the ceiling as shown in the schematic representations of Figures 4.4 and 4.5. Each of the windows are made of three separate pieces of Kevlar fabric with two sewn and glued seams approximately 40 mm wide that run the length of the test section at locations around 30 cm above and below the floor and ceiling, respectively. They are tensioned in both the horizontal and vertical directions with a tensioning frame to a nominal tension of 1500 N/m as measured by a Newman ST-Meter 2E tension meter (Devenport *et al.* 2010b). The tensioning frame has dimensions of 5.37 m-by-2.51 m and is held clamped to the test section frame by corner L-brackets along the perimeter. The clamping location is offset from the wall opening so that the Kevlar is stretched over the opening. Magnets spaced roughly 5cm apart run the perimeter of the opening to keep the Kevlar firmly pressed against the test section under loading conditions. The floor and ceiling surfaces are again made from aluminum plates 0.61 m (24 in.) on a side as in the hard-wall test section. However, the plates are this time perforated to allow transmission of sound to volumes of space above and below the test section designed to absorb sound. Kevlar is stretched over the top of the aluminum plates to provide a smooth, uninterrupted flow surface.

The Kevlar fabric used on the walls, ceiling, and floor is Kevlar 120 scrim which consists of plain woven fibers of Kevlar 49 as seen in the cutout of Figure 4.3 and was selected for its

characteristic of transmitting acoustic waves with relatively low attenuation (Devenport *et al.* 2010b). There are nominally 13.4 fibers per cm (34.0 per in.) at a thickness of 0.08 mm and with a dry weight of 58 g/m^2. According to Zhu *et al.* (2012) who tested Kevlar 49 fiber with 6.7 fibers per cm (17.0 per in.), the apparent poison ratio versus strain of the fibers is highly nonlinear, and the modulus of elasticity is in the range 113-138 GPa for the woven fabric specimens. King (2006) notes that Kevlar yarns are linearly elastic after being uncrimped until they fail. The flexural rigidity of the Kevlar fabric as calculated from the values above is on the order of 0.007 N/m.

As acoustic waves pass through the low-attenuating Kevlar they enter the anechoic chambers on either side of the test section to be measured by acoustic instrumentation such as seen in Figures 4.3b-c. As seen in Figures 4.4 and 4.5, the chambers each run 5.6m long in the streamwise direction, thus they are longer than the streamwise length of the Kevlar walls but not as long as the whole 7.3 m length of the test section. The chambers are each 3.0 m wide and 3.4 m high, measured from the outer walls which are fashioned from square steel beams that support 19 mm thick medium-density fiberboard (MDF). Panels of MDF are joined with 1.3 cm-by-5.7 cm (0.5 in.-by-2.25 in.) strips of wood that overlap and screw into the panel on either side. The joints are covered in paint although in some areas the seal provided by the paint has cracked. Lining the inside of the MDF walls, floor, and ceiling are foam wedges that absorb frequencies of sound above 140 Hz. The wedges are 0.61 m tall and vary in width depending on their location. Around the Kevlar windows, quarter-elliptical foam pieces mate up to the Kevlar at the floor and ceiling leaving just open the 1.85 m test section height. At the upstream and downstream ends of the walls, the closest row of wedges are pressed against the Kevlar thus covering roughly 30 streamwise centimeters of fabric.

Behind the quarter-elliptical foam pieces are areas of Kevlar fabric both above and below the test section that account for the 0.68 m difference in heights of the inner test section and Kevlar tensioning frame. These sections of fabric are exposed to the volumes of space above and below the test section floor and ceiling which are typically filled with foam wedges to again absorb acoustic waves and prevent reflection back into the test section.

The volumes of space above and below the test section are designed to be sealed from the control room, thus ideally yielding the test section and chambers an isolated system permitting no mass exchange with the control room. The chambers themselves do not have perfect sealing, but it is generally believed that mass is conserved in the volumes above and below the test section.

4.4. Airfoil Models

The main aim of this study is to directly compare the aerodynamics of the hard-wall and Kevlar-wall test sections by observing pressure data measured on airfoils in both test sections. Specifically, the three airfoils tested were a 0.914 m chord and a 0.203 m chord NACA 0012, and a 0.610 m chord DU00-W-212. The airfoils were selected to provide a validation of the panel method correction described in Section 2.4.2.1 over a range of airfoil chord lengths. The sets of the two NACA 0012 airfoils allow for comparison of the correction scheme on an identical profile over differing chord length from 0.21 to 0.91 m. Additionally, the symmetry of the NACA airfoils allows for the isolation of the correction effects due to blockage as opposed to those due to lift interference when the airfoil is tested at zero angle of attack. All three airfoil models span the 1.85 m height of the test sections, the span-ends being taped with aluminum foil tape and also sometimes Mylar® to smooth the junction region. The airfoils are all instrumented for pressure measurements near their midspans.

The 0.914m (36 in.) NACA 0012 as shown in Figure 4.6a and d is constructed of a composite fiberglass exterior enclosing a core of steel ribs and polyurethane foam. The airfoil profile and port locations were measured by a FaroArm® Coordinate Measurement Machine as described in Devenport *et al.* (2010a). The FaroArm has a rated accuracy of ±0.025mm, however,

experiences by engineers at the SWT dictate that this accuracy is around ±0.5mm. Comparing 300 measured profile y-coordinates near the midspan of the airfoil with the theoretical y-coordinates for the measured x-coordinates, the measured profile differs slightly in its thickness from the theoretical profile. The mean increase in the thickness direction of the measurement relative to the theoretical shape is 0.10% and 0.08% chord, or 0.93mm and 0.74mm, for the upper and lower sides of the airfoil, respectively. The added thickness of the airfoil originates from the base profile as well as the presence of a hatch located across midspan on one side of the airfoil which provided access to the pressure instrumentation inside the model. The hatch is on the suction-side at positive angles of attack, and tape is used to smooth over the transition to the hatch around all four edges. Trials of the theoretical and measured profiles in a panel method solver showed the deviation of the airfoil profile from the theoretical to be of little aerodynamic consequence (*ibid.*). Processing of airfoil pressure data used the theoretical rather than the measured profile. The 0.914 m (36 in.) NACA 0012 has 81 pressure taps of 0.5 mm diameter near the midspan region that are spaced apart in the spanwise direction in an attempt to avoid contamination of the downstream ports by the upstream ports. The ports are spaced apart by 1-3 mm spanwise in the leading edge region and by up to 12 mm spanwise over the rest of the airfoil. The spanwise offsets create rows of taps that are angled roughly 13 degrees from the chordwise direction. The rows double back after the midchord location so that the ports do not go further than a distance of 7% chord from the midspan location. After checking the pressure-holding capability of each port as described in the following section, 72 of the 81 ports were deemed useable. The pressure port locations for this airfoil and the remaining two airfoils below are tabulated in Appendix A.

The 0.610m (24 in.) DU00-W-212, a 21.2% thick profile designed at Delft University for wind turbine research (Timmer and Van Rooij 2003), is fabricated from 72 aluminum laminates, each 25.4 mm thick in the spanwise direction, that are held in compression by 12.7 mm diameter threaded rods running the entire span of the airfoil. There is no more than 0.04 mm step between adjacent laminates. It has a removable leading edge 1 m in span that extends back to the 40% chord location which can be seen in Figure 4.6b and e. There is a 0.13 mm gap between the leading edge module and the main body in the chordwise direction and a 1 mm gap between the same in the spanwise direction (Joseph 2014). Both of these gaps are covered by tape during tests. Although the airfoil is adaptable for use with the SWT's boundary layer control system, this system was not used for the current testing. There are gaps up to several centimeters at the spanwise ends of the airfoil to accommodate the control system, but these were covered with thin Mylar® sheeting held in place by aluminum foil tape. The DU00-W-212 has 73 ports of 0.5 mm diameter, 64 of which were found capable of holding pressure. The spanwise placement of the pressure taps for the DU00-W-212 angles away from the midspan line from the leading edge until the midchord location at which point the taps return to the leading edge spanwise location and again angle away from the midspan line until reaching the trailing edge.

The 0.203m (8 in.) NACA 0012 consists of machined aluminum plates joined at the chordline and is shown in Figure 4.6c. The aluminum plates are each roughly 0.67 m in spanwise length but are staggered so that the pressure side joints between different spanwise panels occur halfway between the suction side joints of the same. The joints between spanwise panels were taped to reduce the impact of any steps. The airfoil has 40 pressure taps, 23 of which were found capable of holding pressure, that are offset approximately 150 mm from midspan as shown in Figure 4.6f so as not to coincide with the location of the joints between different spanwise panels. The spanwise placement of pressure taps forms a single line at an angle to the chord line as shown in the figure.

For the runs in the tripped condition, airfoils in the SWT were fitted with serrated trip tape of the type three-dimensional Turbulator tape from the Glasflügel Company that was 0.425 mm high and extended from 5-6% chord. The tape was adhered to foil mounting tape that was 0.1 mm high and extended from 5-11% chord. The 0.91 m NACA 0012 with and without the trip are shown in Figure 4.7.

Zero angle of attack location is set for each airfoil by aligning the chordline at the leading and trailing edges to the tunnel centerline as given by the joints in the floor panels. Alignment is thought to have been within 1 mm at the trailing edge of each airfoil, which over the ¾ chord moment arm produces uncertainties of ±0.08 degrees, ±0.13 degrees, and ±0.38 degrees for 0.914 m NACA 0012, the 0.610 m DU-000-W212, and the 0.203 m NACA 0012, respectively. Additional uncertainty in the absolute angle of attack may be present due to any misalignment of the test section with the freestream velocity. The zero angle of attack was checked on the two symmetric airfoils by examining for the symmetry of the pressure distributions.

4.5. Pressure Measurements

Standard measurement techniques were used to gather the airfoil pressures. Pressure taps in the airfoil models were connected to 1.6 mm Tygon® tubing which led to an Esterline 9816/98RK pressure scanner with a range of ±2.5 psi, accuracy of ±0.15% full scale (which accounts for hysteresis, nonlinearity, and non-repeatability), or ±26Pa, and resolution of ±0.003% full scale, or ±0.5Pa. Pressure measurements are averaged over 25 readings and the pressure integrated along the chordwise direction to yield lift and pitching moment. Periodically during a test day, scanners were re-zeroed to reduce drift effects on the measurements. The operating temperature range of 0-50 degrees Celsius was never exceeded in the indoor control room during testing.

The pressure-holding capability of each tap in the model was checked with a handheld Fluke 7181G Pressure Calibrator by covering the model's port opening with the manometer tubing, applying a pressure on the order of 10 in. of water from the manometer, and checking the pressure reading from the Esterline scanner to compare with the manometer reading. Pressure ports that were clogged or leaking were removed from the data acquisition software.

An alternate pressure scanner was sometimes employed which is the 16TC/Digital Temperature Compensated (DTC) Gen 2 scanner by Pressure Systems, Inc. Each of these scanners have 32 ports and one reference port with a range of ±2.5 psi and a rated accuracy of ±0.03% full scale, or ±5 Pa. Each scanner is temperature compensated by an internal temperature sensor and internally stored temperature calibration data. This compensation capability makes the DTC scanners ideal for in-tunnel mounting. As such, they are used on the downstream wake rake to be described below and in the anechoic chambers, both of which applications expose the scanners to the wind tunnel flow temperature. Measurement averaging and re-zeroing procedures were the same for the DTC scanners as for the Esterline scanners.

A wake rake consisting of 120 Pitot probes was used to measure drag and wake cross-sections downstream of the model as seen in Figure 4.8. All but 7 of the 120 probes are made of 1.6 mm diameter stainless steel tubing and measure the stagnation pressure over the width of the tunnel. The remaining 7 probes are Pitot-static probes of type Dwyer 3 mm-diameter model 167 which are spaced evenly along span of the wake rake to measure both stagnation and static pressure. The probes are connected to one of the four DTC Gen 2 pressure scanners that can be seen spaced over the top side of the rake in Figure 4.8a.

The rake is formed by a streamlined strut of chord 16.5 cm (6.5 in.) and thickness 2.5 cm (1 in.) from which extend support rods and the probes. The probes extend ahead of the streamlined body by 0.31 m (12.25 in.) measured from the probe tip to the center of the strut. The Pitot tubes are spaced apart by 25 mm (1 in.) in the outer regions and 6 mm (0.25 in.) in the center region which equates to spacing of 15 and 40 tube diameters, respectively. The wake rake is located either 1.75 m or 2.78 m downstream of the model quarter-chord location for the hard-wall and Kevlar-wall test sections, respectively. The instrumentation wiring from the rake exited the tunnel through the starboard-side rake slot machined into the tunnel walls, and excess length of wires were taped to the tunnel wall to avoid flapping in the tunnel flow. For drag measurement, the rake was positioned midway between the test section floor and ceiling. For verification of the two-

dimensionality of the flow over the airfoil, the rake was traversed from 5 cm-178 cm (2 in.-70in.) above the tunnel floor, typically in increments of 10 cm (4 in.) with increments of 2.5 cm (1 in.) near the floor and ceiling.

After re-zeroing of all pressure ports and taking measurements, the rake data was post-processed to calibrate out bias which originate from uncertainty in the pressure transducers, possible misalignment of the Pitot probes, and interference on the static pressure measurement due to the blockage effects of the probe tubes and strut. The highest C_p value recorded by given a Pitot probe over the course of an angle of attack sweep occurs when the probe is experiencing the full dynamic pressure of the tunnel flow. However, the measured value may deviate slightly from unity due to the uncertainty of the pressure transducers or any misalignment of the probe with the freestream direction. A calibration is performed by taking the difference between the highest C_p value recorded and unity. This difference is then added to all subsequent readings made by the given probe. The difference between the stagnation pressure measured by each of the Pitot probes and the static pressure measured by the 7 static pressure ports yields the dynamic pressure at the given location. The rake wake was used only for tests with Reynolds number less than or equal to 2.25×10^6 due to unsustainable flow-induced vibration at higher Reynolds that caused the rake to oscillate in the spanwise direction such as a vibrating, simply-supported beam.

The freestream velocity and pressure in the test section are derived from measurements with four static pressure ports: two in the contraction and two settling chamber. The redundancy allows for calculating an average of two pressures at each location. The freestream velocity is inferred from these static pressures through calibration constants which are set based on independent velocity measurements by a Pitot-static probe. Assuming the calibration of the wind tunnel contraction and settling chamber ports to have negligible uncertainty, the sources of uncertainty in the measurement of the freestream velocity are the contraction pressure measurement, settling chamber pressure measurement, the barometric pressure measurement, and the freestream temperature measurement. Depending on the freestream dynamic pressure, the contraction and settling chamber pressures are measured with the Esterline scanner using either a model with range of ±10 in. of water and accuracy of 4 Pa or a model with range of ±2.5 psi and accuracy of 26 Pa. The barometric pressure is measured with a Validyne DB-99 Digital Barometer with resolution of 0.01 in. of mercury and the freestream temperature is measured with an Omega Thermistor type 44004 with accuracy ±0.2°C.

The freestream values calculated correspond to the front of the test section. In the hard-wall test section, the freestream velocity is increased slightly moving in the streamwise direction due to the reduction in flow area caused by the boundary layer growth along the walls. The increase in freestream velocity is accompanied by a decrease in freestream pressure. The following equation is used to correct C_p data measured over models for the drop in freestream static pressure between the upstream measurement location and the model location

$$C_p{}' = \frac{C_p - C_{p,rinf}}{1 - C_{p,rinf}} \qquad \text{Equation 4.1}$$

$$C_{p,rinf} = -0.00025083 U_\infty + 0.0178625. \qquad \text{Equation 4.2}$$

These relations are derived from measurements of the floor pressures in the hard-wall test section made along the length of the test section with no model in-place. There is a slight dependence on freestream velocity such that the static pressure drop is less severe at higher velocities which follows since the boundary layer thickness decreases with velocity. Unless otherwise noted, all data from the SWT's hard-wall test section are corrected with Equation 4.1 before any other corrections are applied. Unlike in the hard-wall test section, the boundary layer in the Kevlar-wall

test section develops differently due to the Kevlar porosity, and this development is intended to be captured implicitly by the panel method simulation described in Section 2.4.2.1.

4.6. Uncertainties

Uncertainties of the freestream properties, similarity parameters, and aerodynamic coefficients in the SWT were calculated using a jitter analysis. The primary measurements include the model pressures, model pressure tap locations, model chord length, contraction pressure, settling chamber pressure, barometric pressure, and temperature. The nominal values of these measurements for selected tests and their uncertainties are tabulated in Appendix B with the exception of the model pressures and pressure tap locations. Appendix B demonstrates a numerical approach to the jitter analysis where the product of the partial derivative with respect to each jittered variable and the magnitude of the jitter is calculated rather than calculating the separate terms. Each primary measurement including all of the model pressure ports are individually perturbed by their given uncertainty, and the changes in the aerodynamic coefficients due to each perturbation are calculated. The root-mean-square (rms) value of all the perturbations are finally calculated to yield the overall uncertainty of the measurement.

Some uncertainties that are not accounted for in the jitter analysis but believed to be small are uncertainties due to the calibration constants used in calculation of the freestream velocity, the unsteadiness of the freestream flow, the freestream pressure drop through the test section as given by Equation 4.1, the correlation time of structures in the boundary layer passing of the airfoil pressure transducers, and the two-dimensionality of the flow. The calibration constants are trusted with a degree of confidence since C_p values on leading edge pressure ports of the airfoil can read nearly exactly unity for certain angles of attack meaning the calibration constants are faithfully calculating the stagnation pressure. The rms fluctuation in velocity has only been measured as high as 0.031% as shown in Table 4.1 which is negligible compared to the uncertainty in the freestream velocity measurement already present due to the uncertainties in the primary measurement instruments which is no less than 0.5%. The pressure data are an average of 25 points taken at a sampling rate of 100 measurements per channel per second. These samples are not guaranteed to be independent of each other if the correlation time of the boundary layer is large. However, given that multiple pressure scanners are used to measure airfoil pressures in most tests, the sampling time of the pressure data are longer than 1 second which allows for the passing of many correlation times. As will be demonstrated below, the two dimensionality of the flow at the pressure tap locations is verified with wake rake cross-sections downstream of the airfoil.

The jitter analysis outlined in Appendix B presents the uncertainties in the primary measurements, intermediate calculations such as air density and freestream velocity, and final quantities such as Reynolds and Mach numbers. The uncertainty of the freestream velocity is ±0.2 m/s at a nominal 34 m/s and increases to 0.8 m/s at a nominal 71 m/s. Typically, total uncertainty would decrease with increasing freestream velocity since the uncertainties of the pressures used to infer the freestream velocity become smaller relative to the nominal pressures as the velocity increases. In this case, the higher freestream velocity requires the use of a pressure scanner with larger range and lower accuracy than the lower velocity requires, so the uncertainty in the freestream velocity is *greater* at the higher velocity case. The details of the pressure scanner selection are given in the footnotes of Appendix B.

The range in uncertainty of the freestream velocity predicted by the jitter analysis of the primary measurement instruments' quoted accuracies considering all the run conditions included in this study is from 0.5% all the way to a rather large 1.7%. While the uncertainties presented on the plots in this study are derived from the jitter analysis and therefore include this uncertainty in freestream velocity, we suspect that the freestream uncertainty is in reality lower than that

calculated from the jitter analysis. The quoted accuracy of the Esterline pressure scanners used for the freestream velocity measurement includes not only uncertainty due to hysteresis and non-linearity but also due to non-repeatability, the effect of which should be minimized by the internal averaging procedure of the pressure scanners, a procedure which is additional to the external averaging of 25 pressures mentioned previously. An analysis of the stagnation C_p's measured by the wake rake indicate that the accuracy of the freestream velocity is considerably better than that predicted by quoted uncertainty of the scanners. For these reasons and by the results of repeatability tests described later in this section, it is suspected that the uncertainties derived from the jitter analysis are exaggerated although they will be used in the remainder of this study.

The uncertainty in the measured Reynolds number using the jitter analysis ranges from as low as $3x10^3$ for the 0.20 m NACA 0012 airfoil to as high as $4x10^4$ for the higher velocity cases of the 0.91 m NACA 0012 airfoil. The uncertainty in the Mach number ranges from as low as $6x10^{-4}$ for the 0.20 m NACA 0012 airfoil to as high as $3x10^{-3}$ for the 0.61 m DU00-W-212 airfoil.

Next are considered the uncertainties in the aerodynamic coefficients. One case of the uncertainties for lift and moment coefficients for the 0.91 m NACA 0012 model are given in Figure 4.9 for freestream velocities of 34 and 71 m/s, or Reynolds numbers of $2x10^6$ and $4x10^6$. A major source of uncertainty in the measurement of the aerodynamic coefficients is again the freestream velocity. The peak uncertainties in lift and moment coefficient at a Reynolds numbers of $2x10^6$ are ±0.0216 and ±0.0044, respectively, as seen in Figure 4.9a-b. These compare to ±0.0345 and ±0.0025, respectively, for Reynolds numbers of $4x10^6$ as in Figure 4.9c-d. The freestream velocity uncertainty is the dominant uncertainty in the lift coefficient, at least for high angles of attack where the lift accuracy is typically most critical. The airfoil pressure uncertainties produce the largest uncertainties in the moment coefficient.

These calculated uncertainties in lift and moment coefficient are slightly larger but similar to previous findings at the SWT in 2010 where the lift and moment coefficients were measured twice with an identical setup but after a complete uninstallation and reinstallation of the model. These uncertainties, which contain contributions from both the angle of attack and lift measurements between 50-60 m/s, were ±0.012 and ±0.0014 for the lift and moment coefficients, respectively. An estimation of the uncertainty in the drag coefficient was made with a similar repeatability study and found to be 5% of the measured drag value which will be used in the remainder of this study.

The uncertainties derived from the repeated tests suggest that the angle of attack uncertainty is quite small since the repeated test uncertainties are already lower than the independently calculated uncertainties in the lift and moment coefficients. Due to the angle of attack zeroing process as described in Section 4.4, the uncertainty in the absolute angle of attack varies with the chord of the airfoil and is also affected by both the alignment of the test section with the freestream flow. The relative uncertainty within any given angle of attack sweep is around 0.1 degrees. As the magnetic encoder used to measure rotation has resolution of 0.003 degrees, this relative angle of attack uncertainty is not due to the instrumentation but rather to a slight amount of rotation of the model originating in the pin joint between the airfoil shaft and the turntable sleeve. This uncertainty is a static value for any given angle of attack but exists nonetheless.

4.7. Kevlar Pressure-Velocity Measurement

One objective of this research is to quantify the relationship between the pressure difference across the Kevlar and the resulting transpiration velocity through it. An experiment was devised to measure the pressure-velocity relation for the Kevlar walls during the operation of the facility as part of an airfoil test which is described in Chapter 5. The experiment consists of two

parts, the pressure difference measurement and the velocity measurement, which are accomplished with static pressure ports and a hot-film anemometer, respectively.

The measurement of the first of these, the pressure difference over a Kevlar wall, is a novel development. Both the pressure in the anechoic chamber as well as the static pressure along the tunnel-side of the Kevlar is required to compute the pressure difference. The chamber pressure is simply made with open-ended Tygon® tubing leading directly to a pressure scanner. The static pressures along the tunnel-side of the Kevlar are measured with the schematically illustrated system in Figure 4.10. A static pressure port mounted to the wall connects to Tygon tubing which leads under a tape strip providing stain relief. The tubing then runs down the wall, being tape at points along the way to prevent flapping during tunnel operation, and to the pressure scanner.

The static pressure port is made by sanding off one side of a polypropylene connector designed to accept 1.59 mm (1/16 in.) inner diameter tubing. Figure 4.11 illustrates the process by which the pressure ports are installed. First, the woven Kevlar fibers in the vicinity of the pressure port are stretched and pushed aside to open a passageway through the wall using thin electrical wire, the result being seen in Figure 4.11a. The polypropylene connector is then threaded with a thin electrical wire (b), dabbed with high temperature hot-glue (c), and bonded to the chamber-side of the Kevlar wall (d) and (e). The wire acts to plug the connector's hole during gluing and locate it on the wall. After drying, the wires are pulled out from the tunnel-side (f) and reamed out with either the wire or a 0.508 mm (0.020 in.) drill bit and handheld chuck to remove excess glue (g). Finally, remaining debris is blown out from the port by use of compressed air (h).

An important aspect of this design is that the port does not penetrate the Kevlar, and therefore does not add any protrusions to the tunnel-side Kevlar flow surface. During the installation process above, excess glue seeps through the Kevlar and hardens on the tunnel-side surface as shown in Figure 4.12a. These surfaces were smoothed by rubbing a finger over the port opening several times until the glue crumbled away, resulting in the surface as shown in Figure 4.12b. Several ports proved difficult to smooth over and remained similar to Figure 4.12a.

All wall pressure measurements were made using the DTC Gen 2 pressure scanners. The pressure-holding capability of each port was checked with a handheld, digital manometer in a similar way to the model pressure-checks described above. Covering the tunnel-side port opening with the manometer tubing and applying a pressure on the order of 10 in. water from the manometer, the pressure reading from the DTC scanner is compared with the manometer reading. While the Kevlar is porous, it is still possible to perform such a pressure check because the polypropylene port and its glue make the Kevlar locally non-porous. The ports leaked air faster than typically seen in other pressure checks presumably because of the difficulty of making a good seal of the pressure calibrator tubing over the woven Kevlar surface. However, as this should not be an indication of leakage of the pressure line itself, the majority of the ports were passed in the pressure checks.

The second measurement of the pressure-velocity relationship measures the flow velocity through the Kevlar at the corresponding location to the wall pressure measurement. The instrument use was an HHF1000 Series hotwire anemometer from Omega Engineering, Inc. The anemometer has flow velocity range up to 25 m/s, operating temperature range from -40 to 120 degrees Celsius, velocity reading resolution 0.01 m/s, velocity reading accuracy of 1.5% full scale, or 0.38 m/s, 200msec response time to velocity fluctuations, and 2 minute settling time for temperature variations. The anemometer contains three resistance temperature detectors (RTD's) mounted in a 6.35 mm outer diameter, 305 mm long probe. The body of the anemometer is strapped with thread and tape to the Kevlar wall below the midspan line which allows the probe to extend up to the midspan region as shown in Figure 4.13a, and the probe tip is held in place by thread sewn through the Kevlar as in (b) and (c). The digital display of the anemometer was captured and relayed to the control room by the video camera shown in (d).

4.8. Kevlar Wall Pressure Distribution Measurements

Using the same pressure port design and installation procedure as in the previous section, the pressure distributions over the entire Kevlar walls were also measured. The fully instrumented port and starboard walls are shown pictorially in Figure 4.14a-b, respectively, and graphically in Figure 4.15. The most critical area on the wall is the midspan since these pressures were used to provide an alternate lift measurement other than the airfoil pressure measurements. At midspan and with a streamwise spacing of 30.5 cm (12 in.), 15 ports on the port wall and 16 on the starboard wall were found usable including the midspan port used for the pressure-velocity characterization explained in the previous section. Three spanwise rows of ports are also present and intended to demonstrate the degree to which the flow is spanwise uniform with 7 spanwise ports at quarter-chord and 5 spanwise ports at the 2 other streamwise locations as shown in Figure 4.15.

Data from wind tunnel walls are adjusted by the reference wall pressures which are the static pressure measured with no model in the test section (Ulbrich and Steinle 1995). The difference of the with-model pressures and without-model pressures reveal explicitly the effects of the model on the walls. Therefore, before testing with any model present, wall pressure measurements were taken while running the wind tunnel from 10-80 m/s in increments of 5 m/s. Given that the leading edge of the rake probes are positioned just 52 cm downstream of the last wall ports, the furthest downstream wall measurements may potentially have experienced some blockage effects from the wake rake although the influence was not expected to be large.

4.9. Kevlar Wall Deflection Distribution Measurements

In addition to the wall pressures, a system to measure the deflection distributions of the Kevlar walls was developed. Previous deflection measurements on Kevlar walls have been made using a traversing rig of infrared sensors developed at the Japan Aerospace Exploration Agency (Ito *et al.* 2010). However, the current measurement system leverages the technique of stereo photogrammetry. The system consists of cameras mounted in each anechoic chamber and viewing targets, or markers, on the Kevlar walls. As the walls deflect under wind loading, images are taken and processed with stereo range-finding techniques to calculate the out-of-plane Kevlar deflection. Stereoscopic range-finding uses a calculation known as direct linear transformation (DLT) which calculates the three-dimensional coordinates of a point identified in two images. The location of a specified point is first expressed in terms of its pixel location in the first image and then in the second image. If the positions and orientations of the cameras are known ahead of time, then DLT is used to calculate the position in three-dimensional space of the given point relative to the either of the cameras.

The nominal resolution, ΔZ, of a depth measurement from a stereoscopic system is given by

$$\Delta Z = \frac{Z^2}{fB + Z\Delta d}\Delta d \qquad \text{Equation 4.3}$$

where Z is the depth to the measurement plane, B the baseline, f the focal length, and Δd the size of one pixel element on the sensor as shown in Figure 4.16a. Design of the stereoscopic system for the SWT was made in light Equation 4.3, as a tradeoff exists between the variables Z, B, and the correlated field of view of the two cameras. Spacing the cameras closer to the measurement plane is very advantageous because the resolution of the system goes by the square of Z. However, closer camera placement requires that the cameras be farther tilted towards each other which introduces errors in the reprojection of the images during processing (Grewe and Kak 1994). Also, increasing B improves resolution but can lead to a smaller correlation region between cameras and

occlusion of markers around the edges of the field of view. Camera systems with more than 2 cameras can additionally produce more accurate results than the 2 camera case, however, such systems were not considered for the current measurements due to the complexity of the post-processing for those systems.

Several configurations of camera placement in the anechoic chambers were tested with the likely best configuration as shown in Figure 4.16b. The cameras are separated by a B of 3.9 m in the streamwise direction, are situated at a Z of 2.1 m from the Kevlar wall, and are positioned midway between the floor and ceiling. The system is composed of four Canon Rebel T3 cameras, each mounted to aluminum camera stands that are rigidly fixed in the outside corners of the anechoic chambers. The optical axes of the cameras are oriented roughly at 45 degree angles to the Kevlar walls such that each camera captures the whole view of its respective Kevlar wall. With such a setup and with the given cameras, which have 18 mm focal length and 5.15×10^{-6} m/pixel sensor size, the theoretical ΔZ as given by Equation 4.3 is 0.3 mm.

Prior to taking measurements with a stereoscopic system, two pieces of information must be found through calibration: the intrinsic parameters of the camera sensing elements and lenses and the extrinsic parameters relating the positions and orientations of the two cameras relative to one another. The calibration method of Zhang (2000) which is implemented in an openly available Matlab source code (Bouguet 2010) was used for the present measurements. The method involves calibration of each pair of cameras with a checkerboard grid such as the one shown in Figure 4.17d. Sun and Cooperstock (2005) show that the calibration error in Zhang's data levels out with about 100 training points per calibration pattern and note that this calibration requires a planar pattern to be oriented at different angles in front of the cameras. Zhang recommends more than 10 orientations at an angle of 45 degrees for best accuracy. The preceding guidelines were used when designing the stereo calibration procedure.

The calibration grid, constructed with care to be as flat as possible, is made on a single piece of 12.7 mm (0.5 in.) thick rigid plastic approximately 61 cm-by-91 cm (24 in.-by-36 in.) in area. It is supported by 80x20® aluminum braces adhered to the shortside edges and in the lateral direction with double-sided carpet tape from Scotch® as shown in Figure 4.17a. Double-sided tape is applied to the plastic, and the checkerboard-printed paper printed is rolled over the strips and smoothed out after each strip of tape to minimize bubbles as also shown in Figure 4.17b-c. The grid has 23-by-18 squares which correspond to 374 usable training points. Each square is exactly 3.048 cm (1.2 in.) on a side as printed with a plotter. For the calibration, nearly 80 pairs of images each were captured for the port- and starboard-sides, each pair with the checkerboard in a different location and/or orientation which conservatively adheres to Zhang's guidelines. The relative locations of the cameras and calibration grid locations for the port and starboard Kevlar walls are shown in Figure 4.18a-b. The locations of the calibration grid in of each of the 80 images was for the most part random although some areas of the measurement space could not be imaged due to difficulty in supporting the calibration grid which was done manually.

After collecting the images, processing is necessary to locate and index the corners of the checkerboard in each image. Using the code of Bouguet (2010), the calibration grid is oriented in the software with the orientation indicator as seen in Figure 4.17d. The code then estimates the location of each of the 374 training points and determines their locations precisely with a corner-finding algorithm. For the present testing, the search size window in the latter step was begun at 10-by-10 pixels and then recomputed at 5-by-5 pixels. Given the corner locations in each image and assuming that the corners correspond to a perfectly flat, equally spaced grid of points, the calibration code returns each camera's intrinsic parameters of focal length, principal point, skew, and distortion as well as the extrinsic rotation and translation vectors between pairs of cameras.

There are several corrections that camera calibrations may apply such as radial distortion correction including estimates of up to the 6th order radial term of the lens, decentering distortion correction by allowing the principal point of the camera to vary from the default origin, and skewness correction by allowing for skew in the x- and y- pixel directions of the camera sensor.

Based on the recommendations of Sun and Cooperstock (2005) that were also confirmed by trial runs, all three of these corrections are included except that the radial distortion is only estimated up to the 4th order term.

A suitable marker that is easily identifiable in image processing was found to be the fluorescent stickers shown in Figure 4.19a. By illuminating the anechoic chamber with fluorescent lights, each of the 12.7 mm (1/2 in.) diameter fluorescent stickers lights up brilliantly, thus being easily distinguishable from its surroundings as shown in Figure 4.19b. Both the Kevlar walls are marked with a grid of stickers as shown in the figure which are evenly spaced approximately 15 cm (6 in.) apart in both the horizontal and vertical directions to form an 11-by-26 matrix of stickers. In a 15-by-15 square cm of Kevlar, the total area fraction occupied by the stickers is less than 1%, so the presence of the stickers should have a negligible effect on the aerodynamic behavior of the Kevlar.

During airfoil testing, cameras captured the locations of each sticker on the Kevlar walls for the full range of angles of attack tested. Near simultaneous, remote capture of pictures is accomplished by connecting the cameras to a central computer with a USB hub and with the software DSLR Remote Pro Multi-Camera by Breeze Systems. A Matlab code was used to filter the pixels of the images by color and locate the centroids of the groups of pixels that corresponded to each individual marker. The marker locations were stereo-triangulated to give the three-dimensional location and thus deflection of each point in the grid. The 11x26 grid of deflected points were then fit with a surface fit. In the present study, the surface fitting employed is a polynomial surface, 6th order in both x- and y-directions and including all interaction terms. As a practical matter, the polynomial is a 4th order polynomial that is multiplied by 2 x-terms and 2 y-terms that force the surface fit to go to 0 at the Kevlar boundaries. The coefficient of determination, R^2, was used to verify the appropriateness of the surface fit, and typical values were 0.99 and above.

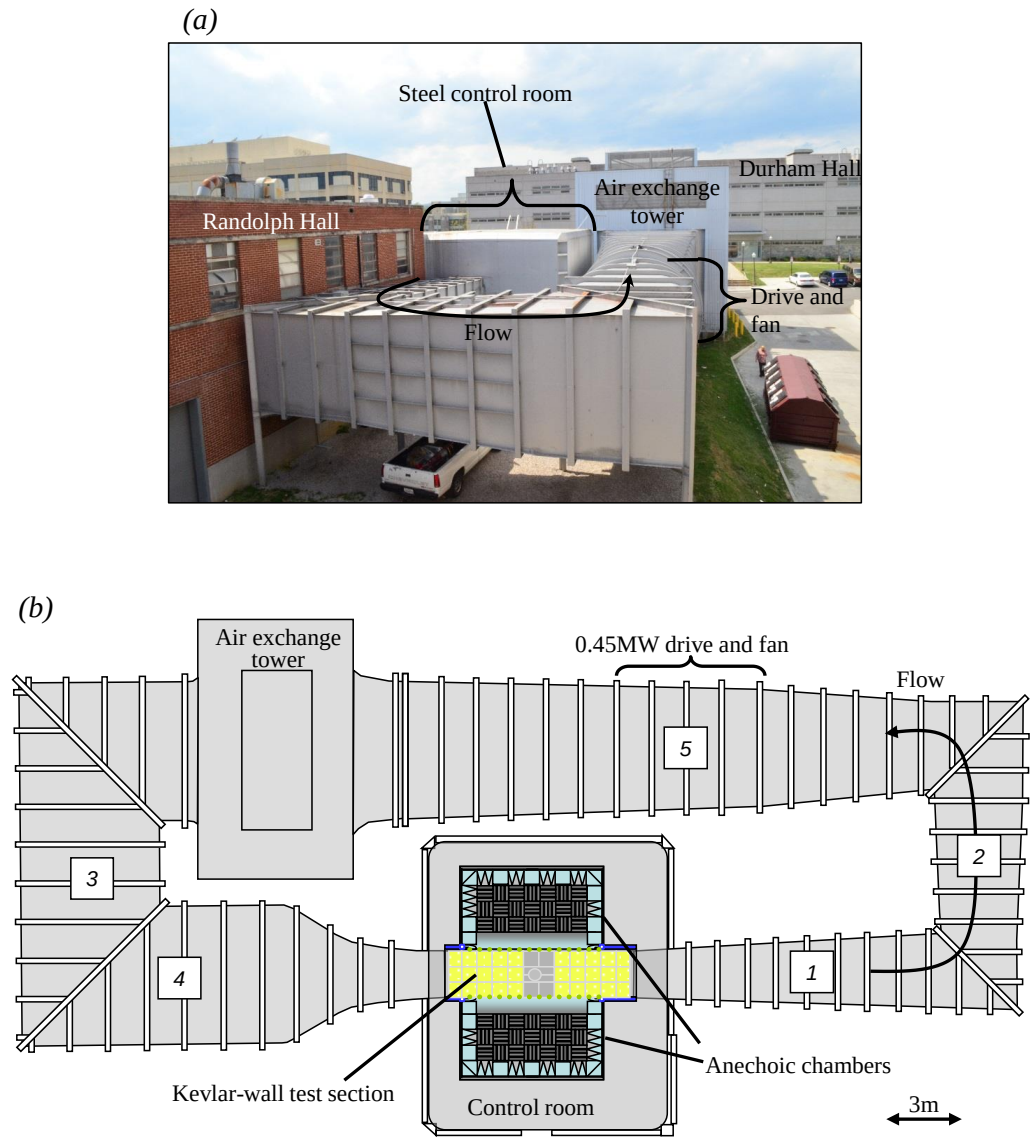

FIGURE 4.1. *(a)* Photograph and *(b)* plan view schematic of the closed-circuit Virginia Tech Stability Tunnel. The steel control room is sealed from inside Randolph Hall by an airlock. The tunnel is in anechoic configuration as depicted in *(b)* with the Kevlar-wall test section flanked on either side by anechoic chambers. (Illustration credit: Dr. William J. Devenport.)

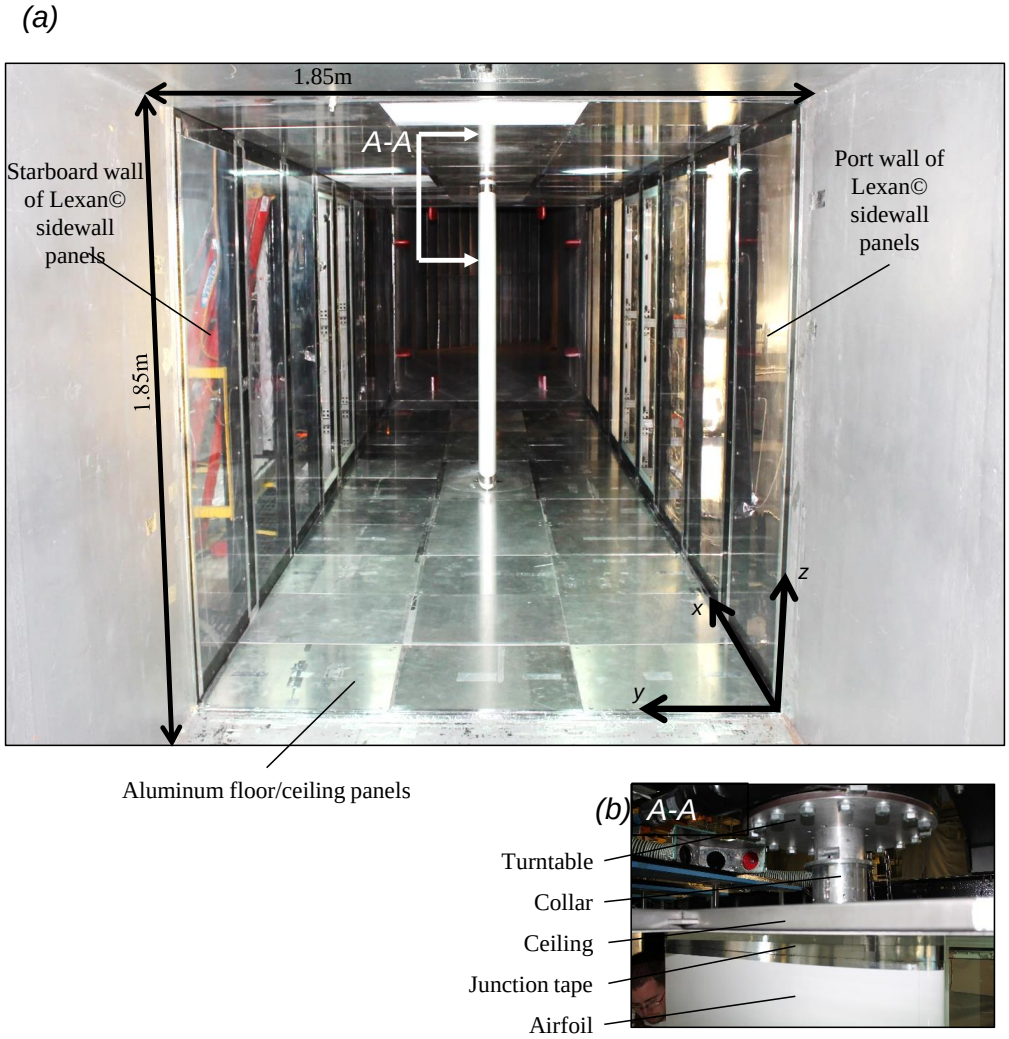

FIGURE 4.2. *(a)* Downstream-looking view and *(b)* section view of the ceiling of the 1.85 m-by-1.85 m hard-wall test section with a full-span airfoil model installed. The end of the contraction and the start of the constant-area test section is given by the location $x = 0$.

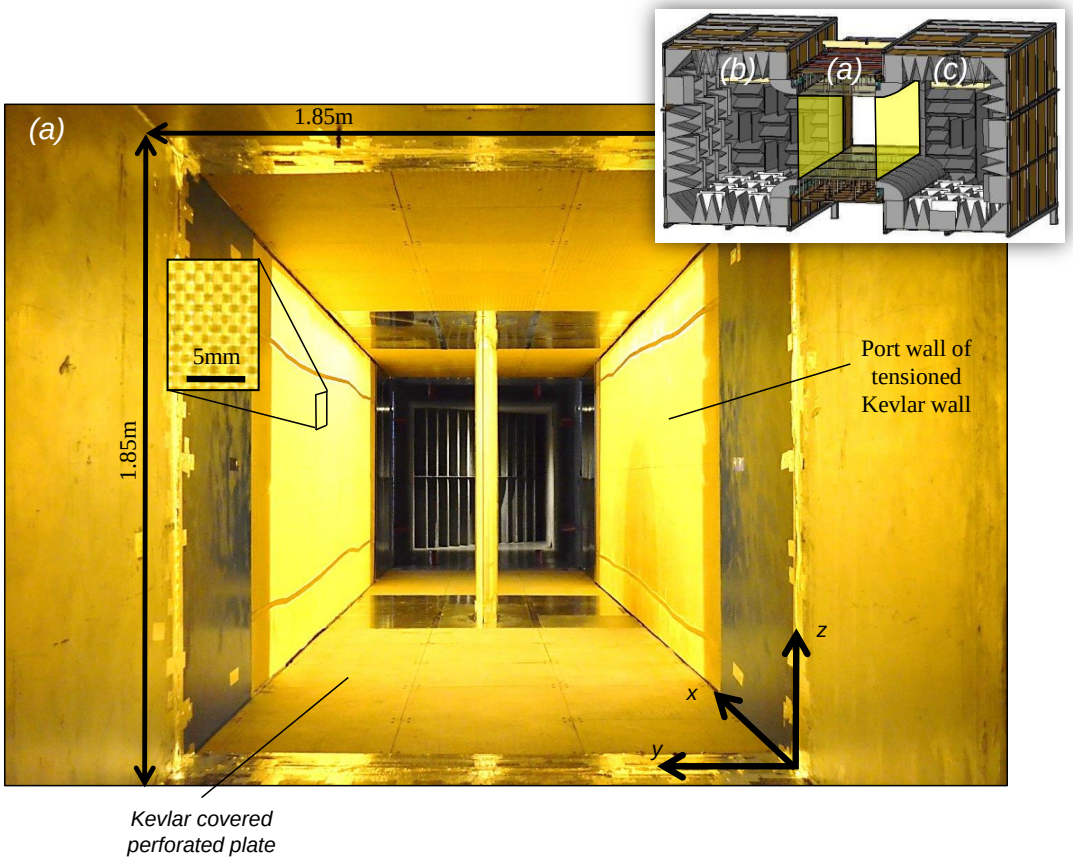

FIGURE 4.3. *(a)* Downstream-looking view of the 1.85 m-by-1.85 m Kevlar-wall test section with a full-span airfoil model installed. *(b)* Starboard anechoic chamber with a microphone array and *(c)* port anechoic chamber with a microphone array. The end of the contraction and the start of the constant-area test section is given by the location $x = 0$. The sidewalls are made of tensioned Kevlar cloth, and the floor and ceiling are made of either aluminum panels or perforated aluminum panels covered with Kevlar cloth. The test section used for the current testing was configured as pictured in *(a)* except with the Kevlar covered panels replaced with standard aluminum panels to allow for pressure instrumentation on the floor.

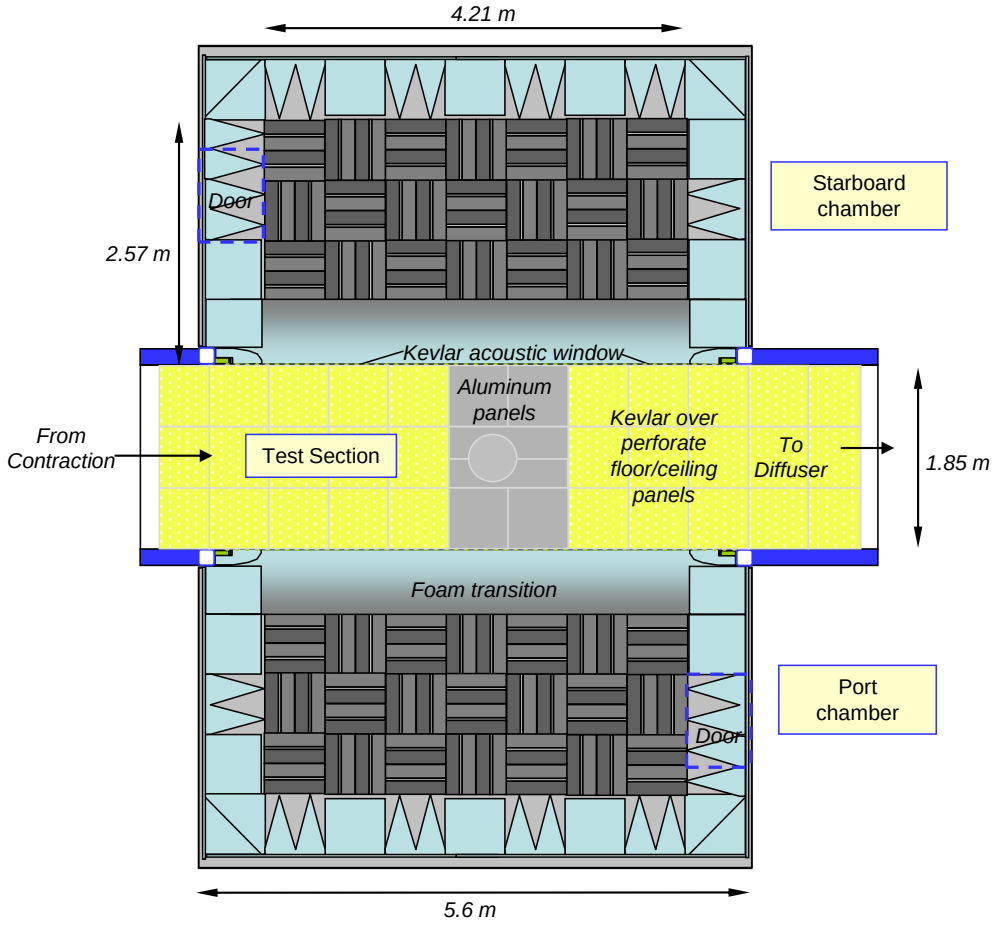

FIGURE 4.4. Plan view cross-section of the Kevlar-wall test section (center) between the two anechoic chambers. (Illustration credit: Dr. William J. Devenport.)

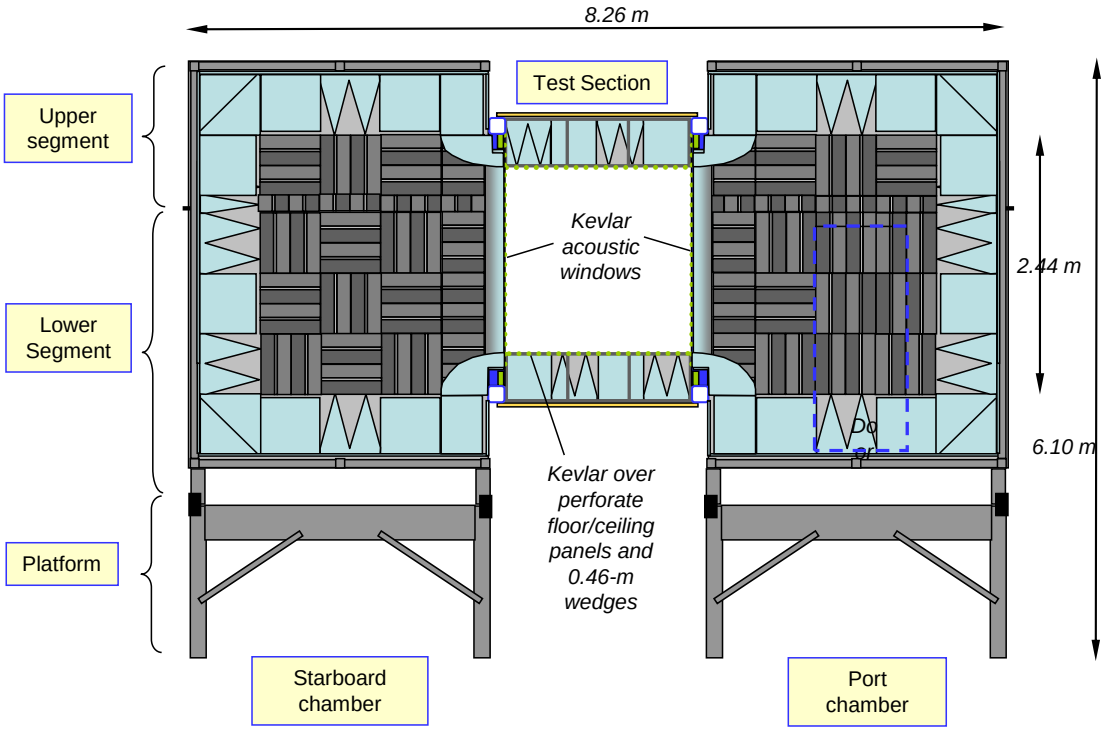

FIGURE 4.5. Cross-section of the Kevlar-wall test section (center) between the two anechoic chambers looking downstream. (Illustration credit: Dr. William J. Devenport.)

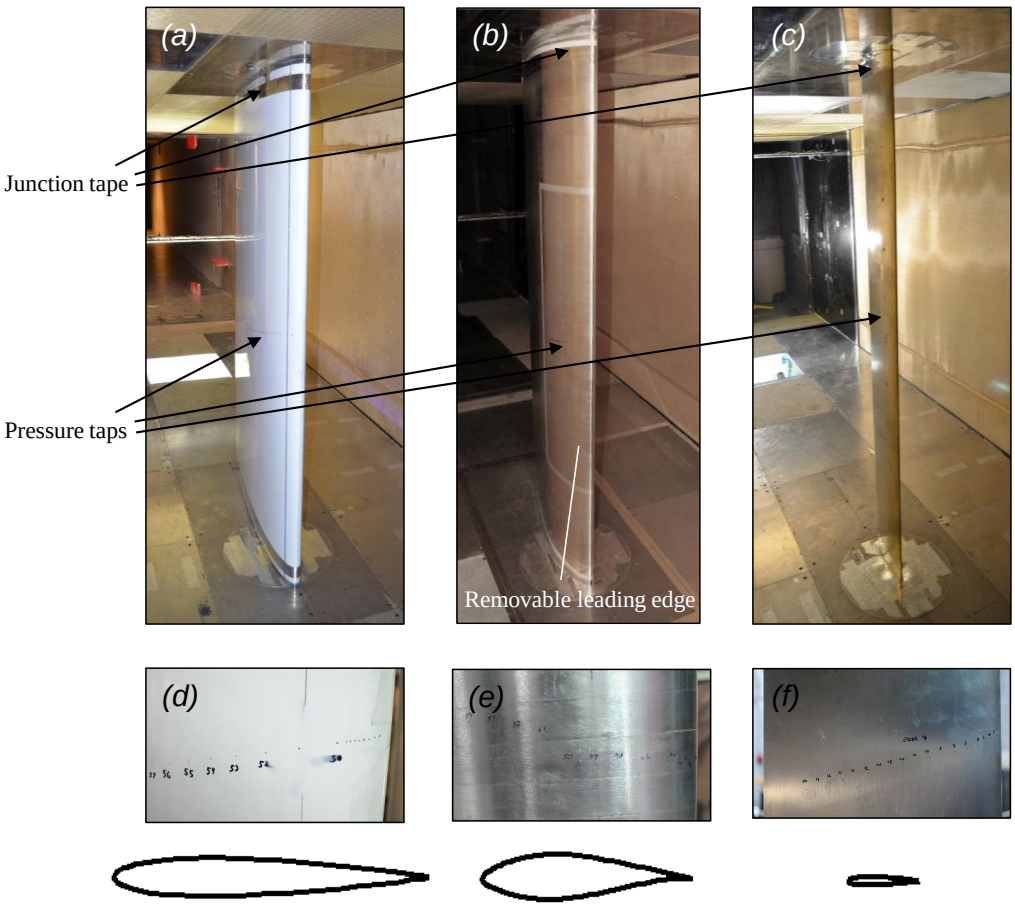

FIGURE 4.6. (a) - (c) Isometric view and (d) - (f) close-up view of the surface pressure taps for the 0.91 m NACA 0012, 0.61 m DU00-W212, and the 0.20 m NACA 0012 airfoils, respectively. In (d) - (f), the pressure taps are visible just above or below the labels written in black marker. The profiles at the bottom of the figure show the relative proportions of each of chord length.

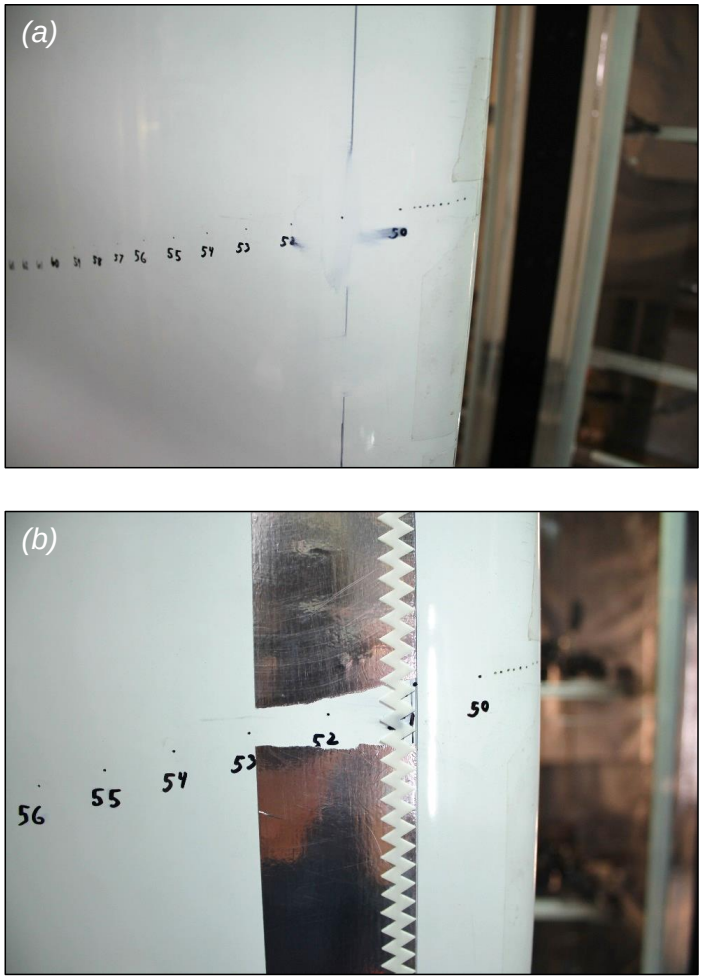

FIGURE 4.7. Close-up of the midspan, leading edge region of the 0.91 m NACA 0012 airfoil in the (a) untripped and (b) tripped conditions. The leading edge of the trip is installed at 5% chord and is mounted on foil tape to bring the total trip height to 0.525 mm.

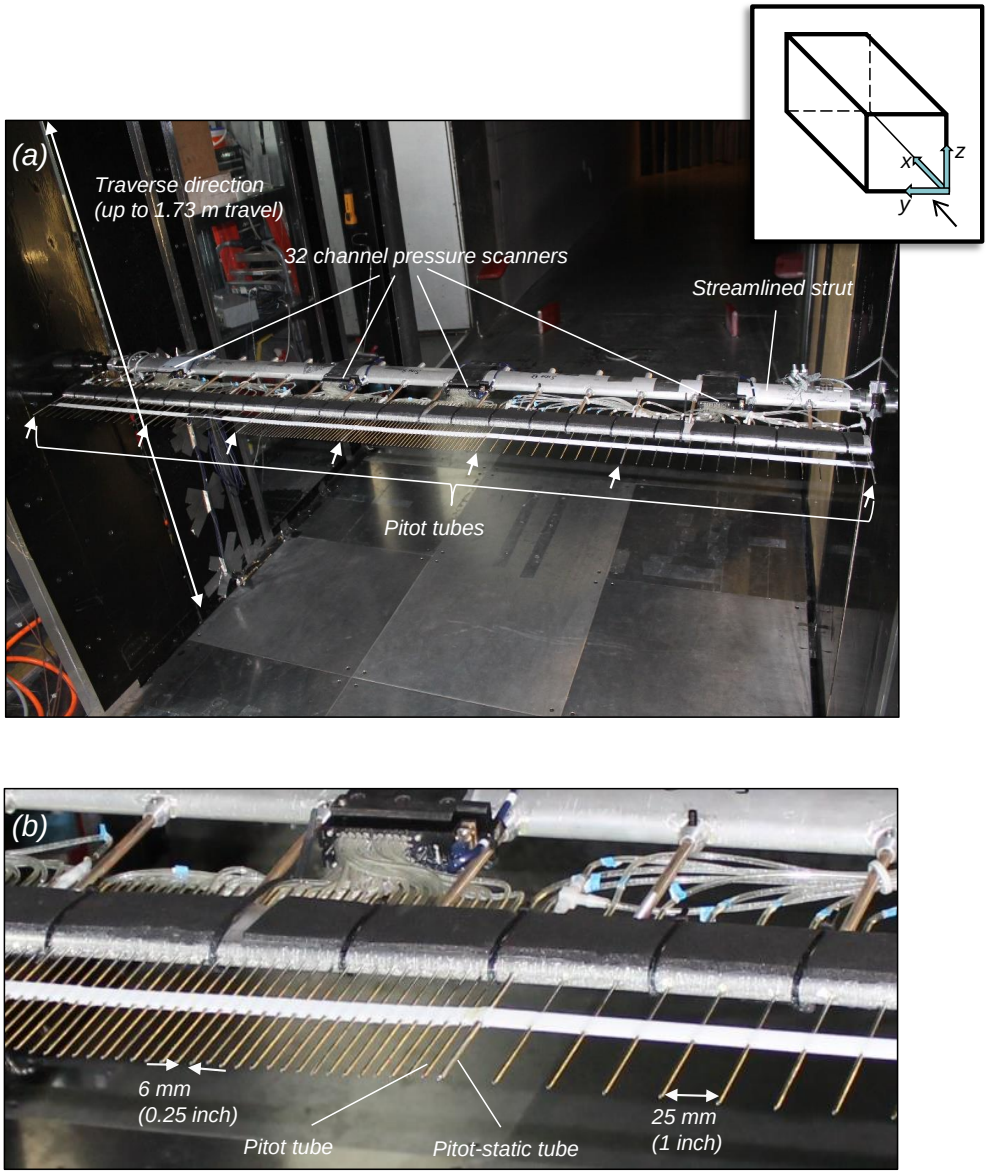

FIGURE 4.8. (a) Wake rake mounted in the rear of the test section as seen from the port-side of the test section and looking downstream and (b) a detail view of the Pitot and static probes. Static probes in (a) are indicated by the arrow heads.

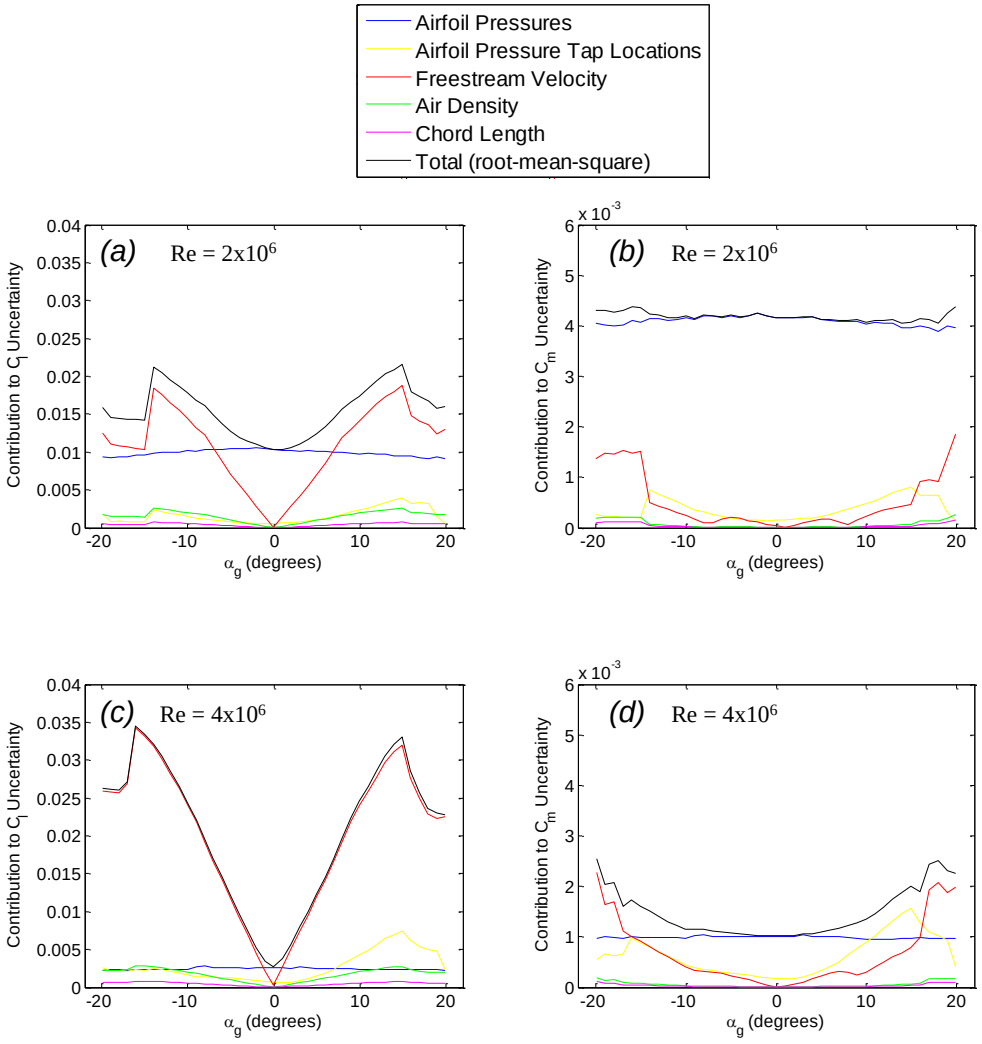

FIGURE 4.9. Uncertainties in the measured (a), (c) lift coefficients and (b), (d) moment coefficients for the case of the 0.91 m NACA 0012 airfoil at the nominal Reynolds numbers indicated.

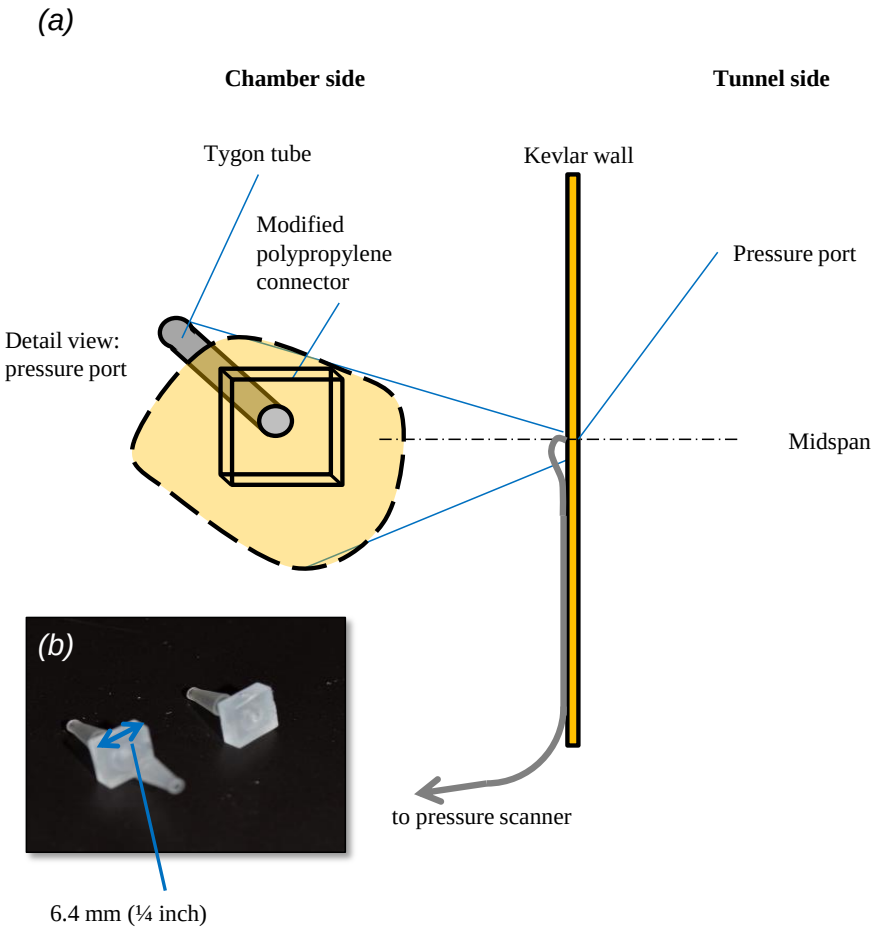

FIGURE 4.10. (a) Side view and detail view schematics of the Kevlar-wall mounted pressure taps and (b) picture of the polypropylene connector (left) before and (right) after flattening of the Kevlar-side face.

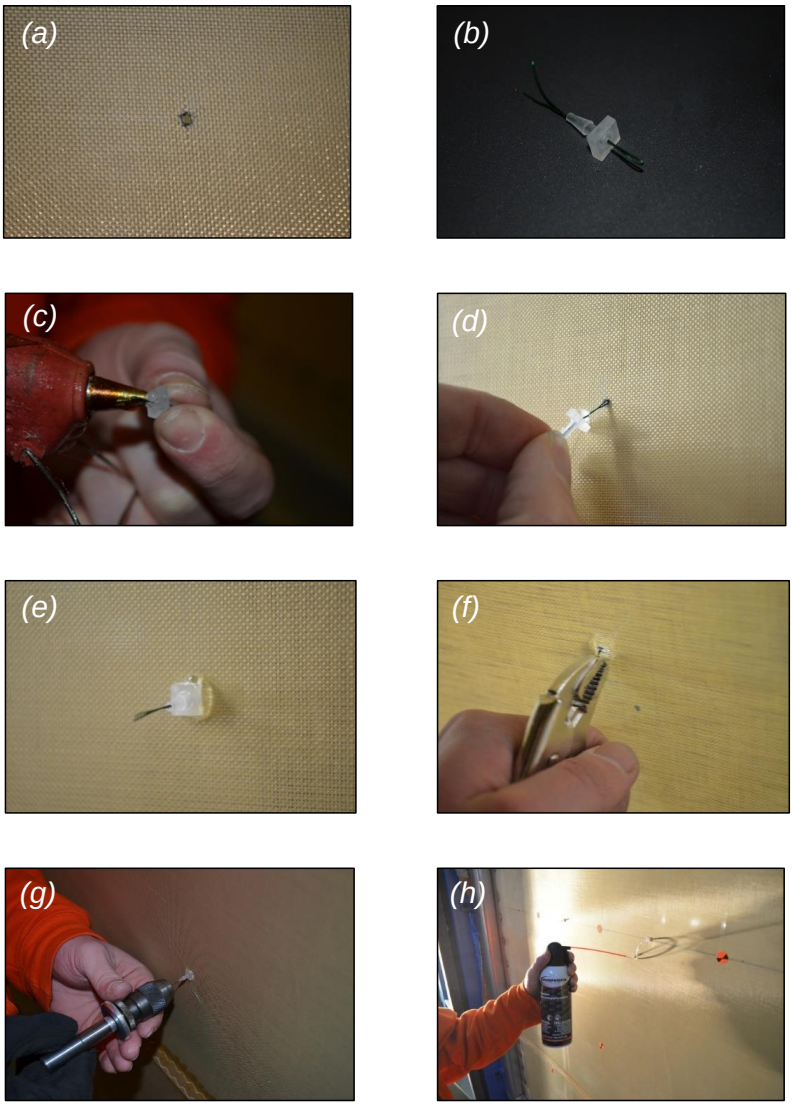

FIGURE 4.11. Step-by-step installation procedure for the Kevlar-wall mounted pressure taps.

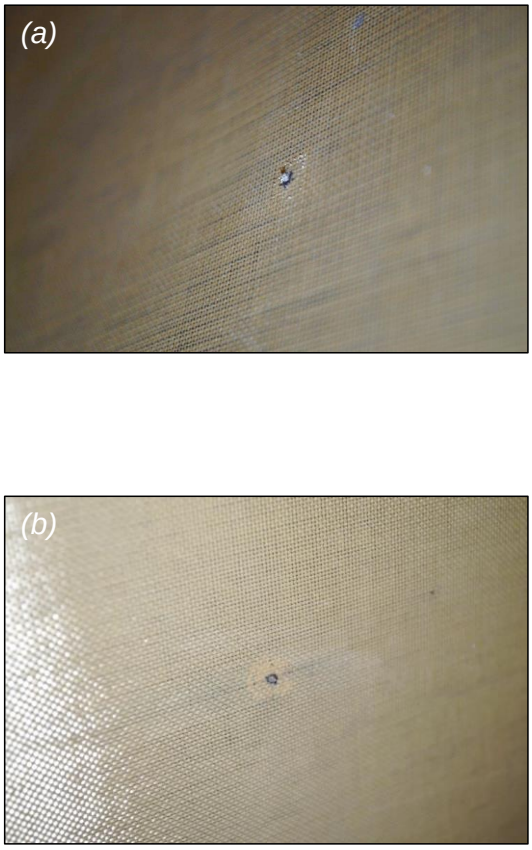

FIGURE 4.12. Tunnel-side view of pressure taps through the Kevlar including (a) an example of a poor surface finish because of extra hot-glue that is not removed easily and (b) an example of a good surface finish.

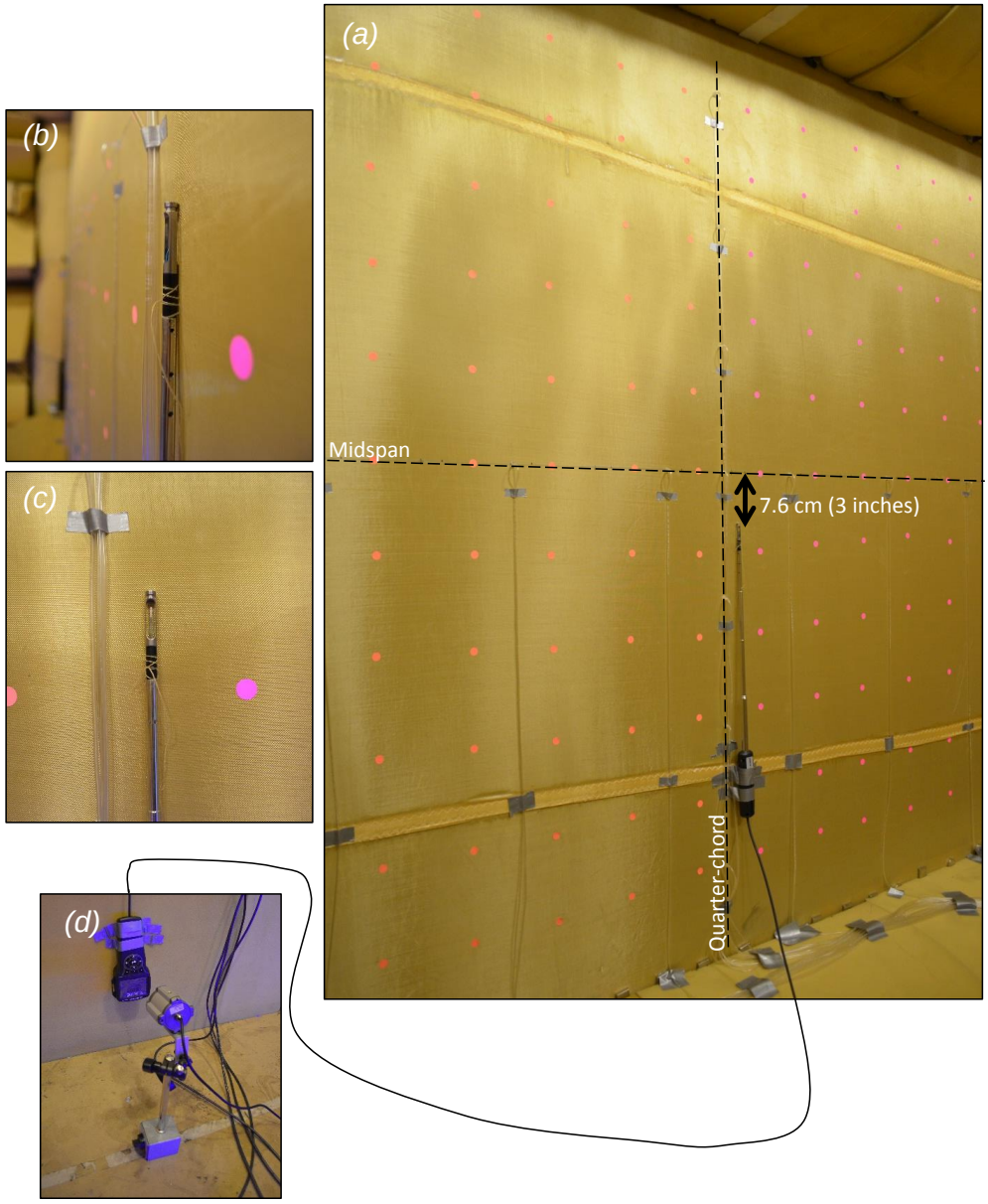

FIGURE 4.13. (a) Chamber-side view of the hot-film anemometer and Kevlar-wall mounted pressure port setup. (c)-(d) Close-up views of the hot-film anemometer probe tip. (d) Hot-film anemometer digital display, and the video camera used to relay readings to the control room.

(a) port

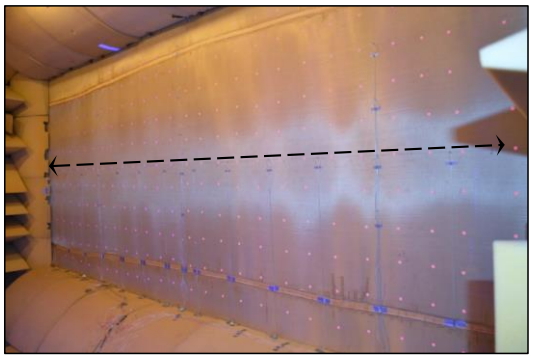

(b) starboard

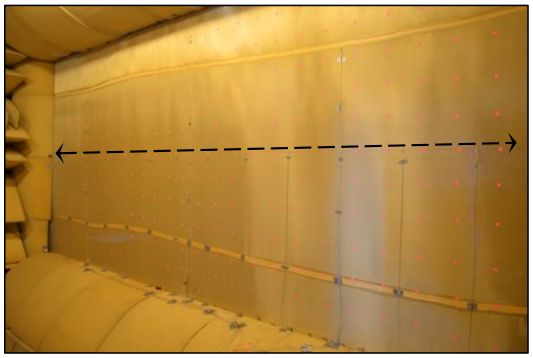

FIGURE 4.14. Chamber-side view of the Kevlar walls in the (a) port and (b) starboard anechoic chambers. The midspan of the test section is indicated by the dashed lines.

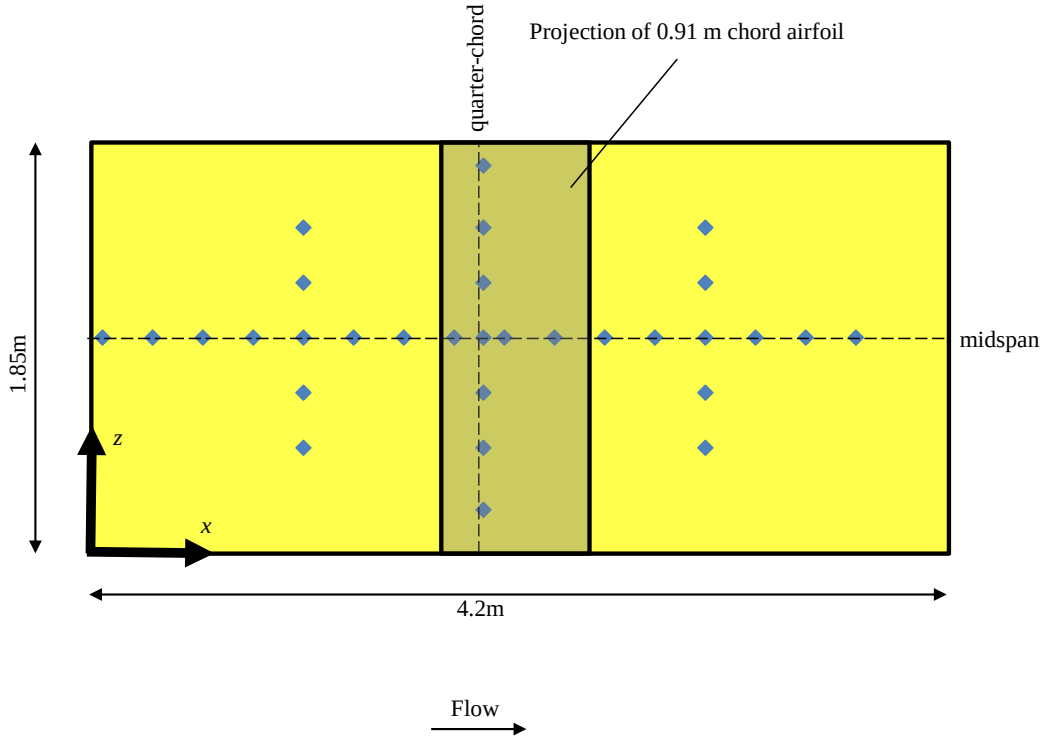

FIGURE 4.15. Arrangement of the Kevlar-wall mounted pressure taps. The layout is the same for the port and starboard walls.

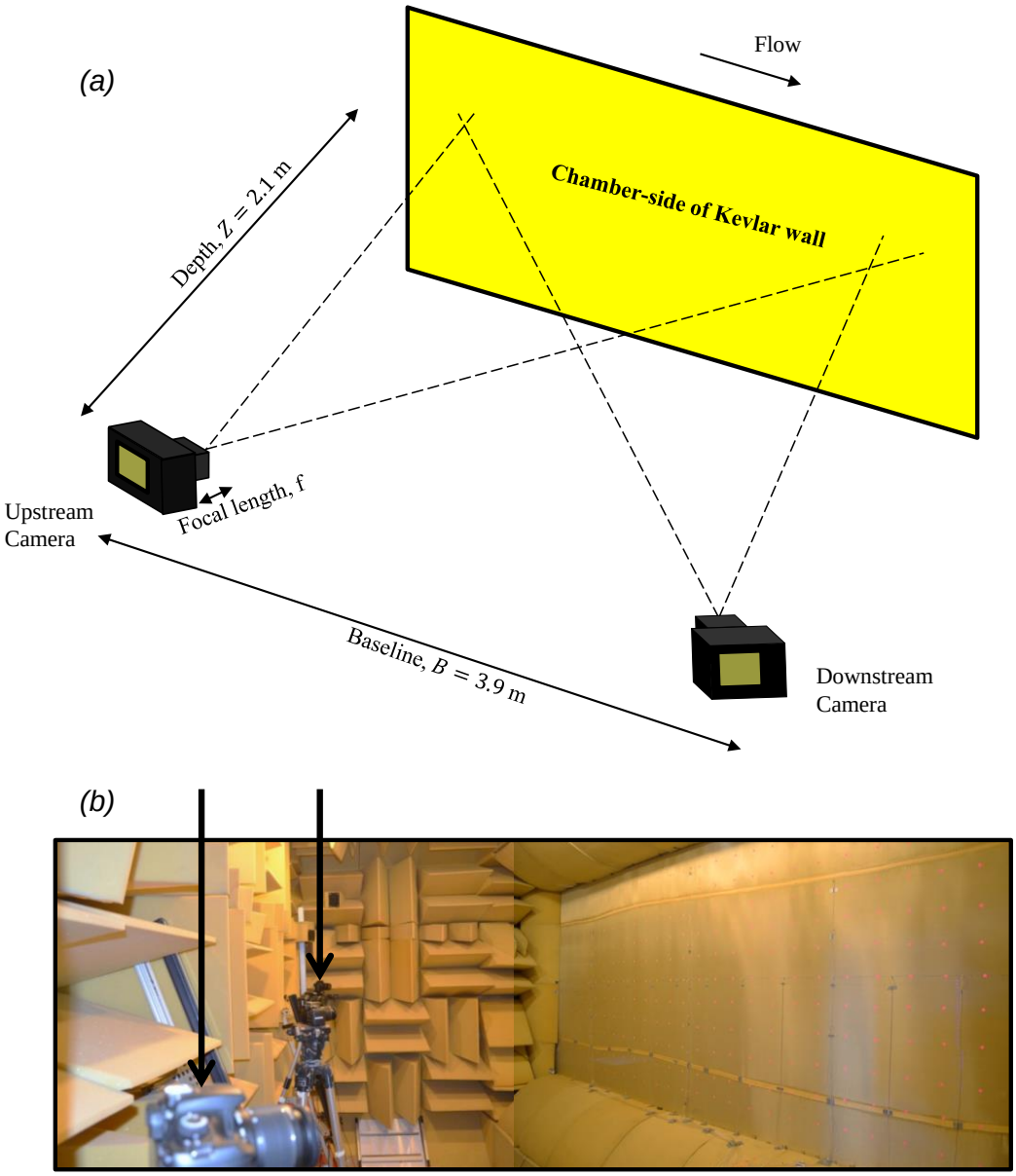

FIGURE 4.16. (a) Chamber-side schematic of the stereo camera setup relative to the measurement space on the Kevlar wall and (b) stitched photograph of the cameras and Kevlar wall. In (b), the cameras are indicated by the arrows. The cameras are rigidly mounted at the mid-height of the chambers aluminum braces that are not clearly visible.

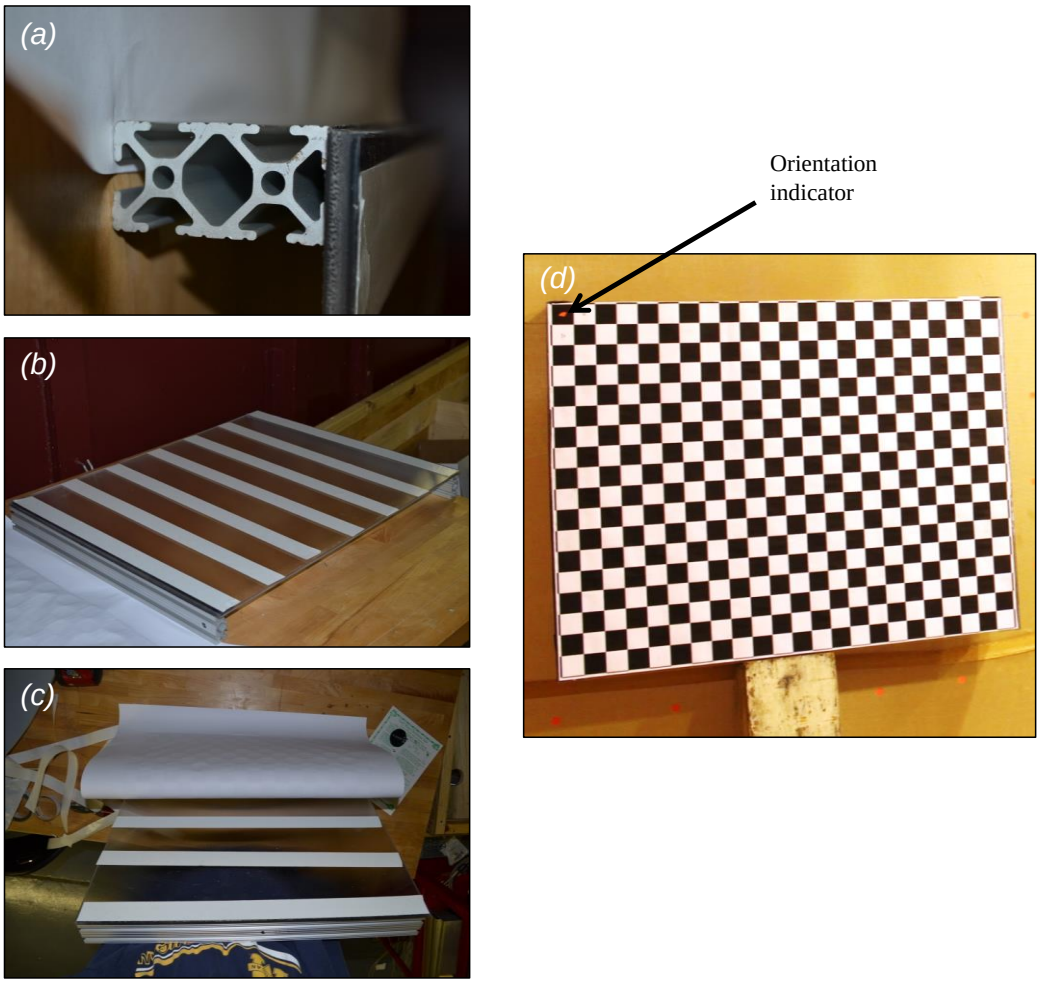

FIGURE 4.17. Fabrication of the calibration plate beginning with (a) aluminum braces providing rigidity for a plastic plate. (b) Double-sided tape adhered to the plastic receives the checkerboard calibration pattern as printed from a plotter. (d) Calibration plate in-use with the orientation marking indicated by the black arrow.

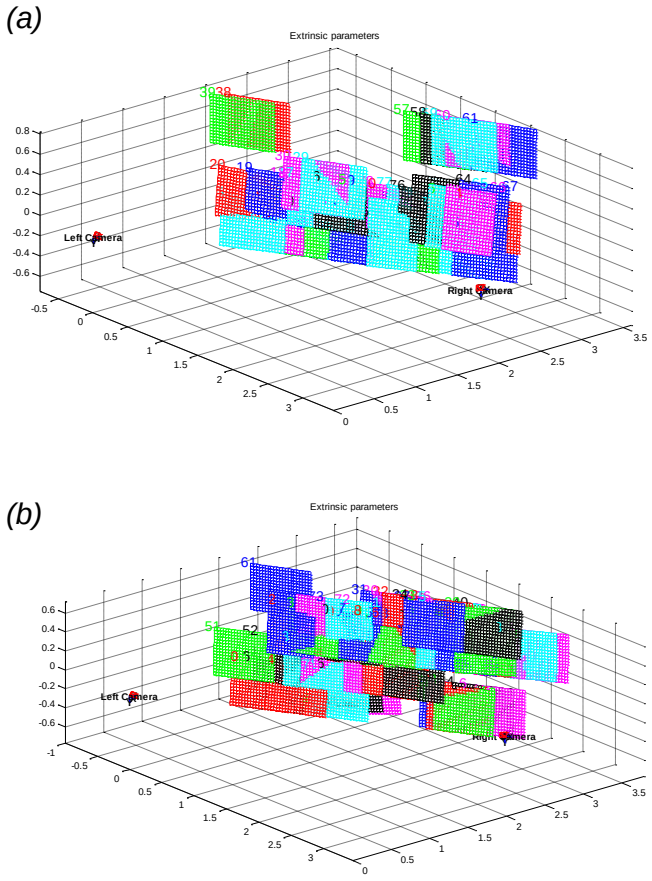

FIGURE 4.18. Relative locations of the cameras and calibration plate locations for the (a) port-side and (b) starboard-side Kevlar walls. Roughly 80 different orientations were captured for each Kevlar wall.

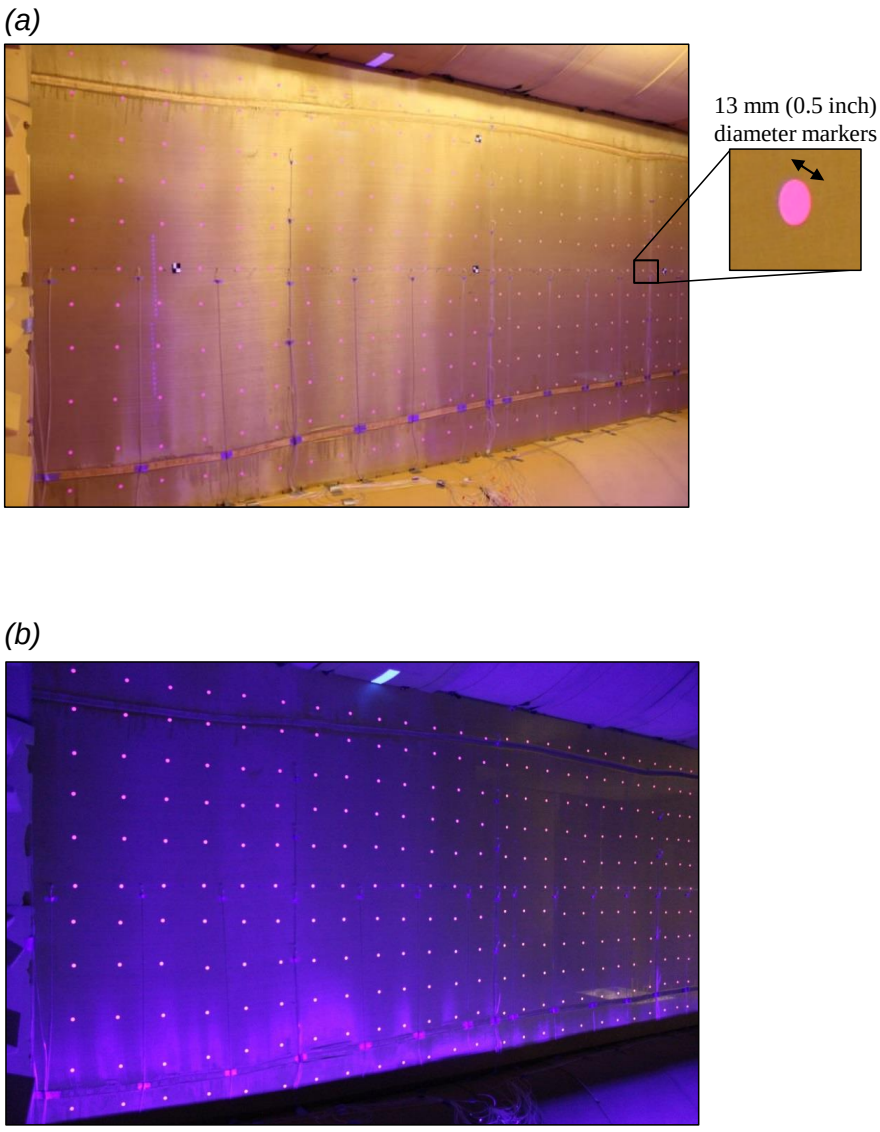

FIGURE 4.19. Kevlar wall with sticker markings and wall pressure ports shown in (a) ordinary lighting and (b) under fluorescent lighting. The grid markers are 13 mm (1/2 inch) diameter fluorescent stickers arranged in an 11-by-26 matrix and spaced 15 cm (6 inches) apart equally in both the horizontal and vertical directions.

CHAPTER 5. Results and Analysis

Results and analysis are presented first for the validation of the hard-wall test section at the SWT in order to provide a thorough understanding and confidence in the performance of this test section. Subsequently, the aerodynamic corrections of the Kevlar-wall test section will be discussed in-depth, both expounding on the findings of Devenport *et al.* (2013) and making additional analyses on the sensitivity and validation of the panel method simulation.

5.1. Validation of Hard-Wall Test Section

The performance of the hard-wall test section of the SWT is assessed in Section 5.1 for flow uniformity, consistency with other facilities, lift symmetry, and the effect of vortex generators.

5.1.1. Flow Uniformity

Cross-sectional and streamwise flow uniformity are important considerations for wind tunnels, and preliminary testing in the SWT was performed to assess the uniformity in the freestream without any models in the test section.

Measurements of the SWT's flow uniformity have been previously by Choi and Simpson (1987). The tunnel at the time of Choi and Simpson's measurements featured much the same hardware as in the current study including the same turning vanes at all 4 corners of the circuit and the same 7 turbulence screens in the settling chamber. Two major differences are the fan blades which were replaced in 1996 and the acoustic lining currently used throughout the circuit.

Barlow *et al.* (1999) state that a test section should have no more than 0.50% variation across its cross-section from the mean dynamic pressure or, equivalently, 0.25% variation from the mean velocity. Variation in flow angle should be kept within 0.10 degrees, at least near the region of the model. While no measurements were taken to quantify the variation in flow angle, the wake rake was used to measure the velocity variation in the test section both at upstream and downstream locations in the test section, converting the measured total pressure, p_0, and static pressure, p_s, to the velocity fraction, $\frac{V}{V_\infty}$, with the use of the air density, ρ, by

$$\frac{V}{V_\infty} = \sqrt{\frac{p_0 - p_s}{0.5\rho V_\infty^2}} \qquad \text{Equation 5.1}$$

The uncertainty in $\frac{V}{V_\infty}$ is due to the uncertainties of the pressure transducers measuring p_0, the uncertainty in the freestream static pressure p_s, the uncertainty of the temperature measurement for calculating ρ, and the uncertainty in the freestream velocity measurement. A jitter analysis on these measurements similar to that shown in Appendix B yields a 20:1 odds uncertainty in $\frac{V}{V\infty}$ of 0.6%. The uncertainty in $\frac{V}{V\infty}$ may be smaller than that calculated by the jitter analysis due to the post-processing calibration of each Pitot-probe. The calibration sets each of the Pitot C_p values to exactly unity when the probes are experiencing freestream inviscid flow which reduces any bias offset associated with the p_0 measurement as described in Section 4.5. Even with these considerations, the uncertainty of the Pitot measurements from probe to probe is still a large source of uncertainty as will be shown below. The p_s used in Equation 5.1 is taken to be the freestream static pressure at the test section entrance rather than the static pressures of the 7 Pitot-static probes due to questions about the calibration of these static probes. Thus, additional uncertainty not accounted for in the jitter analysis is introduced since neither local variations in static pressure across the test section nor the static pressure drop through the test section are considered.

A full cross-section of the empty test section with the rake in the front of the test section positioned the probe tips at x=0.15±0.012 m according to the coordinate system introduced in Chapter 4, and the cross-sectional profile is shown in Figure 5.1a. The values are plotted as the percent change from the nominal freestream value, in this case 59m/s, as measured by the pressure ports in the contraction and settling chamber. The Lexan wall panels used to accommodate the rake at the front of the test section began experiencing flow-induced vibrations as freestream velocity increase, so the maximum velocity was limited to 59 m/s.

While the normalized velocity is 0.6% uncertain as noted above, the full range of velocities in Figure 5.1a represent a span of 0.5% freestream velocity. The many vertically or near-vertically sloped contour lines, therefore, seem to be a result of either the non-local measurement of static pressure or more likely, the uncertainty between Pitot probes. The uncertainty in the Pitot transducer measurement does not appear to be due to non-repeatability but rather hysteresis or non-linearity as indicated by the repeating contour patterns. Many of the finer contour shapes are therefore attributable to the uncertainty of the Pitot measurement rather than actual gradients in the flow. In other words, there is greater uncertainty between measurements made by different Pitot probes in the y-direction than between successive measurements made by the same probe in the z-direction. The analysis below, therefore, focuses on the velocity gradient $\frac{dV_\infty}{dz}$ rather than $\frac{dV_\infty}{dy}$, although such a gradient may also be present but masked by the measurement uncertainties.

Looking at the overall trends, a small $\frac{dV_\infty}{dz}$ is present with the velocity being roughly 0.15% freestream larger at the top of the test section than at the bottom. The recommendation of Barlow *et al.* (1999) that the velocity be everywhere within 0.25% of the reference freestream value is satisfied everywhere outside of the boundary layer. The boundary layer height on the sidewalls is less than the closest measurement to the wall of 3cm at this streamwise location.

Full cross sections of the empty test section were also taken with the rake in the rear where the probe tips were at x=6.44±0.012 m as shown in Figure 5.1b. A spanwise gradient still exists and generally the velocity outside the boundary layer is within 0.25% of the reference freestream value with the one main exception being the low pressure region on the floor at $y \approx 1.6$m of Figure 5.1b. The following measures were applied to the floor in an attempt to prevent this low pressure region: taping the joints on the floor and ceiling plates over the whole streamwise length of the starboard-side, taping the corner nearest the separation over the whole streamwise length, smoothing a section of the contraction floor where a dip exists, and removing a protruding screw in the end of the contraction. None of these measures had a visible effect on the low pressure region, nor did laying tufts along the test section floor reveal any changes in the flow leading up to the region. It is believed that this region is a weak corner vortex originating from the corner between the starboard wall and the floor that has been displaced inboard. Weak corner vortices which are prominent in the other three corners can arise due to stretching in the contraction of shear-induced secondary flows initiated in the settling chamber and slight leaks in the test section corners. Although present in the upstream, as well, they only on appear in the cross-section as they have had longer time to develop. The boundary layer at this downstream location has grown from the upstream case and is now everywhere thick within the two-dimensional flow regions at least 7cm and up to 15cm.

Figure 5.2a-c shows a comparison of the velocity cross-sections at the rear of the test section for nominal freestream velocities of 40, 60, and 80m/s, respectively. The velocity gradient in the z-direction, as well as the vertical contours due to the uncertainty between adjacent Pitot probes, is again present at all three velocities, and the corner vortices behave similarly across the range of velocities.

5.1.2. Comparison of Airfoil Measurements with Data from Other Facilities

Airfoil tests in the hard-wall test section provided a basis for which to compare with data from other sources and a baseline with which to compare the SWT's own Kevlar-wall results. The 0.91 m NACA 0012 airfoil was selected as the primary model with which to compare to data from other sources due to the its large chord which puts an extreme test on the interference corrections and due to the abundance of data in the literature on this cross-section.

McCroskey (1987) gives a compilation of many tests on full-span NACA 0012's including remarks on the experimental methods and data from each study. The work of Ladson (1988), who employed a similar test matrix and setup to that in the current paper, was placed in the top category of integrity of experimental methods as they "clearly stood out as having been conducted with the utmost care and/or as most nearly eliminating the important sources of wind-tunnel errors." Ladson performed experiments at the Langley Low-Turbulence Pressure Tunnel (LTPT) using a 0.6010m chord NACA 0012 in a full-span, 0.914m-by-2.286m test section. Untripped and tripped runs were made at lower Reynolds numbers of 2.00×10^6 and 2.00×10^6, respectively, and at higher Reynolds numbers of 3.94×10^6 and 4.00×10^6, respectively. Similarly, the present SWT runs were made at corresponding Reynolds numbers of $1.99 \times 10^6 \pm 1 \times 10^4$, $1.99 \times 10^6 \pm 1 \times 10^4$, $3.90 \times 10^6 \pm 4 \times 10^4$, and $3.91 \times 10^6 \pm 4 \times 10^4$. These Reynolds numbers for the SWT are reported as averages of the Reynolds numbers recorded throughout the angle of attack sweep, the standard deviation across a sweep being at most 2.03×10^4. The Reynolds numbers of the SWT data vary from those of the corresponding Ladson data at most by 9×10^4. The Mach numbers of the Ladson experiments were controlled at 0.15 for all Reynolds numbers. Those of the SWT experiments were 0.10 ± 0.0007 and 0.21 ± 0.002 for the low and high Reynolds number cases, respectively. Both Ladson and the SWT data are corrected with the method of Allen and Vincenti (1944). Ladson reports wall interference corrections to be around 2% of the aerodynamic coefficients. For the SWT test which had nearly twice the ratio of chord to test section height, lift coefficient corrections were between 7-8% and angle of attack corrections were up to 0.8 degrees at maximum lift.

Detailed information about the model preparation and test setup of Ladson is important to compare with the same done at the SWT which is presented in Section 4.4. The model coordinates of Ladson were accurate to within 0.02% chord as compared to 0.10% for the SWT's 0.91 m NACA 0012. The Ladson model was instrumented with 3 separate chordwise rows of pressure taps each with 24 taps spaced across the pressure and suction-sides with diameter 1.52 mm. The center, chordwise row of pressure taps was 10.67 cm from the model centerline. The SWT model has nearly twice the density of ports in the chordwise direction and three times smaller diameter taps at 0.5 mm which show the SWT setup to be more than adequate to reproduce the results of Ladson. Both test setups employed a wake rake roughly 1m downstream of the airfoil to provide drag data.

The pressure transducers used by Ladson to measure airfoil and wake pressures had an uncertainty of 0.25% of reading. For the higher Reynolds test conditions of Ladson, this corresponds to an uncertainty of better than 0.012 as compared to 0.004 at the SWT. The accuracy of the freestream velocity measurement in the Ladson experiment was significantly higher than at the SWT as their freestream velocity pressure transducers had an uncertainty of 0.02% of reading or less as compared to 0.5% of full-scale for the SWT's instrumentation. The overall uncertainties of the corrected angle of attack, lift, moment, and drag coefficients for Ladson were estimated by repeating the zero degree angle of attack measurement and found to be ± 0.01 degree, ± 0.004, ± 0.0002, and ± 0.0002, respectively. As stated in Section 4.6, the uncertainties at the SWT are several times larger.

Measurements in Ladson and at the SWT were taken at both free transition and fixed transition of the boundary layer. For the latter, Ladson used a trip with carborundum grit no. 60 adhered to strips that wrapped around the leading edge to the 5% chord locations on either side of the airfoil. The nominal height of no. 60-grit is trip is 0.265 mm, so the trips would have been

slightly thicker when including the mounting tape. Ladson also provides data for an 80-grit trip of the strip type beginning at 5% chord and extending 1% chord chordwise on both the suction- and pressure-side.

The trip typically used in the SWT as described in Section 4.4 is a serrated pattern with total height of 0.525mm, almost double the height of the Ladson trip but not extending around the leading edge. This trip was used in the SWT for the runs of the 0.91 m NACA 0012 at the nominal Reynolds number of $2x10^6$. For testing the case of the nominal Reynolds number of $4x10^6$, a custom in-house trip was made following the guidelines of Braslow and Knox (1958) to more closely match the trip of Ladson. The trip was composed of no. 60 carborundum grit adhered to strips of 3M™ Removable Repositionable Double Coated Tape 9425. The grit and strips were a total of 0.4 mm high and extended from 5-6% chord and were not mounted on foil tape. While the roughness of this custom trip closely matched that of the Ladson trip, the custom trip again did not wrap around the leading edge as in Ladson. A sample of the trip is compared to that of Braslow and Knox in Figure 5.3. While the 60-grit grain size of the SWT trip is for some unknown reason slightly larger than the 60-grit grain size of the Braslow and Knox, the density of grains for the SWT trip was controlled to imitate that of Braslow and Knox. Braslow and Knox had 8-9 grains per 1/16 in.^{2}, and the SWT trip had around 7-11 grains per 1/16 in.^{2}, with the sample in Figure 5.3b having 10 grains per 1/16 in.^{2}.

Figure 5.4 plots the corrected lift coefficient, C_{lc}, of Equation 2.17 versus the corrected angle of attack, α_c, of Equation 2.8 for the untripped and tripped tests of the NACA 0012 airfoils from both wind tunnels at nominal Reynolds of numbers of $2.00x10^6$ in subplots a-b and $4.00x10^6$ in subplots c-d. The SWT data includes error bars from the jitter analysis and 0.1 degree angle of attack uncertainty as stated in Chapter 4. All data in the figure pass by the origin as the NACA 0012 is a symmetric airfoil with zero lift at zero angle of attack. In both Reynolds numbers at the untripped condition as shown in Figure 5.4a and c, the SWT data shows angularity in the lift curve slope centered at an angle of attack of 7 degrees which will be discussed below. The untripped data from both tunnels also reach positive stall around 16 degrees angle of attack without respect to Reynolds number. However, the SWT data generally undershoots the Ladson data in the high lift region which culminates in the maximum lift coefficient in Figure 5.4c for the SWT being 4% smaller at 1.425 than that of Ladson at 1.484. For the tripped conditions as shown in Figure 5.4b and d, the angularity in the SWT data is gone. The SWT data again stalls around 16 degrees while the Ladson stalls early at 14-15 degrees. The early stall of the Ladson data is believed to be a result of the trip extending all the way around the leading edge of the airfoil. The significance of Ladson's 80-grit strip-type trip data in the figure, which matches the stall angle of the SWT more closely, will be discussed further below. Despite this noticeable difference in stall angle, the overall agreement of the lift curve slopes is slightly better in the tripped condition than in the untripped condition.

A detailed comparison between these lift data is enhanced by plotting the ordinate as the difference between the corrected lift and the thin-airfoil theory lift coefficient, or $C_{lc} - 2\pi\alpha_c$, such as done in Figure 5.5. As expected based on thin-airfoil theory's assumptions of small angles, minimal disturbance of the freestream, and negligible thickness, the data's deviation from the theory is small at low angles of attack but sharply increases as flow separation begins to influence the flow over the airfoil. The differences between the Ladson and SWT data are similar between Reynolds numbers but strongly affected by the tripping condition with the tripped data in better agreement. For the untripped data in Figure 5.5a and c, the SWT data are offset around 0.10 below the Ladson data starting from 6 degrees angle of attack and continuing until stall. In the SWT data there can also be seen a dip in the $C_{lc} - 2\pi\alpha_c$ value around 6-7 degrees that is not present in Ladson. For the tripped data in Figure 5.5b and d, the agreement between data is closer and is everywhere within 0.05 on the ordinate until the effects of flow separation begin around 14 degrees. As the flow separation begins, the SWT lift decreases more slowly than and eventually stalls after the Ladson data.

Figure 5.6 plots the corrected moment coefficient, C_{mc}, of Equation 2.18 versus the corrected angle of attack, α_c, for the same test cases as considered above. Again, the best agreement between Ladson and the SWT occurs for the tripped condition, although the SWT data is generally offset above the Ladson data and outside of the range of the error bars. In the untripped data, both Ladson and the SWT moments level out around 10 degrees before increasing again, although the SWT's data shows much more rise in the early linear region and even dips to a sharp point before increasing again.

Figure 5.7 plots the corrected drag coefficient, C_{dc}, of Equation 2.19 versus the corrected angle of attack, α_c, for the nominal Reynolds number of $2.00\text{x}10^6$ since no drag data is available from the SWT at the higher Reynolds number. Figure 5.7c-d show the drag buckets of the data in Figure 5.7a-b, respectively. Unlike for the lift and moment data, the drag in the untripped condition is in fairly good agreement. The difference at zero degrees angle of attack is just 2 counts, or 0.0002, and the SWT everywhere agrees with Ladson within the error bars as shown in Figure 5.7c. For the untripped condition, both data show a rise in drag at 7-8 degrees angle of attack with the SWT having a pronounced peak. For the tripped condition, the wrap-around trip of the Ladson experiment appears to again be mainly responsible for the differences in stall angle as the Ladson airfoil stalls sooner and more suddenly than the SWT airfoil. Ladson states that, compared to narrow trip strips, the wrap-around trip increases drag at zero angle of attack by about 0.01 for a range of Reynolds and Mach numbers. Although the difference between the Ladson wrap-around trip data and the SWT strip trip data is not this large, the observed difference at 0.001 is 5 times larger than the difference in the untripped data.

At least two main features standout from comparisons of Figures 5.4-5.7: delayed stall in the tripped SWT data relative to the Ladson data and some disagreement in both the linear and transition regions between the untripped lift and moment data. Examining the first, the stall angle of the SWT has been seen to be delayed relative to Ladson by 1-2 degrees. Evidence for the cause of the delay is given by Ladson who indicates that their trip configuration, which wraps around the leading edge from 5% chord on the suction-side to 5% chord on the pressure-side, reduces the maximum lift obtained by an airfoil by up to 25% relative to the same airfoil with strips of trip tape located just at the 5% chord locations. Even stronger evidence is found in the data Ladson provides for an 80-grit trip of the strip type rather than the wrap-around type. This data is seen in the b and d subplots of Figures 5.4-5.7. In Figure 5.4b and d, the lift coefficient from the 80-grit strip trip at high lift falls above that of and stalls after that of the SWT data. Thus, the 60-grit, wrap around trip and the 80-grit, strip trip sandwich the SWT data, indicating that the difference in stall angle between Ladson and the SWT is directly related to the trip configuration.

It can be explained why the lift data from the strip type trip of Ladson still does not exactly match that of the SWT because it is made from 80-grit size carborundum grains which are roughly 0.165mm in diameter. The 80-grit trip, therefore, would have a total height less than a third that of the serrated trip used for the SWT data in Figure 5.4b, for instance, and less than half that used in Figure 5.4d. Although the 80-grit trip data for C_{lc}, $C_{lc} - 2\pi\alpha_c$ and C_{mc} generally shows less agreement with the SWT than the 60-grit trip data in most aspects, the C_{dc} comparison is helped by the switch to the 80-grit trip. Looking at the drag, the stall behavior of the SWT data, which was delayed relative to the original 60-grit wrap around trip data, falls quite close to the stall behavior of the 80-grit trip. In summary, it can be said that the SWT trip performs more similarly to the 60-grit, wrap-around trip for the linear region and even near flow separation except that it replicates the drag near stall of the 80-grit, strip trip. The data suggests that uniform trip *height* is the most important parameter for matching lift and moment data between tests but trip *length* around the leading edge is the most relevant parameter for matching transition and stall characteristics.

A second main difference between the Ladson and SWT data is in the untripped data. Differences are seen most notably in C_{lc}, $C_{lc} - 2\pi\alpha_c$ and C_{mc} throughout the linear region and into the transition region. The uncertainties of the aerodynamic coefficients and the angle of attack

measurement in the SWT have been quantified in Section 4.6 but are not sufficient to explain the differences with Ladson. However, as will be shown below, the differences between the SWT and Ladson data are, in fact, within the limits of the experimental variation that might be expected between tests made at different wind tunnels. A list of potential factors contributing to the untripped differences and any residual tripped differences are presented in the paragraphs below with the most likely factors highlighted at the end. Listed in increasing order of effect on the present measurements, the potential factors identified are the two-dimensionality of the flow, variation in chord to tunnel width ratio, differences in surface preparation of the airfoils, differences in the exact airfoil profile, differences in airfoil pressure taps, differences in Mach numbers, and differences in freestream turbulence levels.

To verify the two-dimensionality of the flow in the SWT data, cross-sections of the stagnation C_p over the test section were obtained with a wake rake sweep 1.06 m downstream of the trailing edge of the model as shown in Figure 5.8a-d for the untripped run at Reynolds number 1.99×10^6 and for angles of attack of 0, 5, 10, and 15 degrees, respectively. The figure uses the coordinate system introduced in Figure 4.2 and 4.3. Two-dimensional flow is maintained over the majority of the span for angles of attack from 0-10 degrees. Stall occurs at 16 degrees for this case, and the cross-section at 15 degrees angle of attack shows flow separation originating both around z = 1.2 m and from the junction of the airfoil and floor. It was later determined that the floor separation was due to a gap in the taping of the Mylar near the leading edge of the airfoil junction. Subsequent wake rake measurements of the floor region showed the abnormal separation shown in Figure 5.8d to be gone. Among the angle of attack sweeps of Figures 5.4-5.7, the poor taping was only present for the low Reynolds number, untripped tests which corresponds to subplots (a). Based on the consistency of these subplots with those of (b) - (d), the floor separation does not appear to have had a large impact on the midspan pressure readings.

The chord-height, (c/h), ratio for the Ladson and SWT tests were 0.26 and 0.5, respectively. Therefore, the SWT puts the second-order correction theory of Allen and Vincenti (1944) to a greater test than Ladson who also used Allen and Vincenti for their corrections. Allen and Vincenti recommend their second-order theory for $(c/h) < 0.7$ when testing low loadings and for $(c/h) < 0.4$ when testing near the maximum lift of the model. To increase confidence in the SWT interference prediction which is outside of Allen and Vincenti's recommendation, the two-dimensional panel method described in Section 2.4.2.1 was run for the hard-wall case with the porosity and deflection portions of the code disabled. Panel method solutions of wind tunnel flow solve the same potential flow problem as done in Allen and Vincenti but without neglecting higher-order terms of (c/h). The comparison of the panel method and Allen and Vincenti lift corrections is shown in Figure 5.9. The panel method correction does raise the lift curve slope slightly, but this amounts to an increase in maximum lift coefficient of only 0.8% and a decrease in corrected angle of attack by 0.19 degrees for the most extreme case. Neither of these changes is significant enough to account for the differences between the Ladson and SWT data.

As noted above, the ordinates of the SWT's 0.91 m NACA 0012 are more off-design than those of the Ladson model, having an increased thickness of roughly 0.18% chord from the theoretical NACA 0012 profile. This difference was studied using the coupled inviscid/viscid flow solver XFOIL (Drela 2013) by simulating the flow around the theoretical and measured profiles. There is some aerodynamic impact of the added thickness, although the details of the impact are masked by poor convergence of the XFOIL solution. Further work towards these ends may be appropriate in the future to exactly quantify the effect of the off-design shape on the aerodynamic performance of the 0.91m NACA 0012 airfoil.

The Ladson airfoil was machined from aluminum billet to a surface finish of approximately 32 rms μin., from which it was hand polished with 400-grit carborundum paper. The SWT airfoil is fabricated from fiberglass exterior which has not been measured for surface roughness. A study by Young (1990) describes a hand-finished fiberglass wind tunnel model with surface roughness

of 15-35 μin. rms which is likely similar to the SWT model, so there is no evidence to suggest the surface finishes between Ladson's and the SWT's models were significantly different.

The pressure tap geometry and arrangement on the airfoil may affect data especially in the untripped configuration if the taps inadvertently add instability to the flow and cause premature transition. The SWT model appears to be better suited to avoid this problem as its taps are both smaller in diameter and spaced out in the spanwise direction to limit the contamination of downstream ports by inadvertent tripping of the flow from upstream ports. Differences between Ladson and the SWT due to inadvertent tripping are possible. If so, the Ladson data would be more tripped relative to the SWT data.

The Mach number difference between the two tunnels was as large as 0.06 with Ladson controlled at 0.15 for all cases and the SWT at 0.10 or 0.21 for the nominal Reynolds numbers of $2x10^6$ and $4x10^6$, respectively. The corresponding Prandlt-Glauert compressibility factor is 0.989 for Ladson and 0.995 or 0.978 for the SWT, respectively. However, this compressibility difference would not seem to explain the differences between Ladson and the SWT because for *both* nominal Reynolds numbers of $2.00x10^6$ and $4.00x10^6$, the SWT lift data falls just below that of Ladson at positive angles of attack. In the high lift region of Figure 5.4a and c where the Mach number of the SWT data is below and above, respectively, that of the Ladson data, the SWT data undershoots the Ladson data in both cases. Adjusting the SWT lift data to a Mach number of 0.15 with the Prandlt-Glauert transformation, the low Reynolds number data would *increase* by 0.64% and high Reynolds number data would *decrease* by 1.11%. While the increase would be beneficial for our purposes, the decrease would put the Ladson and Mach number-adjusted SWT at further odds.

Turbulence levels at the Langley LTPT where the Ladson data was taken are thought to be higher than they were originally in the 1940's due to the damage to the heat exchanger and screens (Ladson 1988). If the turbulence level of the Ladson tunnel was higher than that of the SWT, then it is predicted that boundary layer transition on the airfoil would occur sooner along the chord for Ladson and produce a higher effective Reynolds number in the boundary layer. The higher effective Reynolds number would delay the onset of trailing edge flow separation and raise the lift coefficient of the Ladson data with respect to the SWT data in the high loading regime as seen in the data. Turbulence levels have lessened effect on the tripped data which is also borne out in the good agreement of the tripped data between Ladson and the SWT. Data from several additional tests are presented below to examine the effect of facility turbulence on lift data.

Additional lift data from the three the low-speed facilities that were ranked first in McCroskey (1987) are given in Figure 5.10. The data are derived from Abbott and Von Doenhoff (2012), Gregory and O'Reilly (1973), Ladson (1988), and the SWT. Reynolds numbers of the untripped data in Figure 5.10a, range from $3x10^6$ to $6x10^6$ while Mach numbers are 0.3 or below. Consistently, the SWT data undershoots the other references in terms of the slope of the lift curve just as in the Ladson data. The stall angle of the SWT data falls in the middle of the range compared to the other data. Reynolds numbers of the tripped data in Figure 5.10b, range from $4x10^6$ to $6x10^6$ while Mach numbers are again 0.3 or below. Although the tripped data set is smaller, the SWT data now aligns much better with the other references just as it had done for the Ladson tripped data.

The data of the studies in the previous paragraph derive from the 3 wind tunnels listed in Table 5.1. Turbulence data from each of these tunnels was gathered from the references listed in the second column of the table and plotted in Figure 5.11. Turbulence intensity, $u'/U_\infty(\%)$ is plotted logarithmically versus the Reynolds number where the Reynolds number is referenced to the chord length of the corresponding NACA 0012 study for the given tunnel. Some explanation is required for the Langley LTPT. The turbulence levels of the original tunnel in the 1940's are given by Von Doenhoff and Abbott (1947) for the case of 4 atmospheres of total pressure. Over the years, some of the turbulence-reducing screens had been removed and others tainted by oil and debris (McGhee *et al.* 1984). Also, a set of cooling coils is believed to have contaminated the flow with additional turbulence (Ladson 1988). Ladson made their measurements when this was the

state of the tunnel, so it is expected that the turbulence levels were very much larger than the 1940's era levels. After the Ladson experiments, the tunnel was repaired and restored to a similar state as its original construction which resulted in the second set of turbulence data shown. It is noted that even *after* the repair, the turbulence levels as measured by McGhee *et al*. are generally higher than those in the SWT. This historical information is a strong indicator that the turbulence level at the time of Ladson's experiment and the turbulence levels in all of first-ranked NACA 0012 studies were higher than those currently in the SWT. This difference is therefore the probable cause of the difference in lift and moment behavior between the SWT and Ladson data.

TABLE 5.1. Wind tunnel turbulence data for three low-speed facilities, and the correspondence between airfoil data of Figure 5.10 and the facility information of Figure 5.11.

Wind Tunnel:	Turbulence Data:	Airfoil Data:	Reference Airfoil Chord:
Langley LTPT	Von Doenhoff and Abbott (1947), McGhee *et al.* (1984)	Abbott and Von Doenhoff (2012), Ladson (1988)	0.61m (Ladson)
NPL 9ft x 13ft	Bradshaw and Ferriss (1962)	Gregory and O'Reilly (1973)	0.76m (Gregory and O'Reilly)
SWT	2006	current study	0.91m

One of the features in the linear region of the untripped, 0.91 m NACA 0012 of the SWT not found in the Ladson data is the angularity in the lift curve slope centered at an angle of attack of 7 degrees. In fact, this angularity is clearly visible in each of Figure 5.4-5.7 in the untripped data of subplots (a) and (c). Ladson's data hints at this angularity, especially in the drag data, but does not show near the severity as the SWT data. The reason for this is found in the stall characteristic of the NACA 0012. Stall can be either turbulent separation originating at the trailing edge and propagating forward on the airfoil, laminar separation originating after the pressure peak, a combination of trailing edge and leading stall, or separation at the leading edge of a thin ($(t/c) \leq 0.09$) airfoil (McCullough and Gault 1951, Gault 1957). McCullough and Gault state that symmetric airfoils with thicknesses between 0.09 and 0.15 such as the NACA 0012 are likely to experience leading edge stall. Gregory and O'Reilly, however, propose that for some range of Reynolds numbers, the NACA 0012 exhibits the last category of stall: both leading edge laminar separation and trailing edge stall.

During the laminar separation process, a separation bubble appears after the pressure peak which moves forward as the angle of attack increases. The laminar flow separates from the airfoil surface and continues on a path roughly tangent to the angle at which it separated until the flow transitions to turbulence wherein it spreads out and reattaches to the airfoil surface. Stall occurs when the angle of attack is so severe that the transition to turbulence does not result in reattachment. Therefore, unlike stall originating from the trailing edge which produces a gradual decrease in maximum C_l after stall, leading edge stall incurs a sudden drop-off in C_l after stall because the flow on the suction-side progresses from attached along much of the chord to almost completely unattached.

For trailing edge stall, the mechanism that causes flow separation is the adverse pressure gradient acting against the turbulent boundary layer over the length of the chord. Trailing edge stall airfoils benefit from vortex generators or trip strips because these increase the effective Reynolds number in the boundary layer which and allow attached flow to be sustained to higher angles of attack and higher maximum lift.

The angularity of the NACA 0012 data between 7-10 degrees angle of attack at the SWT appears to be a nuance of the NACA 0012 performance that is only elucidated for testing in low turbulence environments. Though not yet verified with flow visualization, we believe that the SWT turbulence environment permits the formation of a laminar separation bubble while that of Ladson does not. The droop in the SWT lift data of Figure 5.4a and c leading up to 7 degrees indicates the growth of the separation bubble after the pressure peak. As the angle reaches 7 degrees, some small surface imperfection of the airfoil becomes significant and provides enough tripping to substantially reduce the extent of the laminar separation. This reduction in laminar separation suddenly raises the SWT lift back to a level comparable with Ladson. Continuing through the angle of attack sweep, the extent of the turbulence in the Ladson airfoil's boundary layer is still greater than that of the SWT's which delays the onset of trailing edge flow separation and produces the larger lift observed in Ladson's high angles of attack. The presence of the laminar separation bubble is not detectable in the pressure distributions over the airfoil although there is unfortunately a small gap in these distributions just after the pressure peak due to faulty pressure ports.

The angularity has also been observed in the untripped testing of the 0.20 m NACA 0012 in the SWT, as well as in Critzos *et al.* (1955). The SWT data was taken at $0.50\text{x}10^6 \pm 8\text{x}10^3$ Reynolds number and 0.11±0.002 Mach number. The Critzos *et al.* data was taken at $0.5\text{x}10^6$ Reynolds number, 0.15 Mach number, and 1 atmosphere total pressure in the Langley LTPT. It is unknown to the author to what extent the turbulence level in the LTPT had been affected by the degradation described by McGhee *et al*. at the time of Critzos *et al.'s* testing in 1955. Comparing the SWT's 0.20 m NACA 0012 airfoil with the similar fullspan airfoil of Critzos *et al.*, the Critzos *et al.* model made of machined steel had a slightly smaller chord at 0.15m chord and half the span at 0.91 m. Instead of using pressure distributions such as in the SWT, the aerodynamic coefficients were measured with a strain gage balance. One end of the span was attached to the multi-component strain gage balance and one end to a gimbal that allowed rotations about the quarter-chord axis. Considering the uncertainty of the strain gage balance, the uncertainties in C_l, C_m, and C_d were ±0.049, ±0.016, and ±0.017, respectively, although repeated tests of the same measurement indicated lower uncertainties. The data were corrected for solid and wake blockage and lift interference using theoretical predictions as well as measured wall pressures for the wake blockage. Tabulation the Critzos *et al.* data was hampered by poor resolution of the source figure in the paper, most noticeably for the drag data.

Figure 5.12 compares the SWT data to that of Critzos *et al.* Similarly to the SWT's 0.91 m NACA 0012 data, there is a droop in C_{lc} in the early linear region as shown in Figure 5.12a. In this case, C_{lc} rebounds to a larger value due to reduction in size of the presumed laminar separation bubble at around 5 degrees rather than 7 degrees as seen previously. The SWT data follows that of Critzos *et al*. through the angularity about 5 degrees and through the flow separation regime. The plots of $C_{lc} - 2\pi\alpha_c$ and C_{mc} in Figures 5.11b-c, respectively, show the angularity leading up to 5 degrees angle of attack and show good agreement between the shape of the plots. The drag comparison in Figure 5.12d is compromised by poor resolution of the Critzos *et al.* source figure as noted above.

5.1.3. Lift Symmetry

In the comparison of the 0.91 m NACA 0012 with the Ladson (1988) data, the majority of the data was for positive angles of attack. The symmetric NACA 0012 profile offers the opportunity to compare the symmetry of measurements made at positive and negative angles of attack. Figures 5.13-5.15 compare the positive angle of attack data with the negative angle of attack data when it is reflected over the abscissa and ordinate for the plots of $\mathrm{C_{lc}}$ and $\mathrm{C_{mc}}$ and over the ordinate only for the plots of C_{dc}. The zero-lift angles of attack of subplots (a)-(d) are -0.05, -0.03, -0.14, and -0.14 degrees, respectively, and these have been subtracted out of the plots before the

reflections were performed. Uncertainties in both the angle of attack and coefficients are given for the positive angle of attack data.

For the lift data in Figure 5.13, the positive angle of attack data is generally below that of the negative angle of attack data although the difference is within the limits of the uncertainty for most of the pre-stall data. For the low Reynolds number cases of Figure 5.13a-b, the negative angles stall one degree before the positive angles. For the high Reynolds number cases, however, the negative angles stall one degree after the positive angles as in the untripped data of Figure 5.13c and at the same nominal angle as in the tripped data of Figure 5.13d. Rather than asymmetric flow in the facility, the variation in stall angle is more likely a consequence of slight irregularities between the suction and pressure-sides of the airfoil, especially the suction-side hatch described in Section 5.4 and also subtle irregularities in the surface preparation between the pressure- and suction-sides of the airfoil. For the moment data in Figure 5.14, the negative angles generally have a slightly larger C_{mc} although the variation could be within the limits of the uncertainties when accounting for the uncertainty of the negative angle of attack data as well as that of the positive. The pre-stall behavior of the drag data is in agreement everywhere except in the range 5-9 degrees of the untripped data of Figure 5.15a. Here, the positive angle of attack data sees a bulge and then a fall in drag while the negative angle of attack data slowly rises.

It is suspected that in both the C_{lc} and C_{dc} data, the asymmetry in the linear region is related to the hatch which is located on the suction-side of the airfoil at positive angles of attack. Since flow separation originates on the suction-side of an airfoil, the airfoil's boundary layer development is especially sensitive to slight irregularities in the geometry on this side. A slight step in the suction-side profile due to the presence of the hatch could be thought to energize the boundary layer and produce the observed bulge in the drag plot as the step rotates to face the free-stream head-on. This slight tripping effect would also explain the lower lift of the positive angle of attack data throughout the untripped lift curves of Figure 5.13a and c since tripping generally leads to a slight decrease in an airfoil's lift coefficient.

5.1.4. Vortex Generators

The effect of the number of vortex generators at the start of the diffuser downstream of the test section has also been quantified through testing. The baseline number of generators typically used at the SWT is 8 as shown in Figure 5.16a. These generators are located downstream of the trailing of the test section at a location of x =8.6 m and are alternately angled at ±15 degrees from the streamwise direction. Each generator has a roughly rectangular plan-form with rounded leading edge and tip and a tapered trailing edge. The dimensions of each are 30cm-by-17cm-by-3cm. After measurements of the baseline, an additional 8 were added as shown in Figure 5.16b. The uncorrected lift comparison is shown in Figure 5.16c for angles of attack from 5-15 degrees. The lift coefficient with the 16 generators is slightly greater than that with 8 generators. At the maximum lift angle of attack of 15 degrees, the difference between uncorrected lift coefficients is 0.7%. It is noted that the difference in the lift coefficient between cases decreases steadily with angle of attack. The differences may be due to true differences in steady-state aerodynamics but also might be a result of the tunnel circuit settling to steadier conditions as the lift polar progresses from 5 to 15 degrees.

5.2. Auxiliary Boundary Condition Measurements in Kevlar-Wall Test Section

Having an understanding and confidence in the hard-wall test section characteristics, we now focus on the measurements taken in the Kevlar-wall test section. Before proceeding with the results of the airfoil tests and panel method correction in the Kevlar-wall test section, a description

of two auxiliary measurements related to the Kevlar walls is presented. One of the critical features of the panel method simulation is the handling of the flexible, porous boundary conditions of the Kevlar walls. Expounding on the work presented in Devenport *et al.* (2013), two such boundary conditions measured and analyzed below are the Kevlar porosity relation and the leakage area between the anechoic chambers.

5.2.1. Kevlar Pressure-Velocity Relationship

Knowledge of the pressure-velocity relationship through the Kevlar walls is critical to the modeling of the wall's boundary conditions. This relationship has been previously measured at the SWT with an experimental test rig outside of the wind tunnel. A Kevlar swatch was stretched over the end of a pipe, a pressure difference applied, and the resulting flow velocity measured. These tests were done with and without flow blowing across the mouth of the pipe with good agreement between the two cases that yielded constants of $k_c = 0.06251$ m/s/Pa and $k_p = 50$ Pa as appearing in Equation 2.26 and repeated here for convenience

$$v_{normal} = k_c \Delta p^{0.5} \left(\frac{\Delta p}{\Delta p + k_p} \right)^{0.073} \qquad \text{Equation 2.26}$$

where v_{normal} is the normal velocity through Kevlar and Δp is the pressure difference across the Kevlar. At low pressure differences, the Δp in the denominator of the last term on the right-hand side becomes negligible, and v_{normal} goes as the 0.573 power of Δp. At higher pressure differences, the term in parenthesis asymptotes to unity, and v_{normal} goes as the 0.5 power of Δp, exactly as the inviscid flow of Bernoulli's equation. The difference in power-law behavior from inviscid flow at low pressures is attributed to the smaller Reynolds number of the flow at these pressures.

Equation 2.26 has only been measured for pressure differences up to 200Pa. However, tests in the SWT produce pressure differences across the Kevlar much higher than this, up to 1,000Pa for a 0.91 m model at maximum freestream velocity. Additionally, it was thought important to test the Kevlar *in-situ* in the wind tunnel as the Kevlar fibers could act as lifting bodies when exposed to a significant cross-flow such as the tunnel freestream, thus altering their pressure-velocity characterization.

As introduced in Section 4.7, an experiment was devised to measure the pressure-velocity relation for the Kevlar walls during the operation of the facility as part of an airfoil test. Specifically, with the 0.91 m NACA 0012 airfoil mounted in the test section, pressure taps were mounted on the Kevlar walls, and a hot-film anemometer was positioned just outside the wall of the port chamber as shown in Figures 4.10-4.15. Given that the pressure-velocity characterization is an intrinsic property of the Kevlar and not likely a function of position on the Kevlar wall, it was considered sufficient to measure the pressure-velocity relationship over a small number of locations, one on the port and one on the starboard walls. Since flow around the midspan of the test section is presumed to be two-dimensional, the measurement of pressure and velocity can be made at slightly varying spanwise positions without expecting error. As shown in Figure 4.13a, the anemometer probe tip is 7.6 cm (3 in.) below the midspan line of the tunnel. Two pressure ports located 2.5 cm downstream of the probe tip bookend the anemometer such that its hot-film sensor is 7.6 cm below the midspan port and the same distance above the next lowest port. The pressure at the anemometer's exact spanwise location was linearly interpolated. The two devices are mounted at the airfoil's quarter-chord location in order to experience the maximum pressure difference induced by the airfoil. Locating the system at the position of maximum pressure difference, as well as using the largest model available, allows the pressure-velocity curve to be characterized along the full range of pressure differences that the Kevlar walls might experience, roughly -1000 to 1000 Pa. During the airfoil runs, pressure and velocity data were recorded over the full range of angles of attack from -20 to 20 degrees in order to get a fully populated sampling of pressure differences, although the usable data from any given run was limited to flow either in or out of the test section

because the anemometer was not bi-directional. Measures were taken to control the experimental setup throughout different data collection runs. The anemometer probe head was sewn tightly against the Kevlar by loops of thread both above and below the probe head and was checked after each run to make sure it had not become loose.

The data from three angle of attack sweeps performed with the 0.91 m NACA 0012 at the largest $4x10^6$ Reynolds number in the test matrix are shown in Figure 5.17. These data include both suction and blowing, or flow into and out of the test section, respectively, measured once on the port-side and twice on the starboard-side. The shape of these three curves have some differences but do encompass the curve of Equation 2.26 for the full range of pressure differences. The scaling differences and scatter of the data are suspected to be due to the problems with the temperature calibration, temperature operating range, and sensitivity of the anemometer to battery charge. The fact that the data does not return to the origin for any of the three runs could be attributable to a threshold of around 0.3 m/s in the velocity measurements. The few sporadic points in the high pressure range of the two blowing runs correspond to the first several measurements of each of the runs before there had been sufficient time for the anemometer to settle to the temperature of the flow entering from the wind tunnel.

As already noted the pressure-velocity measurements were hampered by repeatability issues of the hot-film anemometer. Factors that affected the repeatability were the operating temperature, flow direction, and charge of battery in the handheld device. The anemometer's factory calibration was used throughout the testing which quotes the temperature compensation down to 40 degrees Fahrenheit, however, the factory calibration was only performed at 65 degrees Fahrenheit. The time constant for temperature stabilization is given as approximately 2 minutes. Uncertainty of the velocity measurements due to temperature were a result of the freestream temperatures being sometimes lower than 40 degrees Fahrenheit during the testing, the two minutes warm-up time not being provided necessarily, and the temperature differences between the air in the anechoic chamber and the freestream flow which magnified the temperature response time issue. The direction of the flow through the Kevlar also could not be gaged by the anemometer because of the guide vanes on either side of the hot-film sensor as seen in Figure 4.13b-c. The hot-film anemometer was at times suspected of being strongly sensitive to the amount of charge in its AA batteries.

Another factor contributing to the scatter of the data in Figure 5.17 is the effect of stretching of the Kevlar on its porosity. This effect will tend to increase the average pore size between Kevlar fibers in regions of Kevlar experiencing a large pressure difference, thus causing the curves of Figure 5.17 to drift upwards from $n = 0.5$ power-law behavior. Equation 2.30, which predicts the change in the porosity coefficient, k_c, of Equation 2.26 as a function of the strain experienced by the Kevlar walls, can be used to estimate the effect of stretching on the measured pressure-velocity data. Taking the maximum deflection in the direction normal to the Kevlar to be roughly 1% of the streamwise Kevlar wall length as verified by measurements presented later, the spanwise-averaged strain of a simplified defelciton contour would be approximately 0.004 m/m. This stain translates into a roughly 3% change in k_c. Such a change in k_c alters the curvature of the pressure-velocity data which is observed somewhat in Figure 5.17 beginning at a Δp of 600 Pa.

Although the data in Figure 5.17 suffer from repeatability problems, the overall shape of the data supports Equation 2.26. The power-law behavior of the pressure-velocity relationship at high pressures as well as low pressures and in the presence of tunnel flow has been measured. Further measurements would be beneficial to gather data with a greater degree of certainty and potentially fine-tune Equation 2.26.

5.2.2. Measuring the Leakage Area

Devenport *et al.* (2013) identified the leakage area as an important parameter in correcting aerodynamic data of Kevlar-wall test sections. The leakage area represents the effective free-flow area connecting the two anechoic chambers. This value is termed 'effective free-flow' since it is

the area of an opening from the anechoic chamber that for the same pressure difference would pass a mass flow equal to the summed mass flow seeping out of the distributed leakage areas throughout the chamber. Lumping these distributed flow areas into a single value simplifies the modeling of the leakage flow.

The flow physics of the leakage area may be explained as follows. During tunnel operation mass may enter or exit a chamber through three routes: into or out of the test section through the walls, into or out of the control room through leaks in the chamber construction, or into or out of the volumes above and below the test section through the Kevlar fabric covering these areas. It is believed that the dominant route of mass flow is by far the first of these, with mass entering and exiting the test section to produce nearly net zero mass flow through each Kevlar wall. However, zero net mass flow does not occur in practice because of the two latter routes which allow mass exchange, or leakage, between chambers or with the control room. Of these two routes, exchange with the control room is believed to be relatively small, owing only to small leakage areas such as a 5 cm-by-33 cm foam-filled cutout for cable and tubing access and any gaps between MDF sections in the wall construction. Mass leaked to or from the control room can equalize with leaks of the opposite chamber and with the test section through the wake rake slots. Leakage exchange with the opposite chamber, on the other hand, involves a significant amount of mass that must pass through the swatches of Kevlar above and below the test section as shown in Figure 5.18. These swatches account for the 0.68 m difference in heights between the test section's spanwise dimension and the Kevlar tensioning frame. Focusing on this believed dominant source of leakage between chambers, a preliminary experiment without wind tunnel flow was performed to measure the effective leakage area connecting the port and starboard-side chambers through the volumes of space above and below the test section.

The experiment is begun by sealing a given chamber from the test section using impermeable sheeting. Typically the dominant route of mass flow into or out of the chamber, this sealing enforces that there is now zero net mass flow directly between the chamber and the test section. Then, by applying a pressure difference, in this case a suction, to the chamber, the effective free-flow leakage area from the chamber can be evaluated based on Bernoulli's equation and the continuity equation which can be combined to yield a rearrangement of Equation 2.27

$$A_{leak} = \frac{Q}{\left(\frac{(p_1 - p_2)}{\frac{1}{2}\rho}\right)^n} \qquad \text{Equation 5.2}$$

where Q is the volumetric flowrate, p_1 and p_2 are the pressures of the leakage volume and chamber, respectively, ρ is the density of air in the chambers, and n is an exponent equal to 0.5 from Bernoulli's equation.

The setup for the experiment was as follows. Sealing was accomplished with 1-2 mm thick, impermeable plastic sheeting which created a seal around the complete Kevlar wall perimeter with the help of aluminum foil tape as shown in Figure 5.19. Special care was taken around the corners of the Kevlar wall to maintain the sealing. Suction is applied by part of the SWT flow-control system, consisting of a centrifugal blower with a maximum volumetric flowrate of 6,000 CFM. The blower is connected to either of the chambers by with a 30 cm (12 in.) diameter hose that is mounted to a flange which is, in turn, bolted to the outside of the anechoic chamber. The flange and opening for the suction hole are located on the lower, inboard, upstream chamber wall for both chambers as shown for the starboard chamber in Figure 5.20a. The close-up view of the opening in Figure 5.20b shows a screen that was used to prevent any debris from being sucked into the blowers.

The volume of space above and below the test section are typically separated from the test section by perforated aluminum panels covered with Kevlar cloth. For the 3 streamwise rows of floor and ceiling panels nearest to the model mount, the floor and ceiling panels were removed in

order to measure the leakage area of just one chamber at a time. The test section was left open to the control room so that the pressure difference measured was the difference across the Kevlar swatches above and below the test section. Foam wedges, which increase the resistance to leakage between chambers through the volumes both above and below the test section, were in-place as usual everywhere except around these 3 streamwise rows. For measurements on the port-side chamber, suction was applied to the port chamber only with the chamber's access door shut and sealed by its three latches and the starboard chamber left open to control room. The opposite was true for calibration of the starboard-side. The pressure inside the test section was measured using pressure ports in the aluminum floor plates, and the pressure inside the chamber was measured with a pressure line that entered the chamber through the cutout for cable and tubing access which was filled with foam but otherwise open to the control room. Both pressures were measured with the Esterline scanner unit described in Section 4.5.

The blower power was incrementally increased from 0-100% capacity with measurements taken every 10%. As suction was turned on, the impermeable sheet pulled flat against the tunnel-side of the Kevlar wall. By the feeling of a hand from inside the test section around the 3 streamwise rows of removed panels, it was clear that a large amount of flow was entering the chambers through the volumes above and below the test section, thus strengthening the assumption that the dominant source of leakage from the chambers is through these volumes.

Two separate measurements, or calibrations, on each chamber were performed separated by a time of seven weeks. The goal of performing a second calibration after acquiring results in the first calibration was to determine the sensitivity of the leakage area to a full tear-down and reinstallation of the Kevlar-wall test section occurred between the calibrations. The combined data from the two calibrations are shown in Figure 5.21a. As a first observation, the shape of the curves are similar to those of the Kevlar pressure-velocity curves of Figure 5.17. The data shows a nonlinear relationship with the leakage area which starts to level out around 100 Pa to a value of $0.14m^2$ to $0.19m^2$. The port leakage area is relatively unchanged from the first to second measurements, however, the starboard leakage area increases by 29% which is yet unexplained. Using the three curves in best agreement, the effective free-flow leakage area as reported in Devenport *et al.* (2013) was estimated at 0.15 m^2, or approximately the equivalent of a 40 cm-by-40 cm square duct connecting the chambers.

Since the measured leakage areas are consistent at around 0.15 m^2, this value could be compared to a leakage estimate based on physical dimensions from the chamber. In Figure 5.18, the areas of Kevlar above and below the test section that allow air exchange with the opposite chamber are each about 0.12 m-by-5 m in dimension. This equates to 1.2 m^2 of Kevlar exposed to the volumes above and below the test section, which for the current measurement opened to the control room pressure either via the test section. Multiplying the exposed channel area times the 7% porosity of the Kevlar without any consideration to the viscous losses caused by the Kevlar pores yields 0.084 m^2 of leakage area which corresponds to a square duct 29 cm on a side. Thus, the leakage area derived from the exposed Kevlar area is around 60% of the total leakage area measured by applying suction to the chambers. This is consistent with the fact that there are other small sources of leakage from the chambers to the control as described previously.

Finally, the leakage measurement above is input to the panel method simulation with the other inputs as described by Table 2.1. In all Kevlar-wall panel method simulations below, the 0.15 m^2 leakage area is used unless otherwise specified.

5.3. Comparative Tests in the Hard-Wall and Kevlar-Wall Test Sections

As presented in Section 2.4.2.1, two-dimensional Kevlar-wall data is corrected using the approach of Devenport *et al.* (2013) where a panel method simulation solves for the flow in the Kevlar-wall test section accounting for both the flexibility and porosity of the Kevlar walls. The flow solution is then used to infer the blockage and lift interference parameters to be applied to the experimental data to produce the free-flight performance of the model.

In order to assess the accuracy and limitations of the panel method correction scheme, a series of comparative airfoil tests under nearly identical conditions were performed in the hard-wall and Kevlar-wall test sections. Three airfoils were used: the 0.91 m NACA 0012, the 0.61 m DU00-W-212, and the 0.20 m NACA 0012. These airfoils were deliberately chosen to provide a range of chordlengths and thus a range in the magnitude of the aerodynamic corrections. Table 5.2 lists the conditions and angle of attack range of the measurements made with each airfoil.

TABLE 5.2. Summary of comparative airfoil runs performed in the hard- and Kevlar-wall test sections. Comparison cases between test sections are located in the same row numbers.

Hard-wall

	Date	Time	Airfoil	Reynolds No. (in millions)	Mach No.	Trip (% suction, % pressure)	Wake Rake
1	1/8/2013	2:00 PM	0.91 m NACA 0012	1.99	0.10	No	Yes
2	1/10/2013	11:14 AM	0.91 m NACA 0012	1.99	0.10	Serrated (5, 5)	Yes
3	1/10/2013	4:00 PM	0.91 m NACA 0012	3.90	0.21	No	No
4	1/10/2013	2:00 PM	0.91 m NACA 0012	3.91	0.21	60-grit (5, 5)	No
5	1/14/2013	4:45 PM	0.61 m DU00-W-212	2.23	0.17	No	Yes
6	1/15/2013	6:00 PM	0.61 m DU00-W-212	2.24	0.17	Serrated (5, 10)	Yes
7	1/16/2013	5:15 PM	0.61 m DU00-W-212	2.61	0.21	No	No
8	1/16/2013	4:00 PM	0.61 m DU00-W-212	2.64	0.21	Serrated (5, 10)	No
9	1/11/2013	4:25 PM	0.20 m NACA 0012	0.50	0.11	No	Yes

Kevlar-wall

	Date	Time	Airfoil	Reynolds No. (in millions)	Mach No.	Trip (% suction, % pressure)	Wake Rake
1	1/31/2013	3:00 PM	0.91 m NACA 0012	2.01	0.10	No	Yes
2	1/31/2013	6:02 PM	0.91 m NACA 0012	2.00	0.10	Serrated (5, 5)	Yes
3	2/1/2013	1:05 PM	0.91 m NACA 0012	3.92	0.20	No	No
4	2/1/2013	7:00 PM	0.91 m NACA 0012	3.92	0.19	60-grit (5, 5)	No
5	3/25/2013	9:30 AM	0.61 m DU00-W-212	2.24	0.17	No	Yes
6	3/25/2013	1:30 PM	0.61 m DU00-W-212	2.24	0.17	Serrated (5, 10)	Yes
7	3/25/2013	6:00 PM	0.61 m DU00-W-212	2.58	0.20	No	No
8	3/25/2013	5:00 PM	0.61 m DU00-W-212	2.59	0.20	Serrated (5, 10)	No
9	2/4/2013	2:08 PM	0.20 m NACA 0012	0.50	0.11	No	Yes

As described in Section 4.5, surface pressure distributions and lift and moment coefficients were measured for each case of the table using the surface mounted taps on each of these models, and drag was measured using the wake rake system. Additional measurements made in the Kevlar-wall test section for the tests with the 0.91 m NACA 0012 airfoil for the purpose of validating the panel method simulation. These include mean pressures measured in each of the anechoic chambers as also described in Section 4.5, pressure distributions measured over the Kevlar walls using the wall-mounted tap system described in Section 4.8, and wall deflection measurements obtained using the stereo camera system described in Section 4.9.

In this section, comparison between the aerodynamic data of the hard-wall and Kevlar-wall test sections is first made using the three airfoils above. Further developments will then be presented on the lift symmetry in the Kevlar-wall test section, validation of the panel method simulation, sensitivity of the panel method simulation, and new instrumentation for Kevlar-wall test sections.

5.3.1. Comparison of Aerodynamic Data

First is made is made a direct comparison between the corrected aerodynamic measurements made in the hard- and Kevlar-wall test sections. All measurements from the hard-wall test section have been corrected using the hard-wall version of the two-dimensional panel method described in Section 2.4.2.1 where the wall porosity and deflection portions of the code have been disabled. The panel method correction in its hard-wall version has been found consistent with that of Allen and Vincenti (1944) as mentioned in Section 5.1.2. It is preferentially used due to its higher-order accuracy than Allen and Vincente and to be consistent with the Kevlar-wall corrections. All measurements in the Kevlar-wall test section have been corrected using the same panel method simulation except with the porosity and deflection iterations active and with the input parameters given in Table 2.1.

As will be shown in the following sections, there is good agreement between test sections across Reynolds numbers ranging from as low as $0.5\text{x}10^6$ up to $3.9\text{x}10^6$, in both the untripped and tripped condition, and with three separate airfoils of varying chord length from 0.21- 0.91 m. Some of the common differences, such as angle of attack offsets between the hard-wall and Kevlar-wall data and differences in maximum lift and stall angle, are mostly thought to be a result of inconsistencies in wind tunnel operation and procedure. Rather than a fundamental difference in test section behavior, the angle of attack offsets between tests sections are a consequence of the uncertainty associated with setting the zero angle of attack after airfoil installation. To allow a detailed comparison of the data between test sections, the zero-lift angles of attack for each comparison were aligned. The Kevlar-wall data was translated horizontally over top of the hard-wall data which resulted in shifts in angle of attack anywhere from 0.02 degrees at the minimum to 1.19 degrees in an abnormal case of the 0.20 m NACA 0012. Several cases of Table 5.2 have been selected for detailed analysis in the following sections in order to encompass the full range of variation found in a typical test matrix including of variation of airfoils, Reynolds numbers, and tripping conditions.

5.3.1.1. 0.91 m NACA 0012

Figure 5.22 presents the uncorrected and corrected results for the untripped 0.91 m NACA 0012 airfoil at Reynolds numbers of $1.99\text{x}10^6 \pm 1\text{x}10^4$ and $2.01\text{x}10^6 \pm 1\text{x}10^4$ for the hard-wall and Kevlar-wall test sections, respectively, which correspond to Mach numbers of 0.10 ± 0.0007 and 0.10 ± 0.0007. The Kevlar-wall data includes error bars from the jitter analysis as stated in Section 4.6, and the error bars for the hard-wall data are similarly size but not shown for clarity. The 0.1 degree angle of attack uncertainty is not shown, however, the Kevlar-wall data has been translated in the positive x-direction by 0.18 degrees to match the zero-lift angle of attack of the hard-wall data.

The uncorrected and corrected lift coefficients, C_l and C_{lc}, respectively, are shown in Figure 5.22a between test sections. The correction for the hard-wall test section everywhere decreases the magnitude of the lift and increases the angle of attack in accordance with the positive blockage and streamline curvature in hard-wall test sections. The correction for the Kevlar-wall data everywhere decreases the magnitude of the lift and also decreases the angle of attack due to the presence of the porosity-induced change to angle of attack as in Equation 2.29. The C_{lc}'s between test sections are in better agreement than the C_l's and are generally in agreement within the bounds of the error bars. The linear regions for both test sections show the angularity believed to be associated with laminar separation after the pressure peak as discussed in Section 5.1.2. The Kevlar-wall data, possibly experiencing less of this separation effect due to subtle differences in the surface preparation of the airfoil between tests, sits slightly higher in the positive linear region. On the contrary, the Kevlar-wall data has lower magnitude at the higher loading conditions. The maximum C_{lc} for positive angles of attack is 1.353 for the hard-wall and 1.324 for the Kevlar-wall, a 2.1% difference. The stall point at this maximum in the corrected data is 0.5 degrees larger for the Kevlar-wall. The high lift region at negative angles of attack shows a larger difference in stall characteristics with the negative stall point 1.1 degrees larger (in absolute value) for the hard-wall than the Kevlar-wall. It is helpful to point out that each corrected Kevlar-wall data in the high lift region does not correspond to its closest uncorrected neighbor but to the next larger uncorrected point. By this understanding, it is apparent that the magnitude of the correction, including both blockage and lift interference, is larger for the Kevlar-wall data than for the hard-wall data as seen by the larger distance between corresponding uncorrected and corrected data points for the Kevlar-wall as compared to that of the hard-wall data.

Looking at the quantities $C_l - 2\pi\alpha$ and $C_{lc} - 2\pi\alpha_c$ in Figure 5.22b as a comparison tool as done previously in Section 5.1.2, the angularity is again observed in both test sections by the bulge beginning around ±7 degrees with a slightly weaker effect felt by the Kevlar-wall data. While the hard-wall corrections appear to have a larger magnitude than the Kevlar-wall corrections in this plot, the reason is that the ordinate includes terms from both the correction of C_l and α. In the case of the hard-wall, these two corrections have an additive effect with the wall interference correction moving $C_l - 2\pi\alpha$ in the negative ordinate direction for all α. This is as expected for a test section whose correction for positive blockage will decrease the C_l term and whose correction for positive lift interference will increase the $2\pi\alpha$ term, both of these corrections decreasing the magnitude of $C_l - 2\pi\alpha$. In the case of the Kevlar-wall, the correction to C_l is partially negated by the correction to α which has the opposite sign as for the hard-wall case due to wall porosity. It is notable that in the lower loading cases of roughly -8 to 8 degrees, the Kevlar-wall data shows the opposite characteristic; the correction increases $C_{lc} - 2\pi\alpha_c$, or moves it closer to the thin-airfoil theory lift slope. This is a consequence of the Kevlar-wall's large porosity correction dominating the streamline curvature correction to cause an overall decrease in corrected angle relative to the geometric angle.

The agreement of the moment coefficients between the two test sections is compared in Figure 5.22c. The corrections everywhere raise the moment coefficients at positive angles to more positive values. The uncorrected moment coefficients are somewhat different between test sections, but the Kevlar-wall correction brings the data to just slightly below that of the corrected hard-wall data for the majority of the angles. The difference between the uncorrected moments at a nominal 15 degrees angle of attack is 0.0130 while after correction the difference shrinks to 0.0047, or roughly a third of the original difference.

The drag coefficients for the full range of angles of attack are shown in Figure 5.22d and those of the drag bucket are shown in subplot (e). The corrections lower the drag to lower values. Considering the uncertainty of the measurements, the drag coefficients are generally in agreement between test sections. The major exception is the bulge centered on an angle of 7 degrees as also discussed in Section 5.1.2. This bulge is not seen at the symmetric negative angle of attack and is

apparently due to some small imperfection in the airfoil surface. Cross-sectional measurements of the test section with the rake wake at the current run conditions were performed in the hard-wall test section as shown in Figure 5.8. Unfortunately, the angles selected for cross-section included 5 and 10 degrees, but these did not capture any signs of the bulge. Likewise, cross-sections of the stagnation C_p were made in the Kevlar-wall test section for the same run conditions as shown in Figure 5.23. Although 6 and 10 degrees angles of attack were included in the measurements as shown in Figure 5.23b-c, respectively, the origin of the bulge is still not perceivable.

Figure 5.23 shows two-dimensional flow along the span throughout the range of angles of attack measured, the only question being at zero degrees in subplot (a) where there is a slight blip in the C_p's near midspan. This blip is almost certainly related to the asymmetry in the Kevlar-wall's $C_l - 2\pi\alpha$ at zero-lift as shown in Figure 5.22b. A comparison of the cross-sectional stagnation C_p at zero degrees between the hard-wall and Kevlar-wall cases is facilitated by Figure 5.24. The blip may be barely present in the hard-wall data of subplot (a) but is more prominent in the Kevlar-wall data of subplot (b) which may be the result of a change in the surface preparation of the airfoil between tear-down and re-installation of the model in a different test section.

Figure 5.25a-b helps define the individual contributions to the wall interference correction of lift interference and blockage, respectively. By subtracting out both the streamline curvature correction and the geometric angle of attack from the corrected angle of attack as in Equation 2.29, the result is the change in far-field angle of attack experienced by the airfoil due to the porosity of the Kevlar walls, or $\Delta\alpha_{porosity}$. The $\Delta\alpha_{porosity}$ is shown in Figure 5.25a for both test sections. Due to the panel method's optimization of the measured airfoil pressure distributions with those of free-flight as described in Section 2.4.2.1, even the hard-wall data shows a small $\Delta\alpha_{porosity}$. This correction is apparently compensation for inaccuracies in the second-order classical streamline curvature correction of Equation 2.8 and is less than 0.5 degrees within the attached flow region. For the Kevlar-wall case, $\Delta\alpha_{porosity}$ reaches up to 2 degrees, or 13% of the geometric angle of attack.

Figure 5.25b shows the blockage correction, σ, between test sections. Included in this figure is the hard-wall σ calculated by Equation 2.5 from Allen and Vincenti (1944). The hard-wall σ from the panel method optimization varies from 79-120% of the classical prediction with the blockage understandably increasing with distance from the origin. The Kevlar-wall section has a greater variation of σ in both positive and negative ordinate directions. The largest σ is 177% of the classical prediction and occurs at the highest loading condition. This large value is due to the streamline curvature induced by the deflection of the test section walls reducing the effective test section width. The lowest σ is 12% of the classical prediction and comes at the lowest loading condition. Here, the diversion of flow out of the test section acts to relieve the dynamic pressure in the test section.

While studying the separate lift interference and blockage corrections gives an intuitive idea of the flow physics in the test sections, the predicted correction magnitudes can be more effectively judged by examining the corrected pressure coefficients, C_{pc}'s, over the airfoil as in Figure 5.26a-g. Here, there is reasonably good agreement between the two test sections except at the most extreme negative angle of attack because of the difference in stall angle mentioned above. For all the non-stalled region angles of attack, the Kevlar-wall airfoil C_{pc}'s are more positive (lower on the ordinate) on both the pressure and suction-side. If this were primarily a result of incorrect modeling of the lift interference, such as if the porosity correction were over-correcting the angle of attack, then the pressure-side C_{pc}'s would be too positive (too low on the ordinate), but the suction-side C_{pc}'s would be too negative (too high on the ordinate) contrary to the data. Rather, the differences in pressure distributions appear to be predominantly a result of inconsistencies in the modeling of blockage. An over-prediction of blockage refers to predicting σ that is too positive a value. Such a case would cause both the suction- and pressure-side C_{pc}'s to be too positive (too

low on the ordinate) as indeed seen in the data. The suction-side is where blockage effects are felt most strongly since here the velocity variation from the freestream is largest. In fact, the largest gaps between the hard-wall and Kevlar-wall data do occur at the suction peak where suction and thus local flow velocity are the greatest. While the blockage in the Kevlar-wall test section is over-predicted, the effect of this inconsistency is not large when considering the lift curves between test sections. The over-prediction is only observable at the higher loading conditions in Figures 5.22a where too large of a positive blockage correction rotates the high lift data too far clockwise.

Though not noticeable in the lift curve, the inconsistency in the blockage correction is also seen in the zero angle of attack case of Figure 5.26a. As shown by Figure 5.25b, the panel method simulation predicts a σ of roughly zero for the Kevlar-wall test section at this angle. The Kevlar-wall blockage correction is thus quite small as shown by the overlap of the Kevlar-wall's corrected and uncorrected symbols in Figure 5.26a. Assuming that the blockage of the hard-wall test section is correct, the corrected Kevlar-wall data needs a decrease in C_{pc} (move higher on the ordinate). The blockage correction in both high and low lift cases of the Kevlar-wall test section is thus too strong in the sense that it needs to have a less positive value. In other terms, the simulated Kevlar-wall test section needs to tend more towards the behavior of an open-jet test section which has negative blockage.

Figure 5.27 presents the uncorrected and corrected results for the same airfoil but in the tripped condition and at Reynolds numbers of $3.91\text{x}10^6\pm4\text{x}10^4$ and $3.92\text{x}10^6\pm4\text{x}10^4$ for the hard-wall and Kevlar-wall test sections, respectively, which correspond to Mach numbers of 0.21±0.002 and 0.19±0.002. The airfoil had the 0.60-grit strip trip of 0.4 mm height as described in Section 5.2.1 during the tests in both test sections. The trips were mounted at 5% chord on both the suction and pressure sides. The Kevlar-wall data has been translated in the negative x-direction by 0.13 degrees to match the zero-lift angle of attack of the hard-wall data.

Similarly to the results above, the C_{lc}'s in Figure 5.27a are generally in agreement within the bounds of the error bars. As expected for a tripped run, the linear region shows no angularity from any laminar separation after the pressure-peak. The $C_{lc,max}$'s are 1.389 and 1.408 for the hard-wall and Kevlar-wall, respectively, for a 1.4% difference. This higher Reynolds number data understandably shows more delayed stall than the lower Reynolds number data, and again the positive stall angle of the Kevlar-wall data at 16.9 degrees occurs after that of the hard-wall at 15.5 degrees. The negative stall at high Reynolds number is shown to be unusual in both test sections as the lift during deep stall returns to a value near that of the $C_{lc,max}$.

The comparison of $C_{lc} - 2\pi\alpha_c$ between test sections in Figure 5.27b shows none of the angularity of the untripped run considered previously. For this higher Reynolds number case, $\Delta\alpha_{porosity}$ is relatively stronger than previously as the crossover of $C_{lc} - 2\pi\alpha_c$ with $C_l - 2\pi\alpha$ occurs at later at -11 and 11 degrees rather than at -8 and 8 degrees as seen before.

The moment coefficient comparison in Figure 5.27c shows the same correction trend as previously except with much smoother curves through the low loading region due to the tripping of the boundary layer. No drag data is available at this test case.

In Figure 5.28a, the hard-wall change in angle of attack due to optimization is again less than 0.5 degrees within the attached flow regime. For the Kevlar-wall case, the porosity-induced angle of attack change now reaches over 2.5 degrees, or 17% of the geometric angle of attack. In Figure 5.28b, the σ from both test sections is generally lower than that seen for the lower Reynolds number case. At high loading the Kevlar-wall blockage prediction is still over 50% that of the hard-wall, and at very low loading, the Kevlar-wall data now has negative blockage as the diversion of flow out of the tests section produces a local velocity less than the freestream.

The pressure distributions in Figure 5.29 show the same trends as in the lower Reynolds number case with the C_{pc} offset between test sections now more exaggerated. Specifically, the Kevlar-wall data falls noticeably farther below the hard-wall data on the suction-side near the pressure peak which is consistent with the presumed overcorrection of blockage in the Kevlar-wall

test section. The negative σ at low loading results causes a *decrease* in C_p (higher on the ordinate) upon correction. Even so, the offset at zero angle of attack is still present as in the lower Reynolds number data.

5.3.1.2. 0.61 m DU00-W-212

Figure 5.30 presents the corrected results for the DU00-W-212 0.61 m chord at a nominal $2.25\text{x}10^6$ Reynolds number and in the tripped condition. The exact Reynolds numbers are $2.24\text{x}10^6\pm4\text{x}10^4$ and $2.24\text{x}10^6\pm4\text{x}10^4$ for the aerodynamic and anechoic test sections, respectively, which correspond to Mach numbers of 0.17±0.003 and 0.17±0.003. The trip used in both test sections was the serrated trip applied at 5% chord on the suction-side and 10% chord on the pressure-side. The Kevlar-wall data has been translated in the negative x-direction by 0.37 degrees to match the zero-lift angle of attack of the hard-wall data.

The agreement of the corrected lift coefficients in Figure 5.30a is generally within the bounds of the error bars even through the 3-6 degrees region where there are significant differences in the uncorrected data between test sections. In the region of high positive lift, the C_{lc} of the Kevlar-wall data is larger than that of the hard-wall data by a small offset of around 0.05. The $C_{lc,max}$ of the Kevlar-wall section at 1.20 is 3.5% larger than that of the hard-wall section. These results are in contrast with those of the 0.91 m NACA 0012 where there is a small offset in the opposite direction which is assumed to be due to the over-prediction of blockage. The comparison of $C_{lc} - 2\pi\alpha_c$ in Figure 5.30b again shows the strong agreement of the data between test sections in the linear region. The C_{mc} comparison in Figure 5.30c is relatively good for negative angles of attack while the Kevlar-wall data drifts below the hard-wall data for positive angles. The C_{dc} comparison in Figure 5.30d-e shows a definite bulge in the drag centered at -10 degrees in both test sections. In the linear region of -7 to 7 degrees, the corrected Kevlar-wall data just below that of the hard-wall data by around 0.001, or 10 drag counts. Moving towards high positive angles of attack, the flow separation process causes a less severe rise in the Kevlar-wall drag than in the hard-wall drag which corroborates the slightly higher $C_{l,max}$ of the Kevlar-wall data noted above.

Figure 5.31a shows $\Delta\alpha_{porosity}$to be almost 2.5 degrees. Due to the camber of the DU00-W-212, $\Delta\alpha_{porosity}$ is nearly as large as that of 0.91 m NACA 0012 even as it is run at nearly half the Reynolds number. As seen previously, there is negative σ near zero-loading in Figure 5.31b. Upon correction, there is an increase in lift magnitude at these loadings as characteristic of open-jet test sections.

While the 0.61 m DU00-W-212 lift curve might suggest that the slight over-correction of blockage seen for the 0.91 m NACA 0012 is not present for the smaller model, the pressure distributions in Figure 5.32 show the same behavior as previously with the Kevlar-wall C_{pc}'s more positive (lower on the ordinate) than those of the hard-wall on both the pressure- and suction-side. The explanation could be a difference in suction-side boundary layer development between test sections such as stronger tripping for the hard-wall model possibly due to slight differences in the trip strip application.

5.3.1.3. 0.20 m NACA 0012

Figure 5.33a presents the uncorrected and corrected lift results for the 0.20 m NACA 0012 chord at $0.50\text{x}10^6$ Reynolds number and in the untripped condition. The exact Reynolds numbers are $0.50\text{x}10^6\pm3\text{x}10^3$ and $0.50\text{x}10^6\pm3\text{x}10^3$ for the hard-wall and Kevlar-wall test sections, respectively, which correspond to Mach numbers of 0.11±0.0006 and 0.11±0.0006. As noted previously, the Kevlar-wall data for each airfoil has been translated over top of the hard-wall data to match the zero-lift angle of attack for each run condition. In the case of the 0.20 m NACA 0012 airfoil, there was a considerably greater adjustment to the Kevlar-wall data of 1.19 degrees in the negative x-direction.

This abnormally large offset is traceable to twisting of the airfoil as a result of the bottom bearing plate in the Kevlar-wall test section having strong resistance to rotation. During angle of attack sweeps, the relatively small torsional stiffness of the 0.20 m chord airfoil was not enough to keep the airfoil from twisting, and the bottom bearing plate tended to lag behind the top turntable. Since the angle of attack sweeps were performed from negative to positive angles, the lagging bearing plate caused the angle of attack to be more negative than the encoder recorded.

Troubleshooting of the angle of attack measurement was performed as follows. The zero angle of attack position was set using the test section ceiling in both test sections since the encoder was located in the turntable above the ceiling. Then, sweeping through angles of attack with the flow off, the trailing edge of the airfoil at the floor lagged that at the ceiling by between 3.2-6.4 mm which corresponds to an angle of attack difference between 1.2-2.4 degrees. Interpolating to midspan under the assumption of linear twisting, the airfoil's midspan angle of attack lagged the encoder by 0.6-1.2 degrees. This difference is consistent with the 1.19 degree offset applied to the Kevlar-wall data in the x-direction to align the zero-lift angles of attack.

Even amidst the uncertainty of the angle of attack, the C_{lc}'s in Figure 5.33a generally agree within or very near within the limits of the error bars. The angularity in the linear region presumably due to the laminar separation bubble shrinking in size is seen in both test sections except not so strongly for the Kevlar-wall test section at negative angles. The dips in the lift curve at -1 degree and 6 degrees are likely areas where the turntable hit a snag and lagged more than usual. The $C_{lc,max}$'s on the positive side are 0.988 and 0.968 for the hard-wall and Kevlar-wall, respectively, for a difference of 2%. On the negative side, these numbers are similarly -0.960 and -0.9758 for a difference of 1.6%. The positive stall angle is in agreement between test sections at 13 degrees while at negative stall the Kevlar-wall test section shows significant delay of stall relative to the hard-wall test section. Additionally, the deep stall regions of both test sections show the lift returning to a value near $C_{lc,max}$ which is the same characteristic seen in Figure 5.27a for the 0.91 m NACA 0012. The comparison of $C_{lc} - 2\pi\alpha_c$ in Figure 5.33b suffers from scatter due to the error in the angle of attack measurements. The C_{mc}'s in Figure 5.33c show clearly the angularity associated with the laminar separation bubble around 6 degrees, and they demonstrate strong agreement between test sections strong throughout the unseparated flow regime. Unlike for the previous two airfoils, the 0.20 m NACA 0012 shows the Kevlar-wall C_{dc} as in Figure 5.33d-e to be generally larger than the hard-wall data.

The 0.20 m NACA 0012 airfoil exposes one limitation of the panel method simulation in its current state which is its difficulty with handling airfoils of small chordlength. The scatter of the interference predictions from both test sections of Figure 5.34a-b indicate that the simulations did not always reach converged solutions. Evaluation of the numerical output shows that the inner pressure loop described in Section 2.4.2.1 did not converge for most angles of attack nor did the deflection loop for some angles of attack.

Although the correction parameters are relatively small for the 0.20 m chord model, the pressure distributions of Figure 5.35 show the same trend as previously with the Kevlar-wall C_p's more positive (lower on the ordinate) on both the pressure and suction-side, thus supporting the over-correction of blockage hypothesis.

5.3.1.4. Common Characteristics across Airfoils

Summarizing the results for all four of the cases reviewed above, the Kevlar-wall test section performs similarly to the hard-wall test section after aerodynamic corrections are applied. What differences remain can be analyzed with the help of the airfoil pressure distributions which indicate that the blockage correction of the Kevlar-wall test section is too positive, both in high-lift and low-lift situations. Although comparing $C_{lc,max}$ between test sections is unavoidably influenced by the complete removal and reinstallation of the model, the influence of the test section type on $C_{lc,max}$ appears weak. Considering the positive and negative $C_{lc,max}$'s of the four cases

examined above, the largest discrepancy between test sections was 7.4% and the smallest 1.3% with an average absolute value of 2.9% difference.

Because corrections are inherently far-field effects, it is expected that the differences in the predicted Kevlar-wall corrections between test cases should be due to differences in Reynolds number and angle of attack but not due to model thickness nor camber. A comparison of the $\Delta\alpha_{porosity}$ versus deviation from zero-lift angle of attack, or $\alpha_g - \alpha_{0L}$, for the test cases of Table 5.2 is shown in Figure 5.36a excluding the 0.20 m NACA 0012 case do to the convergence problems of the panel method for this airfoil. The effect of the porosity is to reduce the far-field angle of attack from the geometric angle, and thus the slope of the plot is negative for all cases. It is seen that $\Delta\alpha_{porosity}$ goes more or less linearly with $\alpha_g - \alpha_{0L}$ and is most sensitive around the zero-lift angle. The highest Reynolds number data have the largest slopes meaning they are inducing more flow through the Kevlar pores and thus more change in angle of attack.

A comparison of the panel-method optimized blockage correction for the same data is plotted relative to the hard-wall blockage predicted by Allen and Vincenti (1944) as $\Omega = \frac{\sigma}{\sigma_{AV}}$ in Figure 5.36b. The results show some segregation at low-loading but collapse at higher angles of attack. The blockage is consistently greater than unity at around 1.75 at extreme angles of attack and much less than unity at low loading as also observed in subplot (b) of Figures 5.25, 5.28, and 5.31. In general, the blockage may be negative for angles of attack within +/- 5 degrees. For all the cases, the blockage in the Kevlar test section remains below that of the Allen and Vincenti value of $\Omega = 1$ until around 10 degrees. It is a significant point that Kevlar-wall test sections thus require a smaller blockage correction than hard-wall tunnels at low to moderate angle of attack up to 10 degrees. Interestingly, the 0.61 m DU00-W-212 data does not center on the zero-lift angle of attack. Apparently the point of zero-lift does not produce the point of least blockage for this airfoil as the lowest blockage occurs at a geometric angle of attack of -4 degrees.

5.3.1.5. Blockage Considerations

Since the blockage predicted by the panel method for the Kevlar-wall test section appears too positive in both high and low lift cases, some comments on the blockage modeling are made here. In reality, *two* possible scenarios are present and are that either the hard-wall correction is under-predicting the blockage correction (too small the magnitude of a positive value) or that the Kevlar-wall correction is over-predicting the blockage correction (too positive a value, whether positive or negative). The first of these is unlikely given the well-documented performance of hard-wall test sections. An error in the hard-wall modeling might arise from the negligence of the growing viscous boundary layer on the tunnel walls. However, the growing boundary layer is already accounted for in an up-front adjustment to the measured airfoil pressure coefficients based on the measured freestream pressure drop along the length of the test section.

If the Kevlar-wall correction needs improvement as suspected, one possible culprit is the inflow multiplier used to simulate the blockage created by flow re-entering the test section from the chambers with zero streamwise momentum. However, running the panel method simulation with an inflow multiplier of 1.5 rather than the standard 2 actually increased the discrepancy between test sections at least at high lift.

An alternative explanation is that the viscous boundary layer growth on the walls is not accounted for in the *Kevlar-wall* correction. The reason is illustrated by considering the case of an empty test section, wherein the Kevlar walls have been observed on occasion to bow inwards into the test section in contrast to the simulated walls which remain straight. If the viscous boundary layer were included in the simulation, the flow would accelerate as it moves through the test section, causing the static pressure to decrease in the downstream and flow from the chambers to blow into the test section downstream. To maintain a mass balance, mass flow would enter the chambers in the upstream. The chamber pressure would then be a middle value in-between the upstream and downstream static pressures. These pressures acting over the Kevlar would induce the wall to bow

outwards in the upstream and inwards in the downstream. This would result in an effective test section widening at the model location which, when accounted for in the Kevlar-wall correction, may cause the simulated Kevlar-wall correction to yield a more negative blockage correction, as desired.

5.3.2. Lift Symmetry

A concern stemming from Section 5.3.1 is an asymmetry observed in the lift curves of the Kevlar-wall test section. Figures 5.37-39 show the analogous comparison of Figures 5.13-15 but for the Kevlar-wall test section. The zero-lift angles of attack of subplots (a)-(d) are -0.23, -0.16, -0.13, and -0.01 degrees, respectively, and these have been subtracted out of data before plotting. As in the hard-wall case, there is a slightly greater lift magnitude at negative angles than at positive angles. There are many commonalities between Figures 5.13-15 and 5.37-39. The negative data stalls 1-3 degrees before the positive data at the low Reynolds number cases but closer to the positive data at the high Reynolds number cases as shown in the C_{lc} and C_{mc} comparisons. In terms of lift slopes, both the hard- and Kevlar-wall data show good angle of attack symmetry at low Reynolds number but have higher magnitude lift at negative angles for the high Reynolds number case. Both the Kevlar-wall and hard-wall drag data experience the bulge previously described at 7 degrees angle of attack. The above similarities indicate that to a large extend, the asymmetry in both test sections is due to the characteristics of the airfoil rather than characteristics of either of the test sections.

One notable difference, however, between Figures 5.13-15 and 5.37-39 is the larger asymmetry seen in the Kevlar-wall C_{lc} and C_{mc} of subplot (c) and especially of subplot (d). A study was undertaken to determine what effect the Kevlar-wall test section might fundamentally be contributing to the asymmetry.

It is first noted that there is asymmetry in the measured anechoic chamber pressures as well as in the lift which is shown in Figure 5.41a. While the reason for this is not yet understood, the chamber pressures do give a starting point for understanding the asymmetry seen in the Kevlar-wall lift data. The chamber pressures measured in two locations in each chamber are seen in Figure 5.41a a run of the 0.91 m NACA 0012 at a Reynolds number of $4\text{x}10^6$ and in the tripped condition. The overall shape of the chamber pressure curve resembles that of a lift curve which follows since the pressure difference in the chambers is generated by the lift of the airfoil. The chambers reach a larger absolute pressure when they are experiencing the pressure-side of the model with the port and starboard chambers reaching just above 200 and 250 Pa, respectively. When the chambers are experiencing the suction-side of the model, the chamber pressures dip asymmetrically to -100 and -175 Pa, respectively. The starboard chamber thus only holds around 50% the suction pressure than that of the port chamber. This conclusion might also be inferred from the leakage area measurements of Section 5.2.2 where the second measurement of the starboard chamber yielded an irregularly low suction holding capability.

This asymmetric behavior suggests the starboard chamber acts similarly to a reed valve, restricting flow from escaping in one direction while permitting it to enter in the opposite direction. Throughout the airfoil testing in the Kevlar-wall test section, standard operating procedures were maintained in an effort to control the chambers' leakage areas such as closing and locking the anechoic chamber doors during runs and keeping foam wedges in roughly the same positions in the chambers between runs.

Studying the momentum balance in the transverse direction of a rectangular control volume of a test section such as in Figure 5.40 is informative. The balance reduces to

$$C_l = \frac{2}{c}\int_{-\frac{h}{2}}^{\frac{h}{2}} \frac{v_1 u_1 - v_2 u_2}{V_\infty^2}\,dy + \frac{1}{c}\int_{x1}^{x2} (C_{p3}cos\theta - C_{p4}cos\theta)dx + \frac{2}{c}\int_{x1}^{x2} \frac{v_3^2 - v_4^2}{V_\infty^2}\,dx \qquad \text{Equation 5.3}$$

where c is the chord of the airfoil, u is the x-component velocity, v is the y-component velocity, V_∞ is the freestream velocity, C_p is the pressure coefficient along the wall, θ is the elevation from the horizontal of the deflected Kevlar wall, and the limits of integration and subscripts are as defined in Figure 5.40. The first term accounts for transverse momentum entering and exiting the control volume through the test section entrance and exit, respectively. The second term calculates the force acting in the transverse direction by the tunnel walls via the pressure. As will be examined below, the deflection of the port and starboard walls has been measured and found to be approximately the same for symmetric ± angles of attack with the 0.91 m NACA 0012, so the second term does not appear to be the cause of the asymmetry. The third term accounts for the transverse momentum entering or exiting the control volume through the Kevlar walls. It is conceivable that asymmetric chamber pressures could induce asymmetry in the velocities of the third term that would produce corresponding asymmetry in the lift coefficient. However, a detailed study of Figure 5.40 reveals that the effect of the suction-side chamber with lessened suction pressure would increase the net flow out of wall 4 into the test section, assuming the mass exchange with the port chamber remains unchanged. An increase of transverse flow velocity from the suction wall corresponds to increasing v_4 in Equation 5.3 which decreases the lift coefficient. This is, in fact, the opposite of what is observed in the lift data where the lift magnitude is greater when the leaking chamber is situated on the suction-side.

The mass flow in and out of the anechoic chambers is clearly complex and not symmetric and must interact with the mass flow between the test section and control room. Mass exchange between the control room and test section occurs freely in only a limited number of places, mainly at the wake rake slots. A recommendation for future wind tunnel testing is to investigate the effect of covering versus uncovering the wake rake slots and to gage if flow is entering or exiting the test section at these locations slots.

5.4. Validation of the Kevlar-Wall Boundary Conditions

The panel method simulation's handling of the porous, flexible boundary conditions makes it valuable as a predictor of wall interference. In Section 5.2, measurements were described on two boundary conditions: the pressure-velocity relationship across the Kevlar and the leakage area between chambers. These measurements, along with other modeling techniques, were applied to produce corrected aerodynamic data in the previous section. We now return to the boundary conditions and compare the simulated chamber pressures, wall pressure distributions, and wall deflection distributions to those which were measured during the tests described in the previous section. The 0.91 m NACA 0012 is used as the validation test bed in this section because it provides the maximum loading on both the walls and the anechoic chambers of all the airfoils testing. Specifically, the comparison is made with the 0.91 m NACA 0012 data at a nominal Reynolds number of 4×10^6 and either in the untripped or tripped condition with the tripped runs using the serrated trip described in Section 4.4.

5.4.1. Validation of Chamber Pressures

During wind tunnel testing of lifting airfoils, the anechoic chambers on either side of the Kevlar walls build up either a suction or pressure head depending on the rotation of the airfoil. In this section, the measured chamber pressures for the tests of the 0.91 m NACA 0012 airfoil as described in Section 5.3.1 and 5.3.2 are examined in greater detail and compared to the panel method simulated chamber pressures for validation of the simulation.

One of the assumptions of the Kevlar-wall panel method simulation is that the pressure in the anechoic chambers is uniform in space. A simple test to gage the validity of this assumption was performed by selecting two different measurement locations for pressure within each chamber.

One measurement, designed to be in the far-field of the walls, consisted of a Tygon tube and was placed near the chamber wall opposite the Kevlar and connected to the Esterline scanner specified in Section 4.5. The other measurement, designed to be in the near-field of the walls, consisted of an open port of the DTC scanner itself placed on the quarter-elliptical foam sections just below the Kevlar wall.

The measured chamber pressures for the 0.91 m NACA 0012 at a Reynolds number of $4x10^6$ and in the tripped condition are shown in Figure 5.41a. Besides the asymmetry in the slopes, it is notable that the chamber pressure curves resemble closely those of the lift curves in the previous section. This is the guiding principle upon which the correction for three-dimensional flow in Kevlar-walls is based (Ito *et al*. 2010). The airfoil is here seen to induce chamber pressures of ±200 Pa at maximum lift. The largest difference in the data measured between the two locations is in the starboard chamber where differences reach up to 25 Pa, the near-field measurement always giving a more positive pressure. On the port-side, however, the differences are an order of magnitude less. This situation, which is the same in the untripped as well as tripped cases, is unusual for a symmetric airfoil because the data from different locations have a consistent offset in one chamber but no offset in the other. Looking only at the port wall data where there is no offset, the random nature of the differences between far-field and near-field measurements suggest they are due to imprecision of the instrumentation. Then, there is reason to question the zeroing or the calibration of the scanners used on the starboard-side. A zeroing error might occur if the scanner reference port was covered or being handled inadvertently during zeroing. Given that the performance of the far-field scanner, an Esterline unit, undergoes more weekly scrutiny than that of the near-field scanner, an auxiliary DTC unit, it is reasonable to suspect that any bad calibration would lie with the DTC unit.

Furthermore, if there were truly a difference in pressure between the near- and far-fields of the Kevlar walls, it would be caused by the transverse velocity of flow through the Kevlar which would lower the pressure just near the wall before dissipating. The maximum flow velocity through the Kevlar at midspan as measured in Section 5.2.1 was roughly 4 m/s equating to a dynamic pressure of about 10 Pa. Thus, even the maximum transverse velocity over the Kevlar could not account for the difference of 25 Pa between locations seen in the starboard chamber. For non-maximum conditions, then, the velocity through the Kevlar should have a negligible influence on the pressure readings which are measured with the DTC scanners and accurate to ±5 Pa. Assuming then that there is little to no dependence of location on the chamber pressure and that the reliability of the Esterline scanner is high, the far-field measurement will be used in the analysis below.

For the purposes of validating the panel method simulation, comparison of the simulated versus measured far-field chamber pressure coefficients is shown in Figure 5.41b for the 0.91 m chord NACA 0012 airfoil. The main difference between the simulation and measurement, other than the absence of stall in the invsicid panel method data, is the slope of the suction curves. The simulation has slopes that are everywhere more negative than those of the measurement. The simulation predicts that the suction chamber should reach values of suction more than twice as large as those born out in the actual measurements. Such an inconsistency between the simulation and measurement might be due to some reed valve effect as mentioned in the previous section that is not captured in the modeling of the chambers. One idea to bring the simulated suction pressures into agreement with the measured suction pressures is to simply input the measured chamber pressures into the panel method. An attempt to these ends was undertaken by doing away with the leakage model altogether and enforcing instead the measured chamber pressures, however, the panel method has difficulties with convergence in such a case, and no further progress towards this end was made.

5.4.2. Validation of Kevlar-Wall Pressure Distributions

Validation of the panel method simulation versus the measurement is next performed by comparing pressure distributions at geometric angles of attack of -10, 0, and 10 degrees as seen in Figure 5.42. All measured data are again taken with the 0.91 m NACA 0012 at a Reynolds number of $4x10^6$ and the tripped condition. The simulated data is sampled at the control point of each panel within the test section limits and therefore has the same power-law spacing as described in Section 2.4.2.1. The measured data is taken with Kevlar-wall mounted pressure taps introduced in Section 4.8.

Comparing first the pressure distributions along the Kevlar as shown in Figure 5.42a-b for a nominal -10 degrees angle of attack, the C_p is positive on the port-side and negative on the starboard-side for the majority of the test section length in both data, thus yielding negative lift. The concavity of the pressure distributions along the length of the test section is in agreement between data with the possible exception being on the starboard-side between $x =$ 1-2 m on the abscissa. For both the simulation and the measurement, the maximum absolute C_p on the port-side occurs approximately 0.2 m upstream of the maximum absolute C_p on the starboard-side, but the locations of these maximum are shifted roughly 0.2 m downstream in the case of simulation. This difference is relatable to the difference in deflection behavior of the Kevlar walls between the simulation and measurement as examined in the next section. The simulation might have better agreement through improved modeling of the in-flow into the test section from the suction chamber as well as treatment of the Kevlar porosity on a local rather than wall-averaged basis as currently done in Equation 2.30. The latter improvement, for instance, would cause the pores at the point of maximum wall loading to be more open, thus increasing the transverse flow through the walls and changing the local pressure behavior along the walls.

An important difference between the simulation and measurement is that while both data see a drop in C_p from the first upstream to last downstream measurements, the drop is more significant for the measured data. For the simulation, the average C_p at the farthest upstream location is 0.03 and at the farthest downstream location is -0.06. Since the simulation is an inviscid model, the C_p's would be expected to return to zero, or at least near zero since some mass is added to the test section by the in-flow multiplier as in Section 2.4.2.1, as one continues further downstream. For the measurement, the average C_p's at the first upstream and last downstream location are -0.01 and -0.17, respectively, which correspond to a nearly 3 times greater drop in C_p than in the simulation. At first glance, this large drop in C_p appears similar to the description in Section 2.1.5 of wind tunnels of constant cross-section that experience a pressure drop in the streamwise direction due to boundary layer growth along the walls. The boundary layer development in a Kevlar-wall tunnel, however, is different than a typical constant cross-section tunnel, and floor pressure measurements in the empty Kevlar-wall test section show much flatter pressure distributions in the streamline direction than seen in the hard-wall test section. Thus far, the focus of the Kevlar-wall modeling has resided with the Kevlar's porosity and deflection which, if done correctly, should predict any change in static pressure along the length of test section. Addition of a viscous boundary layer emanating from the leading edge of the test section would be a logical next step to improve agreement with the measured data.

Similar conclusions as for the -10 degree angle of attack case are again reached looking at the data for a nominal angle of attack of 0 degrees as shown in Figure 5.42c-d. As expected for a symmetric airfoil at 0 degrees angle of attack, the pressure distributions on the port and starboard-sides are approximately the same. Both the simulation and measurement rise to a maximum C_p upstream of the airfoil and dip to a relatively constant negative C_p for the rest of the test section. Considering the flow path in the test section, it is possible to deduce what is happening to cause the described pressure distribution. The flow develops a slight velocity gradient in the streamwise direction due to solid blockage of the model, as well as wake blockage and boundary growth along

the tunnel walls in the case of the measurement. This change in freestream velocity causes a pressure difference between the upstream and downstream sides of the airfoil that results in recirculation through the chambers. Higher pressure flow upstream of the airfoil passes into the medium-pressure chambers and then out into the lower pressure downstream region. Although one might expect this effect to relieve the pressure gradient through the test section, the effect is self-perpetuating because the recirculation lowers the freestream velocity upstream of the model and increases it downstream where the inflowing air increases blockage, and these two phenomena both work to increase the velocity gradient in the test section in view of Bernoulli's equation. Both the simulation and measurement show this pressure gradient behavior, and the effect is greater in the measurement presumably due to the inclusion of the effects of wake blockage and boundary layer growth on the walls which are not yet incorporated into the panel method.

Figure 5.42e-f shows the pressure distributions for the case of a nominal angle of attack of 10 degrees. The results closely resemble those of Figure 5.42a-b except that the port and starboard-sides are reversed. Again, the measurement C_p's at the end of the test section fall noticeably below those of the simulation because of the pressure drop through the test section, and the simulation has a smaller range overall.

Another important difference between the simulation and the measurement is the range of the pressure differences observed and the corresponding difference in overall lift generated. For the -10 degrees angle of attack data, the maximum C_p's for the simulation and measurement are 0.19 and 0.24, respectively, with the measurement being 26% greater. The minimum C_p's for the same are -0.33 and -0.39, respectively, with the measurement being 18% greater in absolute terms. For the 10 degrees angle of attack data, the maximum C_p's of the measurement is again 26% greater than that of the simulation and the minimum C_p's are identical at -0.33. Calculating the lift from the wall pressures using the control volume of Figure 5.40 along with Equation 5.3, the smaller C_p range of the simulation translates into lower integrated lift values than for the measurement. Performing this integration while neglecting both the transverse momentum flow through the Kevlar-walls and the alteration to the lift-direction component due to the Kevlar deflection, the uncorrected coefficient of lift predicted by the simulation is just -0.572 at -10 degrees angle of attack which is 39% less than the uncorrected lift coefficient from the measured wall data.

The explanation for this is, in part, the neglected transverse momentum in the lift integration. As discussed in Section 2.4.2, to model the blockage effect of flow entering the test section from the anechoic chambers, the in-flow velocity of re-entering flow is doubled. As seen in Section 5.3.2, an increase in the transverse velocity on the suction-side will add momentum in the negative y-direction and reduce lift. This effect, although deemed of secondary importance in Section 5.3.2, is exaggerated by the doubling of the inflow velocity for the case of the simulation. Doubling of the inflow velocity equates to a four-fold change in the v_4^2 term of Equation 5.3. A comparison with the measured and simulated wall pressures in the *hard-wall* test section shows the simulated lift slightly *larger* than the measured lift, thus supporting the claim that porosity and the doubling of the in-flow velocity are responsible for the smaller range of the simulated data.

Summarizing, the agreement for all three angles of attack considered between the measured and simulated pressure distributions' shapes is good while the simulated data generally has lower magnitude because of the doubling of inflow velocity.

5.4.3. Validation of Kevlar-Wall Deflection Distributions

In this section, validation of the panel method simulation's wall deflection is made versus the measured deflections for geometric angles of attack of -10, 0, and 10 degrees. All measured data are again taken with the 0.91 m NACA 0012 at a Reynolds number of 4×10^6 and the untripped condition. For the contour plots in Figure 5.43, deflections out of the test section are given as negative values whereas deflections into the test section are given as positive values. The simulated data are spanwise averaged deflections produced by the finite difference membrane solver of the

panel method simulation. The measured data is taken with stereo camera system introduced in Section 4.9.

Comparing first the distributions for a nominal -10 degrees angle of attack as in Figure 5.43a-b, the deflection is usually symmetric about the mid-span horizontal in the measurement and always in the simulation. The port-(pressure) sides of the simulation and measurement both show deflection out of the flow for the majority of the wall area with a maximum deflection near or just before the quarter-chord location. The starboard-(suction) sides of each data show deflection out of the flow over approximately the first one-third of the test section length and deflection into the flow over the remaining length of the test section.

A notable dissimilarity between the simulation and measurement is the magnitudes of deflection both into and out of the flow. As the case for the wall pressure magnitudes in the previous section, the simulation has everywhere smaller deflections than the measurement. The maximum deflection out of the flow on the port-side is only 50% as large for the simulation as the measurement with values of 43 mm and 86 mm, respectively. The maximum deflection out of the flow on the starboard-side is 53 mm and 82 mm for the simulation and measurement, respectively, with the simulation being 65% as large as the measurement. Modeling parameters affecting the deflection that could account for these differences are the initial Kevlar tension, initial Kevlar strain, and Kevlar modulus of elasticity. These are briefly revisited in Section 5.5.1.

Another difference between Figure 5.43a-b is due to the pressure gradient through the test section which was also seen in the pressure distributions of the previous section. The pressure-(port) side wall, which is generally pushed *out* of the test section by pressure, deflects *into* the flow near the exit of the test section in the case of the measurement only. This is a result of the presumed pressure gradient in the streamwise direction which allows the chamber pressure to push the Kevlar wall into the test section with less resistance than in the simulation where the modeling as yet does not model all the phenomenon that contribute to the pressure gradient. The pressure gradient might be more fully captured in the panel method simulation through either increasing the in-flow multiplier as described in Section 2.4.2.1 to increase the blockage effect of the growing boundary layer or through modeling of airfoil wake blockage and boundary layer growth on the tunnel walls.

Looking at the nominal angle of attack of 0 degrees in Figure 5.43c-d, the deflection distributions are again smaller in magnitude for the simulation. Also, there are significant differences in the streamwise locations of inflection points as the simulation has zero deflection at the quarter-chord location while the measurement passes zero at 1m downstream of quarter-chord. This may also be a consequence of the pressure gradient discussion of the previous paragraph. Note that the simulation is not exactly symmetric between port and starboard-sides because the angle of attack is specified to -0.05 degrees to match the actual achieved angle of attack in the measurement.

Figure 5.43e-f shows the deflection distributions for the case of a nominal angle of attack of 10 degrees. The results are quite similar to Figure 5.43a-b except with the port and starboard-sides reversed. The magnitudes of the deflection for the port and starboard-sides are 23% and 76% less, respectively, for the simulation than the measurement. Again, the deflection into the test section on the downstream starboard-side due to the pressure gradient through the test section and is seen only in the measurement.

The overall goal of the comparison of the simulation and measurement data is determine which, if any, adjustments can be made to the simulation. Considering Equation 2.28, there are three types of terms: deflection derivatives, pressure differences, and tension. In the current formulation of the simulation, tension is the only input while both the deflection derivatives and pressure difference are solved for iteratively. It is therefore desired to determine if an adjustment to the tension of the Kevlar in the simulation may yield better agreement with the deflection measurement. For the cases of +/-10 degrees angle of attack where loading is relatively high, the differences in magnitude between the pressure distributions of the simulation and measurement, between 18-26%, appear relatively small compared to the differences for the deflection distributions, between 23-100%. The good similarity in the shape of the simulation and

measurement deflections suggests that the simulation is simply scaled down compared to the measurement, and scaling of the distribution would equally affect both the deflection magnitudes and the deflection second derivatives which appear in Equation 2.28. If the left hand side of the equation is 23-100% too little in the simulation while the pressure difference term on the right hand side is within 18-26% of the correct value, then one explanation to bring the data into agreement is to lower the tension in the simulation. One study towards this end is presented below in Section 5.5.1, however, the results do not account for the discrepancies observed here between the simulation and measurement.

It is recommended that a finite element rather than finite difference solution be added to the panel method simulation in future versions of the code to capture the coupling of the tension and deflection in the walls more exactly. This would do away with wall-averaging of the strain as done currently in Equation 2.30 which would be appropriate from a structural fidelity point of view as well as an aerodynamic point of view since the pore size could then be modelled as a local rather than averaged value.

5.5. Sensitivity of the Kevlar-Wall Test Section Corrections

Additional correction calculations were performed using the panel method in order to examine the sensitivity of the method, and thus presumably, of the test section itself to key parameters of the Kevlar-walled setup. In each case below, a single parameter is varied to study the effect on the flow in the test section and the resulting corrections to the measured data. These parameters are the initial Kevlar tension, asymmetric Kevlar tension, and leakage area. In each case below, the 0.91 m NACA 0012 data taken at $4x10^6$ Reynolds number and in the tripped condition is used to assess the sensitivities with the tripped data using the serrated trip described in Section 4.4.

5.5.1. Sensitivity to Initial Kevlar Tension

The tensions at the center of each Kevlar wall are believed to be 1550 N/m and 1400 N/m for the port and starboard walls, respectively, as determined by a screen tension meter (Devenport *et al.* 2010b). It is certainly possible that these values have fallen with time due to relaxation in the tensioning rollers or Kevlar fibers. To explore the effect that a lower tension would have on the blockage and lift interference produced by the Kevlar-wall test section, a brief sensitivity study of Kevlar-wall tension was performed.

A value of 1500 N/m is typically assumed for the initial tension of both walls in panel method simulations. Here, a comparison is made of the simulation results run with the standard tension as well as half the standard value, 750 N/m, applied to both walls. The expected result is that lower tension will produce more wall deflection and thus more blockage considering the streamlines in the test section and the narrowed effective height of the test section relative to the model chord as described in Section 2.4.3. As shown in Figure 5.44a, however, lowering the tension increases the maximum C_l which suggests a *decrease* in blockage. Additionally, the lift interference correction puts the lower tension data at smaller angles of attack. Both of these effects, the reduced blockage and larger lift interference correction, contribute to the counterclockwise rotation of the lower tension lift curve relative to the standard case.

First, the blockage differences are examined. The spanwise averaged deflection of the walls for the two tension cases is shown for 10 degrees angle of attack in Figure 5.44b on an offset ordinate axis to show finer resolution. The test section width at the model quarter-chord, $x = 2.489$m, is several millimeters greater for the lower tension case; the walls *are* deflecting more than the standard tension case and thus reducing the effective test section height which should result

in higher blockage. However, the deflection difference is small and examining the panel method optimized blockage value σ as plotted in Figure 5.44c, the 750N/m tension case has smaller blockage than the 1500N/m case with differences on the order of one half the blockage in the high loading cases. Thus, the predicted blockage is surprisingly smaller for the lower tension data even as the predicted wall deflections are larger.

The reason for this apparent contradiction appears to be the mechanism of flow diversion out of the test section in the upstream as described in Section 2.4.3. Figure 5.44d plots the strain in the Kevlar fibers averaged over each wall versus angle of attack. The average strain is more than twice as large on either wall for the lower tension case as the higher tension case. This follows since the loading on the walls is approximately the same for both cases, and equal loading requires the equilibrium tensions be equivalent to satisfy the equilibrium membrane equation. Tension, T, and strain, ε, are assumed to be linearly related through the constitutive stress-strain relation

$$\frac{T}{h} = E\varepsilon \qquad \text{Equation 5.4}$$

where h is the fabric thickness and E is the modulus the elasticity. The modulus is known to be linearly elastic after uncramping (King 2006), so the lower tension case must increase its strain by roughly two times in order to arrive at the same equilibrium tension as the higher tension case which started with an initial strain and tension twice as large as the lower tension case. This higher strain results in higher porosity as governed by the strain multiplier of Equation 2.30, conservatively an increase of around 15% in porosity for the lower tension case. It seems likely, then, that the lower tension case, due to larger pore openings caused by higher strain, is allowing more flow to divert out of the test section in both the upstream location and around the model itself. This flow is then returned to the test section downstream. Therefore, the decreased blockage of the lower tension case occurs through the flow diversion mechanism even as the blockage is increased slightly through the wall deflection mechanism.

Next, the lift interference differences between tension cases are examined. The change in far-field angle of attack due to the porosity of the Kevlar walls, $\Delta\alpha_{porosity}$, is found by subtracting out both the streamline curvature correction of Equation 2.8 and the geometric angle of attack from the corrected angle of attack as described by Equation 2.29. Figure 5.44e plots $\Delta\alpha_{porosity}$ versus angle of attack for both tension cases. The 750 N/m tension case has everywhere the larger porosity influence which is consistent with the larger porosity predicted for the lower tension case.

The correction for streamline curvature also introduces coupling between the blockage and lift interference corrections since Equation 2.8 relies on the blockage value σ. For an angle of attack of 10 degrees, for instance, the lower tension case produces an $\alpha_{porosity}$ equal to 19% of the geometric angle of attack and a subsequent $\Delta\alpha_{sc}$ equal to 5%. The higher tension data has a corresponding 17% reduction and 8% increase. Therefore, the larger pore openings in the lower tension data increase the porosity-driven correction but indirectly decrease the streamline curvature correction because of the reduced blockage caused by larger pores. Summing $\Delta\alpha_{porosity}$ and $\Delta\alpha_{sc}$, the lower tension data sees a 14% reduction in geometric angle of attack and the higher tension a 9% reduction which is equivalent to the 0.38 degree difference observed in corrected angles of attack at a nominal 10 degrees.

In summary, lowering the initial Kevlar tension over the tension ranges considered reduces both blockage and the corrected angle of attack due to larger pore openings and interaction between the blockage and lift interference corrections. Devenport *et al.* (2013) notes that the largest differences between corrected hard-wall and Kevlar-wall data of the same airfoil are a downward shift in the pressure distributions from the Kevlar-wall test section relative to those from the hard-wall test section especially at higher loading which is likely due to overestimating blockage. Halving the tension as shown here does decrease blockage, and while the effect is not large enough to fully bridge the pressure distribution offset, it does reduce the offset especially at high loading.

Looking at the lift curve slope at 10 degrees angle of attack, for instance, the combined effect of the blockage and lift interference corrections induced over a change over 750 N/m tension produce an increase of 6% slope with the lower tension case having 5.993 rad^{-1} and the higher tension case having 5.644 rad^{-1}.

Upon closer examination of the above analysis, it is found that consideration also needs to be given towards refining the initial strain input of Table 2.1 which is currently assumed zero. This assumption, which is not physically correct since the presence of an initial strain requires the presence of an initial strain, leads to an inconsistency in the modeling of the tension that is revealed by closer examination of the above analysis. As modelled in the above analysis, the initial strain and thus porosity of the Kevlar is maintained at the same value regardless of the initial tension specified for the walls. In reality, lower initial tension would produce lower initial strain by Equation 5.4 which would decrease the initial pore size as governed by an equation similar to Equation 2.30. The walls with lower initial tension should also have lower initial strain which would do away with the 15% greater porosity for the lower tension case as stated above. If this were the case, the lower tension case would then have the same flow diversion out of the test section and $\Delta\alpha_{porosity}$ as the higher tension case. The only difference between tension cases would then be the deflection of the walls, and the lower tension case would then create *more* blockage than the higher tension case as originally predicted because of the narrowed effective test section width as discussed in Section 2.4.3. Therefore, the initial Kevlar strain input to the panel method simulation might be altered in future versions to account for the approximate initial strain which will allow for valid comparisons and even optimizations of test section performance between different initial Kevlar tensions. This could be done with Equations 5.5 and 5.6 below which are adaptions of Equations 2.26 and 2.30, respectively, as

$$v_{normal} = (k_{c,1500} - dk_{c0})\Delta p^{0.5}\left(\frac{\Delta p}{\Delta p + k_p}\right)^{0.073} \qquad \text{Equation 5.5}$$

$$dk_{c0} = \frac{\varepsilon_{1500} - \varepsilon_{current}}{2\sqrt{\rho}}a_\varepsilon \qquad \text{Equation 5.6}$$

where $k_{c,1500}$ is the standard k_c of Equation 2.26 as generated empirically for tests of the Kevlar at roughly 1500 N/m initial tension and dk_{c0} is an upfront adjustment to k_c to account for deviations in the current initial strain, $\varepsilon_{current}$, from the 1500 N/m initial strain, ε_{1500}. Further modeling efforts could also include addition of a finite element solution such as described in Section 5.4.3 which would allow modeling of the strain and thus the pore size as a local rather than averaged value.

Comparing the results of this section to those of Section 5.4.3, it is seen that halving the initial tension as done in this section increases Kevlar deflection on the millimeter scale which does not make up for the centimeter scale differences in deflection between the simulation and measurement observed in Section 5.4.3. Higher fidelity modeling of the wall deflection is required in addition to better knowledge of the true initial Kevlar tension to reduce the differences between the simulation and measurement as discussed in Section 5.4.3.

5.5.2. Sensitivity to Asymmetric Initial Tension

Next, the case of asymmetry in the tension of the Kevlar walls is examined. A deviation of +/- 500 N/m from the nominal 1500 N/m was used to create the asymmetry, giving initial tensions of 1000 N/m and 2000 N/m for the port and starboard walls, respectively. Figure 5.45 shows analogous plots to those of Figure 5.44 except that the lower tension case is replaced with the asymmetric tension case. The lift curve comparison in Figure 5.45a, as well as the blockage comparison in Figure 5.45c, indicates that the blockage is not strongly dependent on the symmetry

of the tension over the given range of tensions. The deflections caused by the asymmetric tension are similar to within 3mm to those of the symmetric tension case. However, as shown in Figure 5.45e, there *is* an asymmetry in the angle of attack correction which amounts to a 0.1 degree difference from the symmetric case at -10 degrees angle of attack, for instance. A physical argument for this result is given below.

First is considered the case for negative angles of attack when the lower tension (port) wall is on the suction-side of the airfoil where the wall loading is the largest. Because of the lower tension and thus larger deflection here, the Kevlar strain is about two times that for the symmetric case as seen for the negative angles in Figure 5.45b where the asymmetric strain is 0.033 compared to 0.017 in the symmetric case. This larger strain equates to widening of the pores relative to the symmetric case which allows greater mass flow into the test section from the suction-side wall. On the pressure (starboard) side where the tension is larger than the symmetric case, the effect is the opposite; higher tension produces less strain, narrowing of the pores relative to the symmetric case, and decreased mass flow out of the test section. These two porosity effects on opposite walls counteract each other in terms of $\Delta\alpha_{porosity}$, but the increase in suction velocity dominates as shown in Figure 5.45e where the asymmetric $\Delta\alpha_{porosity}$ is larger at negative angles of attack than that of the symmetric data. The difference ranges from 0.06 to 0.11 degrees in the attached flow regime.

Next is considered the case when the model is rotated to positive angles of attack causing the lower tension (port) wall to experience the pressure-side. The strain is again increased from the symmetric case, but the maximum strain does not spike to a very large value as on the suction-side because the wall loading is lower on the pressure-side. The suction-side strain is conversely lowered from the symmetric case due to the higher initial tension there. The two counteracting porosity effects are in this case of roughly the same magnitude so that $\Delta\alpha_{porosity}$ is not strongly affected by the asymmetric tension. Discounting the abnormally large difference at 1 degree angle of attack, the $\Delta\alpha_{porosity}$ of the asymmetric data is everywhere within 0.05 degrees of that of the symmetric tension in Figure 5.45e over positive angles of attack. Therefore, it has been shown that asymmetric initial tension can create asymmetric angle of attack offsets in Kevlar-wall test sections.

5.5.3. Sensitivity to Leakage Area

All the preceding results have been presented using the leakage area model described in Section 2.4.2 and 5.2.2. For a moment, we take a step backwards to put the leakage area model in context. The panel method simulation can be run with the mass exchange between chambers set to zero to simulate a completely sealed chamber. The simulation can also be run so that the chamber pressures are specified as a single value to simulate two completely unsealed chambers. The simulation including the leakage model is then expected to fall between the cases of the sealed and the unsealed chambers; the leakage area allows more flow between the test sections than the sealed condition but less flow between than the unsealed condition. Figure 5.46 plots the corrected lift data for the unsealed, sealed, and leakage cases using the same 0.91 m NACA 0012 data at $4x10^6$ Reynolds number as the previous two sections. Indeed, the data processed with the leakage formulation, as it is called, lies between the data processed with the sealed and unsealed formulations throughout the linear region of the lift curve. It is noted that the leakage data is biased towards the sealed scenario which is understandable given that the leakage area of $0.15m^2$, or a 40cm-by-40cm square duct, is relatively small compared to the total area of the Kevlar-walls from which the driving force of the mass flow originates. The remainder of the calculations presented below employs the new leakage formulation of the panel method.

Next is considered the sensitivity of the panel method simulation and more importantly, the final corrected quantities, to the input leakage area. Adding to the data of the previous section is plotted in Figure 5.47 the leakage formulation with leakage areas of 0.12, 0.15, 0.18, and 0.30 m^2. Also included in this figure for comparison is the hard-wall data from the corresponding $4x10^6$

Reynolds number run in the tripped condition. As in Section 5.3.1.1, the Kevlar-wall data has been translated in the negative x-direction by 0.13 degrees to match the zero-lift angle of attack of the hard-wall data.

The asymmetry of the lift curve slope about the ordinate in the Kevlar-wall test section is again visible in Figure 5.47a as was discussed in Section 5.3.2. The sealed case matches the hard-wall data the best at negative angles of attack, but the leakage area cases match better at positive angles of attack. The detailed view of the positive angles of attack in Figure 5.47b shows the sealed condition having the best agreement with the hard-wall data at low angles of attack. With increasing angle of attack, the hard-wall data tends in the direction of the unsealed case. Between angles of attack of 5-8 degrees, the hard-wall data falls over top of the 0.12 and 0.15m^2 leakage areas. As the stall angle is approached, the agreement is best with the 0.15 and 0.18m^2 leakage areas.

The concern stemming from Section 5.3.1.5 that blockage is over-predicted could indicate an undervalued leakage area. Doubling the measured leakage area from 0.15 to 0.30 m^2 results in a 0.15 degree larger $\Delta\alpha_{porosity}$ and a 0.068, or -7%, decrease in σ. Translated into the final corrected quantities, doubling the leakage area results in an increase in the corrected lift coefficient of 0.048, or 0.5% and a decrease in α_c of 0.19 degrees. Even for a doubling of the leakage area, then, the change in lift coefficient is relatively small, so the leakage area does not appear to be a major factor in the discussion on the over-prediction of blockage. The difference in α_c with the doubled leakage area at 0.19 degrees, on the other hand, is relatively large. It is sought to find an acceptable uncertainty in the leakage area that will produce relatively small variations in α_c. Increasing the leakage area from 0.15 to 0.18 m^2, a 17% increase, results in a difference in α_c of 0.05 degrees. The difference in lift coefficient between the two cases is just 0.002, or 0.2%. Therefore, in the current panel method formulation, it can be stated that knowing the value of leakage within roughly 20% of the true value should not introduce significant error into the angle of attack or lift coefficient correction.

The leakage formulation described above represents a substantial improvement over the previous assumptions of either fully sealed or fully open chambers as shown in Figure 5.46. In Section 5.2.2, it was seen that the leakage curves exhibit power-law behavior which suggests yet a further refinement to leakage model. In Equation 5.2, the denominator is raised the 0.5 power following Bernoulli's equation for inviscid flow. Given that leakage from the anechoic chambers is through small openings such as the pores of the Kevlar areas highlighted in Figure 5.18, some viscous effects are expected in the leakage flow. Increasing the exponential in the denominator from 0.5 follows the principal of Equation 2.27 which specifies an exponent of 0.57 for low pressure differences across the Kevlar walls. Such an increase would ideally level out the curve of leakage area versus suction pressure which, from a physical standpoint, is intuitive since the leakage area would not be expected to vary significantly with chamber pressure. Equation 2.30 *does* imply that leakage area increases slightly with pressure difference, however, the pressure differences across the leakage volumes are generally lower than those across the Kevlar walls.

Figure 5.21b shows the leakage areas versus suction pressure with the alternative exponent of 0.60 used for Equation 5.2 which produces roughly level curves. The starboard chamber leakage area from the second measurement is roughly constant at 0.11 m^2 while the other leakage areas hover around 0.09 m^2. A leakage area of 0.10 m^2 was selected as an average value to be used for the study of the panel method simulation sensitivity to leakage exponent in the following paragraph. As an point of interest, the 0.57 exponent was trialed as well as 0.60 due to its presence in Equation 2.27, however, the leakage area curves did not level out with the 0.57 exponent as with the 0.60.

Figure 5.48 shows the comparison of lift and pressure data for the inviscid leakage model and viscous leakage models. On the lift curve in Figure 5.48a, the viscous leakage model appears to slightly aid the agreement of the results from the two test sections in the range of around 7-10 degrees until stall although there are no qualitative differences in the pressure distributions at either low or high loading conditions as shown by the 0 and 10 degree angles of attack data in Figure

5.48b-c, respectively. Although there are no standout features that distinguish the two leakage models, physical intuition suggests that a leakage exponent larger than 0.5 is indeed appropriate and adds refinement to the panel method simulation.

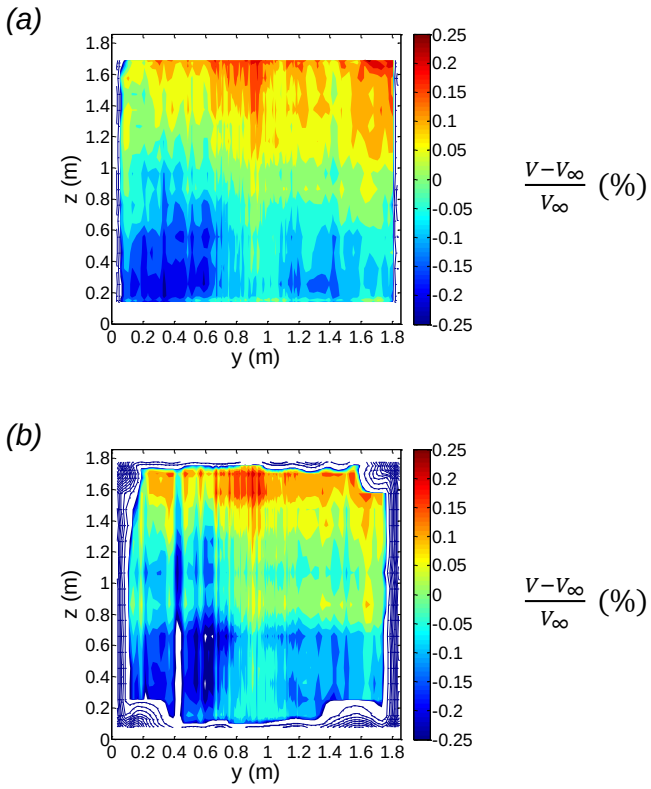

FIGURE 5.1. Percent variation from the reference freestream velocity over the cross-section of the empty hard-wall test section measured at *(a)* the front of the test section and *(b)* the rear of the test section at a nominal 60 m/s velocity. Regions with variation less than -0.25% are white with blue contours indicating the flow structure. The white border around the plot indicates areas of the test section outside of the measurement range of the wake rake.

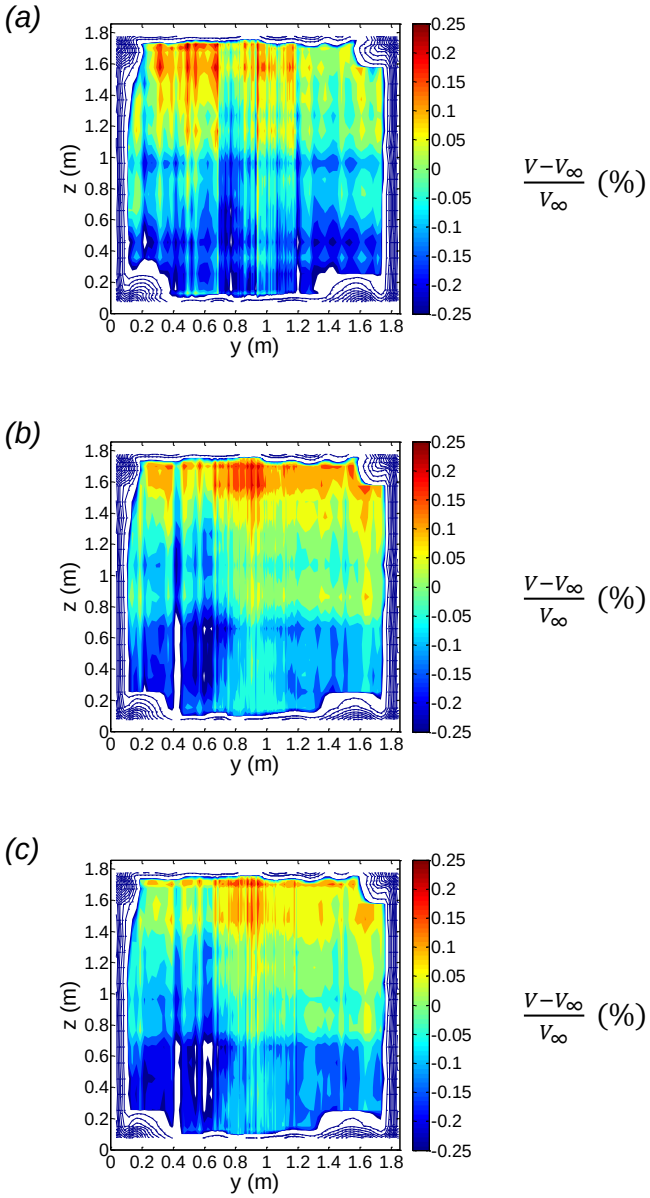

FIGURE 5.2. Percent variation from the reference freestream velocity over the cross-section of the empty hard-wall test section measured at the rear of the test section for nominal velocities of *(a)* 40 m/s, *(b)* 60 m/s, and *(c)* 80 m/s. Regions with variation less than -0.25% are white with blue contours indicating the flow structure. The white border around the plot indicates areas of the test section outside of the measurement range of the wake rake.

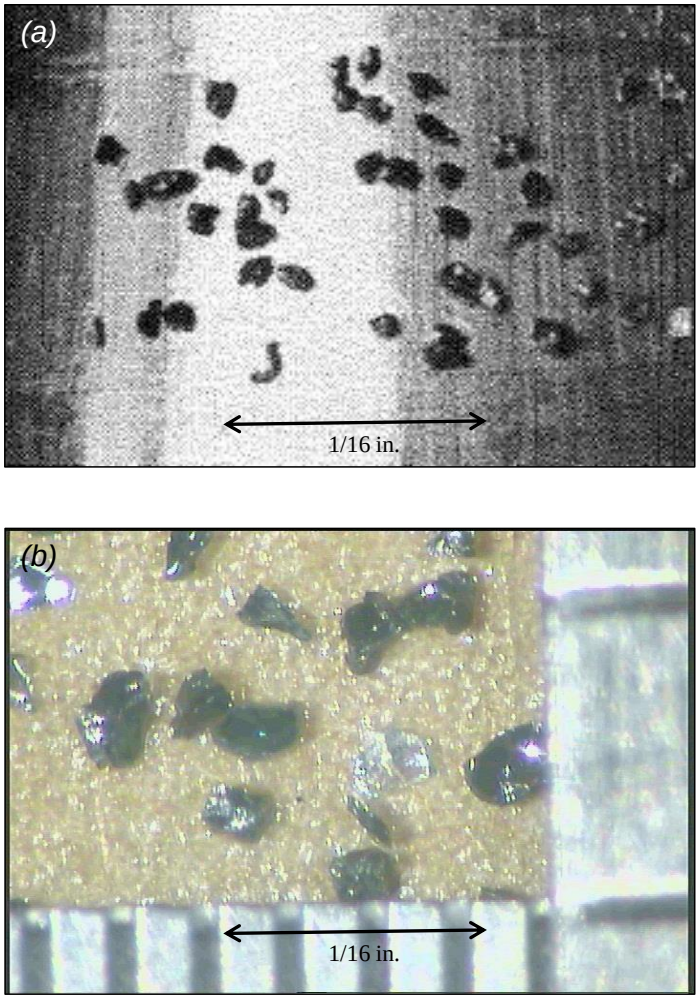

FIGURE 5.3. Comparison of 60-grit trips used by *(a)* Braslow and Knox (1958) and *(b)* the Stability Wind Tunnel. Braslow and Knox had 8-9 grains per 1/16 in.^{2}, and the SWT trip had around 7-11 grains per 1/16 in.^{2}, with the sample above having 10 grains per 1/16 in.^{2}.

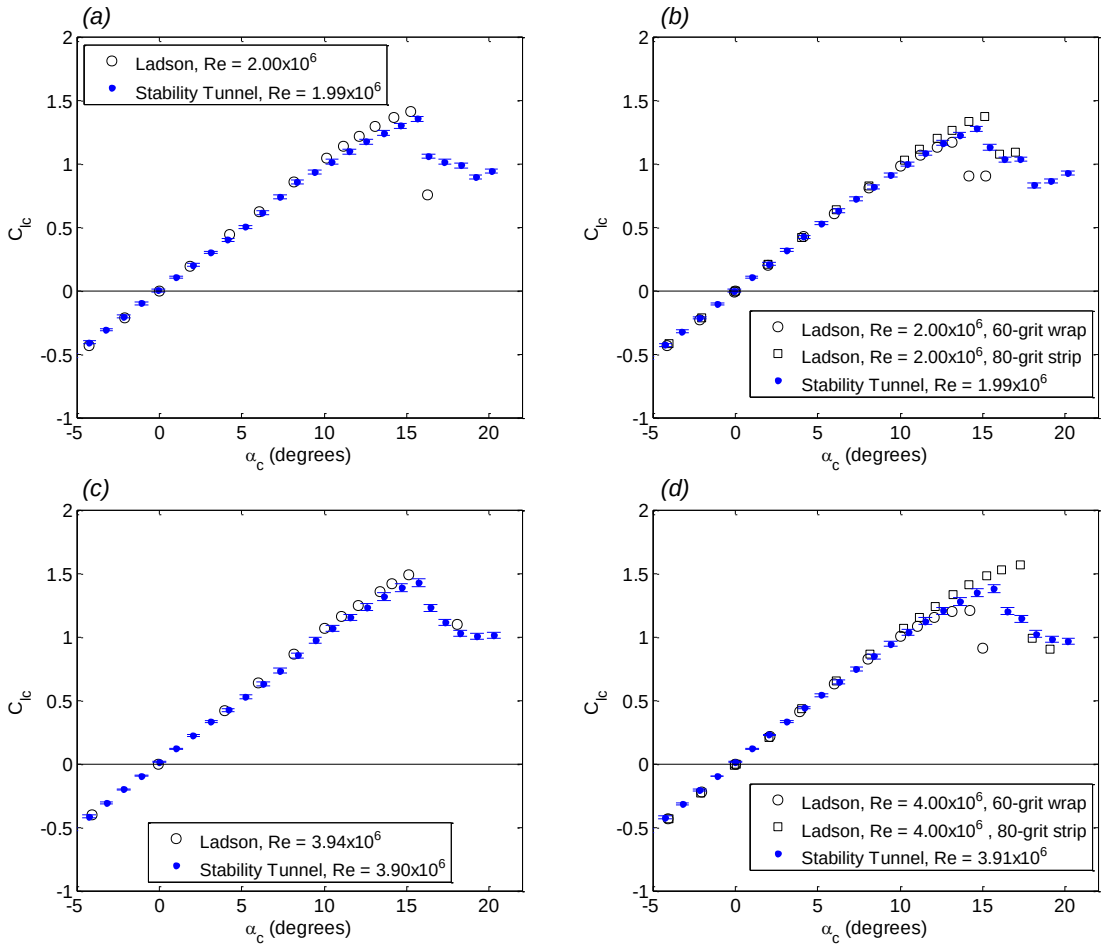

FIGURE 5.4. Comparison of corrected lift coefficient versus corrected angle of attack between the results of Ladson (1988) and the 0.91m NACA 0012 of the Stability Tunnel. Run conditions are *(a)* untripped at nominal Reynolds number of $2x10^6$, *(b)* tripped at nominal Reynolds number of $2x10^6$, *(c)* untripped at nominal Reynolds number of $4x10^6$, and *(d)* tripped at nominal Reynolds number of $4x10^6$. Uncertainty bars are given for the angle of attack and lift coefficient of the Stability Wind Tunnel data.

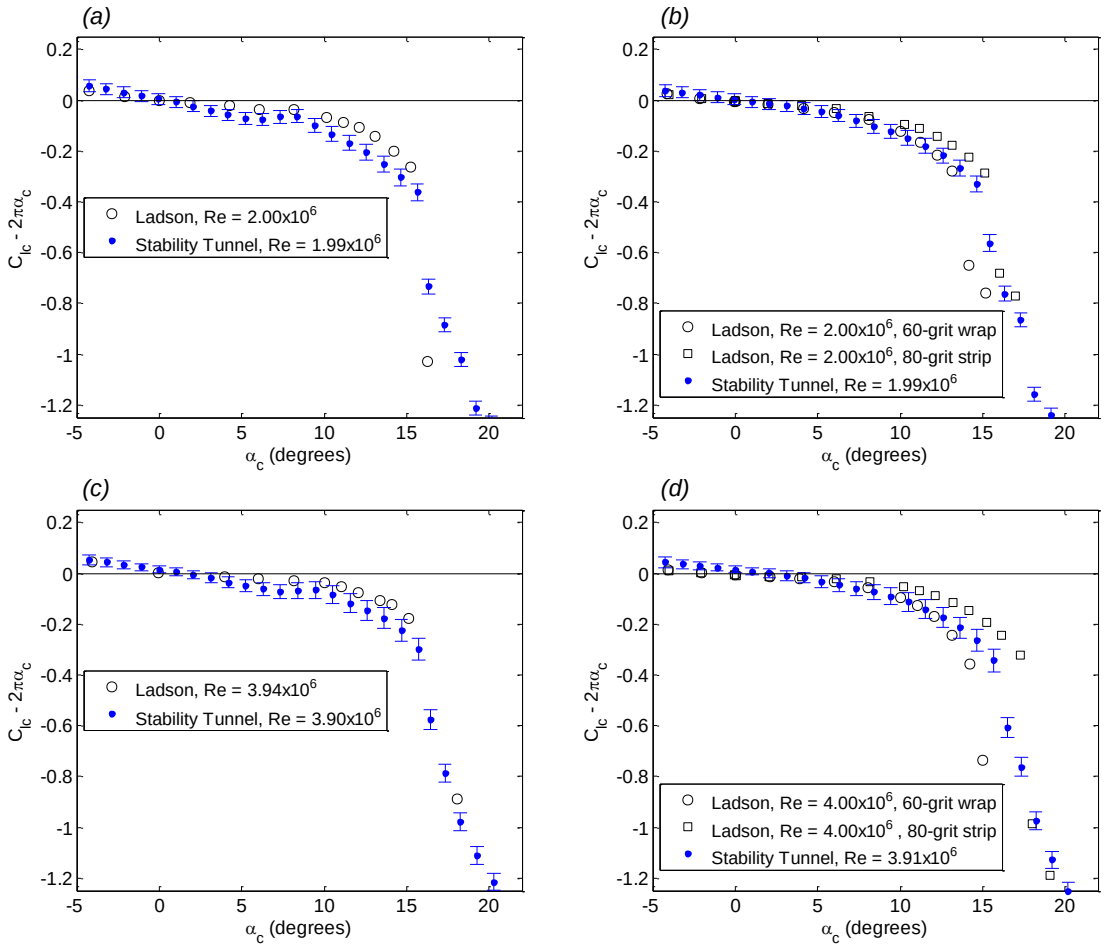

FIGURE 5.5. Comparison of the difference between the corrected lift coefficient and the thin-airfoil theory lift coefficient versus corrected angle of attack between the results of Ladson (1988) and the 0.91m NACA 0012 of the Stability Tunnel. Run conditions are *(a)* untripped at nominal Reynolds number of $2x10^6$, *(b)* tripped at nominal Reynolds number of $2x10^6$, *(c)* untripped at nominal Reynolds number of $4x10^6$, and *(d)* tripped at nominal Reynolds number of $4x10^6$. Uncertainty bars are given for the angle of attack and lift coefficient of the Stability Wind Tunnel data.

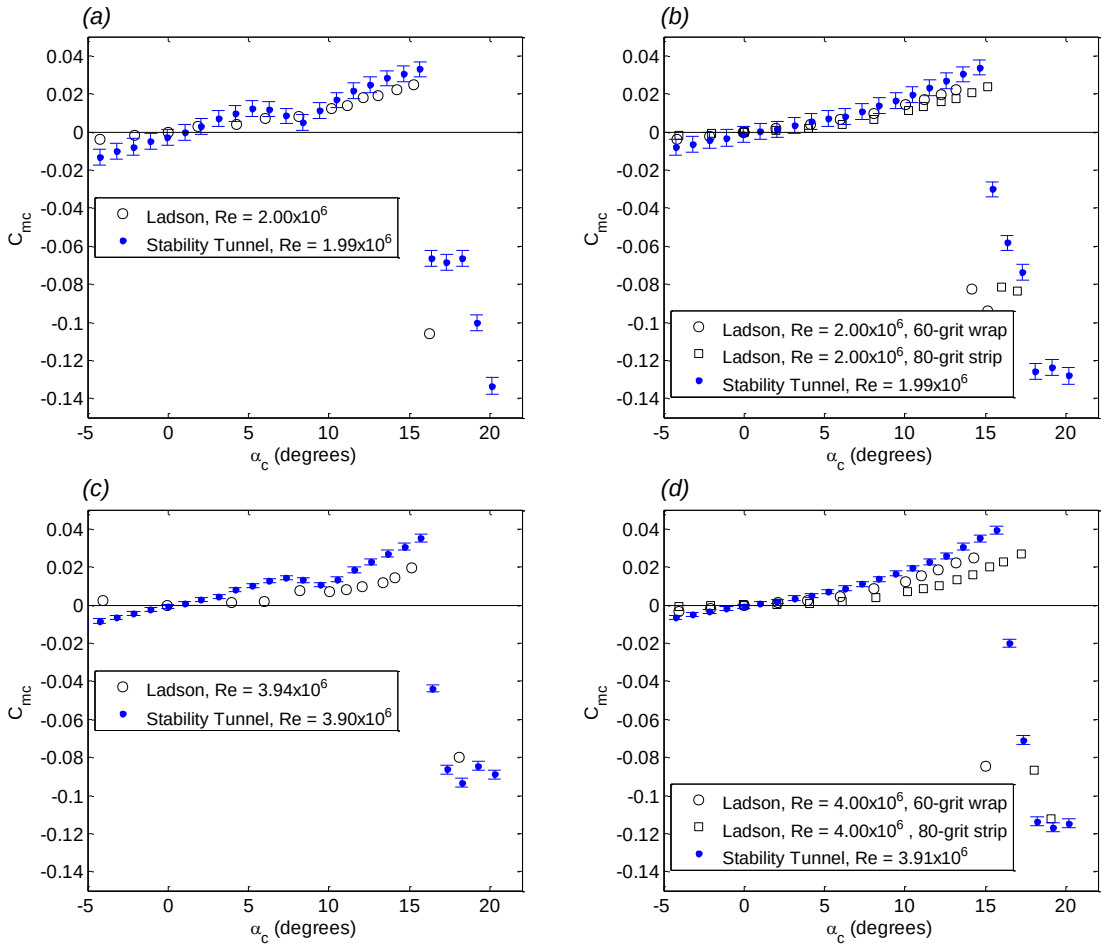

FIGURE 5.6. Comparison of corrected moment coefficient versus corrected angle of attack between the results of Ladson (1988) and the 0.91m NACA 0012 of the Stability Tunnel. Run conditions are *(a)* untripped at nominal Reynolds number of $2x10^6$, *(b)* tripped at nominal Reynolds number of $2x10^6$, *(c)* untripped at nominal Reynolds number of $4x10^6$, and *(d)* tripped at nominal Reynolds number of $4x10^6$. Uncertainty bars are given for the angle of attack and lift coefficient of the Stability Wind Tunnel data.

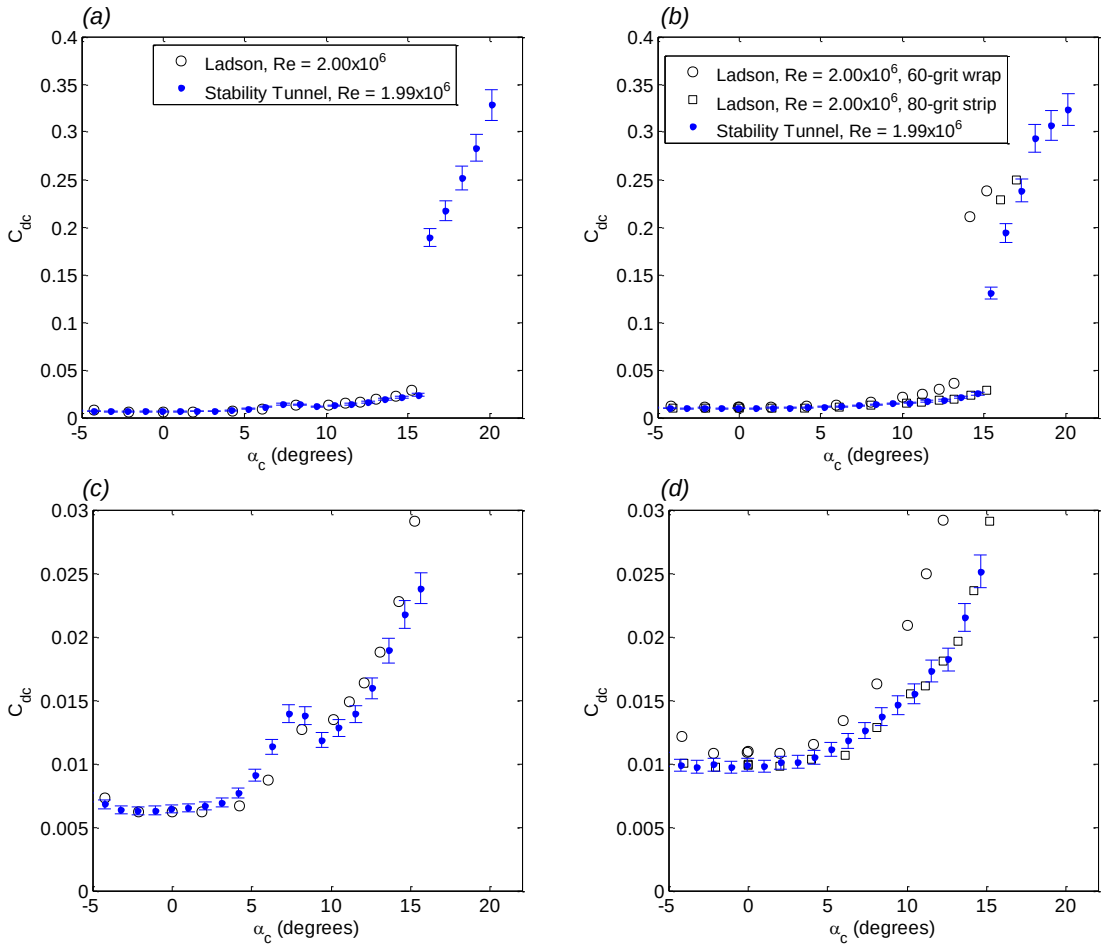

FIGURE 5.7. Comparison of corrected drag coefficient versus corrected angle of attack between the results of Ladson (1988) and the 0.91m NACA 0012 of the Stability Tunnel. No drag data is available from the Stability Tunnel at nominal Reynolds number of $4x10^6$, however, the drag bucket of the lower Reynolds number data are presented here. Run conditions are *(a)* and *(c)* untripped at nominal Reynolds number of $2x10^6$ and *(b)* and *(d)* tripped at nominal Reynolds number of $2x10^6$. Uncertainty bars are given for the angle of attack and lift coefficient of the Stability Wind Tunnel data.

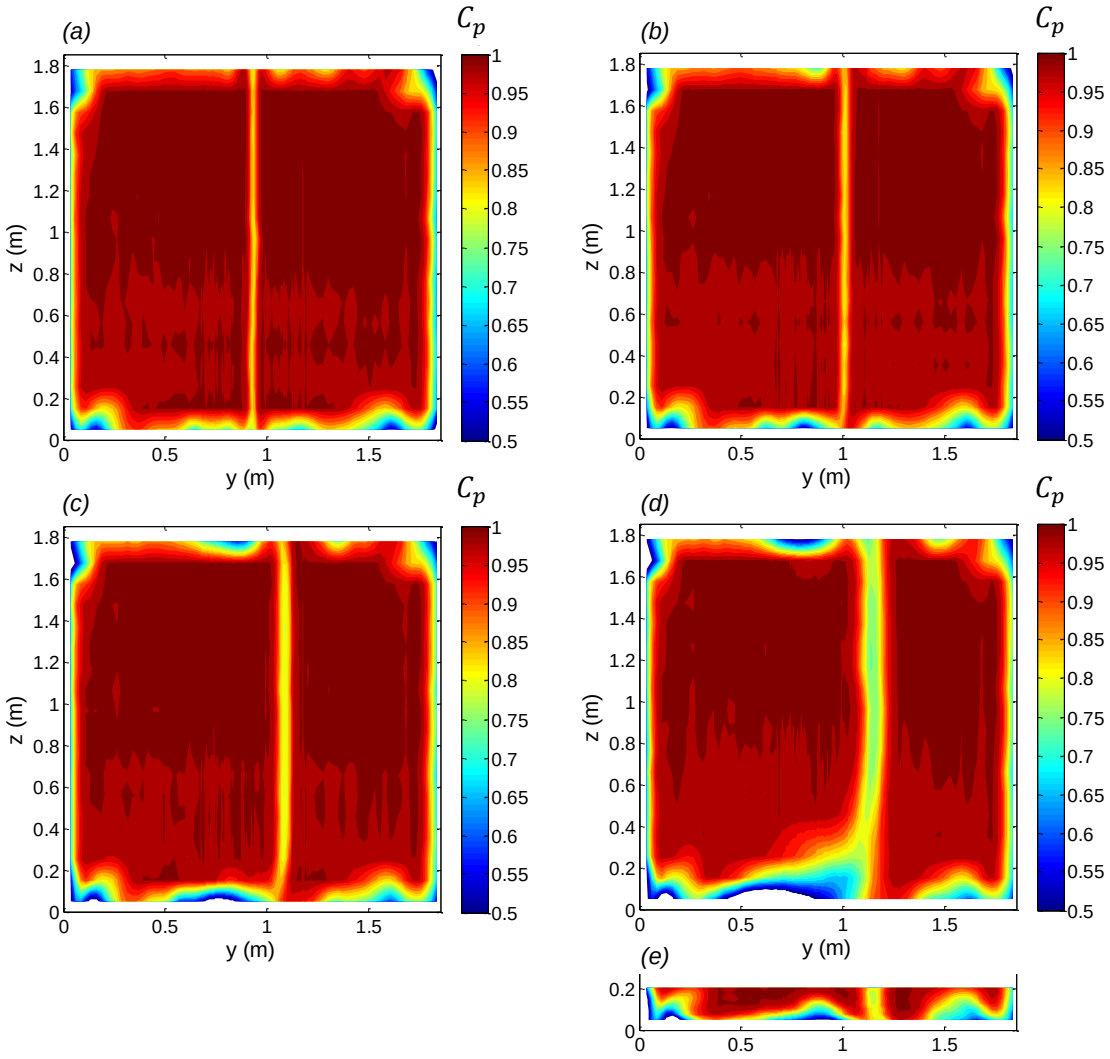

FIGURE 5.8. Wake rake measurements of the stagnation C_P over the tunnel cross-section at the rear of the test section for the 0.91m NACA 0012 airfoil in the untripped condition and at a nominal Reynolds number of $2\text{x}10^6$. Angles of attack are *(a)* 0 degrees, *(b)* 5 degrees, *(c)* 10 degrees, and *(d)* 15 degrees. Subplot *(e)* contains data for $z = 0 - 0.2$ m at the same angle of attack as *(d)* but after retaping of the airfoil-floor junction. The white border around the plot indicates area of the test section outside of the measurement range of the wake rake.

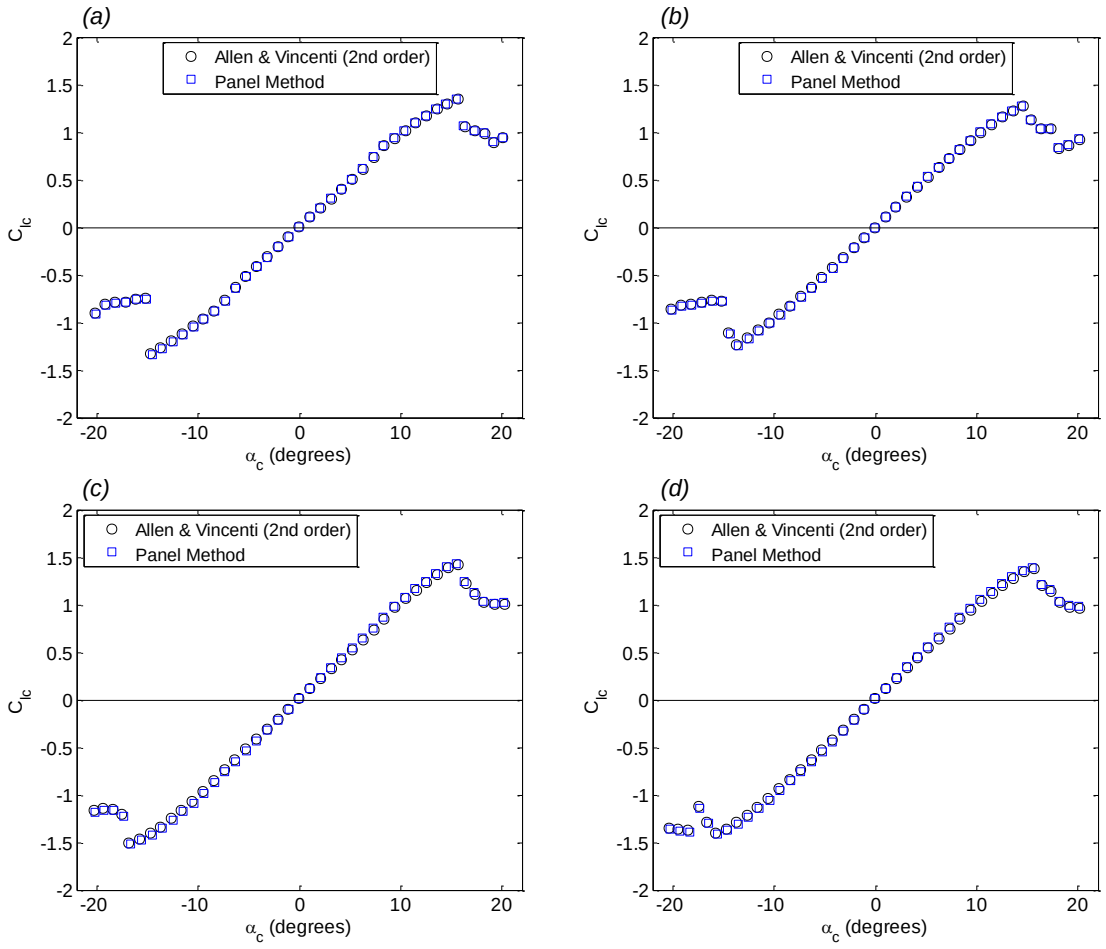

FIGURE 5.9. Comparison of correction methods as applied to data of the 0.91m NACA 0012 in the Stability Tunnel. Run conditions are *(a)* untripped at nominal Reynolds number of $2x10^6$, *(b)* tripped at nominal Reynolds number of $2x10^6$, *(c)* untripped at nominal Reynolds number of $4x10^6$, and *(d)* tripped at nominal Reynolds number of $4x10^6$.

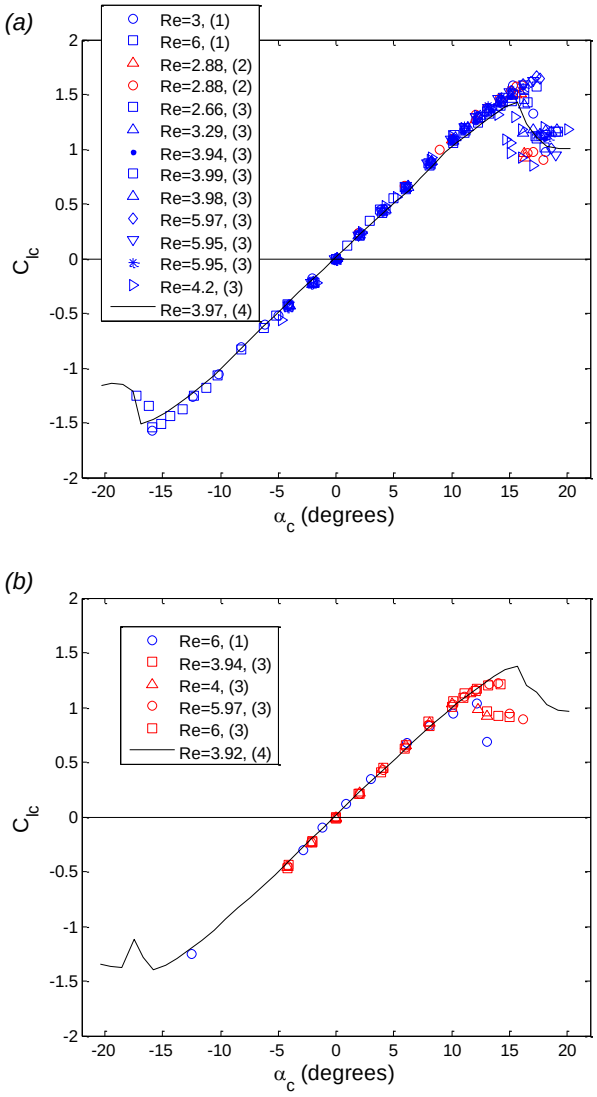

FIGURE 5.10. Review of NACA 0012 airfoil testing ranked first by McCroskey (1987) for experimental integrity including the Stability Tunnel's own 0.91m NACA 0012 data. Untripped data is in *(a)* and tripped data in *(b)*. The numbers in parenthesis indicate the author(s) and location of the study: (1) Abbott and von Doenhoff (1959); Langley Low Turbulence Pressure Tunnel (LTPT), (2) Gregory and OReilly (1973); National Physical Laboratory 9 foot by 13 foot (NPL 9x13), (3) Ladson (1988); LTPT, (4) Stability Tunnel.

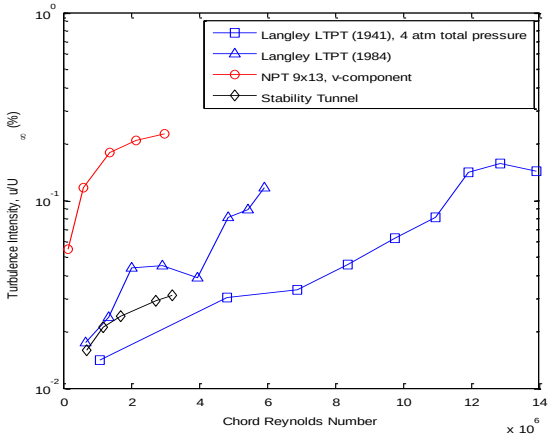

FIGURE 5.11. Comparison of turbulence levels in the facilities of Table 5.1 used to produce the data of Figure 5.10.

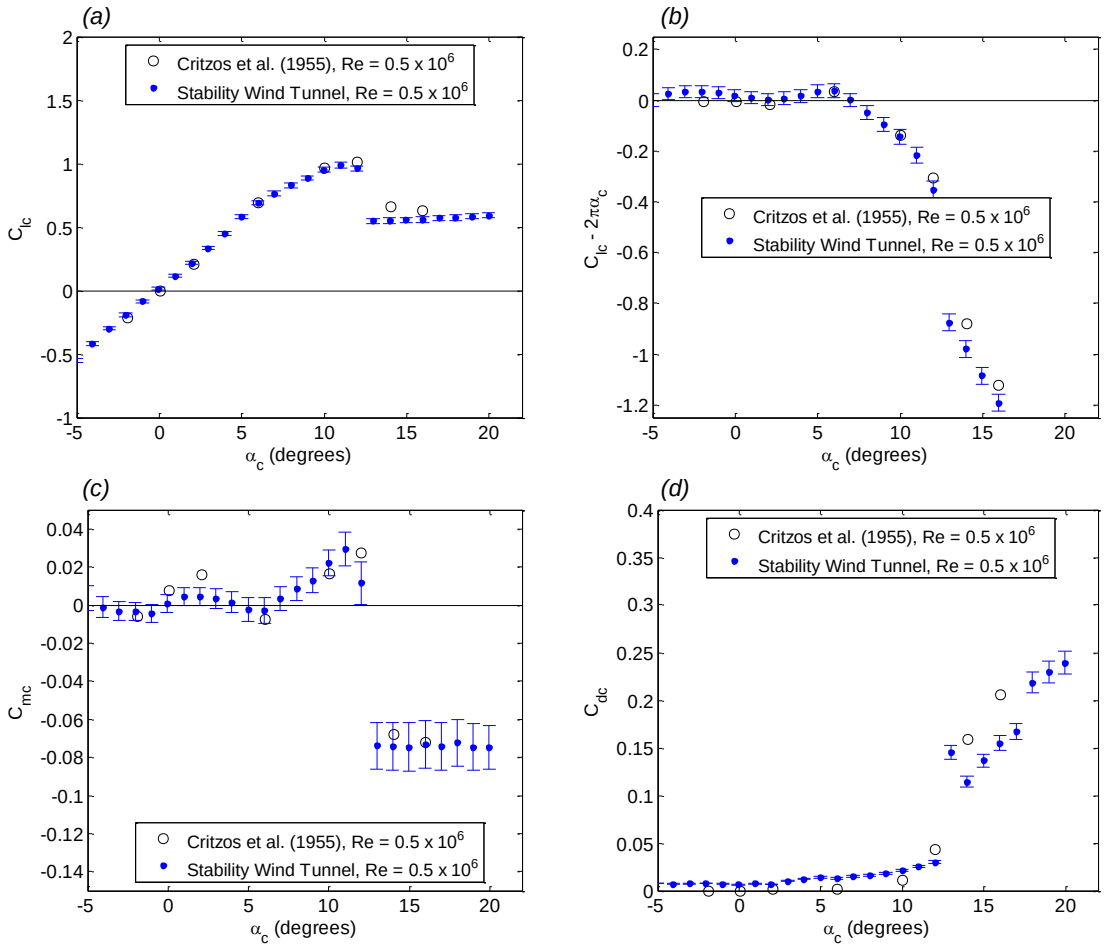

FIGURE 5.12. Comparison between the results of Critzos *et al.* (1955) and the 0.21m NACA 0012 of the Stability Tunnel at Reynolds number of 0.5×10^6 in the untripped condition. *(a)* lift coefficient versus corrected angle of attack, *(b)* difference between the corrected lift coefficient and the thin-airfoil theory lift coefficient versus corrected angle of attack, *(c)* moment coefficient versus corrected angle of attack, *(d)* drag coefficient versus corrected angle of attack. The drag data of Critzos *et al*. was compromised by poor resolution of the source figure.

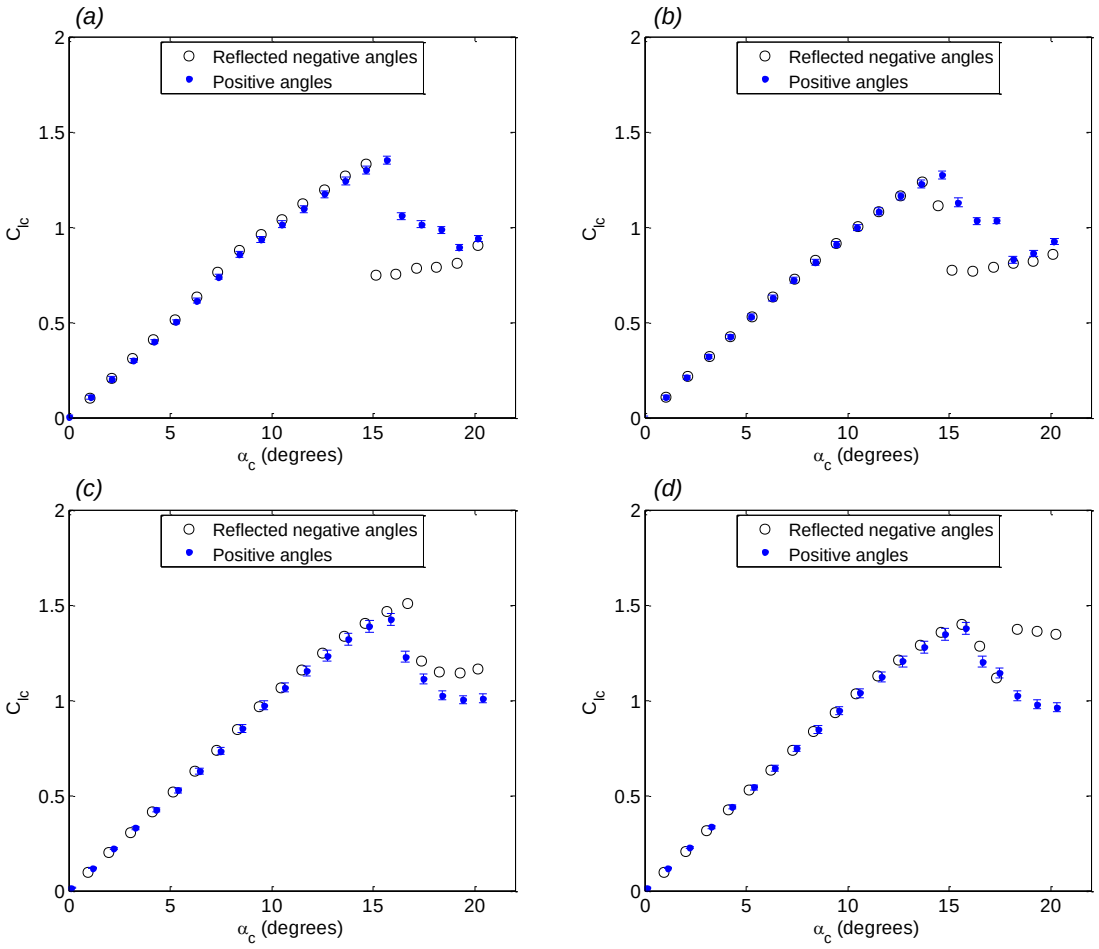

FIGURE 5.13. Angle of attack symmetry of the corrected lift coefficient versus corrected angle of attack for the 0.91m NACA 0012 in the hard-wall test section of the Stability Tunnel. Run conditions are *(a)* untripped at nominal Reynolds number of $2x10^6$, *(b)* tripped at nominal Reynolds number of $2x10^6$, *(c)* untripped at nominal Reynolds number of $4x10^6$, and *(d)* tripped at nominal Reynolds number of $4x10^6$. Uncertainty bars are given for the angle of attack and lift coefficient of the positive angles' data. Before reflecting the negative angle data, the data are shifted horizontally to have zero-lift at exactly zero degrees as reported in the text.

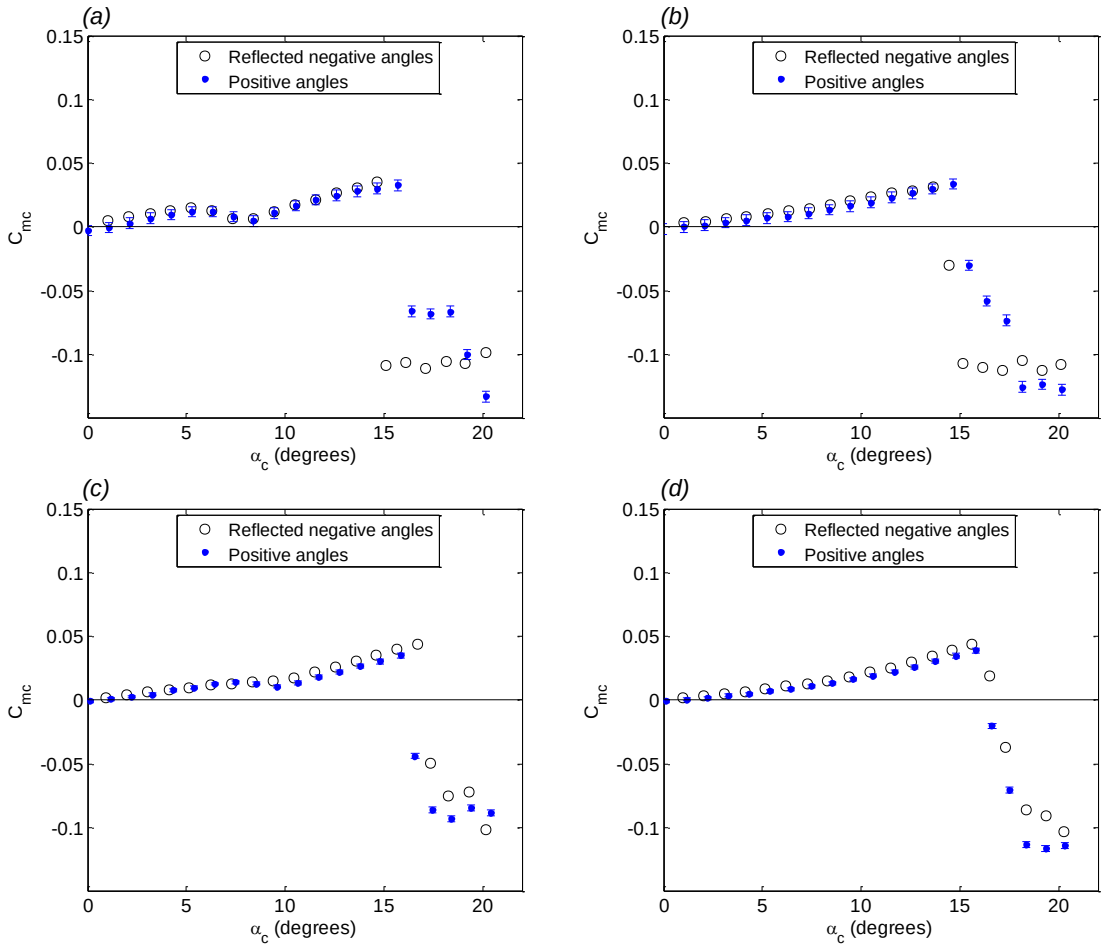

FIGURE 5.14. Angle of attack symmetry of the corrected moment coefficient versus corrected angle of attack for the 0.91m NACA 0012 in the hard-wall test section of the Stability Tunnel. Run conditions are *(a)* untripped at nominal Reynolds number of $2x10^6$, *(b)* tripped at nominal Reynolds number of $2x10^6$, *(c)* untripped at nominal Reynolds number of $4x10^6$, and *(d)* tripped at nominal Reynolds number of $4x10^6$. Uncertainty bars are given for the angle of attack and lift coefficient of the positive angles' data. Before reflecting the negative angle data, the data are shifted horizontally to have zero-lift at exactly zero degrees as reported in the text.

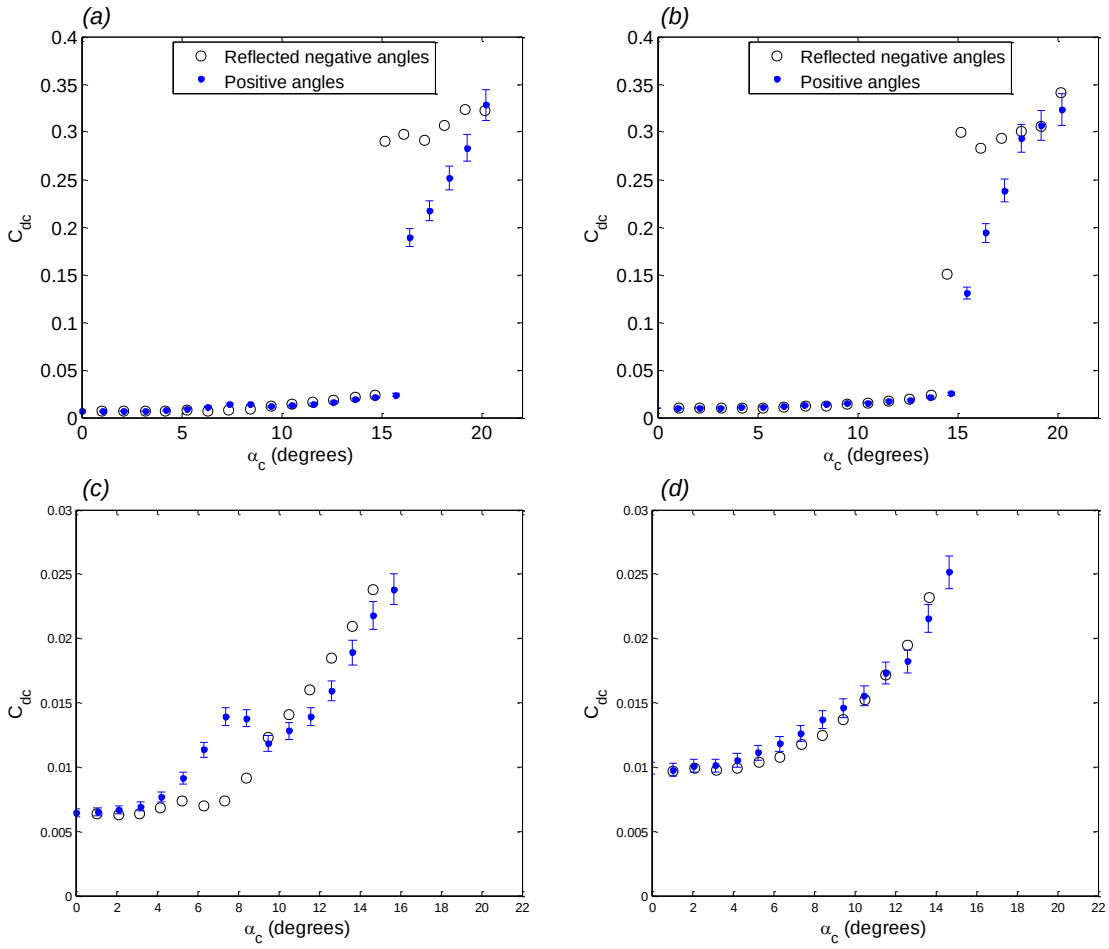

FIGURE 5.15. Angle of attack symmetry of the corrected drag coefficient versus corrected angle of attack for the 0.91m NACA 0012 in the hard-wall test section of the Stability Tunnel. No drag data is available from the Stability Tunnel at nominal Reynolds number of $4x10^6$, however, the drag buckets of the lower Reynolds number data are presented here. Run conditions are *(a)* and *(c)* untripped at nominal Reynolds number of $2x10^6$ and *(b)* and *(d)* tripped at nominal Reynolds number of $2x10^6$. Uncertainty bars are given for the angle of attack and lift coefficient of the positive angles' data. Before reflecting the negative angle data, the data are shifted horizontally to have zero-lift at exactly zero degrees as reported in the text.

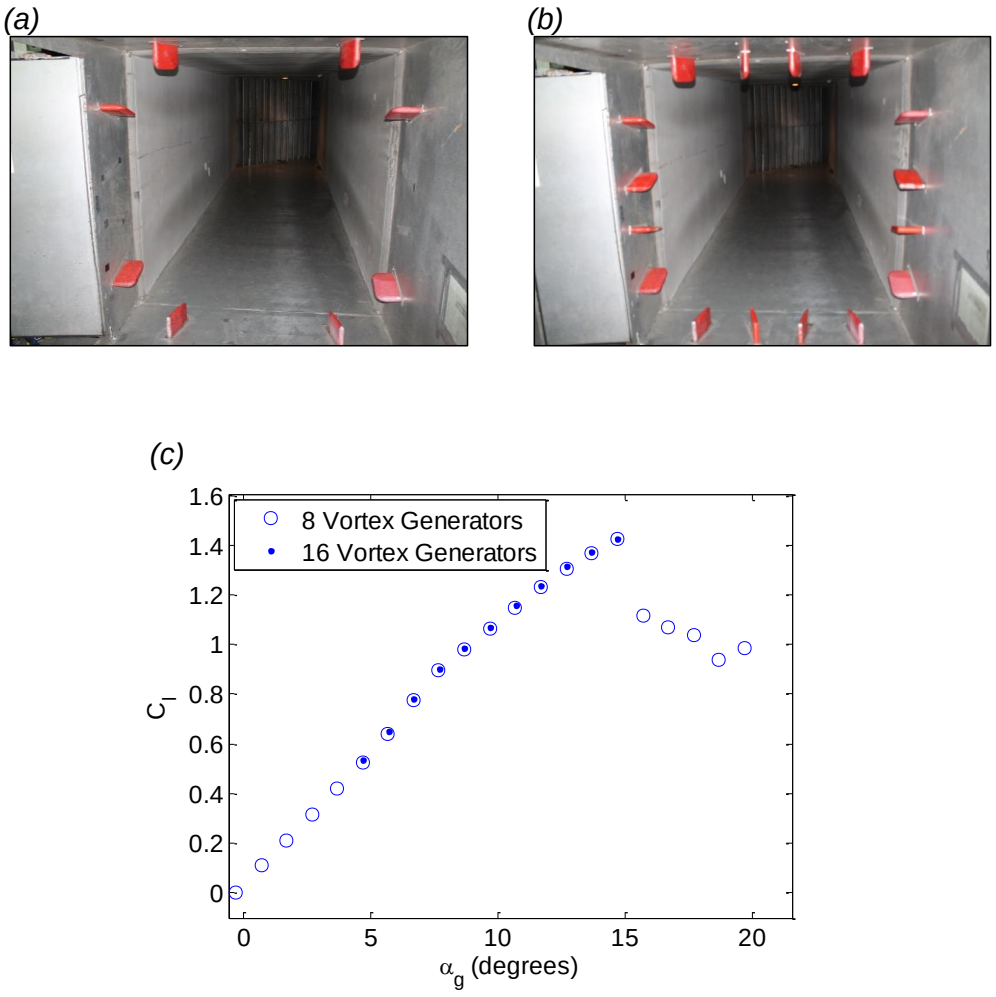

FIGURE 5.16. Downstream-looking view of the diffuser of the Stability Wind Tunnel featuring *(a)* 8 vortex generators and *(b)* 16 vortex generators. *(c)* Comparison of uncorrected corrected lift coefficient versus uncorrected angle of attack for the 0.91m NACA 0012 airfoil with 8 or 16 vortex generators. The run conditions are untripped at a nominal Reynolds number of 2×10^6.

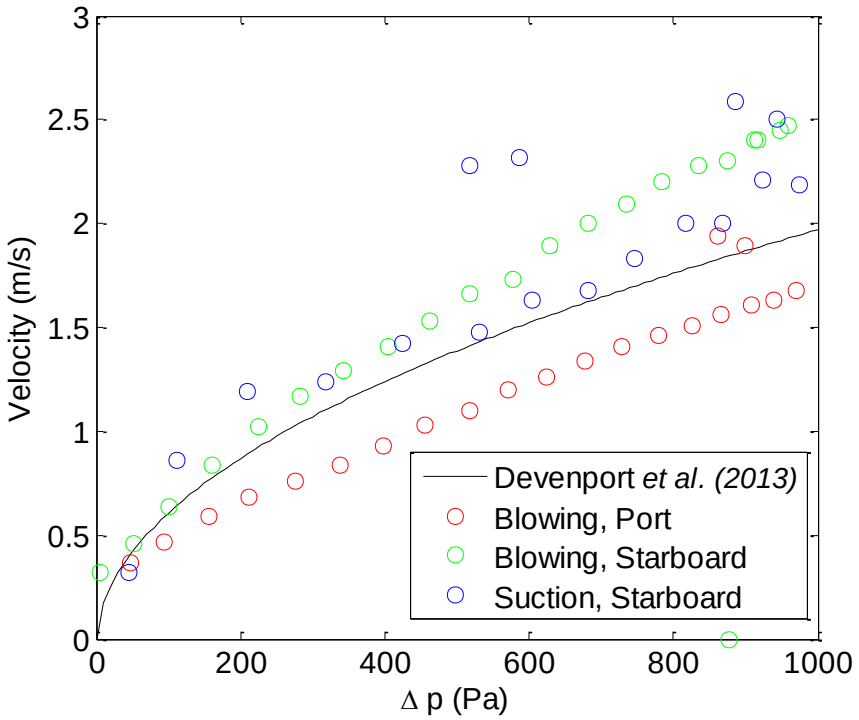

FIGURE 5.17. Pressure-velocity measurements of the present study compared with those of Devenport *et al*. (2013). The present measurements include both blowing (flow into the anechoic chamber) and suction (flow out of the anechoic chamber) from both the port and starboard Kevlar walls.

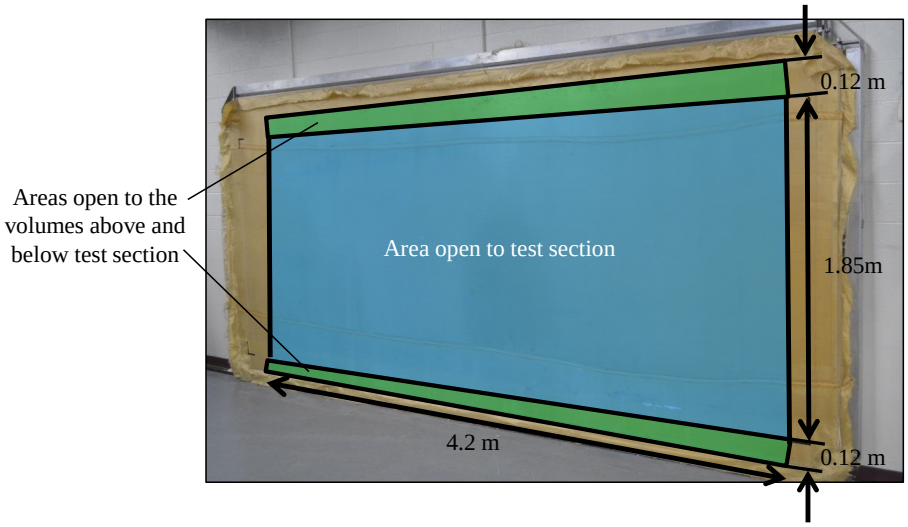

FIGURE 5.18. Uninstalled Kevlar wall showing the approximate size and location of the Kevlar strips above and below the test section ceiling and floor, respectively, that contribute significantly to the leakage area between anechoic chambers.

FIGURE 5.19. Sealing of the port chamber with plastic sheeting. Foil tape was used to seal the edges all the way around the Kevlar including the four corners as detailed above. Two sheets have been joined with foil tape towards the center of the Kevlar wall.

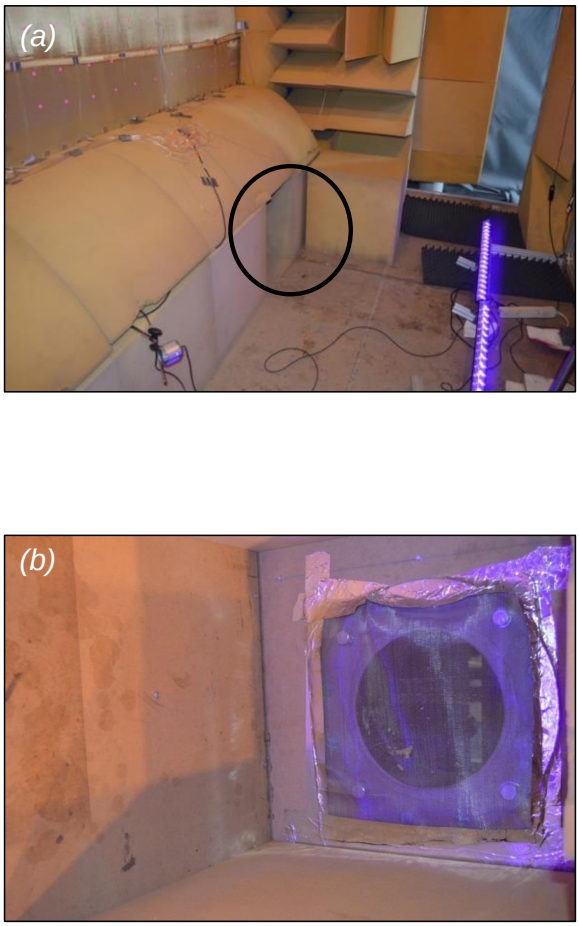

FIGURE 5.20. *(a)* View of the upstream corner of the starboard anechoic chamber a foam block has removed to open the passageway for the suction line. *(b)* Close-up view of suction opening covered by aluminum screen to prevent debris from entering the opening. The opening leads into a corrugated pipe through the flange bolted to the medium density fiberboard construction of the anechoic chamber.

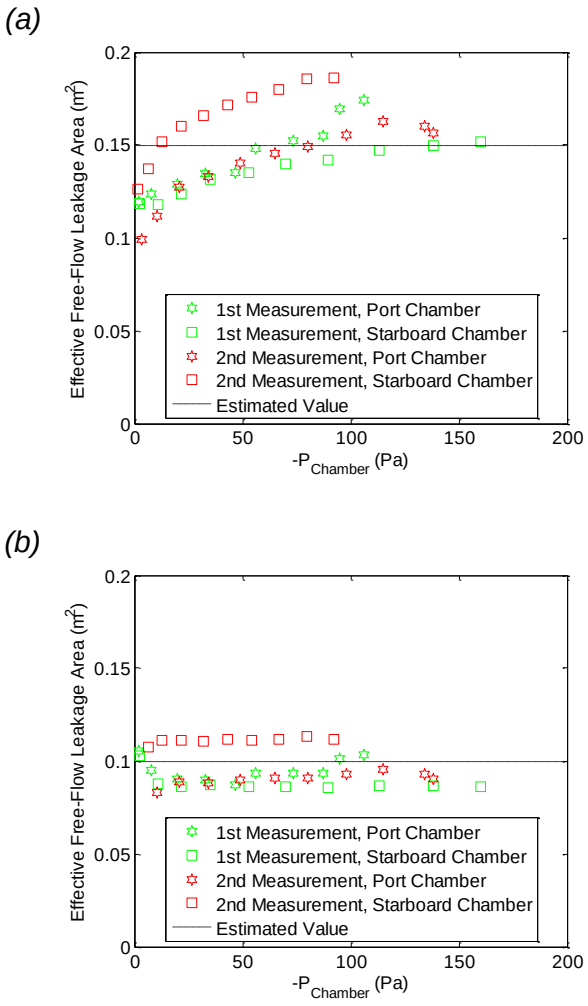

FIGURE 5.21. *(a)* Effective free-flow leakage area versus suction pressure of the anechoic chambers for two calibrations separated by a full tear-down and reinstallation of the Kevlar-wall test section. Data is reduced according to Equation 5.2 with leakage exponents of *(a)* 0.50 and *(b)* 0.60.

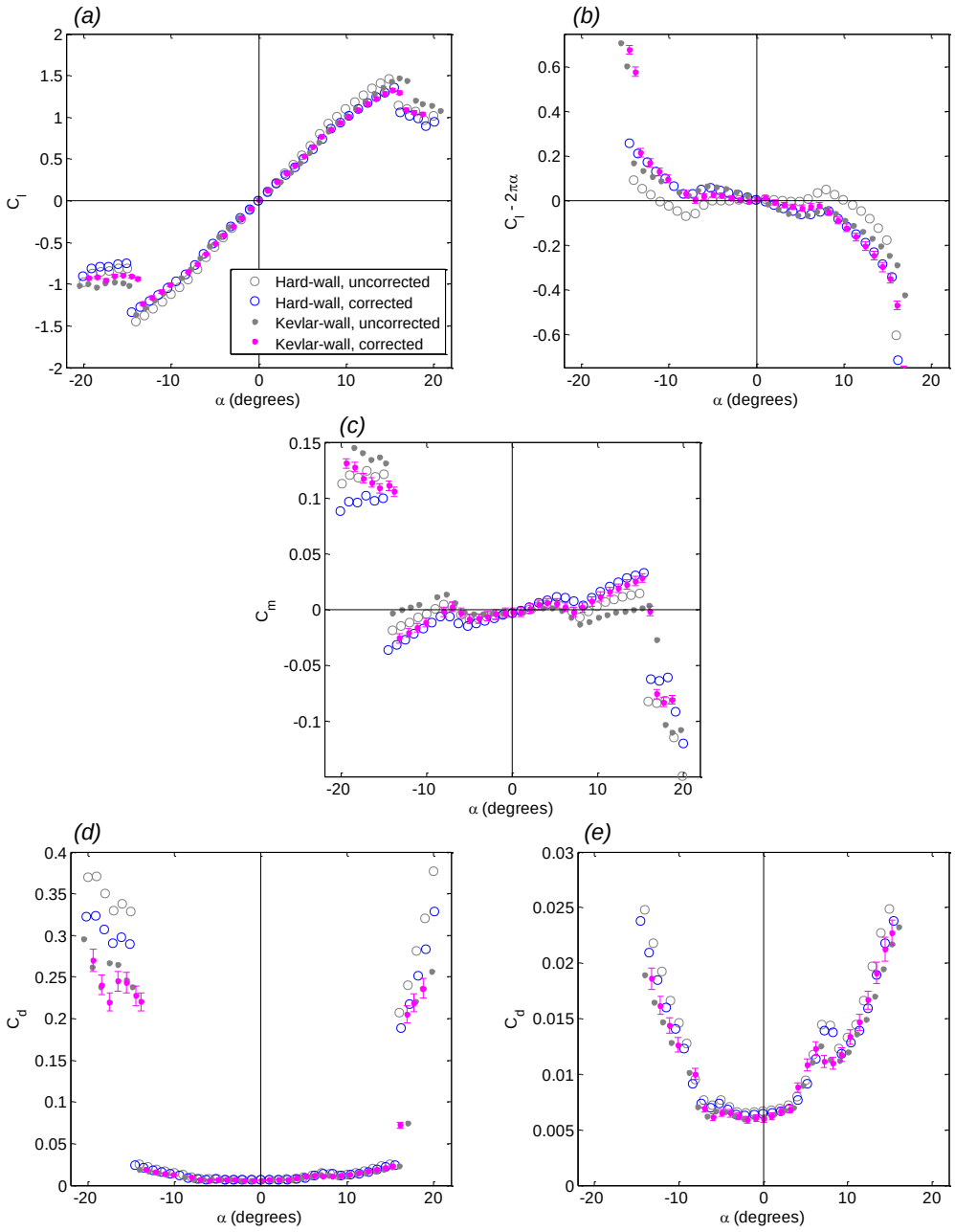

FIGURE 5.22. Comparison of angle of attack sweeps of *(a)* lift coefficient, *(b)* difference between the lift coefficient and the thin-airfoil theory lift coefficient, *(c)* moment coefficient, and *(d)-(e)* drag coefficient between the data from the hard-wall and Kevlar-wall test sections for the 0.91m NACA 0012 of the Stability Tunnel. Run conditions are untripped at nominal Reynolds number of 2×10^6. Uncertainty bars are given for the coefficients from the Kevlar-wall test section with similar sized bars also applying to the hard-wall data.

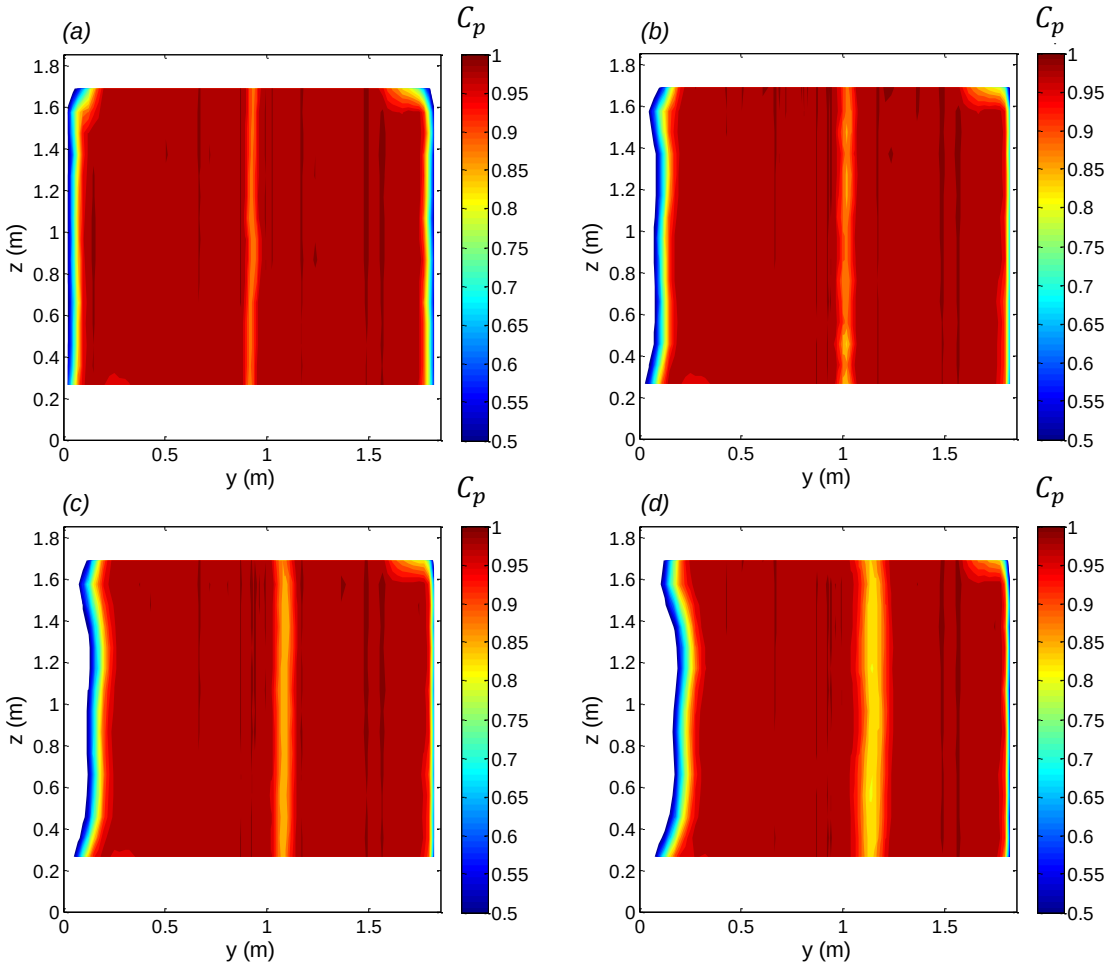

FIGURE 5.23. Wake rake measurements of the stagnation C_P over the tunnel cross-section at the rear of the test section for the 0.91m NACA 0012 airfoil in the untripped condition and at a nominal Reynolds number of 2×10^6. Angles of attack are *(a)* 0 degrees, *(b)* 6 degrees, *(c)* 10 degrees, and *(d)* 15 degrees. The white border around the plot indicates areas of the test section outside of the measurement range of the wake rake.

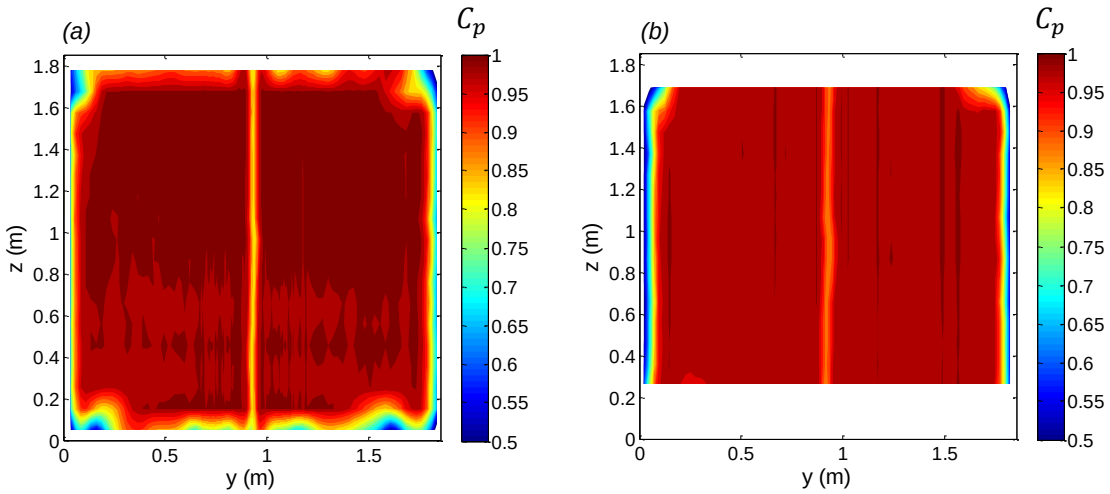

FIGURE 5.24. Wake rake measurements of the stagnation C_P over the tunnel cross-section at the rear of the test section for the 0.91m NACA 0012 airfoil in the untripped condition and at a nominal Reynolds number of $2x10^6$ and at 0 degrees angle of attack. Comparison is made between data from the *(a)* hard-wall test section and *(b)* Kevlar-wall test section, the plots corresponding to subplot (a) of Figures 5.8 and 5.23. The white border around the plot indicates area of the test section outside of the measurement range of the wake rake.

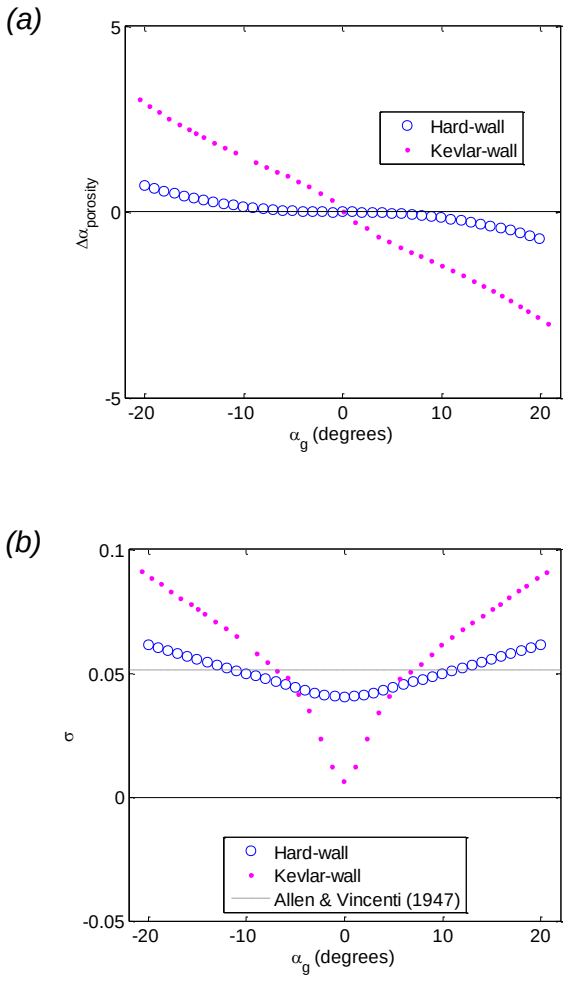

FIGURE 5.25. Comparison of panel method simulation values for *(a)* porosity-induced angle of attack change and *(b)* optimized blockage correction for hard-wall and Kevlar-wall simulation cases. The simulation conditions match those of the 0.91m NACA 0012 at a Reynolds number of 2×10^6. In *(b)*, the classical correction of Allen & Vincenti (1947) is included for reference.

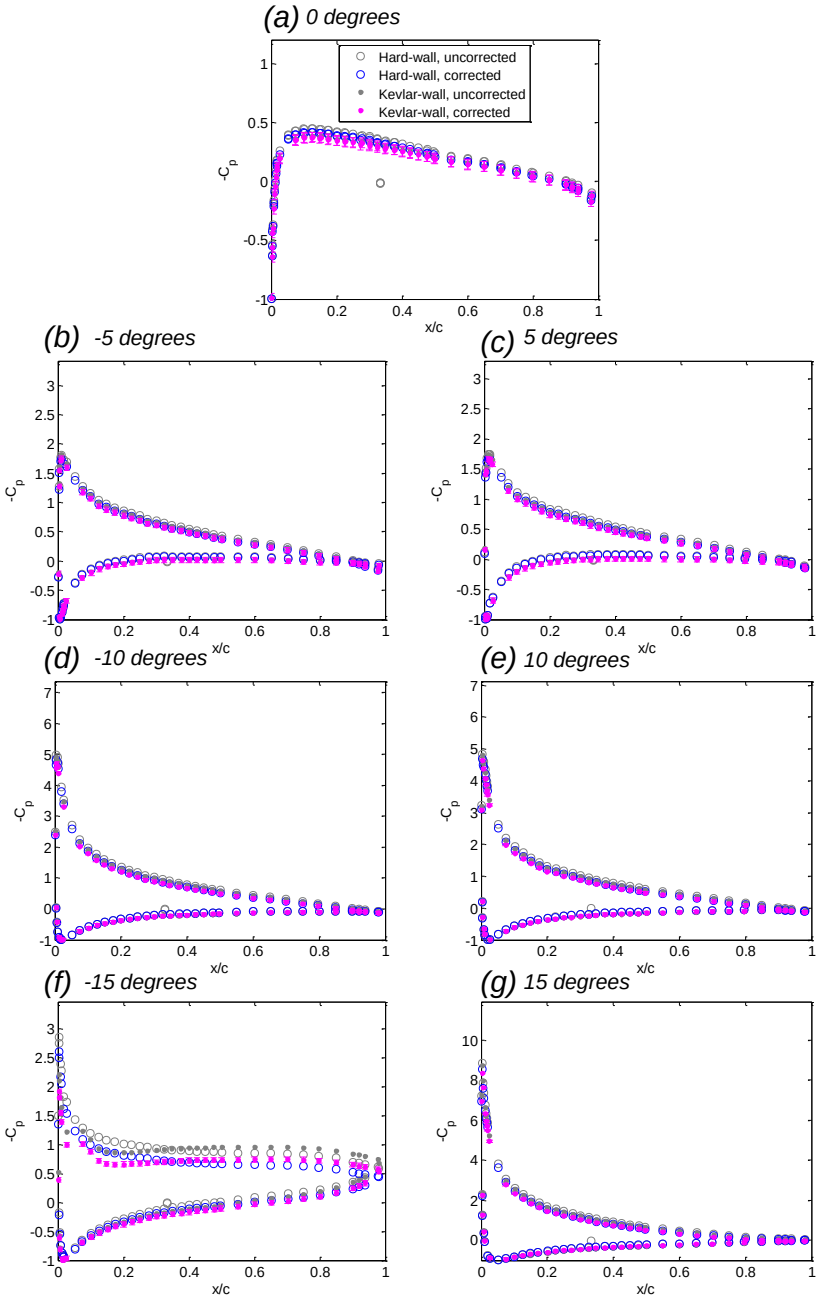

FIGURE 5.26. Comparison of pressure coefficient distributions along the chord at the listed angles of attack between the data from the hard-wall and Kevlar-wall test sections for the 0.91m NACA 0012. Run conditions are untripped at nominal Reynolds number of 2×10^6. Uncertainty bars are given for the coefficients from the Kevlar-wall test section with similar sized bars also applying to the hard-wall data. The pressure data are obtained for the angles of attack listed by linearly interpolating between the nearest two measured angles of attack.

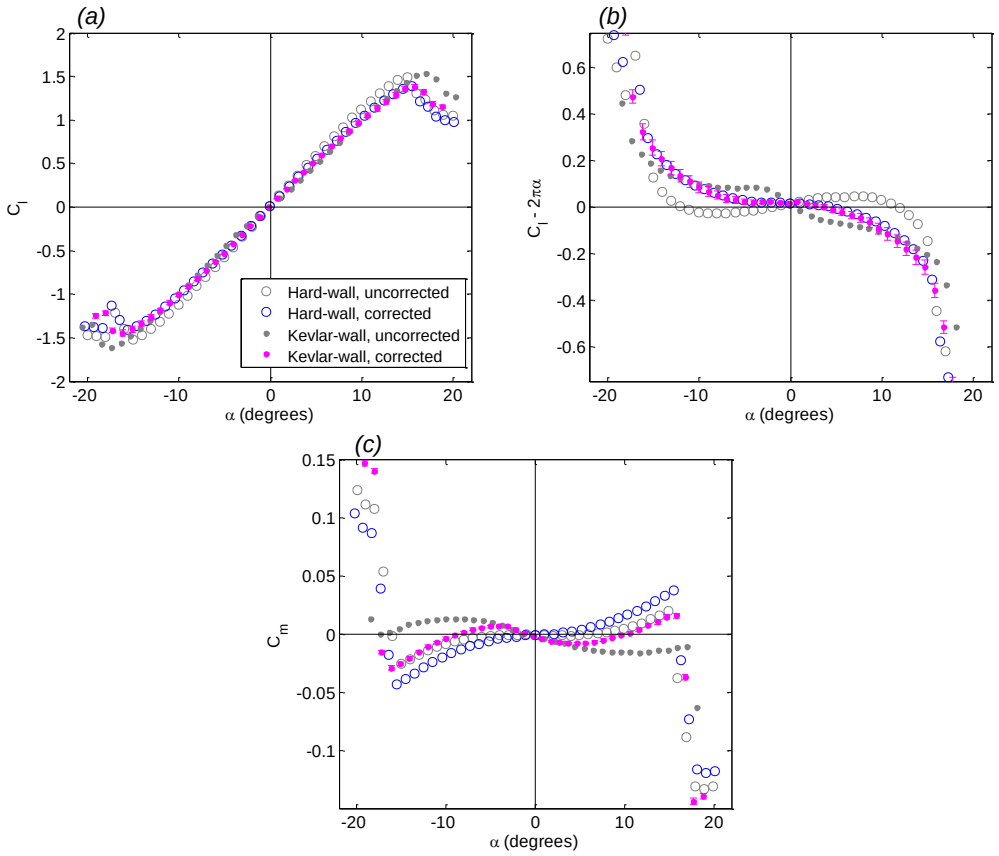

FIGURE 5.27. Comparison of angle of attack sweeps of *(a)* lift coefficient, *(b)* difference between the lift coefficient and the thin-airfoil theory lift coefficient, and *(c)* moment coefficient between the data from the hard-wall and Kevlar-wall test sections for the 0.91m NACA 0012 of the Stability Tunnel. Run conditions are tripped at nominal Reynolds number of 4×10^6. Uncertainty bars are given for the coefficients from the Kevlar-wall test section with similar sized bars also applying to the hard-wall data. No drag data is available for this condition.

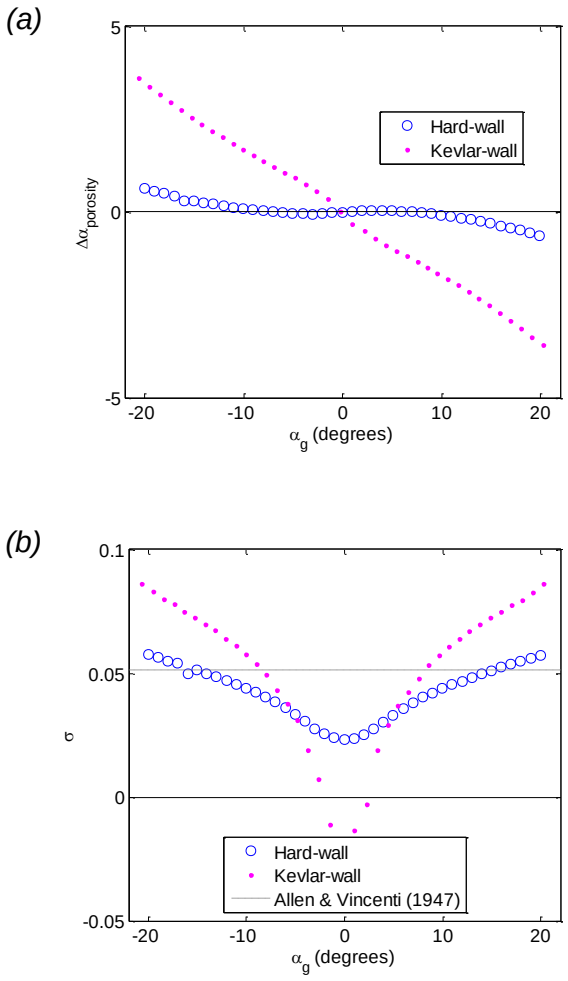

FIGURE 5.28. Comparison of panel method simulation values for *(a)* porosity-induced angle of attack change and *(b)* optimized blockage correction for hard-wall and Kevlar-wall simulation cases. The simulation conditions match those of the 0.91m NACA 0012 at a Reynolds number of $4x10^6$. In *(b)*, the classical correction of Allen & Vincenti (1947) is included for reference.

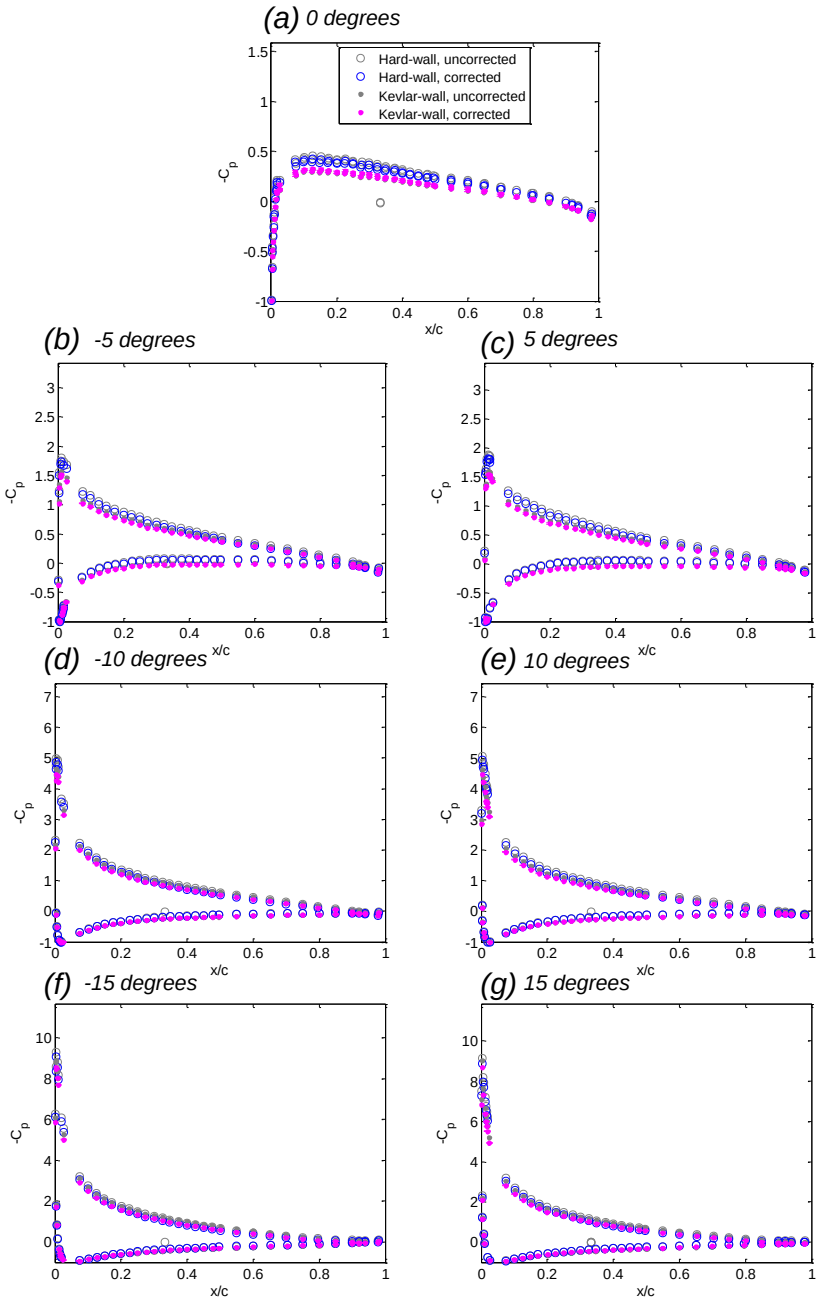

FIGURE 5.29. Comparison of pressure coefficient distributions along the chord at the listed angles of attack between the data from the hard-wall and Kevlar-wall test sections for the 0.91m NACA 0012. Run conditions are tripped at nominal Reynolds number of 4×10^6. Uncertainty bars are given for the coefficients from the Kevlar-wall test section with similar sized bars also applying to the hard-wall data. The pressure data are obtained for the angles of attack listed by linearly interpolating between the nearest two measured angles of attack.

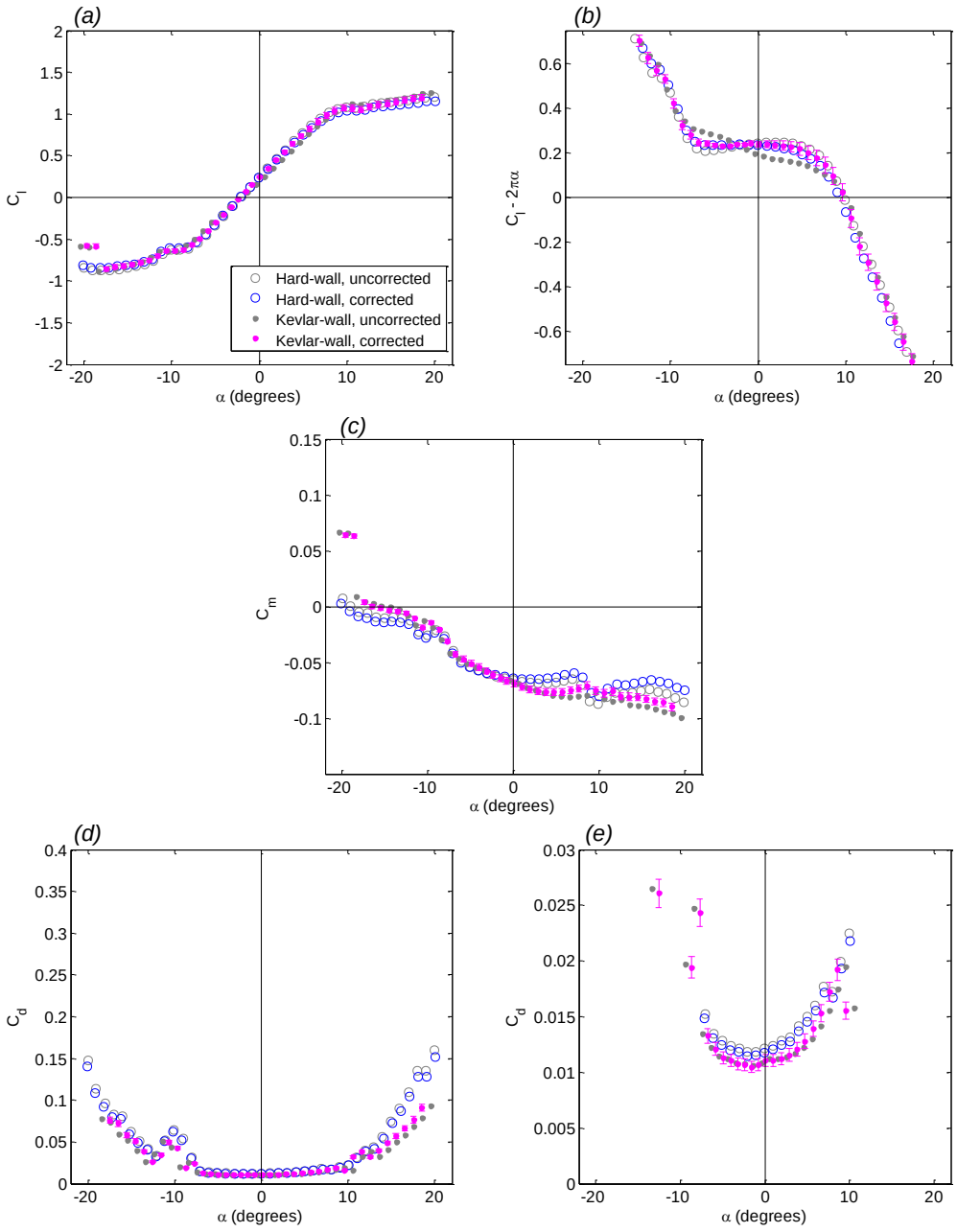

FIGURE 5.30. Comparison of angle of attack sweeps of *(a)* lift coefficient, *(b)* difference between the lift coefficient and the thin-airfoil theory lift coefficient, *(c)* moment coefficient, and *d-(e)* drag coefficient between the data from the hard-wall and Kevlar-wall test sections for the 0.61m DU00-W-212 of the Stability Tunnel. Run conditions are tripped at nominal Reynolds number of 2.25×10^6. Uncertainty bars are given for the coefficients from the Kevlar-wall test section with similar sized bars also applying to the hard-wall data.

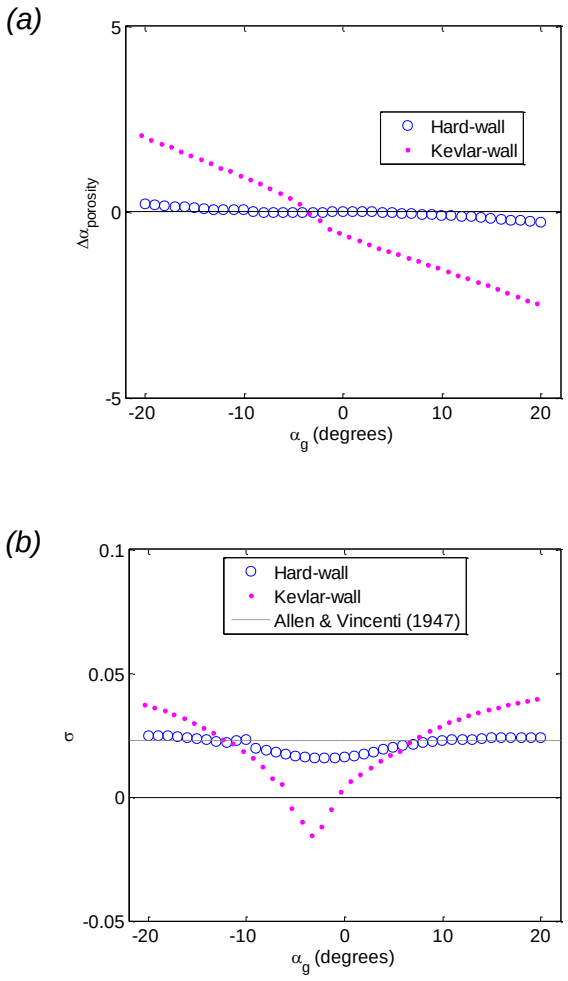

FIGURE 5.31. Comparison of panel method simulation values for *(a)* porosity-induced angle of attack change and *(b)* optimized blockage correction for hard-wall and Kevlar-wall simulation cases. The simulation conditions match those of the 0.61m DU00-W-212 at a Reynolds number of 2.25×10^6. In *(b)*, the classical correction of Allen & Vincenti (1947) is included for reference.

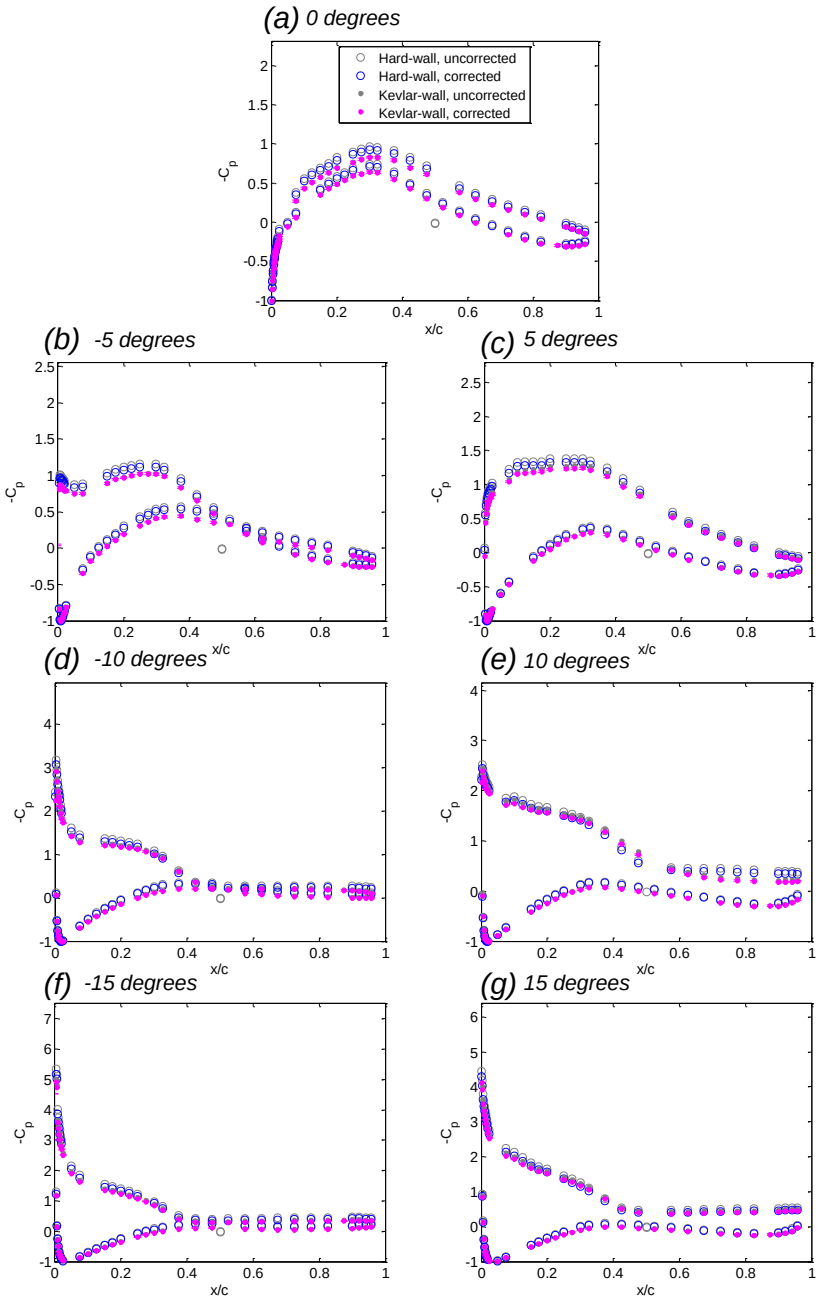

FIGURE 5.32. Comparison of pressure coefficient distributions along the chord at the listed angles of attack between the data from the hard-wall and Kevlar-wall test sections for the 0.61m DU00-W-212. Run conditions are tripped at nominal Reynolds number of 2.25×10^6. Uncertainty bars are given for the coefficients from the Kevlar-wall test section with similar sized bars also applying to the hard-wall data. The pressure data are obtained for the angles of attack listed by linearly interpolating between the nearest two measured angles of attack.

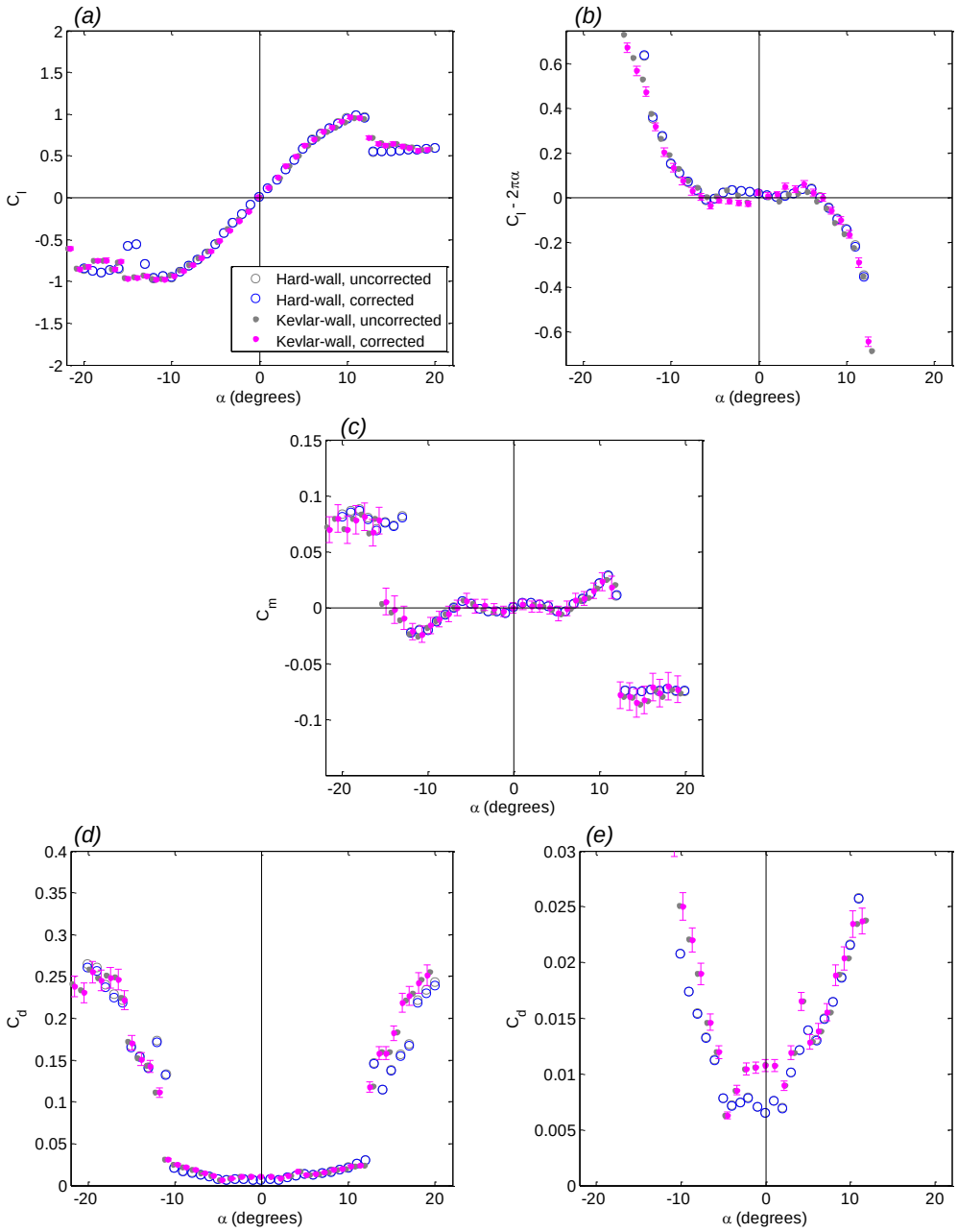

FIGURE 5.33. Comparison of angle of attack sweeps of *(a)* lift coefficient, *(b)* difference between the lift coefficient and the thin-airfoil theory lift coefficient, and *(c)* moment coefficient between the data from the hard-wall and Kevlar-wall test sections for the 0.20m NACA 0012 of the Stability Tunnel. Run conditions are untripped at nominal Reynolds number of 0.5×10^6. Uncertainty bars are given for the coefficients from the Kevlar-wall test section with similar sized bars also applying to the hard-wall data.

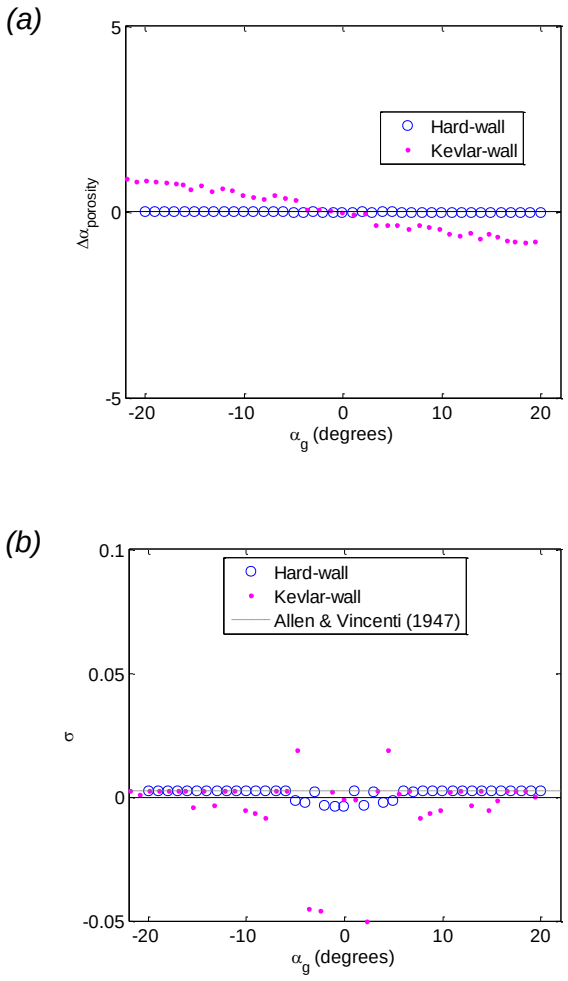

FIGURE 5.34. Comparison of panel method simulation values for *(a)* porosity-induced angle of attack change and *(b)* optimized blockage correction for hard-wall and Kevlar-wall simulation cases. The simulation conditions match those of the 0.61m DU00-W-212 at a Reynolds number of 2.25×10^6. In *(b)*, the classical correction of Allen & Vincenti (1947) is included for reference.

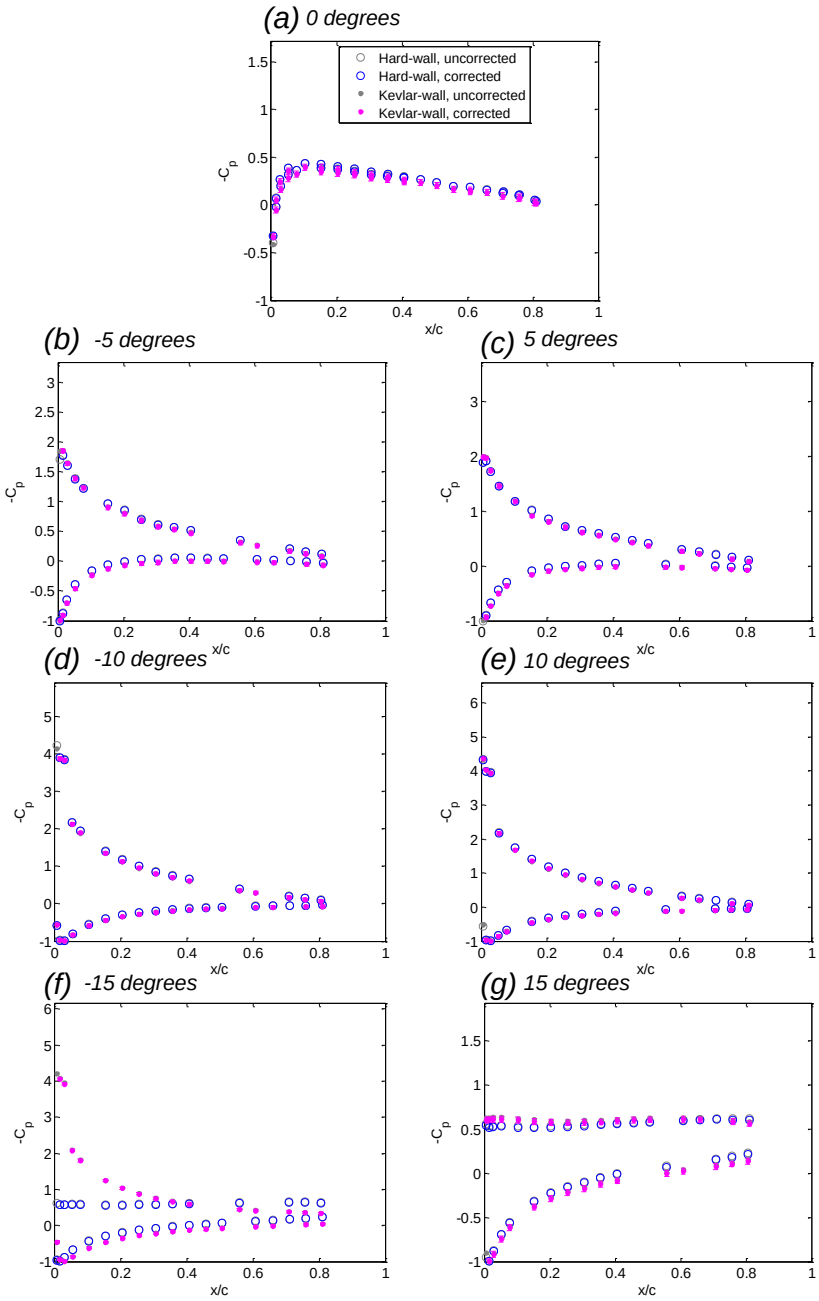

FIGURE 5.35. Comparison of pressure coefficient distributions along the chord at the listed angles of attack between the data from the hard-wall and Kevlar-wall test sections for the 0.20m NACA 0012. Run conditions are untripped at nominal Reynolds number of 0.5×10^6. Uncertainty bars are given for the coefficients from the Kevlar-wall test section with similar sized bars also applying to the hard-wall data. The pressure data are obtained for the angles of attack listed by linearly interpolating between the nearest two measured angles of attack.

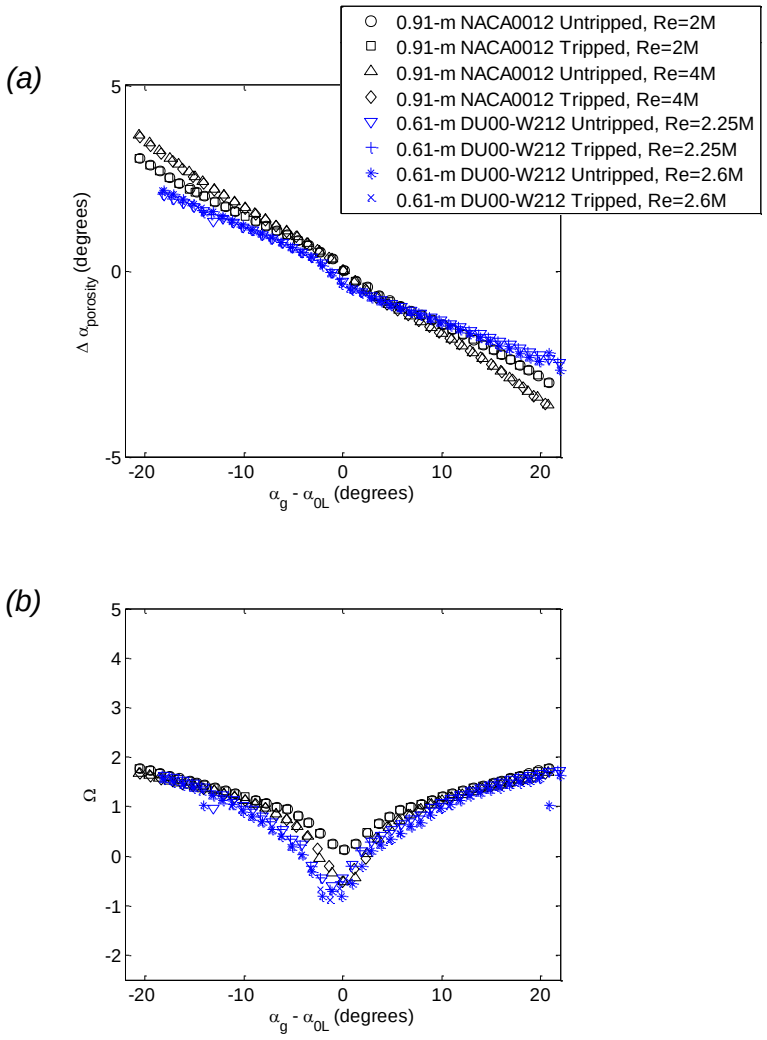

FIGURE 5.36. Comparison of panel method simulation values for *(a)* porosity-induced angle of attack change and *(b)* optimized blockage correction normalized on the classical prediction of Allen & Vincenti (1947) for hard-wall and Kevlar-wall simulation cases. Data include all cases of Table 5.1 except for the 0.20 m NACA 0012 case.

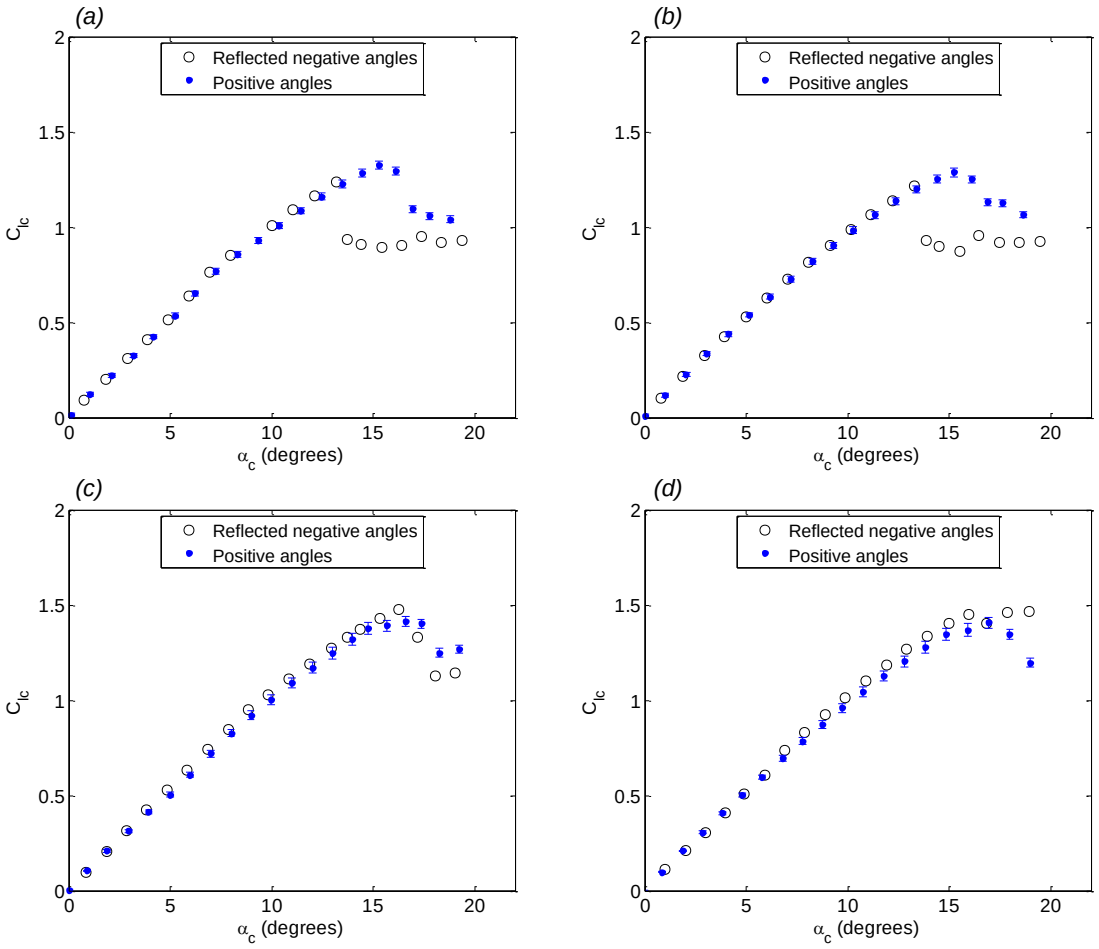

FIGURE 5.37. Angle of attack symmetry of the corrected lift coefficient versus corrected angle of attack for the 0.91m NACA 0012 in the Kevlar-wall test section. Run conditions are *(a)* untripped at a Reynolds number of 2.01×10^6, *(b)* tripped at a Reynolds number of 2.00×10^6, *(c)* untripped at nominal Reynolds number of 3.92×10^6, and *(d)* tripped at nominal Reynolds number of 3.92×10^6. Uncertainty bars are given for the angle of attack and lift coefficient of the positive angles' data. Before reflecting the negative angle data, the data are shifted horizontally to have zero-lift at exactly zero degrees as reported in the text.

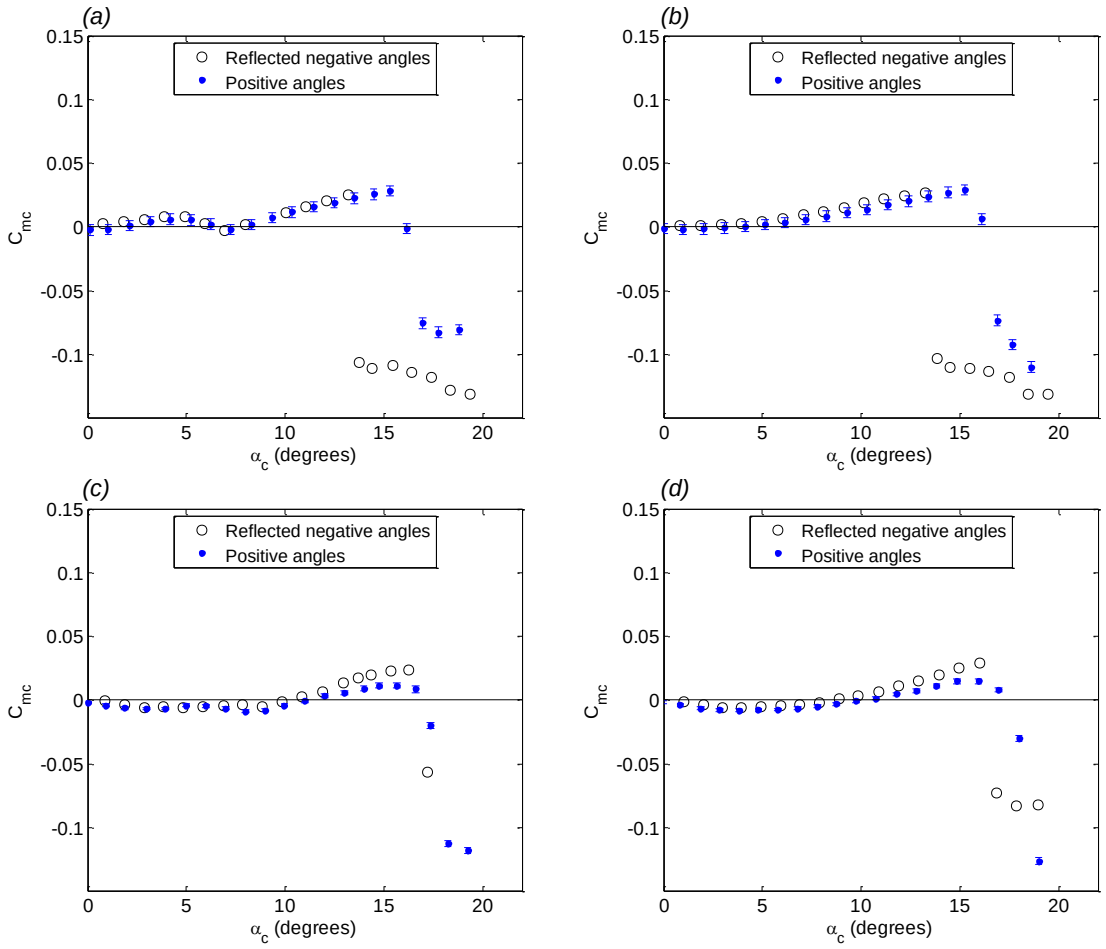

FIGURE 5.38. Angle of attack symmetry of the corrected moment coefficient versus corrected angle of attack for the 0.91m NACA 0012 in the Kevlar-wall test section. Run conditions are *(a)* untripped at a Reynolds number of 2.01×10^6, *(b)* tripped at a Reynolds number of 2.0×10^6, *(c)* untripped at nominal Reynolds number of 3.92×10^6, and *(d)* tripped at nominal Reynolds number of 3.92×10^6. Uncertainty bars are given for the angle of attack and lift coefficient of the positive angles' data. Before reflecting the negative angle data, the data are shifted horizontally to have zero-lift at exactly zero degrees as reported in the text.

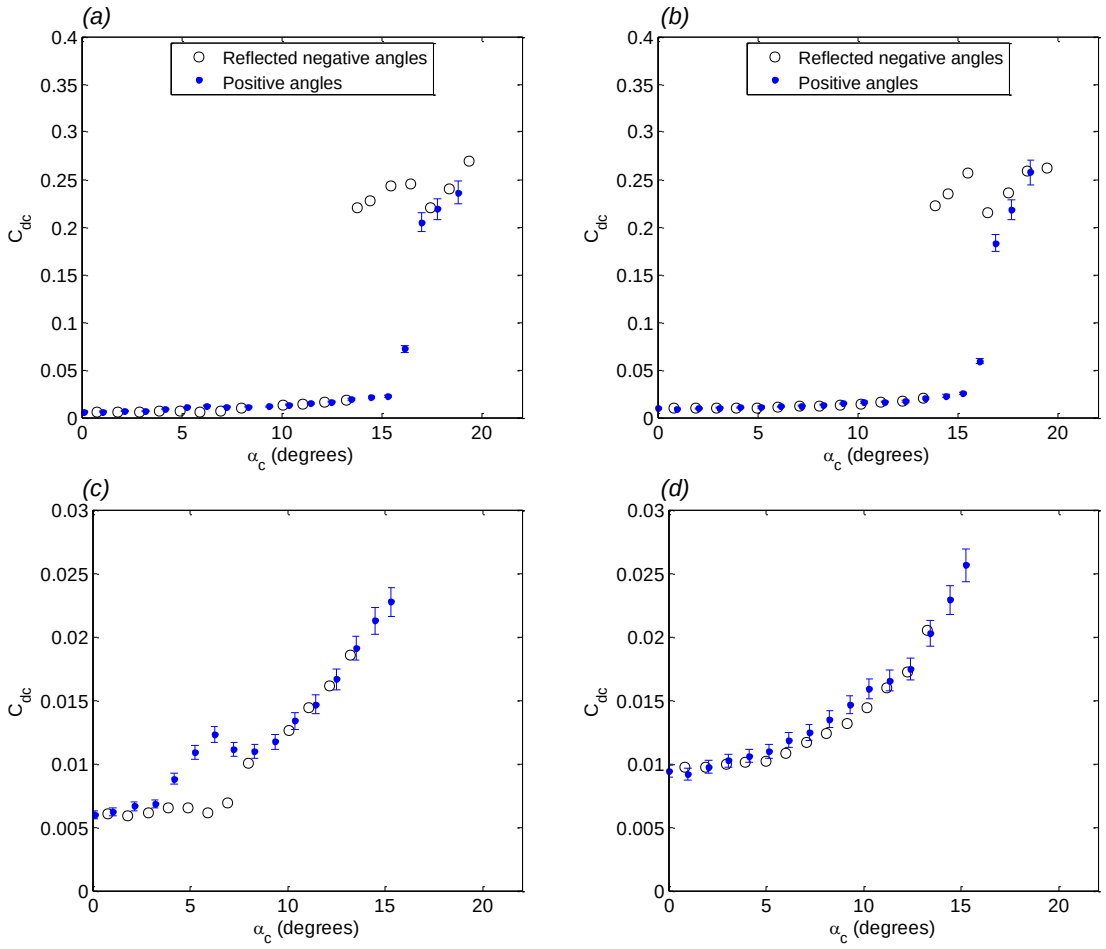

FIGURE 5.39. Angle of attack symmetry of the corrected drag coefficient versus corrected angle of attack for the 0.91m NACA 0012 in the Kevlar-wall test section. No drag data is available from the Stability Tunnel at nominal Reynolds number of $4x10^6$, however, the drag buckets of the lower Reynolds number data are presented here. Run conditions are *(a)* and *(c)* untripped at a Reynolds number of $2.01x10^6$ and *(b)* and *(d)* tripped at a Reynolds number of $2.00x10^6$. Uncertainty bars are given for the angle of attack and lift coefficient of the positive angles' data. Before reflecting the negative angle data, the data are shifted horizontally to have zero-lift at exactly zero degrees as reported in the text.

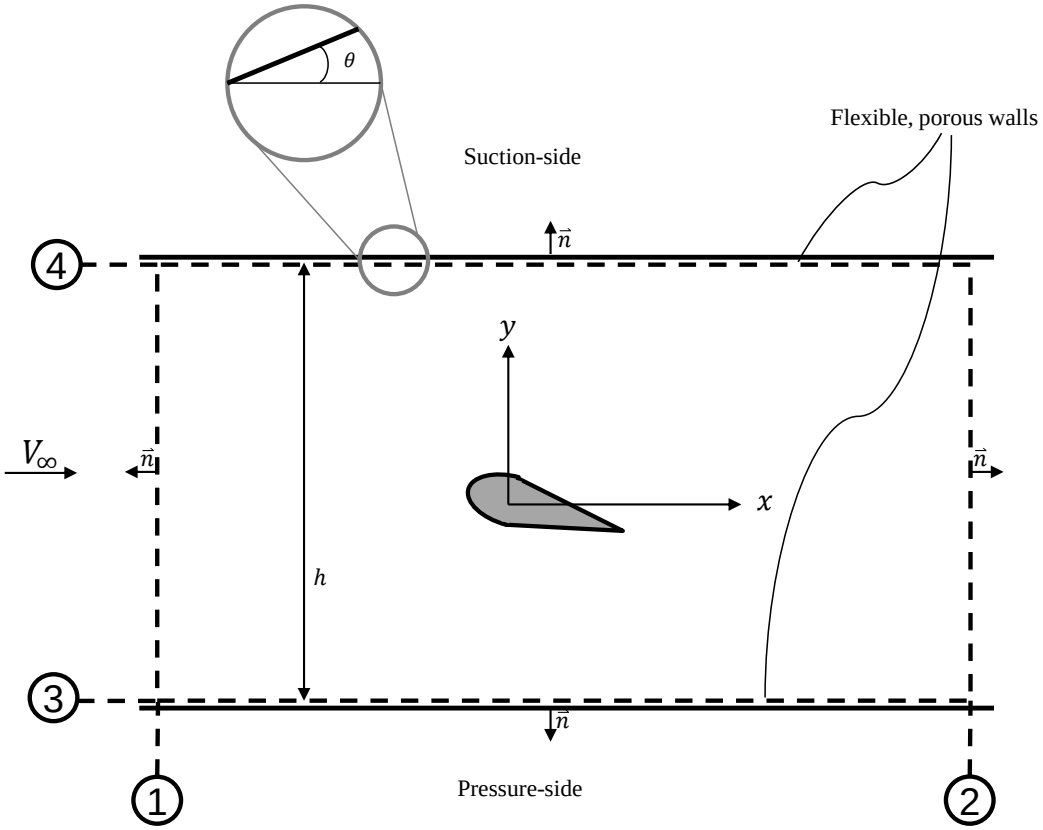

FIGURE 5.40. Two-dimensional control volume of a wind tunnel test section.

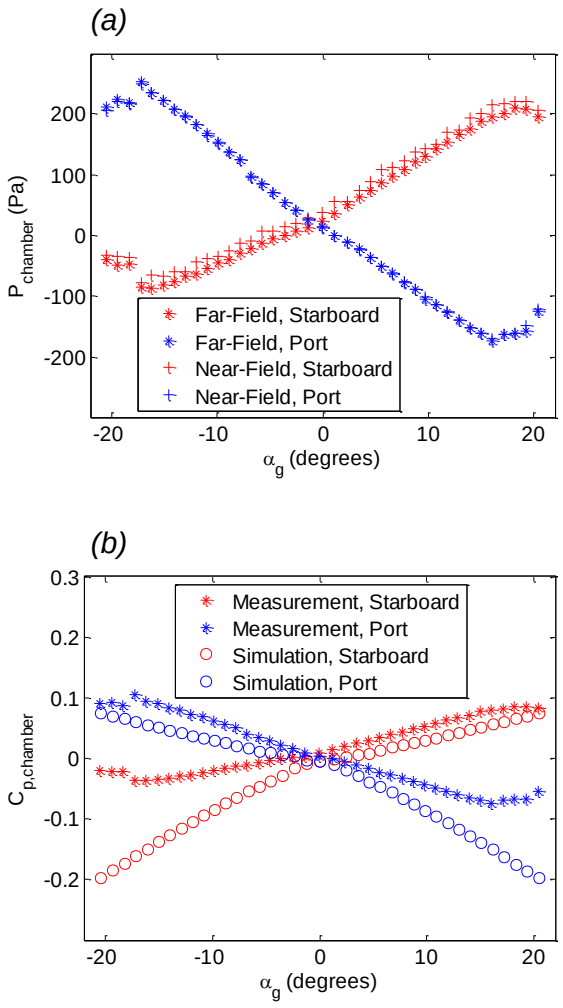

FIGURE 5.41. Anechoic chamber pressures versus angle of attack *(a)* plotted as dimensional pressures with varying measurement location between the near- and far-field in the chamber and *(b)* plotted as C_p and comparing the far-field measurement and the simulated values. All measured data are for the 0.91m NACA 0012 at nominal Reynolds number of 4×10^6 and in the tripped condition.

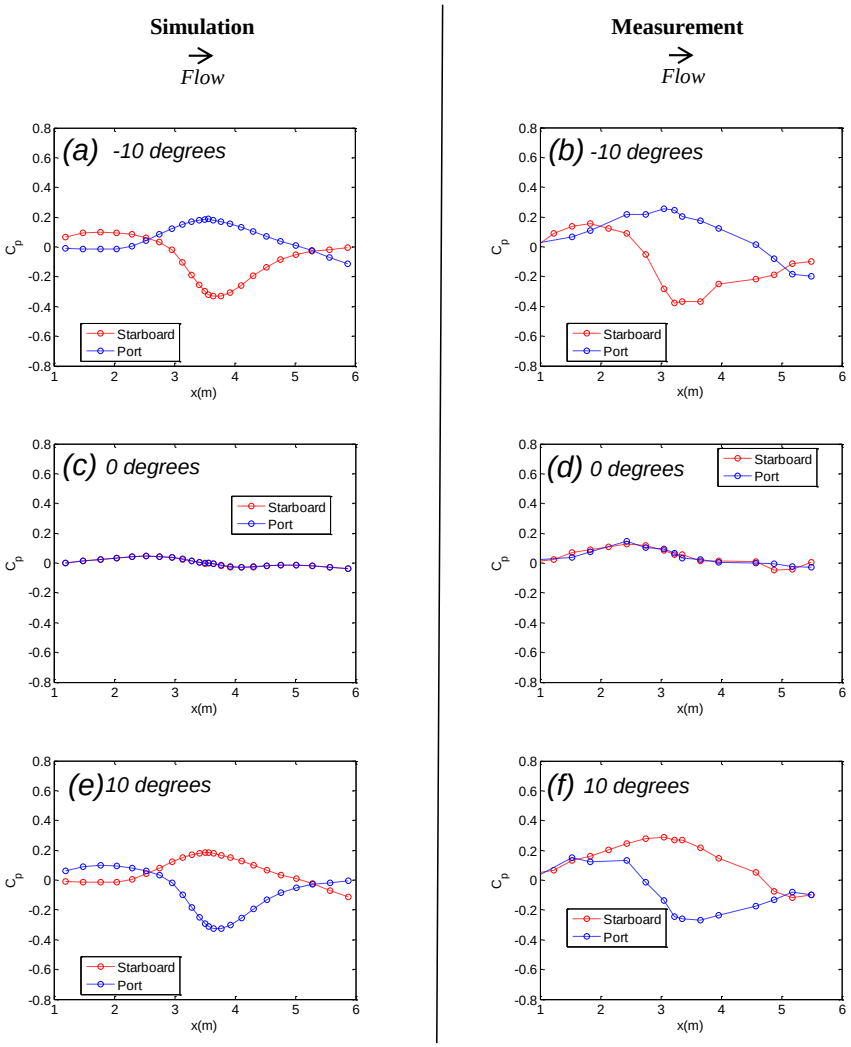

FIGURE 5.42. Comparison of the simulated and measured C_p's on the Kevlar walls for nominal angles of attack of -10, 0, and 10 degrees. All measured data are for the 0.91m NACA 0012 at nominal Reynolds number of 4×10^6 and in the tripped condition.

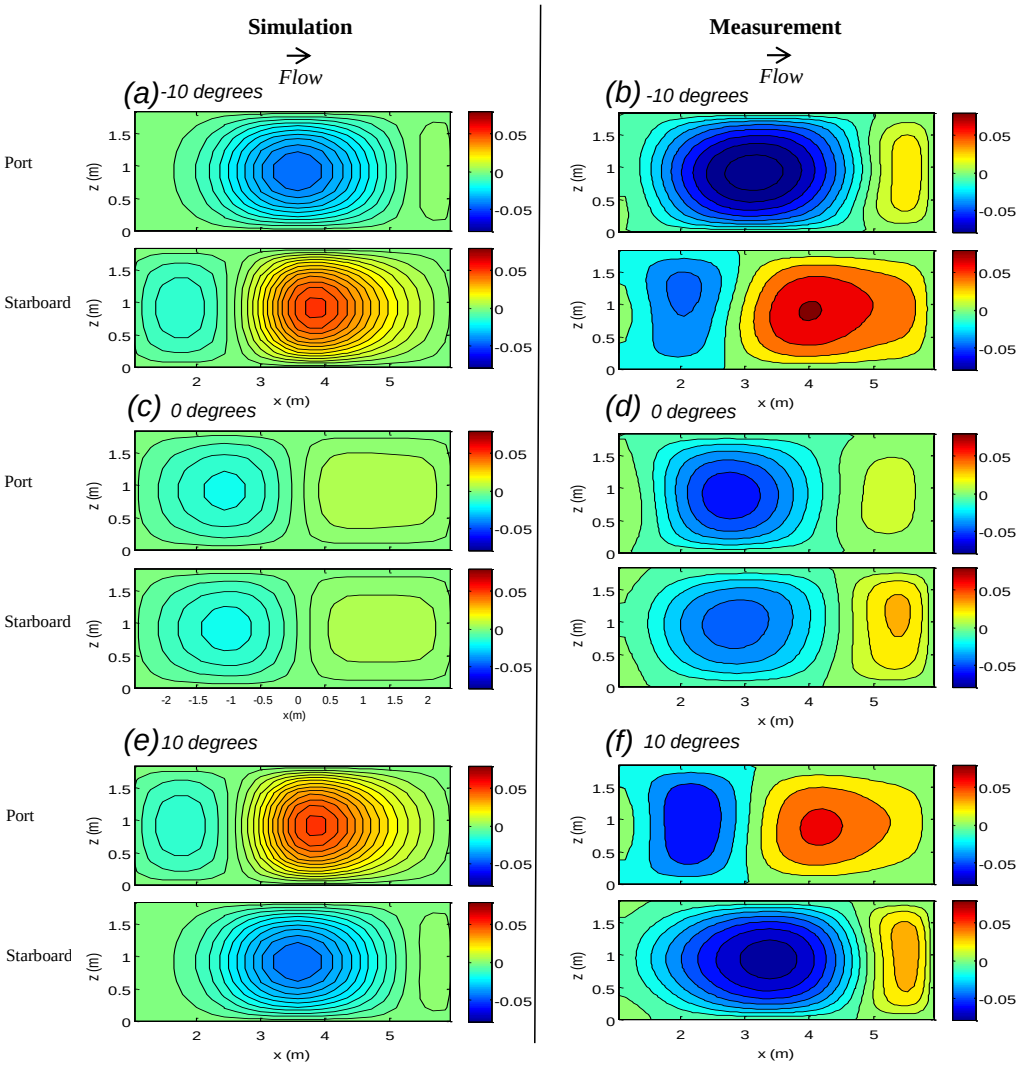

FIGURE 5.43. Comparison of the simulated and measured Kevlar wall deflections for nominal angles of attack of -10, 0, and 10 degrees. The positive *y*-direction is the direction into the test section. All measured data are for the 0.91m NACA 0012 at nominal Reynolds number of 4×10^6 and in the untripped condition.

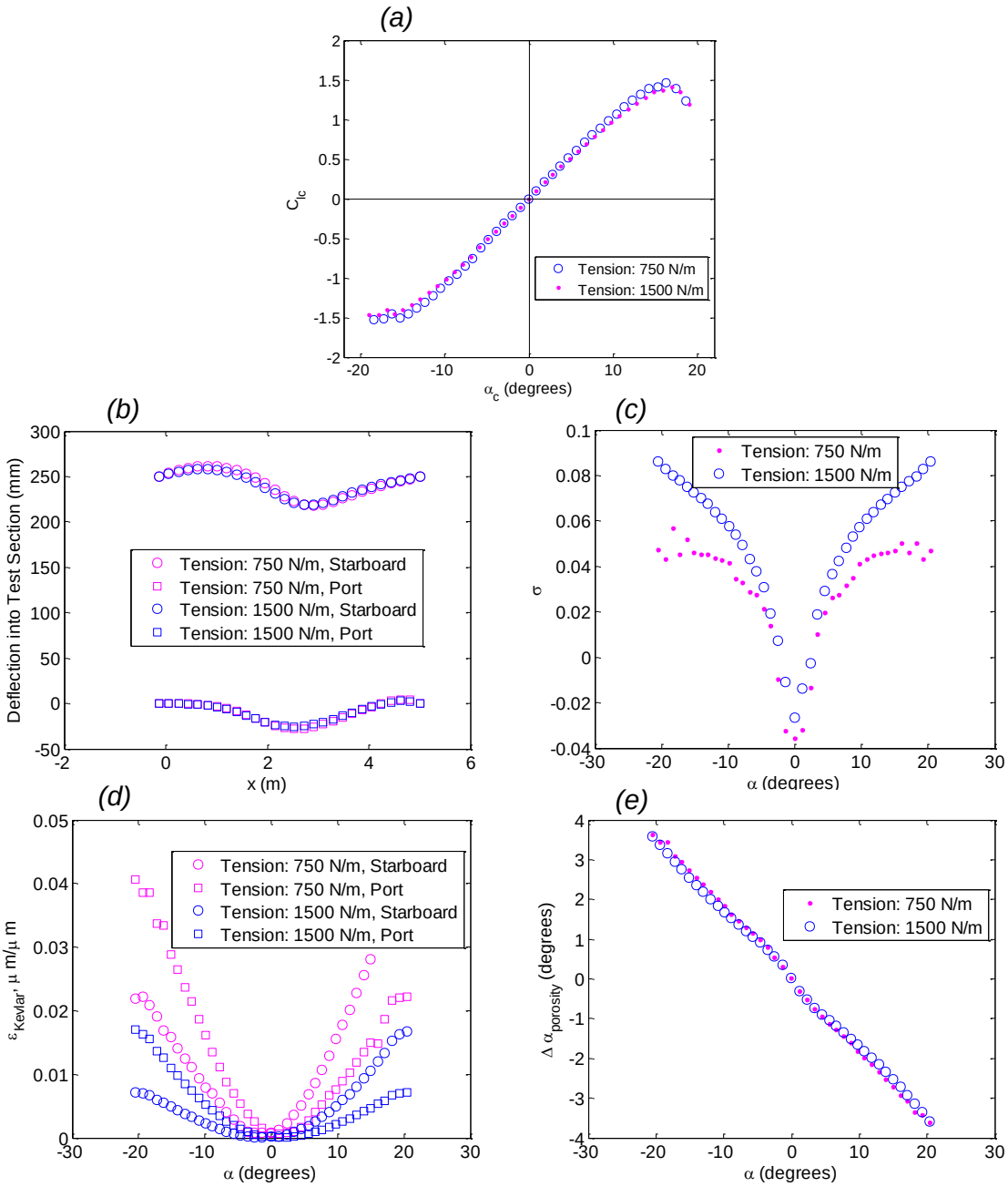

FIGURE 5.44. Sensitivity of panel method simulation to initial Kevlar tensions of 750 and 1500 N/m. *(a)* lift coefficient versus angle of attack, *(b)* Kevlar deflection versus streamwise location *x*, *(c)* panel method optimized blockage versus angle of attack, *(d)* wall-averaged strain versus angle of attack, *(e)* porosity-induced angle of attack versus (geometric) angle of attack. All data are for the 0.91m NACA 0012 at nominal Reynolds number of 4×10^6, and the experimental data in *(a)* is in the tripped condition.

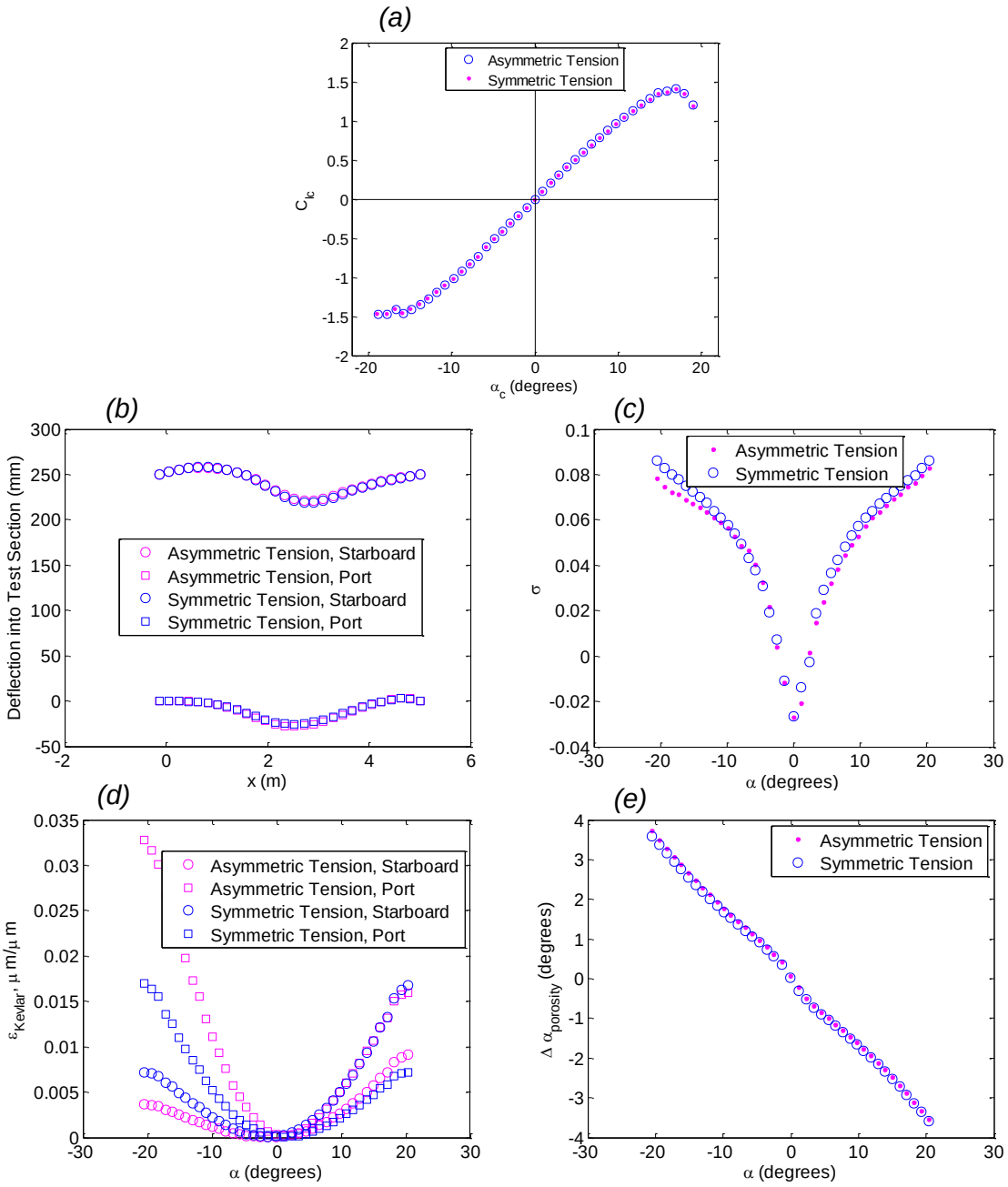

FIGURE 5.45. Sensitivity of panel method simulation to asymmetric initial Kevlar tensions. The tensions in the asymmetric case are 1000 and 2000 N/m for the port and starboard walls, respectively. *(a)* lift coefficient versus angle of attack, *(b)* Kevlar deflection versus streamwise location x, *(c)* panel method optimized blockage versus angle of attack, *(d)* wall-averaged strain versus angle of attack, *(e)* porosity-induced angle of attack versus (geometric) angle of attack. All data are for the 0.91m NACA 0012 at nominal Reynolds number of 4×10^6, and the experimental data in *(a)* is in the tripped condition.

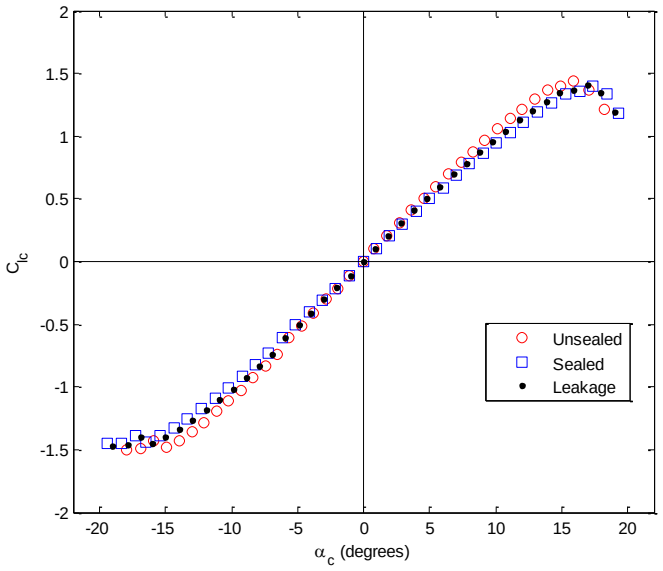

FIGURE 5.46. Corrected lift versus corrected angle of attack for three different formulations of the panel method correction corresponding to three difference mass flow conditions between the anechoic chambers. All data are for the 0.91m NACA 0012 at nominal Reynolds number of 4x106 and in the tripped condition.

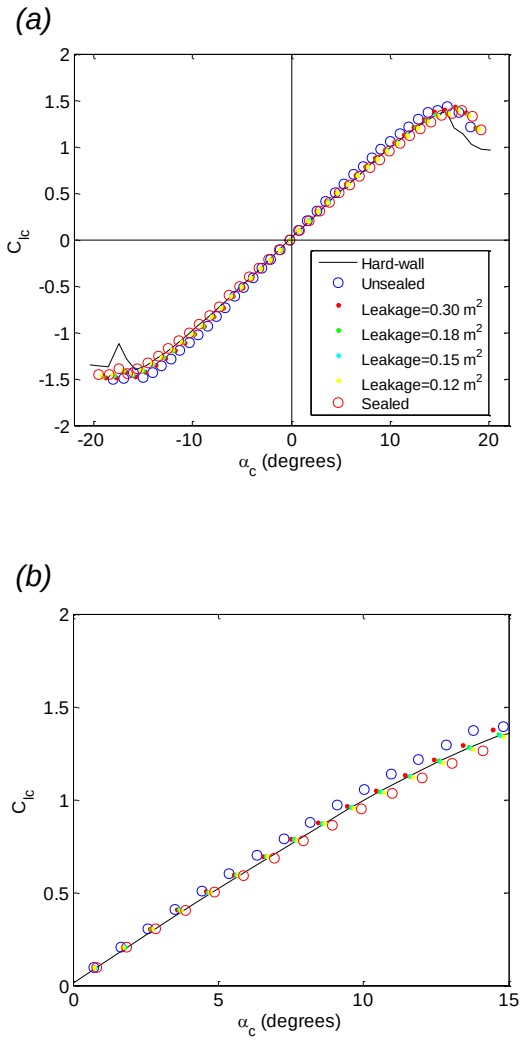

FIGURE 5.47. Corrected lift versus corrected angle of attack for three different formulations of the panel method correction, in addition to the hard-wall data, for *(a)* the full lift curve and *(b)* the attached flow regime on the positive side. Various leakage areas are used for the leakage formulation as shown in the legend, and hard-wall data is included for comparison. All data are for the 0.91m NACA 0012 at nominal Reynolds number of 4×10^6 and in the tripped condition.

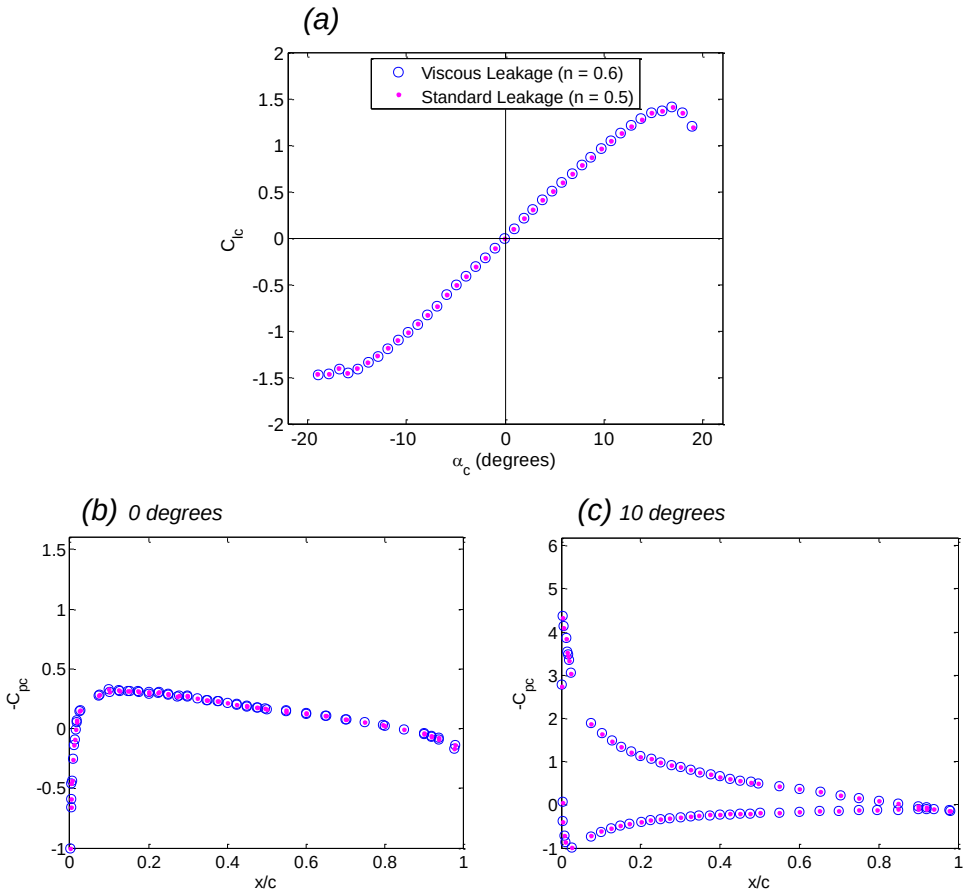

FIGURE 5.48. Comparison of the viscous and leakage formulation using the exponents of 0.6 and 0.5 in the denominator of Equation 5.2. *(a)* Lift versus angle of attack, *(b)*-(c) pressure distributions along the chordlength for angles of attack of 0 and 10 degrees, respectively. All data are for the 0.91m NACA 0012 at nominal Reynolds number of 4×10^6 and in the tripped condition.

CHAPTER 6. Conclusions and Recommendations

6.1. Conclusions

This study was performed to understand the aerodynamic performance of Kevlar-wall test sections and their corrections for two-dimensional, lifting models such as tested at the SWT. An initial study on the characteristics of the SWT's hard-wall test section revealed a small gradient in the freestream flow with roughly 0.15% greater mean velocity at the top of the test section than the bottom. The SWT is known to have low turbulence levels, even relative to facilities such as the Langley Low Turbulence Pressure Tunnel and the National Physical Laboratory 9 ft.-by-13 ft. Tunnel, and these levels allowed for the relatively rare observance of a laminar separation bubble on a NACA 0012 profile. Testing of this symmetric NACA 0012 model further confirmed the flow uniformity in the hard-wall test section.

For the Kevlar-wall test section, multiple aspects of the performance were studied. The power-law behavior of the Kevlar cloth's pressure-velocity relationship at high pressures as well as low pressures and in the presence of tunnel flow was quantified. Side-by-side comparison of the hard- and Kevlar-wall test sections reinforced the panel method correction approach of Devenport *et al.* (2013). The linear region lift curves between test sections were generally in agreement and the average difference in $C_{lc,max}$'s was 2.9% difference. On all the airfoils tested in the Kevlar-wall test section, the effect of the porosity is to reduce the far-field angle of attack from the geometric angle which amounts to an overall decrease in angle of attack upon correction which is the opposite of hard-wall correction process. A significant advantage of Kevlar-wall test sections is that they require a smaller blockage correction than hard-wall tunnels at low to moderate angle of attack up to 10 degrees. At higher angles of attack, however, the Kevlar-wall test section requires a greater blockage correction than the hard-wall by up to 75% more. The overall magnitude of the correction, including both blockage and lift interference, is generally larger for the Kevlar-wall data than for the hard-wall data.

It was found slight asymmetric performance with angle of attack in the Kevlar-wall test section and asymmetric leakage characteristics of the anechoic chambers. Novel boundary measurements on the Kevlar walls including measurement of pressure and deflection distributions showed good agreement of the measured and panel method simulated wall pressures and exposed the need for higher fidelity structural modeling of the Kevlar wall deflections.

The panel method simulation was used to predict the sensitivity of Kevlar-wall test section to several parameters. The initial Kevlar tension was found to have a small but significant effect on the correction magnitudes. For instance, reducing the tension from the standard 1500 N/m to 750 N/m produced an increase of 6% slope in the corrected lift curve. Asymmetry in the initial Kevlar tension between port- and starboard-walls has a relatively insignificant effect on the correction magnitudes as the asymmetry produced an asymmetric angle of attack offset of 0.06 to 0.11 degrees in the attached flow regime. A study of the panel method simulation's sensitivity to leakage area that to avoid large errors in the correction process, it is necessary to determine the leakage area of a Kevlar-wall tunnel to within roughly 20% certainty.

6.2. Recommendations for Future Work

Recommendations stemming from this paper are below given in the areas of aerodynamic modeling of the panel method simulation, structural modeling of the simulation, and operating procedures.

6.2.1. Aerodynamic Modeling

Higher fidelity modeling of the aerodynamics in the panel method simulation would lead to better prediction of correction values. One improvement that could be made in future versions of the code is to add modeling for viscous boundary layer growth such as by including constant-strength sources at each wall panel. The strength of the source panels would be tuned so that the empty test section case of the panel method produces walls that bow inwards similarly to the measured deflections for the empty test section case. The viscous boundary layer would at times be drawn into the suction chamber and at times contribute to the growth of the boundary layer on the pressure side or suction side. The viscous boundary layer may induce a streamwise pressure gradient which would help the simulation to match the measurements made in Section 5.4.3. Additionally, the pressure gradient might be induced by the addition of wake blockage in the simulation

Related to the leakage mass flow between anechoic chambers, it is recommended to use to use the viscous leakage formulation in future testing. This formulation uses an exponent of $n = 0.6$ exponent in the leakage calculation with measurements showing a leakage area of 0.10 m^2 to be appropriate. An alternative path for improving the modeling of the chamber pressures and to deal directly with the asymmetric chamber pressure issue discussed in Section 5.3.2, the measured chamber pressures could be simply input into the panel method simulation to bring the simulated pressures into agreement with the measured pressures. This would require adaption of the simulation since preliminary attempts at the preceding recommendation yielded convergence issues for the simulation.

6.2.2. Structural Modeling

Higher fidelity modeling of the structural behavior of the Kevlar walls in the panel method simulation would also lead to better prediction of correction values. The biggest discrepancy in the current structural modeling is the centimeter scale differences in deflection magnitudes between the simulation and measurement as observed in Section 5.4.3. Higher fidelity modeling of the wall deflection such as through finite element rather than finite difference treatment of the walls would capture the coupling of the tension and deflection in the walls more exactly and potentially reduce the discrepancies of Section 5.4.3. Additionally, better knowledge of the true initial Kevlar tension should also reduce these discrepancies.

Adding a finite element solution would also do away with wall-averaging of the strain as done currently in Equation 2.30 which would be appropriate from a structural fidelity point of view as well as an aerodynamic point of view since the pore size could then be modelled as a local rather than averaged value.

As discussed in Section 5.5.1, another change to the panel method simulation would be to the handling of the initial Kevlar strain input. Adopting an approach such as with Equations 5.5 and 5.6 would allow for valid comparisons and even optimizations of test section performance between different initial Kevlar tensions.

With the higher fidelity of structural modeling garnered from the above improvements to the panel method simulation, it would be appropriate to make a study on the optimum initial tension for Kevlar-wall test sections. Higher initial tension produces less deflection and so less blockage at high loading. Higher initial tension also leads to larger pore openings in the Kevlar which may be beneficial from an aeroacoustic measurement point of view and for decreasing blockage magnitudes through greater flow diversion out of the test section. On the contrary, the larger pore openings would likely increase the lift interference correction magnitudes. Identification of the optimum tension value with all these factors in mind might produce a test section with closer characteristic to those of a hard-wall test section and facilitate greater acceptance of the Kevlar-wall test section in both the aeroacoustic and aerodynamic communities, as well as be helpful for Kevlar-wall test section designers.

6.2.3. Operating Procedures

A recommendation for future wind tunnel testing is to investigate the effect of covering versus uncovering the wake rake slots and to gage if flow is entering or exiting the test section at these locations slots. Further investigation of the slight asymmetric performance with angle of attack in the Kevlar-wall test section and the asymmetric leakage characteristics of the anechoic chambers is also recommended. The focus might be on the source of asymmetric behavior between the anechoic chambers on the port- and starboard-sides.

Lastly, a general improvement to the SWT operation for both hard-wall and Kevlar-wall test sections would be to use lower uncertainty instrumentation for the measurement of the freestream static conditions. The uncertainty in lift data is generally dominated by the uncertainty in the static pressure measurements used for inferring the freestream conditions. This uncertainty is most exaggerated at high loading where it is at least twice as large as the next greatest uncertainty. As the high loading regime is that at which most wind tunnel users are most concerned with the accuracy of the lift prediction, improvement to the freestream measurement accuracy would be beneficial to many wind tunnel users.

References

Abbott, I. H. and A. E. Von Doenhoff (2012). Theory of wing sections: including a summary of airfoil data, Courier Dover Publications.

Allen, H. J. and W. G. Vincenti (1944). Wall interference in two-dimensional-flow wind tunnel with consideration of effect of compressibility. Washington, DC, United States, National Advisory Committee for Aeronautics**:** 30.

Ashill, P., J. E. Hackett, M. Mokry and F. Steinle (1998). Boundary Measurement Methods. AG-336.

Barlow, J. B., W. H. Rae, Jr; and A. Pope (1999). Low-speed wind tunnel testing (3rd revised and enlarged edition), John Wiley and Sons, Inc.

Bernstein, S. and R. G. Joppa (1976). "Development of Minimum-Correction Wind Tunnels." Journal of Aircraft **13**(4): 243-247.

Bouguet, J. Y. (2010). Camera Calibration Toolbox, California Institute of Technology.

Bowcutt, K. (1985). The use of panel methods for the development of low-subsonic wall interference and blockage corrections. American Institute of Aeronautics and Astronautics, Aerospace Sciences Meeting, 23 rd, Reno, NV.

Bradshaw, P. and D. Ferriss (1962). "Measurements of Free Stream Turbulence in some Low Speed Tunnels at NPL'." R & M **3317**.

Braslow, A. L. and E. C. Knox (1958). Simplified method for determination of critical height of distributed roughness particles for boundary-layer transition at Mach numbers from 0 to 5, National Advisory Committee for Aeronautics.

Brown, K., W. Devenport, A. Borgoltz, H. Ura and K. Yamamoto (2014). "Towards Interference Corrections for Three-Dimensional Models in Kevlar-Walled Anechoic Test Sections."

Choi, K. and R. L. Simpson (1987). "Some mean velocity, turbulence, and unsteadiness characteristics of the VPI & SU Stability Wind Tunnel." AOE Dept., Virginia Tech, Blacksburg VA.

Critzos, C. C., H. H. Heyson and R. W. Boswinkle (1955). Aerodynamic Characteristics of NACA 0012 Airfoil Section at Angles of Attack from 0 to 180 Degrees, National Advisory Committee for Aeronautics.

Devenport, W., R. Burdisso, H. Camargo, E. Crede, M. Remillieux, M. Rasnick and P. Van Seeters (2010a). Aeroacoustic Testing of Wind Turbine Airfoils, National Renewable Energy Laboratory.

Devenport, W. J., R. Burdisso, A. G. Borgoltz, P. Ravetta and M. Barone (2010b). Aerodynamic and Acoustic Corrections for a Kevlar Walled Anechoic Wind Tunnel. 16th AIAA/CEAS Aeroacoustics Conference. Stockholm, Sweden.

Devenport, W. J., R. A. Burdisso, A. Borgoltz, P. A. Ravetta, M. F. Barone, K. A. Brown and M. A. Morton (2013). "The Kevlar-walled anechoic wind tunnel." Journal of Sound and Vibration **332**(17): 3971-3991.

Drela, M. (2013). XFOIL.

DuPont (2000). Technical Guide to Kevlar.

Ewald, B. F. R. (1998). Wind Tunnel Wall Correction. NEUILLY-SUR-SEINE CEDEX. FRANCE, AGARD.

Gault, D. E. (1957). A correlation of low-speed, airfoil-section stalling characteristics with Reynolds number and airfoil geometry, National Advisory Committee for Aeronautics.

Glauert, H. (1933). Wind Tunnel Interference on Wings, Bodies and Airscrews, AERONAUTICAL RESEARCH COUNCIL LONDON (ENGLAND).

Gregory, N. and C. O'Reilly (1973). Low-Speed Aerodynamic Characteristics of NACA 0012 Aerofoil Section, including the Effects of Upper-Surface Roughness Simulating Hoar Frost, Citeseer.

Grewe, L. L. and A. C. Kak (1994). Stereo vision. Handbook of pattern recognition and image processing (vol. 2), Academic Press, Inc.

Ito, T., H. Ura, K. Nakakita, Y. Yokokawa, W. F. Ng, R. A. Burdisso, A. Iwasaki, T. Fujita, N. Ando, N. Shimada and K. Yamamoto (2010). Aerodynamic/Aeroacoustic testing in Anechoic Closed Test Sections of Low-speed Wind Tunnels. 16th AIAA/CEAS Aeroacoustics Conference 2010. 31st AIAA Aeroacoustics Conference, 7-9 June 2010, Reston, VA, USA, American Institute of Aeronautics and Astronautics, Inc.

Iyer, V. and J. L. Everhart (2001). Application of Pressure-Based Wall Correction Methods to Two NASA Langley Wind Tunnels. 19th AIAA Aplied Aerodynamics Conference. Anaheim, CA.

Joppa, R. G. (1973). Wind tunnel interference factors for high-lift wings in closed wind tunnels. Washington, D.C., National Aeronautics and Space Administration.

Joseph, L. A. (2014). Transition Detection for Low Speed Wind Tunnel Testing Using Infrared Thermography. Aerospace and Ocean Engineering, Virginia Polytechnic Institute and State University. **Master of Science**.

King, M. J. (2006). A continuum constitutive model for the mechanical behavior of woven fabrics including slip and failure, Massachusetts Institute of Technology.

Krynytzky, A. (1998). Conventional Corrections in Ventilated Test Sections. AGARD-AG-336. NEUILLY-SUR-SEINE CEDEX. FRANCE.

Ladson, C. L. (1988). Effects of independent variation of Mach and Reynolds numbers on the low-speed aerodynamic characteristics of the NACA 0012 airfoil section [microform] / Charles L. Ladson. [Washington, DC] : [Springfield, Va. :, National Aeronautics and

Space Administration, Scientific and Technical Information Division ; For sale by the National Technical Information Service].

Lee, K. (1981). "Numerical simulation of the wind tunnel environment by a panel method." AIAA Journal **19**(4): 470-475.

Lock, C. (1929). "The Interference of a Wind Tunnel on a Symmetrical Body. R. & M. No. 1275." British A. R, C.

McCroskey, W. J. (1987). A Critical Assessment of Wind Tunnel Results for the NACA 0012 Airfoil. TM-100019, NASA

McCullough, G. B. and D. E. Gault (1951). Examples of Three Representative of Airfoil-section Stall at Low Speed, National Advisory Committee for Aeronautics.

McGhee, R. J., W. D. Beasley and J. M. Foster (1984). "Recent modifications and calibration of the Langley low-turbulence pressure tunnel."

Mokhtar, W. A. and C. P. Britcher (2004). "Boundary interference assessment and correction for open test section wind tunnels using panel methods." AIAA Paper **609**: 093-2003.

Mokry, M. (1985). Subsonic Wall Interference Corrections for Half-Model Tests using Sparse Wall Pressure Data. Ottawa, Canada, National Aeronautical Establishment.

Moses, D. (1983). "Wind tunnel wall corrections deduced by iterating from measured wall static pressure." AIAA Journal **21**(12): 1667-1673.

Newman, P. and J. L. Everhart (1998). Conventional Corrections in Ventilated Test Sections. AGARD-AG-336. NEUILLY-SUR-SEINE CEDEX. FRANCE.

Remillieux, M. C., E. D. Crede, H. E. Camargo, R. A. Burdisso and W. J. Devenport (2008). Calibration and Demonstration of the New Virginia Tech Anechoic Wind Tunnel. 14th AIAA/CEAS Aeroacoustics Conference. Vancouver, British Columbia.

Smith, B. S., H. E. Camargo, R. A. Burdisso and W. J. Devenport (2005). Development and Testing of a Novel Acoustic Wind Tunnel Concept. 11th AIAA/CEAS Aeroacoustics Conference and Exhibit.

Smyth, J., M. (1984). Low Speed Wind Tunnel Wall Corrections - A Panel Method Approach. Aeronautics and Astronautics, University of Washington. **Master of Science:** 125.

Sun, W. and J. R. Cooperstock (2005). Requirements for camera calibration: must accuracy come with a high price? Seventh IEEE Workshops on Application of Computer Vision, 2005. WACV/MOTIONS'05., IEEE.

Timmer, W. and R. Van Rooij (2003). "Summary of the Delft University wind turbine dedicated airfoils." Journal of Solar Energy Engineering **125**(4): 488-496.

Timoshenko, S. (1940). Theory of plates and shells. New York; London, McGraw-Hill Book Company, inc.

Ulbrich, N. (2009). Wind Tunnel Wall Interference Corrections (A Brief Overview), Jacobs Technology Inc.

Ulbrich, N. and M. George (2000). "Description of panel method code ANTARES."

Ulbrich, N. and F. Steinle (1995). Semispan model wall interference prediction based on the wall signature method. AIAA, Aerospace Sciences Meeting and Exhibit, 33 rd, Reno, NV.

Von Doenhoff, A. E. and F. T. Abbott (1947). The Langley two-dimensional low-turbulence pressure tunnel, National Advisory Committee for Aeronautics.

Young, C. P. (1990). Design and Fabrication of Instrumented Composite Airfoils for a Cryogenic Wind Tunnel Model, National Aeronautics and Space Administration, Langley Research Center.

Zhang, Z. (2000). "A flexible new technique for camera calibration." Pattern Analysis and Machine Intelligence, IEEE Transactions on **22**(11): 1330-1334.

Zhu, D., B. Mobasher, A. Vaidya and S. D. Rajan (2012). "Mechanical behaviors of Kevlar 49 fabric subjected to uniaxial, biaxial tension and in-plane large shear deformation." Composites Science and Technology.

Appendices

Appendix A: Airfoil Pressure Port Locations

Measurements of the port locations on each of the three airfoil models tested in this study were made with a FaroArm® Coordinate Measurement Machine (CMM) of Fusion model type. The 3 mm diameter probe head was employed. The rated accuracy of the machine is ±0.025 mm, however, based on wind tunnel engineers experience using the CMM this value is taken to be ±0.5 mm.

The pressure tap coordinates are given as values normalized on the chord. All taps on each airfoil are given including those found not to hold pressure as described in Section 4.4. The *x/c* column corresponds to the chordwise distribution measured from the leading edge, the *y/c* column corresponds to the thickness-wise distribution measured from the chordline, and the *z/c* corresponds to the spanwise distribution measured from one end of the airfoil.

0.201 m NACA 0012

Suction Side		*Pressure Side*	
x/c	*y/c*	*x/c*	*y/c*
6.402E-03	1.373E-02	6.370E-03	-1.468E-02
1.488E-02	2.201E-02	1.488E-02	-2.201E-02
2.803E-02	2.733E-02	2.865E-02	-2.934E-02
5.372E-02	3.652E-02	5.281E-02	-3.806E-02
7.948E-02	4.262E-02	7.792E-02	-4.469E-02
1.041E-01	4.694E-02	1.035E-01	-4.965E-02
1.552E-01	5.337E-02	1.541E-01	-5.666E-02
2.067E-01	5.685E-02	2.058E-01	-6.108E-02
2.586E-01	5.838E-02	2.567E-01	-6.345E-02
3.091E-01	5.854E-02	3.088E-01	-6.422E-02
3.612E-01	5.749E-02	3.600E-01	-6.444E-02
4.115E-01	5.552E-02	4.108E-01	-6.315E-02
4.620E-01	5.285E-02	4.622E-01	-6.131E-02
5.125E-01	4.955E-02	5.145E-01	-5.857E-02
5.630E-01	4.553E-02	5.646E-01	-5.534E-02
6.153E-01	4.094E-02	6.153E-01	-5.171E-02
6.677E-01	3.629E-02	6.657E-01	-4.750E-02
7.183E-01	3.108E-02	7.165E-01	-4.308E-02
7.685E-01	2.534E-02	7.657E-01	-3.845E-02
8.197E-01	1.906E-02	8.146E-01	-3.331E-02

0.914 m NACA 0012

Suction Side			*Pressure Side*		
x/c	*y/c*	*z/c*	*x/c*	*y/c*	*z/c*
9.840E-05	1.550E-03	-9.311E-01	2.824E-03	-9.070E-03	-1.060E+00
3.155E-03	1.032E-02	-9.346E-01	4.078E-03	-1.081E-02	-1.057E+00
6.373E-03	1.440E-02	-9.334E-01	8.392E-03	-1.598E-02	-1.056E+00
8.506E-03	1.650E-02	-9.356E-01	1.092E-02	-1.778E-02	-1.056E+00
9.890E-03	1.752E-02	-9.349E-01	1.305E-02	-1.921E-02	-1.053E+00
1.289E-02	1.994E-02	-9.372E-01	1.417E-02	-2.003E-02	-1.055E+00
1.560E-02	2.206E-02	-9.374E-01	1.699E-02	-2.218E-02	-1.054E+00
1.730E-02	2.307E-02	-9.361E-01	1.856E-02	-2.324E-02	-1.054E+00
1.862E-02	2.385E-02	-9.372E-01	2.684E-02	-2.706E-02	-1.053E+00
2.531E-02	2.739E-02	-9.394E-01	5.150E-02	-3.661E-02	-1.047E+00
5.136E-02	3.728E-02	-9.435E-01	7.481E-02	-4.270E-02	-1.042E+00
7.404E-02	4.300E-02	-9.501E-01	9.990E-02	-4.748E-02	-1.035E+00
1.022E-01	4.837E-02	-9.559E-01	1.250E-01	-5.135E-02	-1.030E+00
1.275E-01	5.202E-02	-9.613E-01	1.481E-01	-5.411E-02	-1.023E+00
1.523E-01	5.473E-02	-9.666E-01	1.731E-01	-5.639E-02	-1.018E+00
1.755E-01	5.680E-02	-9.744E-01	2.016E-01	-5.829E-02	-1.012E+00
2.007E-01	5.847E-02	-9.785E-01	2.252E-01	-5.952E-02	-1.008E+00
2.274E-01	5.980E-02	-9.842E-01	2.503E-01	-6.037E-02	-1.001E+00
2.778E-01	6.117E-02	-9.959E-01	2.739E-01	-6.074E-02	-9.947E-01
3.007E-01	6.125E-02	-1.003E+00	3.002E-01	-6.089E-02	-9.906E-01
3.258E-01	6.113E-02	-1.008E+00	3.255E-01	-6.067E-02	-9.848E-01
3.510E-01	6.061E-02	-1.013E+00	3.487E-01	-6.047E-02	-9.773E-01
3.777E-01	5.989E-02	-1.019E+00	3.752E-01	-5.991E-02	-9.733E-01
4.010E-01	5.905E-02	-1.027E+00	4.003E-01	-5.915E-02	-9.642E-01
4.257E-01	5.802E-02	-1.031E+00	4.265E-01	-5.811E-02	-9.606E-01
4.515E-01	5.661E-02	-1.037E+00	4.502E-01	-5.703E-02	-9.542E-01
4.775E-01	5.533E-02	-1.041E+00	4.754E-01	-5.568E-02	-9.484E-01
4.992E-01	5.405E-02	-1.047E+00	5.004E-01	-5.428E-02	-9.444E-01
5.506E-01	5.071E-02	-1.056E+00	5.500E-01	-5.100E-02	-9.301E-01
6.011E-01	4.701E-02	-1.045E+00	6.007E-01	-4.718E-02	-9.430E-01
6.530E-01	4.246E-02	-1.035E+00	6.509E-01	-4.294E-02	-9.559E-01
7.028E-01	3.756E-02	-1.024E+00	7.006E-01	-3.833E-02	-9.646E-01
7.510E-01	3.256E-02	-1.013E+00	7.502E-01	-3.336E-02	-9.780E-01
8.011E-01	2.714E-02	-1.002E+00	7.993E-01	-2.808E-02	-9.895E-01
8.511E-01	2.153E-02	-9.887E-01	8.505E-01	-2.216E-02	-9.992E-01
9.016E-01	1.556E-02	-9.772E-01	9.004E-01	-1.600E-02	-1.013E+00
9.215E-01	1.309E-02	-9.725E-01	9.207E-01	-1.329E-02	-1.016E+00
9.396E-01	1.070E-02	-9.681E-01	9.389E-01	-1.077E-02	-1.022E+00
9.609E-01	7.788E-03	-9.631E-01	9.605E-01	-7.630E-03	-1.026E+00
9.820E-01	4.224E-03	-9.586E-01	9.805E-01	-4.610E-03	-1.029E+00

0.610 m DU00-W-212

Suction Side			*Pressure Side*		
x/c	*y/c*	*z/c*	*x/c*	*y/c*	*z/c*
2.498E-03	3.430E-01	1.342E+00	0.000E+00	3.427E-01	1.342E+00
4.997E-03	3.434E-01	1.343E+00	2.498E-03	3.431E-01	1.342E+00
7.495E-03	3.447E-01	1.344E+00	4.997E-03	3.438E-01	1.343E+00
9.993E-03	3.443E-01	1.345E+00	7.495E-03	3.445E-01	1.344E+00
1.249E-02	3.450E-01	1.345E+00	9.993E-03	3.452E-01	1.344E+00
1.499E-02	3.462E-01	1.346E+00	1.249E-02	3.459E-01	1.344E+00
1.749E-02	3.466E-01	1.347E+00	1.499E-02	3.463E-01	1.346E+00
1.999E-02	3.468E-01	1.347E+00	1.749E-02	3.473E-01	1.346E+00
2.498E-02	3.485E-01	1.349E+00	1.999E-02	3.481E-01	1.346E+00
4.997E-02	3.513E-01	1.351E+00	2.498E-02	3.492E-01	1.348E+00
7.495E-02	3.539E-01	1.354E+00	4.997E-02	3.512E-01	
9.993E-02	3.552E-01	1.357E+00	7.495E-02	3.549E-01	1.355E+00
1.249E-01	3.573E-01	1.354E+00	9.993E-02	3.572E-01	1.357E+00
1.499E-01	3.548E-01	1.377E+00	1.249E-01	3.543E-01	1.354E+00
1.749E-01	3.787E-01	1.384E+00	1.499E-01	3.776E-01	1.378E+00
1.999E-01	3.845E-01	1.391E+00	1.749E-01	3.846E-01	1.384E+00
2.249E-01	3.896E-01	1.397E+00	1.999E-01	3.917E-01	1.389E+00
2.498E-01	3.983E-01	1.408E+00	2.249E-01	3.980E-01	1.398E+00
2.748E-01	4.051E-01	1.410E+00	2.498E-01	4.086E-01	1.404E+00
2.998E-01	4.113E-01	1.425E+00	2.748E-01	4.108E-01	
3.248E-01	4.245E-01	1.430E+00	2.998E-01	4.253E-01	1.424E+00
3.748E-01	4.291E-01	1.438E+00	3.248E-01	4.303E-01	1.433E+00
4.247E-01	4.336E-01	1.451E+00	3.748E-01	4.389E-01	1.437E+00
4.747E-01	4.376E-01	1.465E+00	4.247E-01	4.517E-01	1.465E+00
5.247E-01	4.515E-01		4.747E-01	4.661E-01	1.343E+00
5.746E-01	4.660E-01	1.351E+00	5.247E-01	3.426E-01	1.351E+00
6.246E-01	3.438E-01	1.360E+00	5.746E-01	3.516E-01	1.361E+00
6.746E-01	3.518E-01	1.376E+00	6.246E-01	3.607E-01	1.378E+00
7.245E-01	3.617E-01	1.391E+00	6.746E-01	3.766E-01	1.391E+00
7.745E-01	3.783E-01	1.443E+00	7.245E-01	3.913E-01	1.403E+00
8.245E-01	3.916E-01		7.745E-01	4.044E-01	1.443E+00
8.744E-01	4.035E-01	1.457E+00	8.245E-01	4.113E-01	1.457E+00
8.994E-01	4.439E-01	1.464E+00	8.744E-01	4.245E-01	1.464E+00
9.194E-01	4.573E-01	1.469E+00	8.994E-01	4.291E-01	1.469E+00
9.394E-01	4.643E-01	1.474E+00	9.194E-01	4.336E-01	1.474E+00
9.594E-01	4.696E-01	1.480E+00	9.394E-01	4.376E-01	1.480E+00
			9.594E-01	4.515E-01	1.485E+00

Appendix B: Jitter Uncertainty Analysis

Uncertainty calculations are made with the jitter method using the equations below for the calculation of the uncertainties in freestream velocity, Reynolds number, and Mach number. Uncertainties for the aerodynamic coefficients are calculated as described in Section 4.6.

The following pages in this appendix tabulate the measurements and calculations for specific airfoils and freestream velocities, as well as for the wake rake on the last page. In a few cases, the nominal Reynolds or Mach number calculated may vary slightly from the values reported in Table 5.2 because the values in the table are averaged over a whole angle of attack sweep whereas the values below correspond to the zero degree angle of attack data.

Constants

Settling chamber calibration constant, Cps	0.9871
Contraction calibration constant, Cpc	0.4074
Ideal gas constant for air, R	287.058
Heat capacity ratio for air, γ	1.4

Primary measurements

Model chord length, c

Contraction mean pressure, p_{con}

Settling chamber mean pressure, p_{set}

Barometer reading, p_{atm}

Thermometer reading, T

Intermediate calculations

Reference Pitot-static pressure, $q = \frac{(p_{set} - p_{con})}{(Cps - Cpc)}$

Air density, $\rho = \frac{p_{atm}}{RT}$

Dynamic viscosity, $\nu = \frac{0.0000014578 T^{1.5}}{(T + 110.4)}$

Freestream velocity, $V_\infty = \sqrt{\frac{2q}{\rho}}$

Final calculations

Reynolds number, $Re = \frac{V_\infty c}{\nu}$

Mach number, $Ma = \frac{V_\infty}{\sqrt{\gamma RT}}$

0.91m NACA 0012 at 34 m/s

	Nominal Quantity	Uncertainty
Primary measurements		
Model chord length[1], c (m)	9.131E-01	5.000E-04
Contraction mean pressure[2], p_{con} (Pa)	2.709E+02	3.732E+00
Settling chamber mean pressure[3], p_{set} (Pa)	6.548E+02	3.732E+00
Barometer reading[4], p_{atm} (Pa)	9.401E+04	1.693E+02
Thermometer reading[5], T (K)	2.881E+02	2.000E-01
Intermediate calculations		
Reference Pitot-static pressure, q (Pa)	6.622E+02	9.104E+00
Air density, ρ (kg/m^3)	1.137E+00	2.194E-03
Dynamic viscosity, ν (kg/m/s)	1.789E-05	9.648E-09
Freestream velocity, V_∞ (m/s)	3.413E+01	2.369E-01
Final calculations		
Reynolds number, Re	1.981E+06	1.389E+04
Mach number, Ma	1.003E-01	6.955E-04

[1] Uncertainty estimate based on wind tunnel engineers experience using the FaroArm® Coordinate Measurement Machine (rated accuracy of this machine is ±0.025 mm)
[2] Uncertainty estimate based on the ±0.15% full-scale quoted accuracy of the Esterline 9816/98RK pressure scanner with a range of ±10 in. of water (±10 in. of water scanners used for testing below 50 m/s and ±2.5 psi scanners used for testing above 50 m/s)
[3] Uncertainty estimate based on the ±0.15% full-scale quoted accuracy of the Esterline 9816/98RK pressure scanner with a range of ±10 in. of water (±10 in. of water scanners used for testing below 50 m/s and ±2.5 psi scanners used for testing above 50 m/s)
[4] Uncertainty estimate of 0.05 inches of mercury chosen as a conservative estimate of accuracy based on the resolution of the Validyne DB-99 Digital Barometer at 0.01 inches of mercury
[5] Uncertainty estimate based on the quoted accuracy of the Omega Thermistor type 44004

0.91m NACA 0012 at 71 m/s

	Nominal Quantity	Uncertainty
Primary measurements		
Model chord length[1], c (m)	9.131E-01	5.000E-04
Contraction mean pressure[2], p_{con} (Pa)	1.098E+03	2.586E+01
Settling chamber mean pressure[3], p_{set} (Pa)	2.695E+03	2.586E+01
Barometer reading[4], p_{atm} (Pa)	9.241E+04	1.693E+02
Thermometer reading[5], T (K)	2.955E+02	2.000E-01
Intermediate calculations		
Reference Pitot-static pressure, q (Pa)	2.755E+03	6.308E+01
Air density, ρ (kg/m^3)	1.089E+00	2.127E-03
Dynamic viscosity, ν (kg/m/s)	1.825E-05	9.530E-09
Freestream velocity, V_∞ (m/s)	7.112E+01	8.171E-01
Final calculations		
Reynolds number, Re	3.877E+06	4.470E+04
Mach number, Ma	2.064E-01	2.370E-03

[1] Uncertainty estimate based on wind tunnel engineers experience using the FaroArm® Coordinate Measurement Machine (rated accuracy of this machine is ±0.025 mm)
[2] Uncertainty estimate based on the ±0.15% full-scale quoted accuracy of the Esterline 9816/98RK pressure scanner with a range of ±2.5 psi (±10 in. of water scanners used for testing below 50 m/s and ±2.5 psi scanners used for testing above 50 m/s)
[3] Uncertainty estimate based on the ±0.15% full-scale quoted accuracy of the Esterline 9816/98RK pressure scanner with a range of ±2.5 psi (±10 in. of water scanners used for testing below 50 m/s and ±2.5 psi scanners used for testing above 50 m/s)
[4] Uncertainty estimate of 0.05 inches of mercury chosen as a conservative estimate of accuracy based on the resolution of the Validyne DB-99 Digital Barometer at 0.01 inches of mercury
[5] Uncertainty estimate based on the quoted accuracy of the Omega Thermistor type 44004

0.61m DU00-W-212 at 58 m/s

	Nominal Quantity	Uncertainty
Primary measurements		
Model chord length[1], c (m)	6.096E-01	5.000E-04
Contraction mean pressure[2], p_{con} (Pa)	8.028E+02	2.586E+01
Settling chamber mean pressure[3], p_{set} (Pa)	1.898E+03	2.586E+01
Barometer reading[4], p_{atm} (Pa)	9.245E+04	1.693E+02
Thermometer reading[5], T (K)	2.873E+02	2.000E-01
Intermediate calculations		
Reference Pitot-static pressure, q (Pa)	1.888E+03	6.308E+01
Air density, ρ (kg/m^3)	1.121E+00	2.196E-03
Dynamic viscosity, ν (kg/m/s)	1.785E-05	9.661E-09
Freestream velocity, V_∞ (m/s)	5.805E+01	9.712E-01
Final calculations		
Reynolds number, Re	2.222E+06	3.726E+04
Mach number, Ma	1.708E-01	2.857E-03

[1] Uncertainty estimate based on wind tunnel engineers experience using the FaroArm® Coordinate Measurement Machine (rated accuracy of this machine is ±0.025 mm)
[2] Uncertainty estimate based on the ±0.15% full-scale quoted accuracy of the Esterline 9816/98RK pressure scanner with a range of ±2.5 psi (±10 in. of water scanners used for testing below 50 m/s and ±2.5 psi scanners used for testing above 50 m/s)
[3] Uncertainty estimate based on the ±0.15% full-scale quoted accuracy of the Esterline 9816/98RK pressure scanner with a range of ±2.5 psi (±10 in. of water scanners used for testing below 50 m/s and ±2.5 psi scanners used for testing above 50 m/s)
[4] Uncertainty estimate of 0.05 inches of mercury chosen as a conservative estimate of accuracy based on the resolution of the Validyne DB-99 Digital Barometer at 0.01 inches of mercury
[5] Uncertainty estimate based on the quoted accuracy of the Omega Thermistor type 44004

0.61m DU00-W-212 at 71 m/s

	Nominal Quantity	Uncertainty
Primary measurements		
Model chord length[1], c (m)	6.096E-01	5.000E-04
Contraction mean pressure[2], p_{con} (Pa)	1.132E+03	2.586E+01
Settling chamber mean pressure[3], p_{set} (Pa)	2.710E+03	2.586E+01
Barometer reading[4], p_{atm} (Pa)	9.120E+04	1.693E+02
Thermometer reading[5], T (K)	2.915E+02	2.000E-01
Intermediate calculations		
Reference Pitot-static pressure, q (Pa)	2.723E+03	6.308E+01
Air density, ρ (kg/m^3)	1.090E+00	2.156E-03
Dynamic viscosity, ν (kg/m/s)	1.805E-05	9.593E-09
Freestream velocity, V_∞ (m/s)	7.069E+01	8.219E-01
Final calculations		
Reynolds number, Re	2.601E+06	3.039E+04
Mach number, Ma	2.065E-01	0.002400023

[1] Uncertainty estimate based on wind tunnel engineers experience using the FaroArm® Coordinate Measurement Machine (rated accuracy of this machine is ±0.025 mm)
[2] Uncertainty estimate based on the ±0.15% full-scale quoted accuracy of the Esterline 9816/98RK pressure scanner with a range of ±2.5 psi (±10 in. of water scanners used for testing below 50 m/s and ±2.5 psi scanners used for testing above 50 m/s)
[3] Uncertainty estimate based on the ±0.15% full-scale quoted accuracy of the Esterline 9816/98RK pressure scanner with a range of ±2.5 psi (±10 in. of water scanners used for testing below 50 m/s and ±2.5 psi scanners used for testing above 50 m/s)
[4] Uncertainty estimate of 0.05 inches of mercury chosen as a conservative estimate of accuracy based on the resolution of the Validyne DB-99 Digital Barometer at 0.01 inches of mercury
[5] Uncertainty estimate based on the quoted accuracy of the Omega Thermistor type 44004

0.20m NACA 0012 at 41 m/s

	Nominal Quantity	Uncertainty
Primary measurements		
Model chord length[1], c (m)	2.008E-01	5.000E-04
Contraction mean pressure[2], p_{con} (Pa)	3.726E+02	3.732E+00
Settling chamber mean pressure[3], p_{set} (Pa)	9.131E+02	3.732E+00
Barometer reading[4], p_{atm} (Pa)	9.401E+04	1.693E+02
Thermometer reading[5], T (K)	2.881E+02	2.000E-01
Intermediate calculations		
Reference Pitot-static pressure, q (Pa)	9.324E+02	9.104E+00
Air density, ρ (kg/m^3)	1.137E+00	2.194E-03
Dynamic viscosity, ν (kg/m/s)	1.789E-05	9.648E-09
Freestream velocity, V_∞ (m/s)	4.050E+01	2.016E-01
Final calculations		
Reynolds number, Re	5.168E+05	2.907E+03
Mach number, Ma	1.190E-01	5.910E-04

[1] Uncertainty estimate based on wind tunnel engineers experience using the FaroArm® Coordinate Measurement Machine (rated accuracy of this machine is ±0.025 mm)
[2] Uncertainty estimate based on the ±0.15% full-scale quoted accuracy of the Esterline 9816/98RK pressure scanner with a range of ±10 in. of water (±10 in. of water scanners used for testing below 50 m/s and ±2.5 psi scanners used for testing above 50 m/s)
[3] Uncertainty estimate based on the ±0.15% full-scale quoted accuracy of the Esterline 9816/98RK pressure scanner with a range of ±10 in. of water (±10 in. of water scanners used for testing below 50 m/s and ±2.5 psi scanners used for testing above 50 m/s)
[4] Uncertainty estimate of 0.05 inches of mercury chosen as a conservative estimate of accuracy based on the resolution of the Validyne DB-99 Digital Barometer at 0.01 inches of mercury
[5] Uncertainty estimate based on the quoted accuracy of the Omega Thermistor type 44004

Wake Rake in Empty Test Section at 60 m/s (for the data of Figures 5.1 and 5.2)

	Nominal Quantity	Uncertainty
Primary measurements		
Contraction mean pressure[1], p_{con} (Pa)	8.155E+02	2.586E+01
Settling chamber mean pressure[2], p_{set} (Pa)	1.987E+03	2.586E+01
Barometer reading[3], p_{atm} (Pa)	9.401E+04	1.693E+02
Thermometer reading[4], T (K)	2.881E+02	2.000E-01
Sample value for rake Pitot pressure[5], p_0 (Pa)	2.014E+03	5.171E+00
Intermediate calculations		
Reference Pitot-static pressure[6], q (Pa)	2.020E+03	6.308E+01
Air density, ρ (kg/m^3)	1.137E+00	2.194E-03
Freestream velocity, V_∞ (m/s)	5.962E+01	9.326E-01
Final calculations		
Sample value for velocity fraction, $\frac{V}{V_\infty} = \sqrt{\frac{p_0}{0.5\rho V_\infty^2}}$	9.986E-01	1.565E-02

[1] Uncertainty estimate based on the ±0.15% full-scale quoted accuracy of the Esterline 9816/98RK pressure scanner with a range of ±2.5 psi (±10 in. of water scanners used for testing below 50 m/s and ±2.5 psi scanners used for testing above 50 m/s)

[2] Uncertainty estimate based on the ±0.15% full-scale quoted accuracy of the Esterline 9816/98RK pressure scanner with a range of ±2.5 psi (±10 in. of water scanners used for testing below 50 m/s and ±2.5 psi scanners used for testing above 50 m/s)

[3] Uncertainty estimate of 0.05 inches of mercury chosen as a conservative estimate of accuracy based on the resolution of the Validyne DB-99 Digital Barometer at 0.01 inches of mercury

[4] Uncertainty estimate based on the quoted accuracy of the Omega Thermistor type 44004

[5] Uncertainty estimate based on the ±0.03% full-scale quoted accuracy of the 16TC/Digital Temperature Compensated pressure scanner with a range of ±2.5 psi

[6] Reference Pitot-static pressure is calculated from the contraction and settling chambers' mean pressures (although the wake rake as described in Section 4.5 has static pressure probes as well as Pitot probes, the reference Pitot-static pressure is still calculated in the standard way from the contraction and settling chambers' mean pressures)